Behavior and Kinematic-Based Modeling of Short RC Walls under Seismic Loading

A thesis submitted in partial fulfillment of the requirements for the degree of Doctor of Philosophy in Applied Sciences by

Nikola Tatar

Université de Liège - Faculty of Applied Sciences

September 2020

Author's contact details:

Nikola Tatar

Structural Concrete Laboratory, Urban and Environmental Engineering Research Unit, University of Liège

+1/419, B52 Quartier Polytech 1, Allée de la Découverte 9, 4000 Liège, Belgium

Email: ntatar90@gmail.com, nikola.tatar@tractebel.engie.com

Members of Doctoral Jury

Prof. João Saraiva Esteves Pacheco De Almeida
Université catholique de Louvain

Prof. Paolo Calvi
University of Washington

Prof. Jean-Marc Franssen
Université de Liège

Prof. Vincent Denoël
Université de Liège

Prof. Frédéric Collin.
Université de Liège

Prof. Boyan Mihaylov
Université de Liège

Abstract

Motivated by the prevalence of seismic damage and failures in short walls, this work is a study on predicting their behavior. This was achieved by an experimental study and development/evaluation of several methods of analyses with varying complexity. The main goal was to develop simple and reliable procedures based on macro-kinematic modeling techniques for predicting the seismic response envelopes of short walls. The emphasis was put on the aspect of the practical application of the studied procedures from the viewpoint of modern performance-based design and assessment procedures.

The behavior of short walls was evaluated experimentally by loading to failure three cantilever wall specimens featuring a span-to-depth ratio of 1.7. The applied compression load was varied between the walls. The specimens had light shear reinforcement which is commonly observed in existing structures where modern seismic design concepts were not considered. The experimental data indicated that flexural deformation patterns and failures dominated the behavior of the walls. The lateral resistance of the walls increased with larger compressive load while accompanied with reduced displacement capacity at failure. Detailed measurements of the entire deformed shapes of the walls were conducted in the tests for developing and validating of macro-kinematic modeling procedures.

A new single-degree-of-freedom (SDOF) kinematic approach was developed to predict cyclic response envelopes of flexure-dominated walls. The approach combines an SDOF kinematic representation of the deformations in the wall and a sectional analysis of the base section. In nonlinear constitutive modeling, the approach considers various physical aspects of the behavior of walls, including the development of deformations due to cracking, simplified effects of shear, and modeling of concrete behavior in compression. The validation of the approach against the test data and a literature database showed a good agreement between predicted and observed behavior at both global and local level. The procedure combines simplicity and accuracy, and is suitable for application in performance-based design and assessment procedures.

Shear-dominated short walls were modeled using a three-parameter-kinematic theory (3PKT). The 3PKT uses three degrees of freedom kinematic model to describe the deformation patterns in diagonally cracked walls. In addition to kinematics, the 3PKT also includes equations for equilibrium and constitutive relationships for the load-bearing mechanisms in walls. This modeling approach is herein extended to account for the effects of barbells, strain penetration in the

foundation, cracking above the critical shear cracks, and stirrup ruptures. The validation of the approach with the test data from the literature of squat walls and walls with barbells showed promising results in predicting their global and local response. However, the analysis of the underlying assumptions of the 3PKT kinematics against the data from the experimental study highlighted the approach limitations in predicting the response of flexure-dominated walls.

In comparison to simple modeling, a more complex nonlinear finite element analysis approach in software VecTor2 was applied to short walls. This method is based on two widely-used theories for nonlinear behavior of reinforced concrete, the Modified Compression Field Theory and the Disturbed Stress Field Method. VecTor2 response envelopes were compared against experimental data to evaluate the suitability of this method for practical application. VecTor2 was found to accurately predict the force resistance. The limitations of this method were identifed to adequately predict the displacement capacity of short walls.

In conclusion, the main contributions of this work to the body of knowledge include: 1. the experimental findings from the tests on large-scale walls; 2. the SDOF kinematic model for flexure-dominated walls that can accurately predict both global and local behavior; and 3. the defined limitations for practical application of the 3PKT and SDOF kinematic approaches, and the finite element method in VecTor2.

Acknowledgments

I would like express gratitude to Prof. Boyan Mihaylov for his help in the development of this thesis. I owe thanks to the members of jury Prof. João Almeida, Prof. Paolo Calvi, Prof. Jean-Marc Franssen, Prof. Vincent Denoël, and Prof. Frédéric Collin for devoting their time to review this work.

I am thankful to all the wonderful people I have met at ULiège – all the friends and colleagues that I have interacted with made my studies a truly memorable experience. I would like to thank all the people with who I shared the office over the years, especially Jian Liu, Renaud Franssen, and Chatura Rajapakse.

Lastly, I owe the greatest gratitude to my closest family Stevo, Slavica, and Jovan, for their infinite support and love during my endeavors.

Table of Contents

List of Figures

List of Tables

Symbols

A_s	one-half of total area of longitudinal reinforcement
A_v	area of transverse reinforcement
C	compression force
I_g	gross moment of inertia of concrete section
M_{cr}	cracking moment of concrete section
T	tension force
E_c	concrete modulus of elasticity
F_b	compression force at base of fan
F_{CLZ1}, F_{CLZ2}	compression forces in the concrete of CLZ
F_{cn}, F_{ct}	normal and tangential contact forces at the bottom of critical diagonal crack
F_{ci}	aggregate interlock force

F_d	dowel action force
F_s	force in the stirrups
F_{sc}	force in vertical reinforcement in CLZ
F_t	force in vertical tension reinforcement
G_c	concrete shear modulus
N	axial load
V	shear force and lateral load
V_i	components of shear resistance
V_{max}	peak shear force and peak lateral resistance
a	M/V - wall height subjected to shear
b	width of wall cross section
b_b	width of barbell
c, x_{na}	length of compression zone
d	effective length of section
d_1	distance from compressive edge of section to furthest tension bar
d_b	diameter of vertical bar
d_{bv}	diameter of stirrup
f_b	stresses in compression zone in base section
f_c'	concrete cylinder strength
f_{cc}'	confined concrete strength
f_{ct}	concrete tensile strength
f_{ltp}	effective concrete later pressure
f_t	stresses along vertical tension reinforcement

f_{tc}	tensile strength of concrete
f_y	yield strength of reinforcement
f_{yl}	yield strength of vertical reinforcement
f_{yv}	yield strength of transverse reinforcement
f_u	strength of reinforcement
f_{ul}	strength of vertical reinforcement
f_{uv}	strength of transverse reinforcement
h	length of wall section
h_b	length of barbell
l_{b1e}	characteristic length of CLZ
l_0,l_1	vertical reinforcement pullout length bellow and above foundation
l_t	cracked length along flexural reinforcement
l_k	length of transition zone between fan and rigid block
m	modification factor for vertical strain profile
n	axial load ratio
n_{cr}	number of major diagonal cracks
s_{cr}	crack spacing
x_T	distance to tension force
y_{cr}	cracking height
w	crack width
w_s	crack opening in direction of stirrup
z	lever arm
α	angle of wall diagonal with respect to the vertical axis

α_1	angle of critical crack
γ	shear deformations in the block expressed in terms of drift
σ_c	concrete stress
σ_s, σ_{si}	steel reinforcement strain
δ	lateral drift ratio
δ_{po}	drift ratio due to pullout displacement
δ_u	lateral drift capacity
δ_x, δ_y , δ_z	x-, y-, and z- displacements of points from wall
Δ, Δ_{top}	top lateral displacement
Δ_{exp}	measured top lateral displacement
Δ_c	horizontal displacement at CLZ
Δ_{cx}	vertical displacement at CLZ
Δ_{fl}	top lateral displacement due to flexure
Δ_i	deformations of springs
Δ_{i0}	displacements of ends of springs attached to the fan (offset displacements)
Δ_{po}	pullout displacement of vertical reinforcement
Δ_s	top lateral displacement due to shear
Δ_{sl}	sliding displacement
Δ_y	lateral displacement at first yielding of longitudinal reinforcement
Δ_u	lateral displacement capacity
ε_b	strains across base section
ε_{c0}	concrete strain at peak stress

ε_{cc}	confined concrete strain at peak stress
ε_{cr}	cracking strain in concrete
ε_{cu}	confined concrete ultimate strain
ε_{t}	strains along vertical tension reinforcement
$\varepsilon_{t,avg}$	average strains along vertical tension reinforcement
ε_{y}	yield strain of vertical reinforcement
ε_{u}	rupture strain of vertical reinforcement
ε_{v}	strain in transverse reinforcement
ε_{yv}	yield strain in transverse reinforcement
ε_{uv}	rupture strain of transverse reinforcement
φ_{s}	serviceability limit state curvature
φ_{ls}	damage control curvature
φ_{y}	yield curvature
ρ_{l}	ratio of total vertical reinforcement
ρ_{s}	ratio of confining hoops and stirrups
ρ_{v}	ratio of transverse reinforcement
ρ_{lb}	ratio of vertical barbell or boundary zone reinforcement
ρ_{vb}	ratio of transverse barbell or boundary zone reinforcement
ρ_{lw}	ratio of vertical web reinforcement
ρ_{vw}	ratio of web barbell reinforcement
θ_{b}	angle of force F_b with respect to the vertical axis
θ_{cr}	inclination of dominant shear crack
ϑ	rotation of rigid block

1 Introduction

1.1 Short walls in existing structures

Reinforced concrete (RC) walls are structural components that are commonly encountered in buildings and bridges around the globe. Owing to their relatively high in-plane stiffness, they are widely applied and economical alternative for axial and lateral load resisting systems in civil engineering structures. Walls that are properly designed and positioned in the layout of the structure lead to an adequate response with good control of lateral deflections in structures subjected to seismic loading. A ductile response in slender walls is achieved through proper reinforcement detailing that enables energy dissipation through yielding of flexural reinforcement. While the behavior of slender walls governed by flexure is well understood, predicting the response of short walls is still a challenging problem due to the significant effects of shear forces. Examples of short structural walls as the substructure of bridges are shown in Figure 1-1.

The behavior of walls is generally classified based on the aspect ratio (a/h), i.e. the ratio of shear span to section depth. A wall is considered short if it has an aspect ratio of less than about 3. Within this range of geometry, there is a transition between different shear resisting mechanisms governing the behavior of walls. This was observed in early tests of RC beams without stirrups conducted by Kani (1964). In slender members, the main resisting mechanism is attributed to beam action. In this case, the forces are transferred through the uncracked concrete in the compression zone, aggregate interlock mechanism across the cracks, and dowel action of longitudinal reinforcement. With a decreasing aspect ratio, the behavior becomes dominated by strut (arch) action, in which the forces on the beam are transferred through direct inclined compression (struts). The tests on RC beams have shown that the normalized shear stresses in shorter beams at failure are significantly is larger than in slender members (Kani, 1964).

The interaction between different force-resisting mechanisms and the combination of shear, flexure, and axial forces under seismic loading conditions, renders behavior patterns in such walls complex. Understanding and predicting the behavior of short walls is the main problematics being examined in this thesis.

Highway Brussels-Namur-Ardennes

Overpass on highway A3 near Baelen

Bridge on highway Brussels-Paris

Figure 1-1. Short wall-type bridge piers (Source: Service Public de Wallonie)

1.2 Research Motivation

Contemporary design and assessment building codes impose exigent requirements for seismic resistance of structures. A large number of buildings and bridges built over the last century often do not meet modern seismic safety standards. A recent survey on the seismic vulnerability of European building stock has outlined that a vast majority of the buildings were built without considering seismic provisions in the design (Palermo et al., 2018). As a consequence of traditional design and construction practices, existing structures often feature deficiencies from the perspective of seismic resistance, such as a low amount of transverse reinforcement and a lack of confining reinforcement. These issues can also be accompanied by the detailing deficiencies such as lap splices of inadequate length, not properly closed stirrups (without hooks), and welding of reinforcement rebars that create local brittleness. Such practices lead to brittle failures in structural members and a relatively low capacity to dissipate energy. Damage in walls has been documented after nearly all major earthquakes in the past. A few of the numerous examples of damage and failures in short RC walls of existing buildings and bridges in seismic regions are shown in Chapter 2.

Modern seismic design and assessment procedures of civil structures are based on the concept of performance-based earthquake engineering (PBEE). Considering the inherently stochastic nature of earthquakes, PBEE is envisioned to encompass a probabilistic risk quantification approach. Within this approach, a system performance evaluation is performed through four steps, including seismic hazard assessment, structural response analysis, damage measure evaluation, and loss analysis. Each step of the evaluation can be mathematically characterized by the following variables: intensity measures (IM), engineering demand parameter (EDP), damage measures (DM), and decision variables (DV), respectively. In a broad definition of this framework, these variables are expressed as conditional probabilities of exceedance considering their intrinsic variabilities under the assumption that conditional probabilities between parameters are independent (Moehle & Deierlein, 2004; Günay & Mosalam, 2012).

Current seismic design and assessment guidelines adopting the concept of PBEE (CEN, Eurocode 8, 2005; ASCE 7-16, 2016; ASCE 41-13, 2014) define desired performance objective which is represented by a set of performance levels for discrete hazard levels. The performance assessment is based on a defined set of EDPs which characterize the response of the structural system. The traditional guidelines relied on the use of global EDPs, such as base shear, story forces, and inter-story drifts. However, with the recent advancements in the analysis procedures and computing tools, the current codes promote the use of local EDPs at the sectional and material level. Examples of local EDPs are rebar strain, concrete strain in compression, curvature, curvature ductility, etc. The reason for this is that the local EDPs are better indicators of the extent of damage experienced by the structural system in a seismic event. It was identified that the shortcomings in the PBEE procedures stem from the inconsistencies in the component performance evaluation, which are based on test data, calculated by analytical models, or assumed on the basis of engineering judgment (Moehle & Deierlein, 2004). To attain the key aspect of PBEE, which is a better risk-informed decision making, it is indispensable to use reliable analytical and numerical procedures that can accurately predict all the aspects of the response of structural systems and components.

In the literature, there are many different approaches developed for predicting the behavior of short walls, varying in their levels of complexity. The simplest procedures available in the codes are usually based on empirical models and yield conservative predictions in terms of force and displacement capacity. With the increasing complexity, a majority of the procedures often require a choice of increasing number of parameters to be considered in the analyses. This means that significant expertise and sound engineering judgment is necessary for proper interpretation and application of the results of the analyses. Another trait of existing procedures is that they are often validated only on a few case studies. As a consequence, the actual range of application and confidence in the predictions of systems with varying properties and loading conditions of such procedures are unknown. In addition, a recent study by Almeida et al. (2016), investigated the suitability of different methods of analysis to predict the behavior of walls. The study outlined that there is evidence about inconsistencies of different methods for evaluating the behavior of walls in terms of both global and local response of walls. A gap in the existing procedures is identified in terms of the ease of practical application, extent of applicability, and adequate correlation between predictions of global and local response parameters.

1.3 Research objectives and general methodology

Consistent with the outlined needs of the modern design and assessment procedures, the main goal of this research work is to develop reliable and efficient procedures for predicting the behavior of walls under seismic loading. This goal is subdivided into three main objectives:

1. To provide detailed experimental evidence and analysis on the cyclic behavior of short walls by using modern measurement techniques (i.e. light-emitting diode scanner and digital image correlation)

2. To develop and validate efficient kinematics-based models for the complete global and local behavior of short walls using a small number of degrees of freedom (low fidelity models)

3. To perform an extensive validation of a nonlinear finite element method (high fidelity) for the evaluation of short shear walls, and to propose guidance for the proper application and limitations of the method.

To achieve these objectives, an experimental campaign was planned to test to failure three large-scale wall specimens in a quasi-static cyclic manner under combined actions of axial and lateral load. The emphasis of the tests was to obtain detailed measurements of the global and local behavior, and the complete displacement fields developing across the surface of the test specimens using modern measurement techniques. From the perspective of modeling the behavior of short walls, this research is focused on developing low-fidelity models based on macro-kinematic modeling techniques. Such procedures rely on simplifying the deformations in a wall based on a small number of degrees of freedom. In this context, the experimental data is useful for the validation and development of such kinematic-based procedures. In comparison to simple modeling, the suitability for practical application of a nonlinear finite element method (high fidelity) is evaluated. All the modeling procedures considered are subjected to an extensive validation against the test data in the literature with the intent to provide recommendations for their practical application for studying the behavior of short walls.

1.4 Thesis outline

Chapter 2 gives a brief overview of the state-of-the-art on the problematics of short shear walls in concrete structures. Some notable examples of observed damage and behavior patterns from previous earthquakes are shown. This is followed by a summary of experimental studies reviewed in the development of this thesis. Finally, the main methods for the analysis of walls available in the literature are briefly described and discussed.

In Chapter 3, the experimental campaign performed in the framework of this thesis is presented. The experimental campaign consisted of testing to failure of three large-scale wall specimens under quasi-static reversed cyclic loading. The detailed information about the test specimens, instrumentation, test setup, and loading is presented. This is followed by a presentation and discussion of the test observations.

Chapter 4 is focused on the macro-kinematic modeling of the behavior of short walls. The central modeling approach of this thesis, a three-parameter kinematic theory (3PKT, Mihaylov et al., 2016) for the analysis of shear-dominated walls is summarized. The 3PKT is extended in this thesis to account for additional physical aspects of behavior of short walls and its validation is extended to squat wall specimens. However, the results of the experimental study in Chapter 3 showed the limitations in the formulation of the 3PKT kinematics to adequately describe deformations in flexure-dominated walls. To address this, a new approach based on a single-degree-of-freedom (SDOF) kinematics is proposed. The SDOF kinematics is used as a basis for a complete mechanical model that can predict the load-displacement envelope of flexure-dominated short walls. This approach is thoroughly validated with the available test data in the literature and shows prospects towards the application in performance-based seismic procedures.

Chapter 5 investigates a finite element procedure implemented in the software Vector2. The approach in this software is based on the Disturbed Stress Field Model (DSFM, Vecchio, 2000) and the Modified Compression Field Theory (MCFT, Vecchio & Collins, 1986) for the nonlinear behavior of concrete structures. Analyses were performed on a dataset of available wall tests which were compared to the experimental responses. The results were discussed in terms of the suitability of this method to predict the lateral behavior of short walls.

Finally, Chapter 6 draws the main conclusions of this study and provides recommendations for further development of kinematic-based modeling procedures.

2 Literature Review

2.1 Damage in walls from past earthquakes

The experience collected through observations of damage in walls during previous severe earthquakes gives valuable insight into their behavior. This section shows notable examples of damage and failures that are used to distinguish typical behavior patterns in walls.

The failure modes in walls can be divided into flexural failure, diagonal shear failure, diagonal compression failure, sliding shear failure, out-of-plane buckling failure, and bond failure along lapped splices of anchorage (Priestley & Paulay, 1992). The failures in walls are characterized by a significant degradation or loss of the lateral load-resisting capacity and stiffness and do not imply the collapse of the structure. Upon losing the lateral capacity, walls often retain the ability to transfer vertical loads to a certain extent. However, the load resisting mechanisms in walls are interrelated and the degradation of the horizontal load capacity can ultimately compromise the axial capacity and cause collapse.

Walls designed to withstand seismic actions rely on the energy dissipation through the flexural yielding of the longitudinal reinforcement in defined plastic hinge zones for achieving a ductile response. In cantilever walls, the inelastic deformations in plastic hinges occur at the level of the critical base section. The ductile response is achieved by applying capacity design concepts and proper reinforcement detailing, such that the brittle failure modes limiting the deformation capacity of the wall are suppressed (Priestley & Paulay, 1992). However, older structures designed without seismic provisions are often characterized by brittle behavior in flexure. The examples of flexural damage and failures are associated with the damage in the tension or compression chord at the critical base section, such as rupture of the rebars in tension or crushing of the concrete in compression, are shown in Figure 2-1. Premature failures in flexure are accentuated with inadequate detailing of the flexural and shear reinforcement. Not properly closed stirrups (90° hooks) with large spacing lead to premature crushing of the concrete which is accompanied by the buckling of the reinforcement in compression. The failure along lap splices of insufficient length in critical sections is another example of detailing deficiencies limiting the strength and displacement capacity in flexure.

Figure 2-1. Examples of flexural damage in walls (adapted from Elwood, 2013)

The effects of shear become increasingly evident in the response of walls with decreasing aspect ratios (a/h). Shear failures are considered as highly unfavorable from the point of view of the seismic response of walls due to their brittle nature. Particularly brittle shear failures occur when the shear capacity of a member is lower than the demand corresponding to the yielding moment. This type of failure, a diagonal shear failure, occurs at relatively small displacements thus limiting the deformation capacity of the member. The diagonal shear is characterized as the failure along significant diagonal cracks and can often be accompanied by the axial load failure due to sliding of the supported structure along the cracks. Examples of diagonal shear failures in wall-type piers are shown in Figure 2-2.

Shear failures can occur even if the shear capacity of the member is sufficient to develop the ultimate moment capacity in the critical section. In this case, the shear demand does not significantly increase and the failure is triggered due to the increasing deformation demand on the member and the cyclic degradation of the shear-resisting mechanisms. This type of shear failure, which is preceded by the yielding of flexural reinforcement, is often referred to as the "ductile" shear failure. An example of shear failure due to the increasing inelastic deformations (that caused the loss of axial load carrying capacity) in the plastic hinge region is shown in Figure 2-3.

Hanshin Expressway Pier 57 after Kobe earthquake 1995

(Source: Christopher R. Thewalt, NISEE)

Wu-His bridge after Chi-Chi earthquake 1999

(Source: Jack P. Moehle, NISEE)

Figure 2-2. Diagonal shear failures in bridge piers

Mission Gothic bridge after Northridge earthquake 1994

(Source: Graham C. Archer, NISEE)

Figure 2-3. Shear failure within plastic hinge region

Another type of shear failure shown in Figure 2-4 is referred to as sliding shear failure. The sliding can occur due to the large opening of flexural cracks along the construction joints. With the increasing deformation demand on the member, the accumulation of the inelastic strains can prevent large cracks from closing upon load reversals, which can result in the sliding of the wall along the construction joint. Even though this type of failure is not catastrophic, i.e. it does not cause the loss of strength in the member, the loss of stiffness upon the load reversals affects the redistribution of forces in the structure subjected to ground shaking.

Wu-His bridge after Chi-Chi earthquake 1999

(Source: Jack P. Moehle, NISEE)

Figure 2-4. Sliding shear failure in wall pier

Figure 2-5 shows the examples of damage in walls that were documented after the Chile (2010) and New Zealand (2011) earthquakes (Wallace et al. 2012; Kam et al., 2011). The examples shown include shear failures, compressive buckling failures, shear-compressive failures, and failures due to lateral instability in the boundary elements. The inadequate amounts and detailing of the shear and confining reinforcement were reported as the leading causes of the shear failures and compressive buckling failures, respectively.

The examples of damage shown in this section are intended to distinguish the typical failure modes encountered in short walls. However, it is noted that the failures in walls can occur in mixed modes. One example of such failure is shown in Figure 2-5b and can be described as a shear-compressive failure. A large portion of the wall web failed due to large compressive stresses. The damage also extended diagonally through the web suggesting that the large shear stresses have contributed to the observed failure. Lateral instability failures were observed in the thinner and more slender walls with minimum amounts of reinforcement and higher levels of axial load ratios (Kam et al., 2011).

Shear and axial failures | Lateral instability failure

Compressive buckling failures in boundary zones

a) Chile 2010 earthquake (adapted from Wallace et al., 2012)

Shear-compressive failure | Lateral instability failure

b) New Zeland (2011) earthquake (adapted from Kam et al., 2011)

Figure 2-5. Damage in walls in Chile (2010) and New Zealand (2011) earthquakes

2.2 Experimental studies on short walls

Table 2-1 summarizes the experimental test reports on short walls from the literature considered in this study and briefly describes their content. The descriptions outline the main test variables and characteristics of the walls considered from each reference.

This database represents a collection of tests on cantilever reinforced concrete short walls featuring aspect ratios ranging from 0.3 to 3.1, and it primarily consists of wall specimens with rectangular sections. Several walls with barbell-shaped sections were also considered, although an extensive review of such walls is outside of the scope of this thesis. In terms of reinforcement, a general distinction can be made between walls with non-seismic and seismic reinforcement detailing. The walls with simple (non-seismic) reinforcement detailing usually have uniformly distributed longitudinal and transverse reinforcement. In contrast, the walls with the reinforcement detailed for seismic resistance feature concentrated longitudinal reinforcement and confining ties and hoops in the boundary zones. The specimens in the database have longitudinal web reinforcement ratios ρ_l ranging from 0.18% to 2.5%, while transverse web reinforcement ratios ρ_v are between 0.08% and 1.5%. In the boundary zones, the walls have longitudinal reinforcement ratios ρ_{lb} between 0.9% and 8.3%, and volumetric ratios of the confining hoops and stirrups ρ_s from 0.64% to 4.6%. The walls were subjected to the compression loads corresponding to axial load ratios N/bhf'_c from 0% to 30%. The effects of lap splices or diagonal reinforcement are not studied and walls with such characteristics were not included in the database. The majority of walls in the database were tested under the quasi static-cyclic loading conditions. Only in a couple of studies, the walls were tested under monotonic loading which is indicated in the test descriptions in Table 2-1.

It is noted that three datasets of wall tests were used in different parts of the thesis depending on the modeling procedure being evaluated. The criteria for the selection of the datasets are described in the respective section of the text where they are utilized. Important test observations are also discussed in the evaluation of the modeling procedures considered. The characteristics of the wall specimens in the database, in terms of dimensions and aspect ratios, reinforcement ratios and properties, concrete strength, and level of axial load are summarized in Table 4-2, Table 4-3, Table 4-6. , and Table 5-1. The database consists of a total of 76 tests from 18 different studies.

Table 2-1. Summary of database of wall tests

Reference	Description of test specimens
Bimschas (2010) Hannewald et al. (2013)	Four large-scale wall piers lightly reinforced in shear were tested to failure. Walls featured aspect ratios from 2.2 to 3 and uniformly distributed reinforcement with variable amounts of transverse and longitudinal reinforcement ratios.
Hirosawa (1985)	Ten wall specimens were considered out of a large number of tests summarized in the report. The specimens had an aspect ratio of 1.0, with varying amounts of boundary reinforcement, stirrups, and levels of axial compression load.
Luna et al. (2015)	Twelve rectangular squat walls with aspect ratios between from 0.3 to 0.9 and varying amounts of reinforcement. Axial load was not applied to the specimens.
Tran et al. (2002)	Five rectangular walls with varying aspect ratios (1.5 – 2), axial load level, and design shear stress levels.
Lefas et al. (1990)	Thirteen short rectangular walls were tested under monotonic loading. The study investigates the effect of aspect ratio, axial compression load, concrete strength, and the amount of web horizontal reinforcement on wall behavior.
Wiradinata (1985)	The study considers the effect of aspect ratio on two wall specimens with a/h of 0.3 and 0.6. The walls featured uniformly distributed reinforcement in both directions with confined boundary zones.
Oh et al. (2002)	Three rectangular wall specimens with an aspect ratio of 2 were tested to investigate the effect of the amount of confining reinforcement.
Hsiao et al. (2008)	One squat wall is considered with an aspect ratio of 0.65 and a barbell-shaped section.

Table 2-1. Summary of database of wall tests (continued)

Maier and Thurlimann (1985)	Three rectangular wall specimens considered featuring an aspect ratio of 1 that were tested under monotonic loading. The specimens feature uniformly distributed longitudinal and transverse reinforcement and differ with respect to the provided reinforcement ratios in each direction.
Dazio et al. (2009)	Six rectangular walls were considered with an aspect ratio of 2.3. The specimens differ in the amount of longitudinal web and boundary zones reinforcement, amount of confining reinforcement, and level of axial compression load.
Salonikios et al. (1999)	Six short walls that had aspect ratios of 1 and 1.5 were considered. Other than aspect ratio, the specimens differ with respect to the ratios of longitudinal and transverse reinforcement in the web, volumetric ratio of confining reinforcement, and the level of axial compression load.
Zhang et al. (2010)	Two wall specimens were considered with an aspect ratio of 2, varying in the amount of confining reinforcement in boundary zones.
Ghorbano-Renani et al. (2009)	One wall specimen was considered with an aspect ratio of 2.1 featuring confined boundary zones.
Thomsen (1995)	Two test walls featuring an aspect ratio of 3.1 varying in the amount of the confining stirrups in the boundary zones are considered.
Oesterle et al. (1976)	Two wall specimens featuring aspect ratios of 2.4 with varying amounts of confining boundary reinforcement are considered.
Mestyanek (1986)	Two barbell-shaped walls are considered with aspect ratios of 1.5 and 2 featuring a different height of the sections and concrete strengths.
Hwang et al. (2004)	Two squat walls with aspect ratio 0.51 and barbell-shaped sections, featuring different web widths, longitudinal and transverse web reinforcement ratios were considered.

2.3 Overview of methods for analysis

There exist a range of approaches for calculating the load–displacement behavior of cantilever walls based on different modeling assumptions and featuring variable levels of complexity. Figure 2-6 summarizes some of these approaches arranged in order of increasing complexity and decreasing computational efficiency.

The simplest way to evaluate the response of cantilever walls is to use codified equations for key points along the load-displacement curve (ASCE 41-13, 2014) (Figure 2-6a). These points typically include the development of major shear cracks (point B), the onset of significant plastic deformations (C), the displacement capacity of the wall (D), and the residual lateral resistance at larger drift ratios (E and F). While this approach is convenient and typically provides conservative estimates of displacement capacity, more refined models are needed in cases where conservative predictions may result in costly and disruptive retrofit of existing structures.

A slightly more complex approach consists of the so-called plastic hinge models where all plastic deformations are lumped in a plastic hinge at the base of the wall (ASCE 41-13, 2014; Biskinis & Fardis, 2010; CEN, Eurocode 8, 2005; Priestley et al., 2007) (Figure 2-6b). The moment–rotation relationship of the plastic hinge is obtained on the basis of a moment-curvature analysis and an estimated length of the plastic hinge. However, as this approach focuses on flexural behavior, it is not well suited for capturing shear failures that develop in short walls after flexural yielding.

Approaches that focus on the interaction between flexure and shear in walls include vertical-line-element models and shear-panel-element models (Chen and Kabeyasawa, 2000) (Figure 2-6c). These models feature a simple discretization of the wall by using a small number of nonlinear springs and shear panel elements. They are typically used to represent a portion of multi-story walls located between two floor levels. However, these approaches assume a smooth compression field in the web of the wall, and therefore are not suitable for short walls that develop direct diagonal compression (strut action). Several approaches were extended from the vertical-line-element models (Orakcal et al., 2004; Massone et al., 2006), and they incorporate reinforced concrete panel behavior in a macroscopic fiber-based model. In the literature, there is a number of fiber-based models (Kaba & Mahin, 1984; Petrangeli et al., 1999); however, they were traditionally developed for the analysis of slender elements.

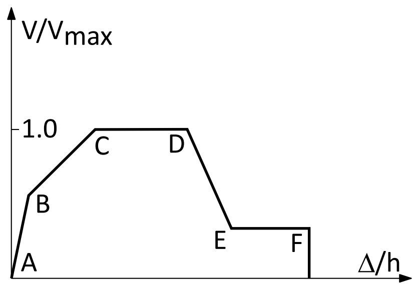

a) Code envelope of V-Δ (ASCE 41 2014)

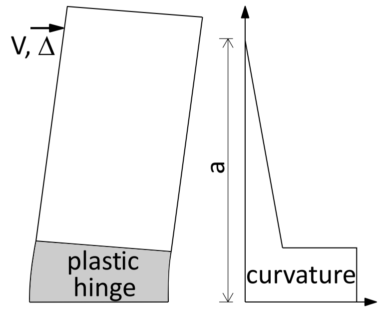

c) Plastic hinge models (Priestley et al, 2007)

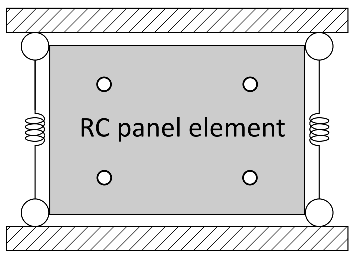

c) Shear-panel-element models (adapted from Chen and Kabeyasawa, 2000)

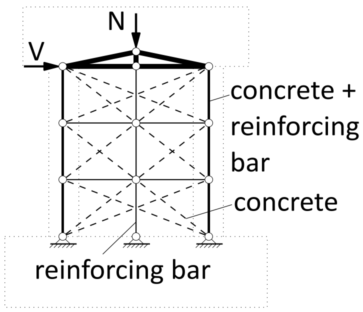

d) Equivalent truss models (adapted from Park and Eom, 2007)

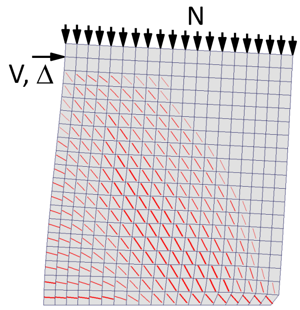

e) Nonlinear finite element models (VecTor2, Vecchio 2000)

Figure 2-6 Modeling approaches for cantilever reinforced concrete walls

In part to address this issue, several researchers have proposed equivalent truss models (Mazars et al., 2002; Park & Eom, 2007; Panagiotou et al., 2012) (Figure 2-6d). In these models, the wall is discretized with a number of horizontal, vertical, and inclined 1D truss elements representing tension reinforcement (ties) and compression stresses in the concrete (struts). The struts and ties are assigned nonlinear load–displacement relationships based on the stress–strain characteristics of the materials. A major difficulty with this approach is the choice of the geometry of the model – i.e. layout and inclination of struts, cross-sectional dimensions of struts, mesh size – that can have a significant impact on the results. In addition, this approach does not model explicitly the critical shear cracks, and therefore is not suitable for evaluating crack widths and the aggregate interlock resistance across the cracks.

The estimation of crack widths as a function of the lateral load is needed in the assessment of walls damaged by strong earthquakes. By comparing measured and predicted crack widths, the predicted load versus crack width response can be used to evaluate the residual capacity of the wall. Crack widths and other local deformations can be evaluated with nonlinear finite element models (FEMs) as shown in Figure 2-6e. Some formulations of the behavior of reinforced concrete membrane elements used for FEM analysis can be found in Bazant & Oh (1995), Vecchio (2000), and Kagermanov & Ceresa (2016). These models account for the complex behavior of cracked reinforced concrete, and in this way, can provide realistic predictions of the state of the structure. At the same time, FEMs require significant time for modeling and computations, as well as significant expertise to use safely as discussed in detail in Chapter 5. Therefore, there is a need for sufficiently simple rational models that can capture the strut action in short walls and at the same time provide estimates of displacement capacity and local deformations.

A macro-kinematic based modeling approach called a three-parameter kinematic theory (3PKT) (Mihaylov, et al. 2016) is herein considered as one of the central methods of analysis. The 3PKT incorporates a kinematic description of deformations in shear-dominated walls. As it uses only three degrees of freedom (DOFs) to capture both global and local deformations, the 3PKT is aimed at combining simplicity and accuracy for predicting the response of shear-dominated walls. Chapter 4 summarizes the formulation of the 3PKT and extends the original approach with considerations of additional physical aspects of the behavior of short walls.

3 Experimental Campaign

3.1 Overview

The experimental program carried out within the framework of this study consisted of testing to failure of three large-scale cantilever wall specimens under the actions of constant compression load and reversed cyclic lateral loading applied in a quasi-static manner. The specimens were meant to represent existing short walls common in the older construction. Such walls are characterized by relatively low transverse reinforcement ratios, no confinement reinforcement, and the absence of seismic detailing of the reinforcement.

The design of the test specimens was conducted taking into account existing databases of short wall tests. In terms of aspect ratio, the value that was found appropriate was 1.7, taking into account the missing values from past tests. The reinforcement was designed to closely resemble a test series by Bimschas (2010) studying existing bridge piers. The main test variable was adopted to be the magnitude of the axial compression load applied on the specimens since it has a significant impact on the failure mechanism and displacement capacity. Increasing compression is also important for consideration due to the evidence of significant increase in traffic loads on existing bridges (Herbrand et al., 2017).

One of the goals of this experimental program is to investigate the displacement capacity and possibility of development of brittle failures in short wall-type piers with detailing deficiencies when subjected to different levels of axial compression. This work also considers kinematic-based modeling techniques that use simplifying assumptions for the deformations developing in the wall. Consequently, the emphasis was put on obtaining the complete deformation patterns and the detailed local measurements in the critical regions of the specimens.

3.2 Test specimens

3.2.1 Geometry and reinforcement layout

The test specimens of this experimental program were three cantilever walls named CW0, CW1, and CW2 which were designed to be identical with respect to all their properties. As the main test variable was the level of axial compression force, walls CW0, CW1, and CW2 were loaded to 0, 10%, and 21% of their axial load capacity bhf'_c, respectively. The dimensions of the test region of the specimens are shown in Figure 3-1. Each wall had a cross-section of a length h=1500 mm and a width b=230 mm with the axis of the horizontal load positioned at 2550 mm from the base section, resulting in the aspect ratio of a/h=1.7. The main information relevant to the geometry, reinforcement layout, and material properties of the test specimens is summarized in Table 3-1.

Figure 3-1. Specimen dimensions (mm)

The reinforcement layout of the test region of all three specimens is shown in Figure 3-2. The specimens featured uniformly distributed reinforcement in the longitudinal and transverse direction. All the specimens were designed to be identical with the longitudinal reinforcement ratio ρ_l of 0.79%, which was provided for specimen CW0 using 24 bars of Ø12 mm. Due to a construction error, specimens CW1 and CW2 were missing two rebars in the two outer layers of the section, rendering their reinforcement ratio slightly smaller (0.72%). The longitudinal bars were anchored deep in the foundation with 90-degree hooks. The transverse reinforcement of the specimens was designed to resemble existing construction, thus featuring a relatively low ratio ρ_v of about 0.15%, provided using closed Ø8 mm stirrups spaced at 300 mm. No special attention was devoted to detailing of the reinforcement; the stirrups were closed with 90-degree hooks and their spacing was kept constant along the length of the wall, as common in existing walls of older construction. The clear cover to reinforcement was 25 mm.

The foundation and top concrete blocks were heavily reinforced to avoid significant cracks and deformations and to obtain the clearest possible boundary conditions for testing.

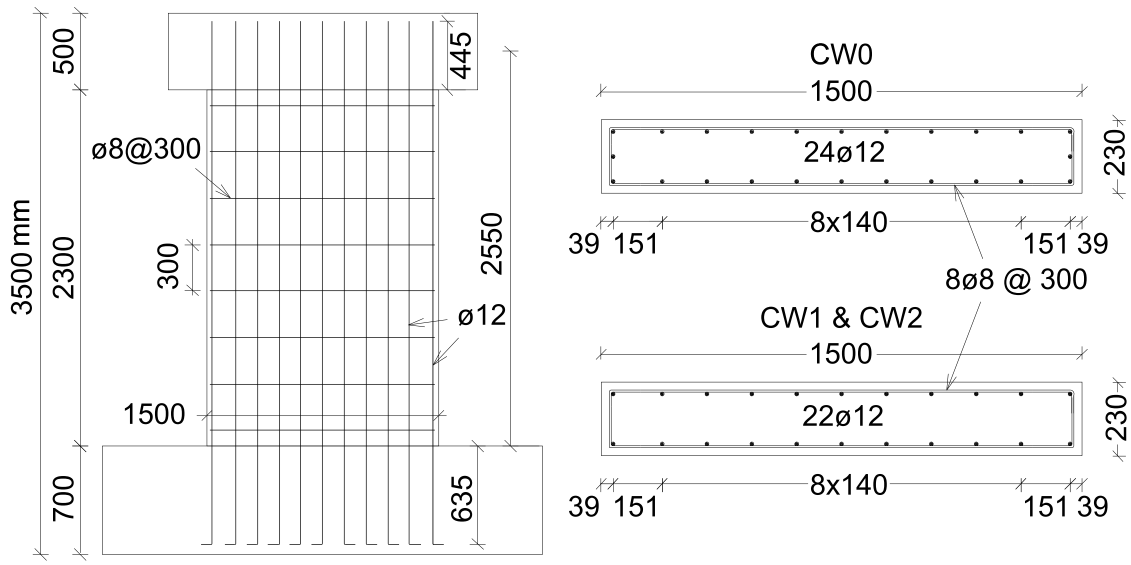

Figure 3-2. Reinforcement layout in test region

Table 3-1. Main characteristics of test specimens

Specimen ID	b mm	h mm	a/h mm	ρ_l %	ρ_v %	f'c MPa	f_{yl} MPa	f_{ul} MPa	f_{yv} MPa	f_{uv} MPa	$\frac{N}{bhf'_c}$
CW0				0.79	0.15	25.2					0
CW1	230	1500	1.7	0.72	0.15	38.1	530	620	540	640	0.10
CW2				0.72	0.15	36.6					0.21

3.2.2 Construction

The construction of the specimens was performed by a contractor in a precast concrete factory. The walls were cast one by one within a time span of a couple of months. Table 3-2. summarizes the dates of the wall construction and the scheduling of the tests.

Table 3-2. Scheduling of construction and testing

Specimen ID	Casting date	Testing date	Age at the day of testing (days)	Test duration (days)
CW0	10/12/2015	17/06/2016	190	2
CW1	08/01/2016	23/08/2016	228	1
CW2	15/01/2016	04/10/2016	263	1

The casting of the specimens was performed in the vertical position, to more closely resemble the cast-in-place of existing structures, and was performed in three phases. The first phase consisted of concreting of the foundation block, the second phase of the wall section, and the third of the top concrete block. To observe possible effects of sliding deformations along the base section, no special attention was devoted to the construction joint surface at the interface of the foundation and wall section, which was kept with its natural roughness. After the specimens were constructed, they were painted in white to achieve better visibility of cracks during testing. Some photos taken during the construction are shown in Figure 3-3.

Figure 3-3. Construction of specimens

3.2.3 Materials

The concrete ordered for the construction of the walls was specified to be of class C25/30, which corresponds to a characteristic cylinder strength (5% fractile) of 25 MPa. Based on past experience, it was expected that the actual mean strength would be in the range of 35 – 40 MPa. The concrete had a maximum aggregate size of 16 mm.

The stress-strain behavior of the concrete in compression was obtained from tests on cylinder samples (Figure 3-4). The cylinders were cast with the wall specimens and were kept close to them in the same curing conditions until the day of testing. Table 3-3 summarizes the information from the compression tests on the cylinders, including the dimensions of the cylinders, compressive strength (f'_c), strain at f'_c (ε_{c1}), and modulus of elasticity (E_c). For wall CW0 and CW1, three cylinders 160/320 mm were tested to obtain the average concrete properties. Cylinders were not cast for wall CW2, so one 115/230 mm cylinder was extracted from the middle top portion of the wall prior to the wall test, away from the failure zone where insignificant deformations were expected. To ensure a smooth flow of the stresses in the wall during the test, the cylindrical opening due to the drilling of the concrete sample in CW2 was grouted. All the cylinders were tested one day before the test of their respective wall.

The reinforcement used for the construction of the walls was BE 500 S, with a characteristic yield strength of 500 MPa. This reinforcement corresponds to ductility class B as per classification in EN 1992-1-1 (CEN, Eurocode 2, 2005). Samples of the reinforcements were tested in tension, resulting in the stress strain behavior of steel shown in Figure 3-5. One sample of the Ø12 longitudinal rebar was tested and had a yield strength of about 530 MPa and tensile strength of 620 MPa. Two samples of the transverse reinforcement Ø8 were tested, with an average yield and ultimate strengths of 540 MPa and 640 MPa, respectively. As evident from Figure 3-5, the reinforcing steel did not have a pronounced yield plateau and was moderately ductile with the average deformation at rupture of about 8%.

Cylinder test

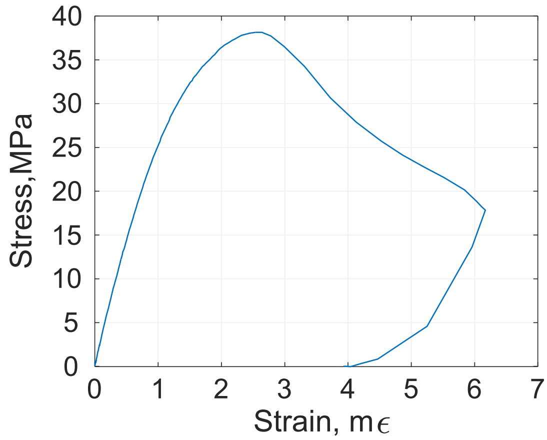

Typical concrete σ-ε curve (wall CW1)

Figure 3-4. Concrete cylinder testing

Table 3-3. Concrete compression tests

Wall ID	Cylinder dimensions			Average measurements		
	Diameter	Height	Measuring base	f'_c	ε_{c1}	E_c
	mm	mm	mm	MPa	mε	GPa
CW0	160	320	166	25.2	2.74	22.3
CW1	160	320	166	38.1	2.52	28.6
CW2	115	230	113	36.6	2.39	27.4

Notation: f'_c - concrete strength; ε_{c1} – strain at peak stress; E_c - modulus of elasticity

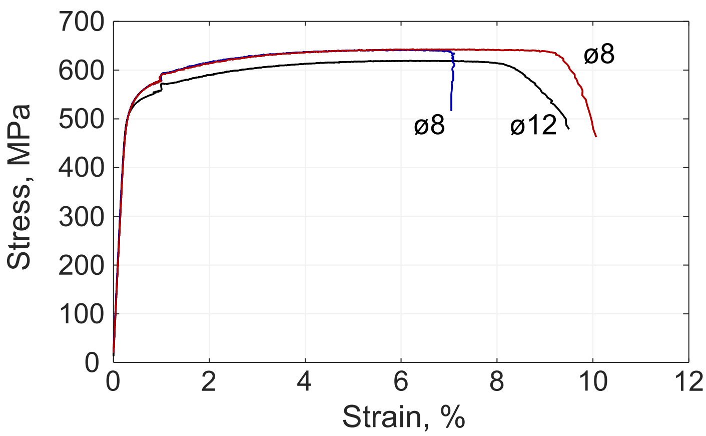

Figure 3-5. Stress-strain relationship for rebars in tension

3.2.4 Test Setup

A drawing of the test setup which was designed to create proper testing conditions for the wall specimens is shown in Figure 3-6. The test setup and tests were realized in the Structural Laboratory (Laboratoire de Mécanique des Matériaux & Structures) at the University of Liége.

The specimens were placed on the strong floor on a layer of dry grouting material to achieve good contact between the surface of the foundation and the strong floor. The foundation of the specimens was anchored to the strong floor via 10Ø36 prestressed DYWIDAG bars. The prestressing force was determined from the condition to avoid any uplift or sliding of the foundation during the tests. Even though the level of the prestressing force should have been enough to prevent sliding of the specimens, stiff plates were placed at the level of the base of the foundation on each side of the specimens to provide additional restraint against this type of movement. The axial load on the specimens CW1 and CW2 was applied by using three pairs of Ø32 DYWIDAG prestressing bars, which were pulled down by three hydraulic jacks installed below the strong floor. The axial load applied in this manner does not introduce second-order (P-Δ) effects in the response of the specimens, as the inclination of the compression force follows the rotation of the top concrete block with increasing horizontal displacements.

The hydraulic actuator that was used to apply the horizontal load had a maximum capacity of 2000 kN in the “pushing” direction and 1000 kN in the “pulling” direction. The maximum stroke of the jack was 400 mm. The actuator was connected to a steel hinge connector, which was attached to the top block by means of eight post-tensioned bars running through openings in the block. On the opposite end, the actuator was connected to a resisting steel frame through another steel hinge connector. The horizontal loading was applied by manually controlling the oil pressure in the hydraulic pump.

Two lateral steel frames that served as lateral supports were placed on each side of the specimen. Supports with teflon pads were attached to the lateral frames and were placed a few millimeters from the top concrete block, thus limiting out-of-plane movement of the walls, while allowing for unrestrained in-plane movement. A photograph of the realized test setup described above is shown in Figure 3-7.

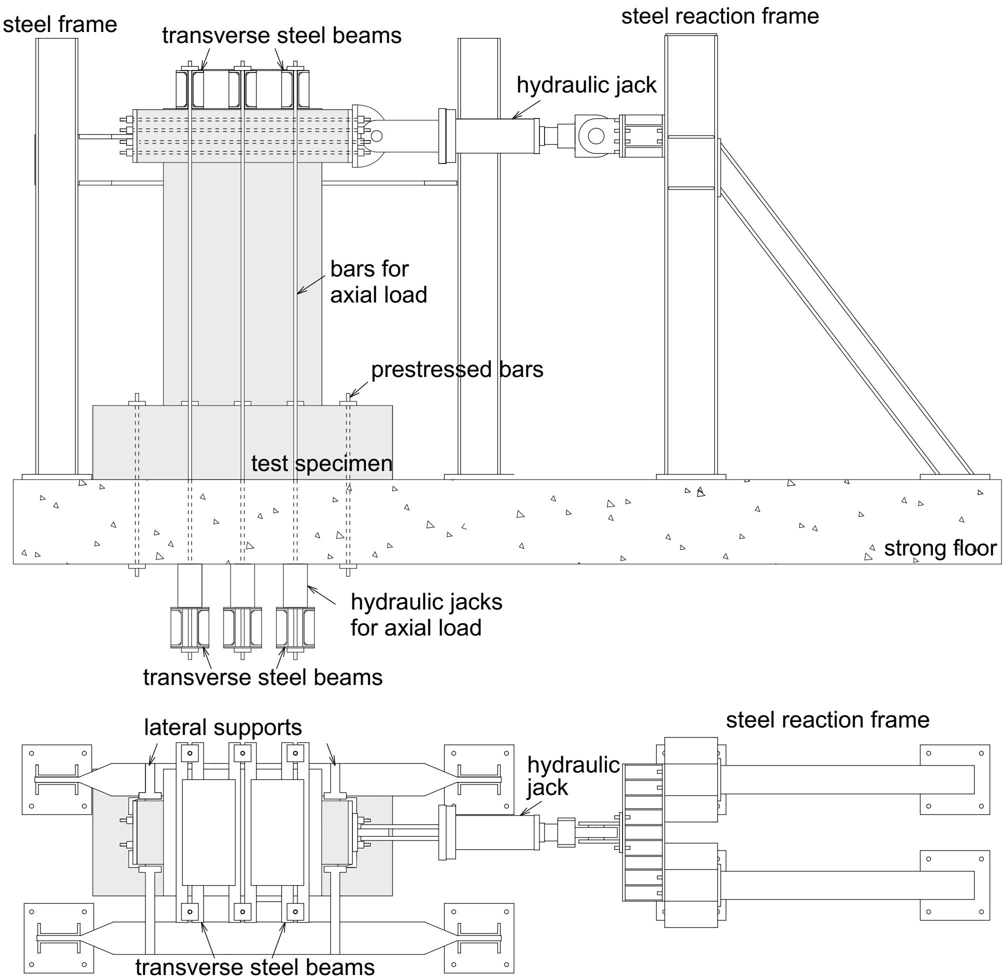

Figure 3-6. Test setup drawing

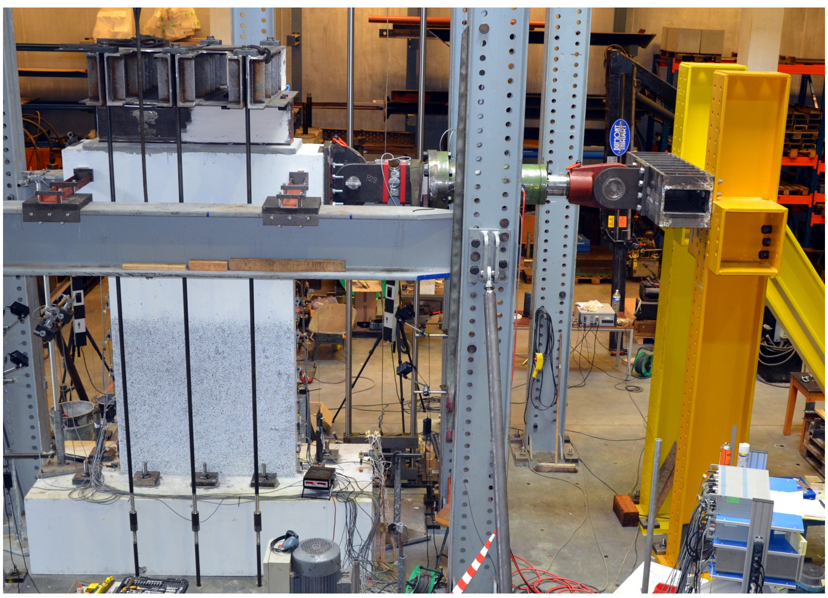

Figure 3-7. Photo of test setup

3.2.5 Measurements

The behavior of the specimens throughout the tests was observed by means of three groups of measuring techniques: hard-wired instrumentation, optical measurements, and manual measurements.

The hard-wired instrumentation consisted of 42 devices, measuring displacements and deformations at various locations on the specimen. The drawing in Figure 3-8 illustrates the layout of the hard-wired instrumentation. The applied load was measured using a load cell (LC) placed in-between the actuator and the specimen. The top horizontal displacement was measured in two locations on the top concrete block using a pair of angular displacement sensors (hdisp_1 and hdisp_2) with the reference support placed on the top of the foundation. The rotation of the top block was measured using an inclinometer (INCL), while the vertical movement near the block corners was measured using displacement transducers vdisp_R and vdisp_L. Eight potentiometer displacement transducers were mounted on each side of the specimens (vdef_R0 through vdef_R7, and vdef_L0 through vdef_L7) to measure the deformations along the side faces of the walls. Two transducers with diagonal orientation (ddef_1 and ddef_2) and a horizontal one (ddef_3) were placed in a square pattern to measure deformations in the bottom half of the wall. The horizontal translation near the base of the wall with respect to the top of the footing (sliding displacement), was measured using transducers sdispR and sdispL. Possible uplift of the foundation block was measured using a pair of potentiometer transducers vdisp_FR and vdisp_FL with respect to the strong floor, while the sliding of the foundation was captured using the hdisp_F.

Before the construction of the walls, the longitudinal rebars of each specimen were equipped with 12 strain gauges, SG1 – SG12, placed at the level of the base section. The location of the gauges in the section is shown in Figure 3-8.

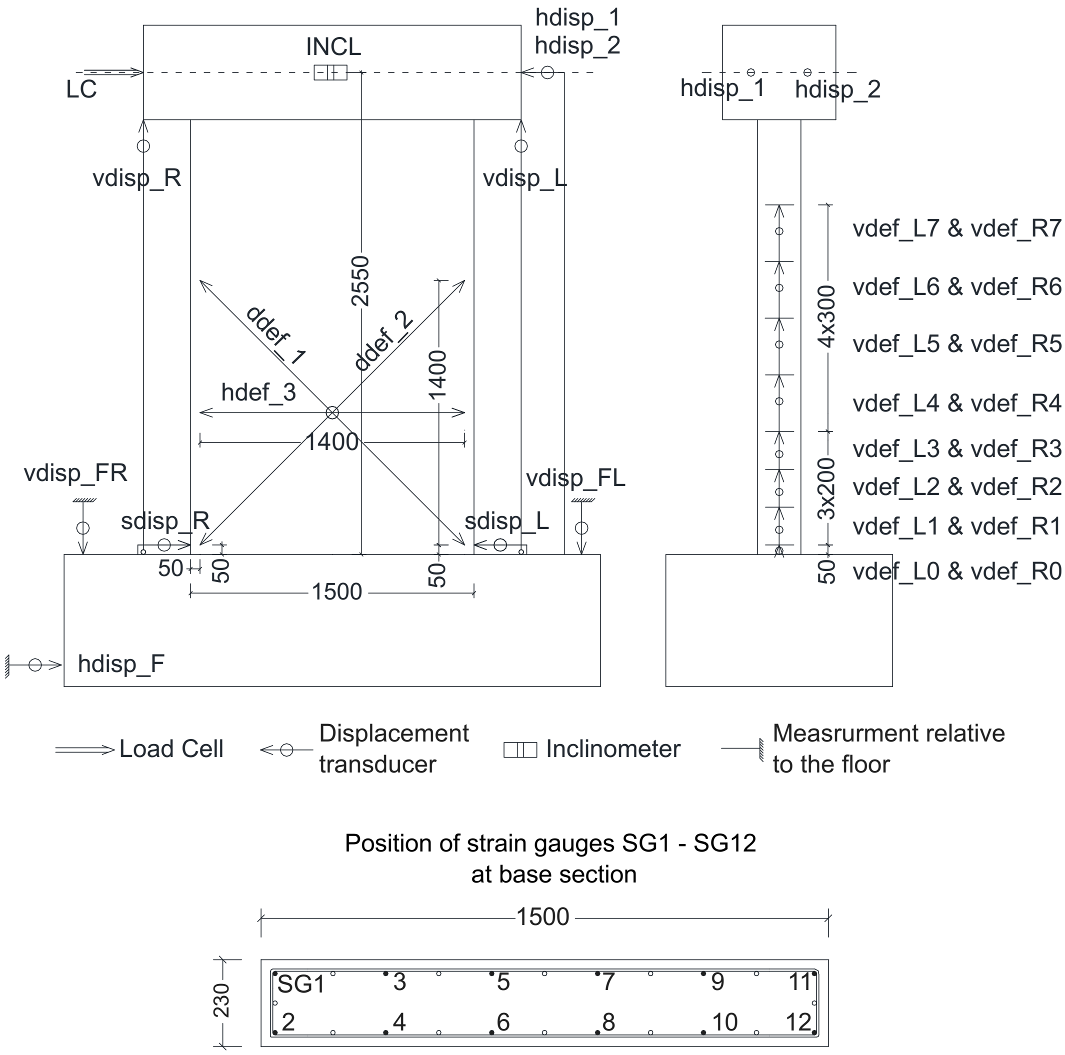

Figure 3-8. Hard-wired instrumentation layout

The modeling of walls considered in this thesis is based on kinematic assumptions for the deformations of the wall, therefore one of the objectives of this test program was to obtain detailed measurements of the deformation patterns across the surface of the walls. To achieve this, two optical measuring systems were used on the opposite faces of each specimen.

On one face of the walls, a system utilizing two cameras capturing the motion of LED (light-emitting diode) markers by Codamotion CX1 (codamotion.com) was used. This system was able to capture the motion of a grid of 54 LED markers glued to the wall's surface and two markers placed on the foundation. The layout of the grid of LED markers is shown in Figure 3-9a.

On the opposite face of the walls, a digital image correlation (DIC) system by LaVision (lavision.com) with two cameras Imager E-lite 5M (2448x2050 pixels) was used. The stereoscopic camera setup allowed full 3D recordings of the surface of walls. Due to the limitation of the equipment, this system was used to record the displacements on the bottom portion of the test region, up to about 1350 mm from the base section. This system requires the application of a random pattern of black speckles on the wall surface. Such speckles were applied by sprinkling black matt paint with a brush. The recording area for the DIC system is shown in Figure 3-9b. The software DaVis (v8.3.1) by Lavision was used to post-process the recordings performed during the tests.

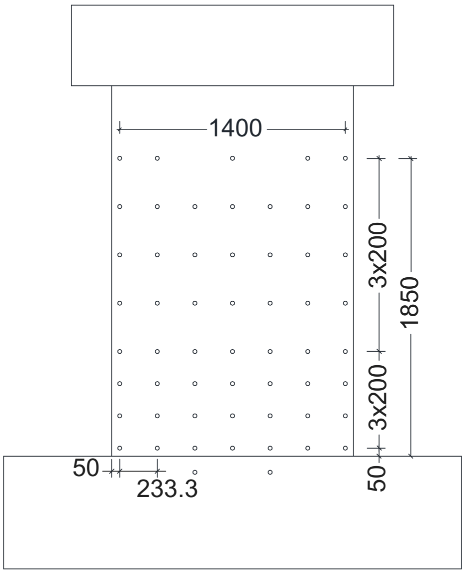

a) Grid of LED markers

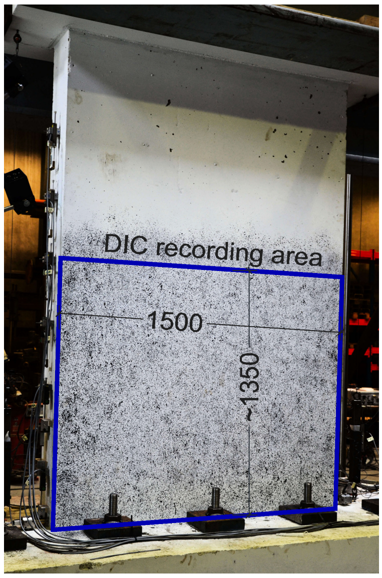

b) Speckles for DIC system

Figure 3-9. Optical measuring systems

Finally, the manual measurements consisted of marking the crack patterns and measuring the crack widths and slip using crack comparators. Cracks were marked and measured multiple times throughout the tests as explained in the following section.

3.2.6 Testing procedure

At the beginning of testing, specimens CW1 and CW2 were first subjected to the axial compressive forces of 1615 and 2650 kN, respectively. This step was skipped in the case of specimen CW0 which featured no axial load. The axial load was kept constant throughout the tests by maintaining a constant oil pressure in the hydraulic jacks below the strong floor (Figure 3-6). Following the application of the axial load, the specimens were subjected to lateral loading applied in a reversed cyclic manner. Figure 3-10 shows the loading protocol adopted for the three tests. The protocol consisted of two parts, targeting predefined force levels and targeting top displacements. The first part of the loading history consisted of three sets of three cycles where predefined force levels were achieved. The force levels of the successive set of cycles were adopted to be about 70%, 80%, and 95% of the flexural capacity V_{flex} of each wall, which was evaluated using the classical sectional approach (software Response2000; Betnz, 2000). The displacement-control part of the loading history consisted of increasing the displacement of each consecutive cycle by a factor of 1.5, starting with the displacement Δ_0 achieved during the last cycle of the force-control part of the loading history. This loading pattern was repeated until the failure of each specimen.

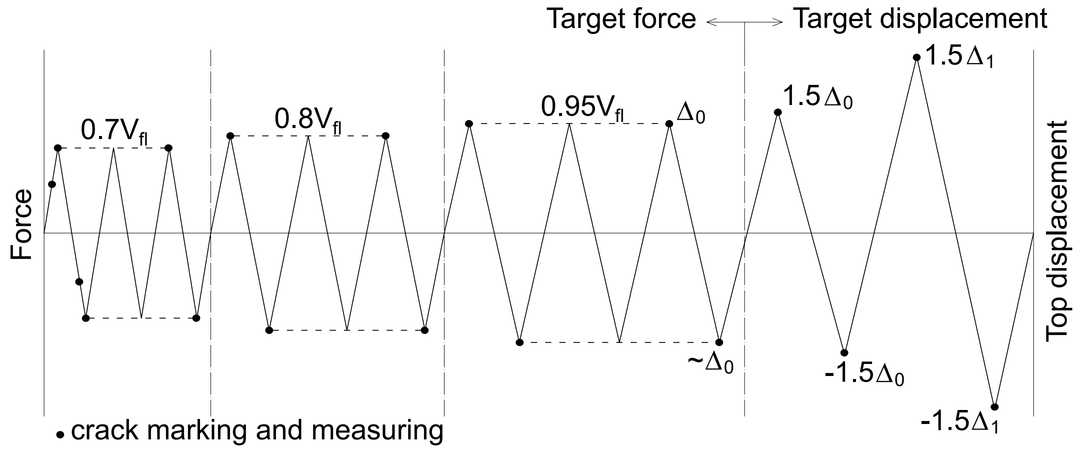

Figure 3-10. Loading history

The testing procedure also included marking the cracks and measuring the crack widths at several stages along the loading history, indicated by dots in Figure 3-10. In the force-control region, the cracks were marked and measured at the peaks of the first and the last cycle in each set of three cycles, in order to capture the effect of cycling on the development of cracks. The only exception to this was the first cycle of the tests where cracks were also marked and measured halfway to the load level to capture the initial cracking. In the target displacement-control region of the loading history, the cracks were marked and measured at the peak of each cycle of loading since the peak displacement was increasing with each consecutive cycle. After achieving the targeted load or displacement, the force in the hydraulic jack was reduced by about 10% so that the specimens could be safely approached and examined.

3.3 Test Results

3.3.1 Specimen CW0

The global response of specimen CW0 in terms of the top lateral displacement versus lateral load relationship is shown in Figure 3-11. This wall had no axial load applied on it. The maximum lateral load sustained by the specimen was 386 kN in the positive direction, and 371 kN in the reverse direction. It failed in the negative direction at a displacement of 66.3 mm, corresponding to a drift ratio of 2.6%. The displacement or drift ratio at failure was adopted to correspond to a 20% drop in the maximum load experienced by the specimen.

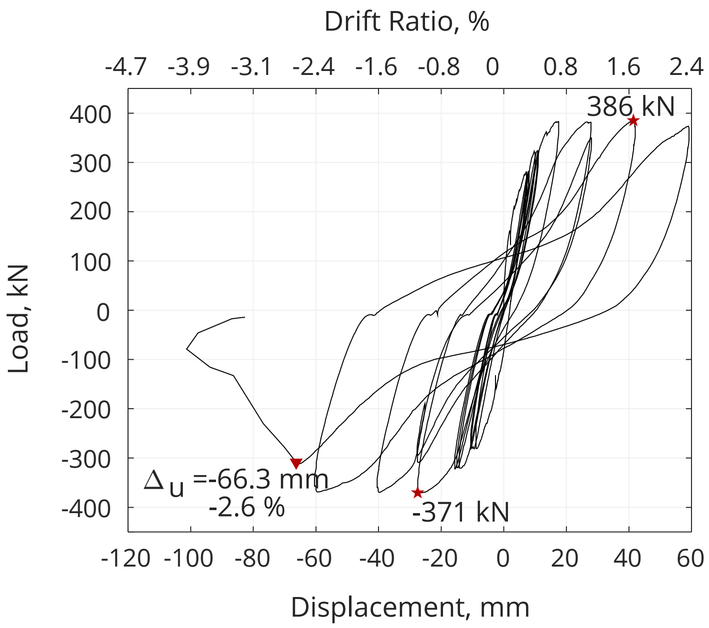

Figure 3-11. CW0 global response

The hysteretic response of specimen CW0 is characterized by a significant amount of pinching in the hysteretic loops. The presence of this phenomenon is a consequence of sliding displacements across the base section. Due to the accumulation of inelastic deformations in the longitudinal rebars, the cracks did not close well upon the load reversals and the wall performed horizontal rigid body movements. This is reflected in the response as a decrease in the tangent stiffness upon reloading. The envelope of the response corrected for the sliding displacements is shown in Figure 3-12. The sliding displacements of the wall were estimated from the displacement transducers measuring the horizontal displacement at 50 mm above the base section, or by averaging the horizontal displacements of the two middle LED markers belonging to the bottom row at the same height from the base section. It can be observed that the sliding displacements become more pronounced with increasing drifts, which is related to increased inelastic deformations in the longitudinal rebars. The maximum sliding displacements accounted for 21% of the total top displacement at failure.

Specimen CW0 failed in flexure due to the rupture of the tensile rebars. The occurrence of failure was followed by a sudden drop in the lateral resistance of the wall. Figure 3-13 shows the photos of the specimen at failure, including details of the ruptured rebars and the compression zone. Buckling of the ruptured rebars in compression was observed in the loading step preceding the failure. In a study by Restrepo-Posada (1992), it has been shown that the buckling leads to the formation of microcracks on the compression side of the rebar, which can lead to premature rupture once the rebar is reloaded in tension. The failure was accompanied by the buckling of the longitudinal bars below the first stirrup on the compressed side of the section, see Figure 3-13c.

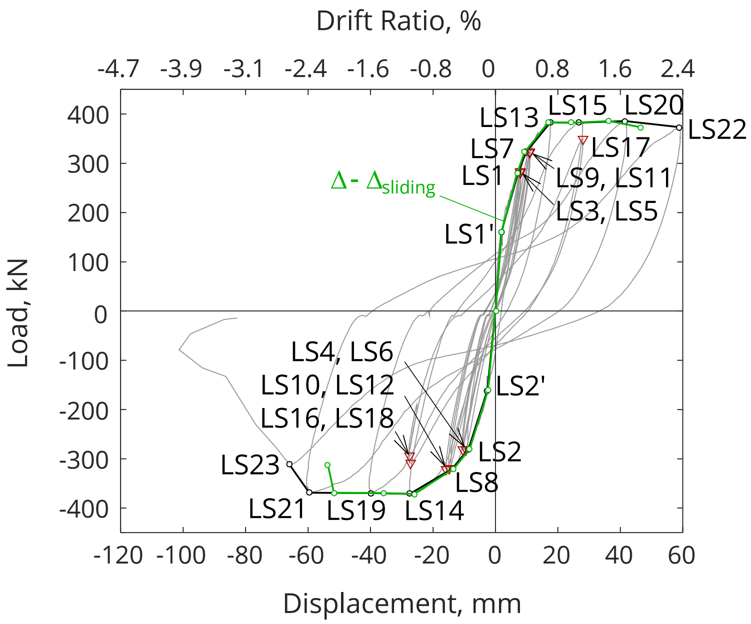

Figure 3-12. CW0 envelope with load stages

Figure 3-12 outlines the envelope of the response of wall CW0 and the peaks of each load stage (LS). The circles connected with a thick black line define the envelope, while the intermediate loading steps are marked with red triangles. The first yielding in the longitudinal reinforcement occurred near LS1 and LS2 at a displacement $\Delta_y = 6.4$ mm, or a drift ratio of 0.25 %. It can be seen that in the two first sets of cycles (LS1 to LS12) the wall did not exhibit any loss of resistance in consecutive cycles. In the following set of cycles (LS13 to LS18), it can be seen that the load was not recovered at the same drift as in the initial cycles. In the succeeding loading stages, the resistance of the wall recovered with the increasing drift ratio and it stayed nearly constant along the plateau of the response until the failure was reached.

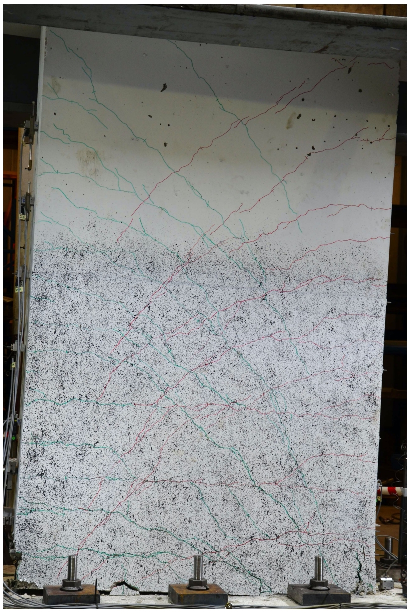

a) CW0 at failure

b) Ruptured rebars in tension

c) Buckling of rebars in compression

Figure 3-13. CW0 failure

The cracking patterns and the measured crack widths at several load stages in each loading direction are shown in Figure 3-14. In the first two loading cycles, LS1' and LS2', few horizontal cracks formed in the lower third of the wall. In the first set of cycles, when the wall was loaded up to 70% of V_{fl} (LS1 to LS6), the cracking extended up to about two-thirds of the shear span. The cracks propagated horizontally along the first third of the section depth from the tension boundary and started inclining along the second third of the section depth. In the following set of cycles, corresponding to a load of 80% V_{fl} (LS7 to LS8), a few cracks formed above the existing cracks and the inclined cracks extended deeper into the section of the wall. At this stage, the wall had cracks nearly across the whole surface with shear cracks propagating deep into the section at an angle of about 45°. After loading the specimen to 95% of V_{fl} (LS13 to LS18) no new major cracks formed. Further in the loading history, the existing shear cracks extended deeper into the section. At LS17 and LS18 it became apparent that slip displacements were occurring across the cracks. The measurements of the slip observed along the major shear cracks are shown in parenthesis in Figure 3-14. The largest crack width throughout the test was the opening of the base crack. From the optical measurements, the crack width just before the very failure (LS23) was estimated to be about 19 mm. The largest shear crack measured was about 1.9 mm wide with a slip displacement of 0.7 mm.

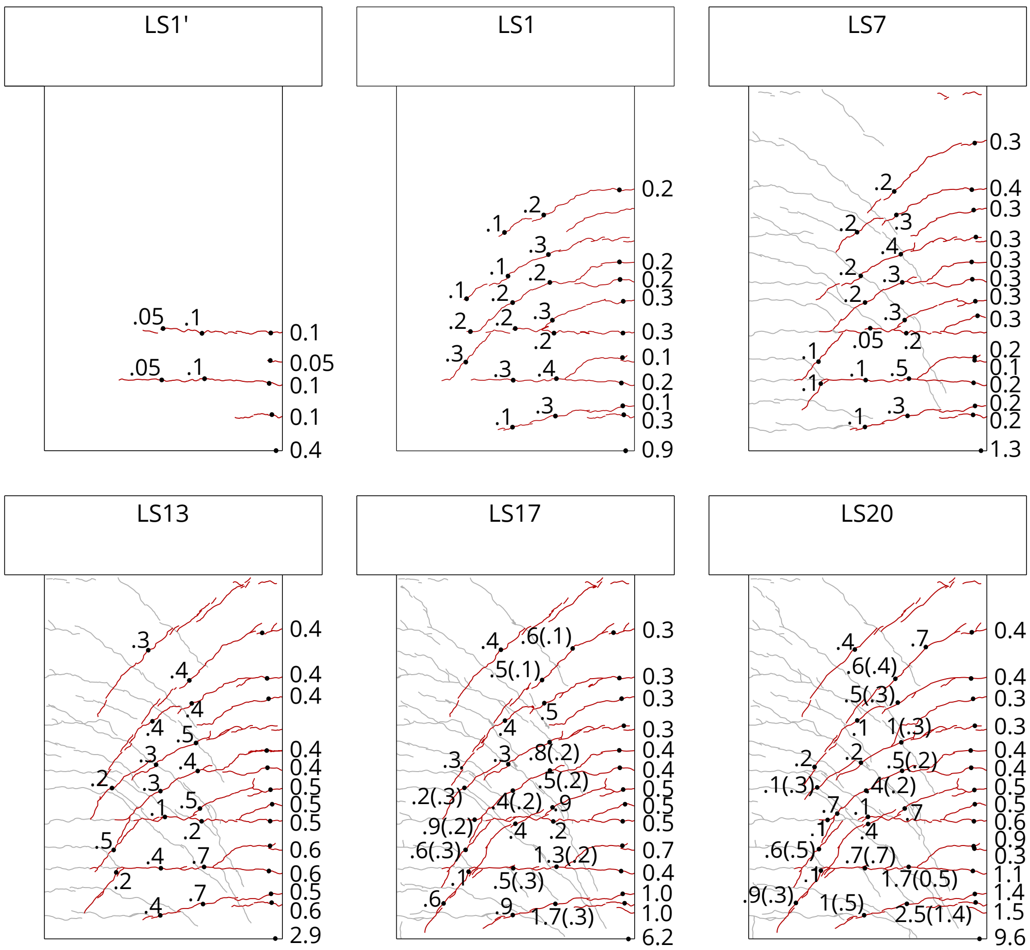

a) Positive envelope

Figure 3-14. CW0 cracking patterns and measured crack widths (slip) in mm

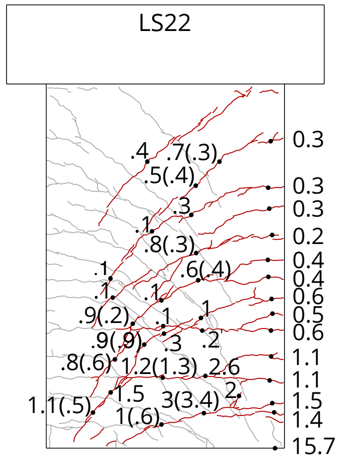

b) Positive envelope

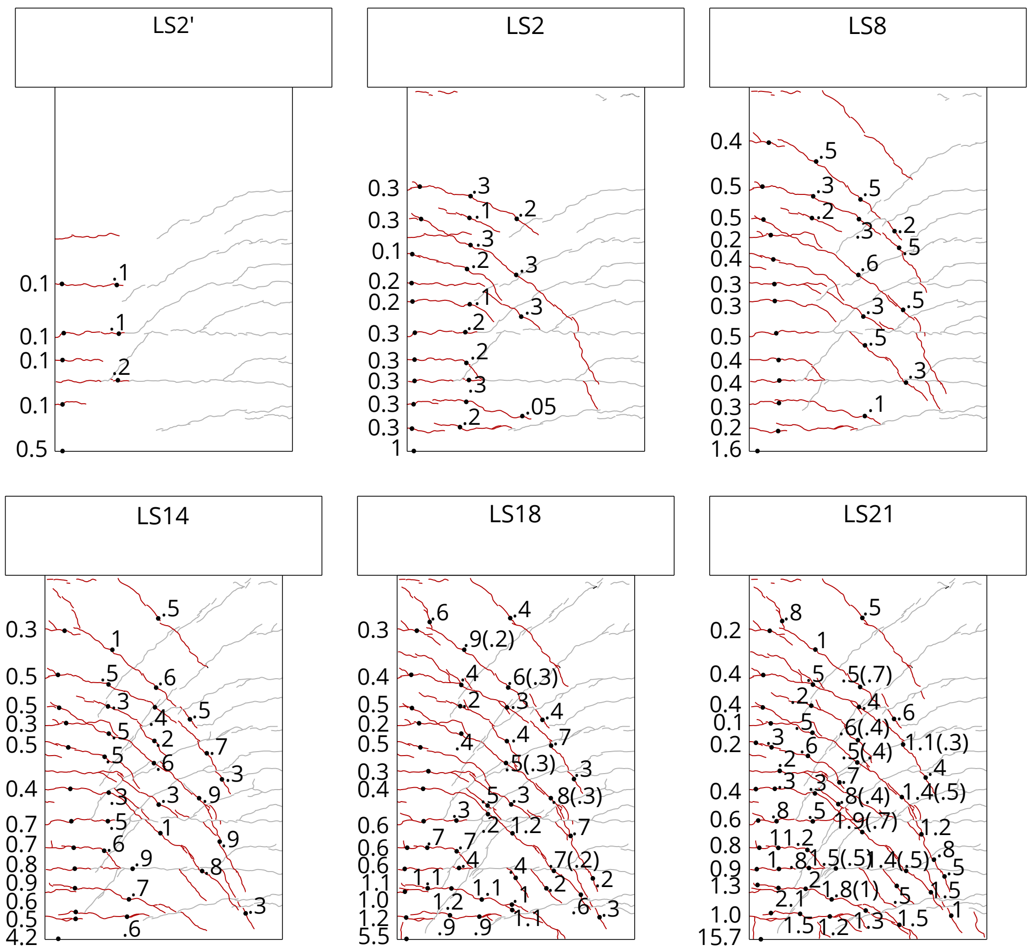

b) Negative envelope

Figure 3-14. CW0 cracking patterns and measured crack widths (slip) in mm (continued)

The longitudinal strains measured on the side faces of wall CW0 using the chains of displacement transducers are shown in Figure 3-15. Displacement transducers vR0 and vL0 (Figure 3-8) were not available for this wall, however, the strains at their location were estimated using the measurements from the DIC system. Consistent with the cracking patterns, the largest deformations were measured in the region near the base crack. The maximum strain measured at this location is several fold greater than the ultimate strain of the longitudinal rebars (ε_u = 80 mε). This strain measurement also includes the anchorage deformations due to the pullout of rebars in tension, therefore it does not represent the actual rebar strain at that location. In both directions, the yielding of the reinforcement propagated up to a height of about 1.5 m from the base section.

The strains in the longitudinal rebars, along the envelope of the response in each loading direction, measured using the strain gauges in the base section are shown in Figure 3-16. The first yielding of the longitudinal reinforcement occurred at LS1 in the positive direction and slightly before the peak of LS2 in the negative direction. The average yield displacement for both directions was about 6.4 mm, and the corresponding drift ratio was about 0.25%. After LS7 and LS8, the strain gauge data deviate from the expected trend and are assumed not to represent reliable measurements. The erroneous values are likely a consequence of the accumulation of plastic strain in the rebars due to the cyclic loading history.

The test data is further used to evaluate the behavior of the shear reinforcement. The horizontal strain measurements near failure in Figure 3-17 were evaluated on the concrete surface using the optical measuring equipment, i.e. the LED scanners and DIC system. In Figure 3-17a, the strain profiles along each row of LED markers were calculated from the relative movement of the adjacent markers, divided by the distance between the markers (i.e. 233 mm). The values shown in the plot represent the maximum value of the strain measured along each row of markers. Figure 3-17b shows the local horizontal strains generated using the data from the DIC system. It can be seen that the strains are concentrated at the location of the cracks and are significantly larger than those in Figure 3-17a.

The horizontal strains obtained from both the LED and DIC systems indicate that the stirrups yielded in the regions of shear cracking. The maximum LED and DIC strains reached respectively 12 mε and 30 mε, while the yield strain of the stirrups was ε_{yv}=2.6 mε. However, it should be noted that, because of the local slip between the stirrups and concrete in the vicinity of the cracks, the local stirrup strain in the crack differs from the strains measured with the optical systems on the concrete surface. As the LED system uses a relatively large averaging length and the DIC system a very small length, the strains shown in Figure 3-17a and Figure 3-17b provide the lower and upper bound estimate of the actual stirrup strain in the cracks, respectively.

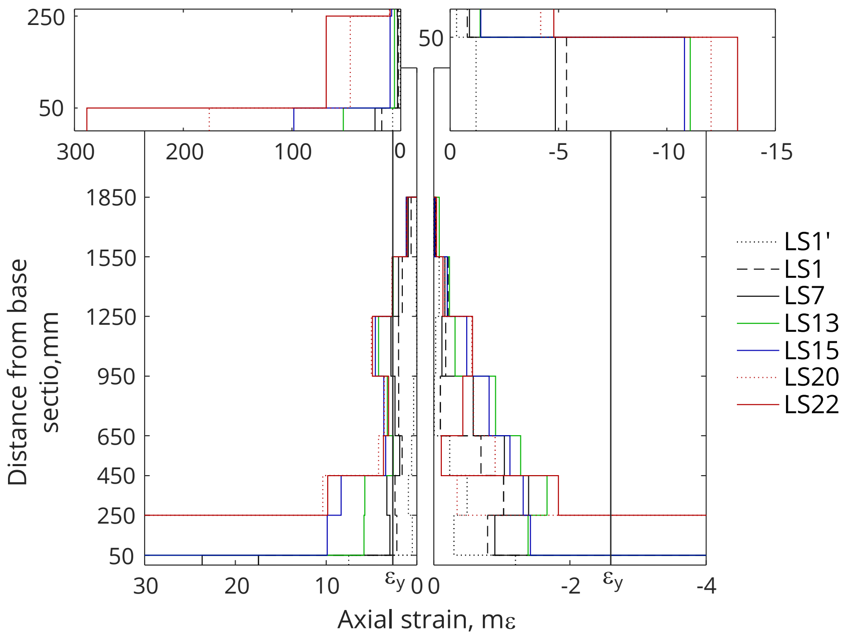

a) Positive envelope

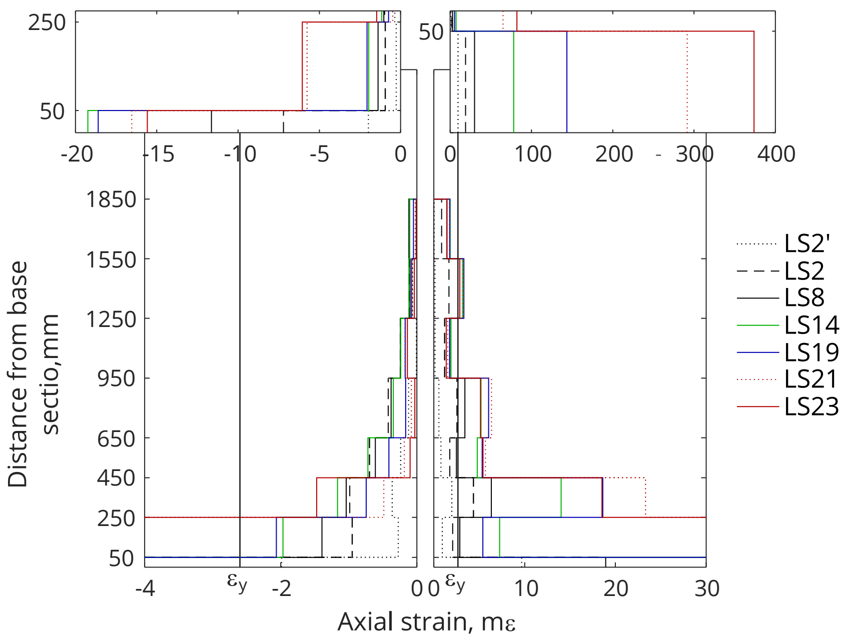

b) Negative envelope

Figure 3-15. CW0 axial strains

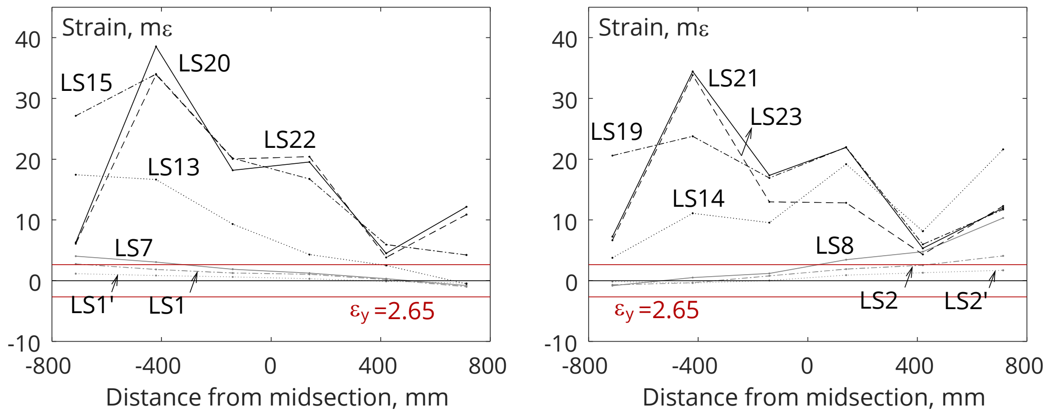

a) Positive envelope

b) Negative envelope

Figure 3-16. CW0 strain gauge measurements

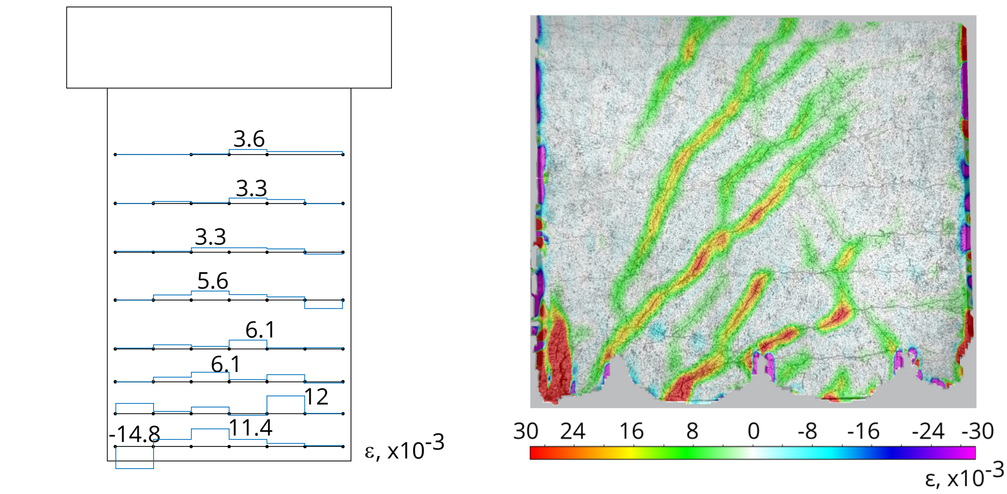

a) Horizontal strains from LED scanners

b) Horizontal strains from DIC system

Figure 3-17. CW0 horizontal strains before failure (LS23)

Another way to detect the yielding of the stirrups is to evaluate the crack width corresponding to yielding and to compare it to the crack width measurements performed at various load stages. To this end, it is proposed to treat each stirrup as a bar anchored in two concrete blocks, one on each side of the crack, and to evaluate the pullout of the bar from each block. The pullout displacement can be evaluated by applying a bond model proposed by Sigrist (1995), which is presented in detail in §4.2.4. As the problem is symmetrical, the crack width is equal to two times the pullout displacement from each of the two blocks.

The results from this approach for ϕ8 bars (the stirrups) and ϕ12 bars (the longitudinal reinforcement) are shown in Figure 3-18. More specifically, the plot shows the predicted relationships between the stress in the bar in the crack and the opening of the cracks. The results for ϕ12 bar can be validated by using the measured opening of the base crack, as well as the strain gauge measurements performed on the longitudinal reinforcement in the crack. The stress in the bar in the crack is obtained from the measured strain by using the experimental stress-strain curves for the steel (Figure 3-5). From Figure 3-18, it can be seen that the bond model gives an accurate estimate of the crack width that causes yielding in the ϕ12 rebars when compared to the measured values for each loading direction. The appropriate prediction of the crack width at yielding was obtained by using a tensile strength of concrete of $0.25 f_c'^{2/3}$ instead of the $0.33 f_c'^{2/3}$ used in the original model by Sigrist (1995). The bond model estimates the yielding of the ϕ8 stirrups at the crack width of about 0.7 mm, which corresponds to the equivalent opening of an inclined 45 ° crack of approximately 0.5 mm. Looking back at the cracking patterns in Figure 3-14, the cracks of about 0.5 mm appeared at the LS8 or when the specimen was loaded to the 80% of V_{fl}.

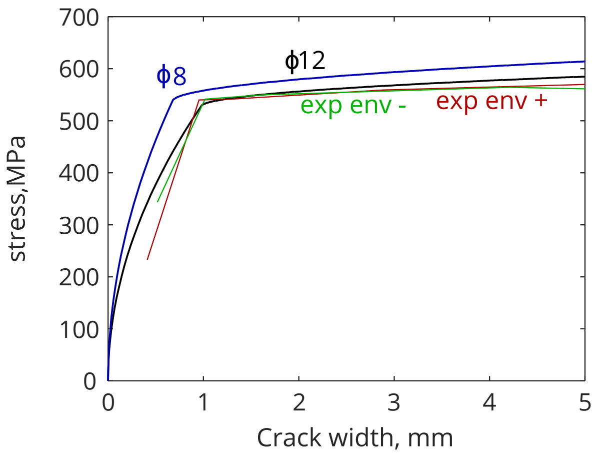

Figure 3-18. Comparison of predicted stress in rebar at crack location against experimental values of the base crack opening of wall CW0

Finally, the recordings of movement of the LED markers allow the visualization of the deformed shapes of specimen CW0 throughout the test. Figure 3-19 shows the evolution of the deformed shape along the envelopes of the response, as well as the deformed shape at the last step of the envelope in each direction (LS22 and LS23). For better visualization of the deformed shapes, the displacements of the markers were magnified 15 times. From the visual evaluation of the deformed shapes, it appears that the horizontal sections remained approximately plane throughout the envelopes of the response. There appears to be some minor shear distortion in the shapes of the quadrilaterals defined by the LED markers, mainly in the row of elements near the base section. Also, it is evident that there is a non-negligible amount of the horizontal rigid body movement due to the sliding deformations along the base joint. Detailed discussion and analysis of these deformation patterns are presented in §3.4.2.

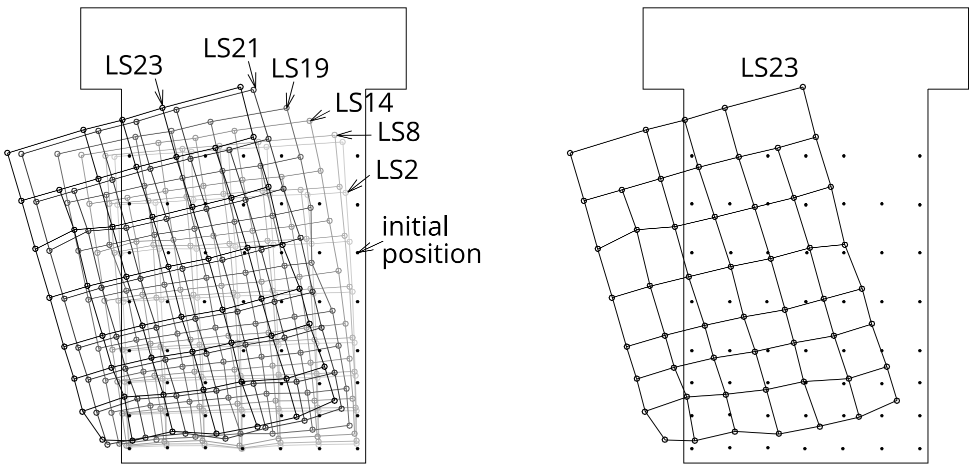

a) Positive envelope

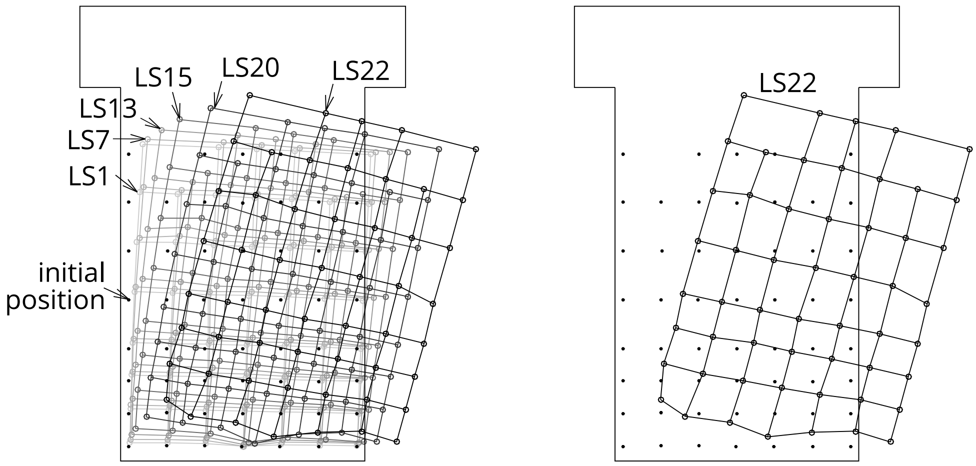

b) Negative envelope

Figure 3-19. CW0 deformed shape (magnification x15)

3.3.2 Specimen CW1

The global response of specimen CW1 in terms of the top lateral displacement versus lateral load relationship is shown in Figure 3-20. Prior to applying the lateral load, the specimen was subjected to an axial compression force of 1315 kN, corresponding to about 10% of the compression capacity of the concrete section

bhf_c'. The maximum lateral load sustained by the specimen was 686 kN in the positive direction, and 672 kN in the reverse direction. The maximum displacement at failure Δ_u was 50 mm, which corresponds to a drift ratio of approximately 2%. As before, the displacement or drift ratio at failure was adopted to correspond to a 20% drop in the maximum load experienced by the specimen.

The hysteretic response of specimen CW1 resembles the response of a "bridge pier under high axial load" as described by Priestley et al. (2007). The specimen exhibited relatively narrow hysteretic loops typical for members with axial compressive load or prestressed concrete members. The presence of axial load prevented large crack widths and ensured that the cracks closed well upon unloading. Even after the global response reached the plateau, indicating significant yielding in the flexural reinforcement, there were relatively small residual deformations upon the unloading.

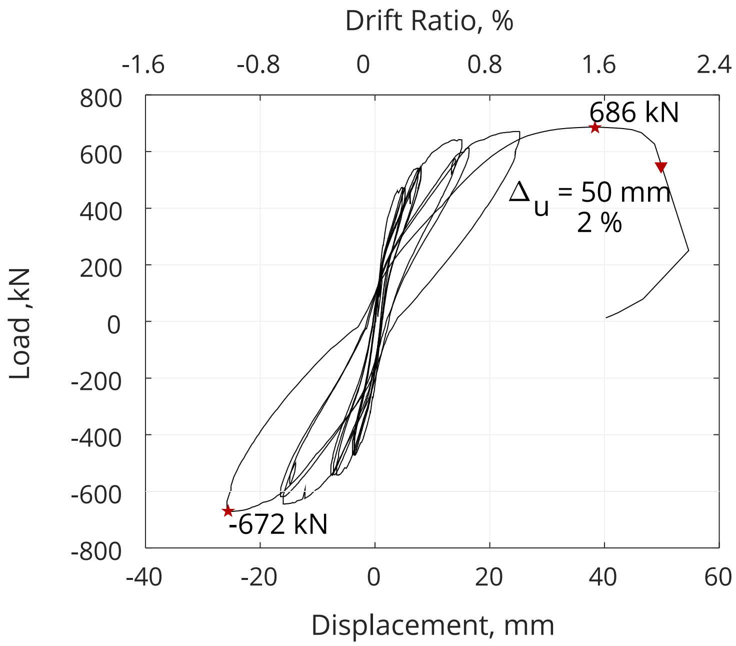

Figure 3-20. CW1 global response

Specimen CW1 failed in flexure due to crushing of the concrete in the vicinity of the base section as shown in Figure 3-21. The occurrence of failure was followed by a sudden drop in the lateral load capacity. The crushing of the concrete in the failure zone was accompanied by the buckling of two rows of longitudinal bars below the second stirrup, which caused the opening of the 90°-hook of the bottom stirrup. Figure 3-21 shows the condition of the crushed zone after the removal of the detaching concrete debris.

Figure 3-21. CW1 failure

Figure 3-22 shows the envelope of the response of wall CW1 and the peaks of each loading stage (LS). The circles connected with a thick black line define the envelope, while the intermediate loading steps are marked with the red triangles. It can be observed that the cyclic loading caused virtually no effect on strength degradation as the resistance of the specimen fully recovered in the consecutive cycles. In this respect, it is worth noting that the first yielding of the longitudinal reinforcement occurred at a displacement $\Delta_y = 7.5$ mm, or a drift ratio of about 0.3%. The resistance continued to increase throughout the test and the wall CW1 reached the peak load at LS19 before the failure occurred.

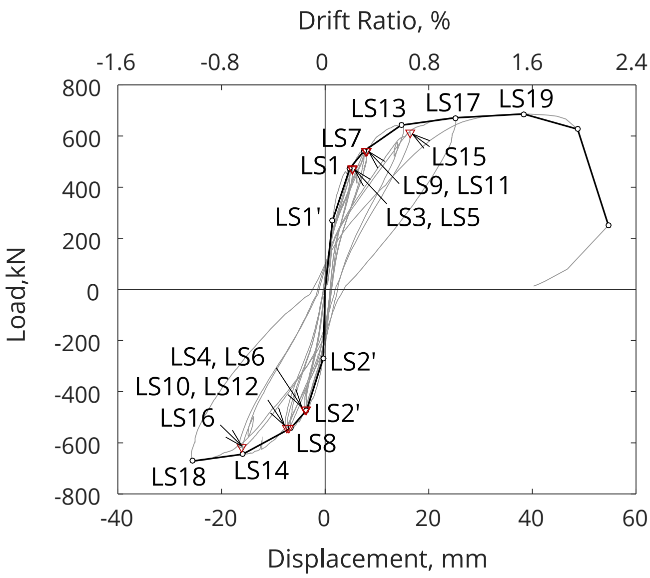

Figure 3-22. CW1 loading stages

The cracking patterns and the measured crack widths at several load stages in each loading direction are shown in Figure 3-23. In the two first sets of loading cycles, corresponding to the lateral load of 70% and 80% of V_{fl} (LS1 to LS12), the formation of horizontal flexural cracks can be observed. The cracks started inclining deeper into the section with the increasing loading. In the following set of cycles (LS13 to LS18) the specimen was loaded to 95% of V_{fl} and the cracking pattern developed fully. Several shear cracks appeared with an inclination of about 45° and their widths measured up to 0.8 mm. At load steps LS17 and LS18, prior to failure, vertical cracks appeared in the compression zone in each direction, indicating the onset of concrete crushing in compression. The largest crack width throughout the test was the opening of the base crack. At the maximum load reached by the specimen (LS19), the crack width evaluated using the DIC system was measured at 6.2 mm.

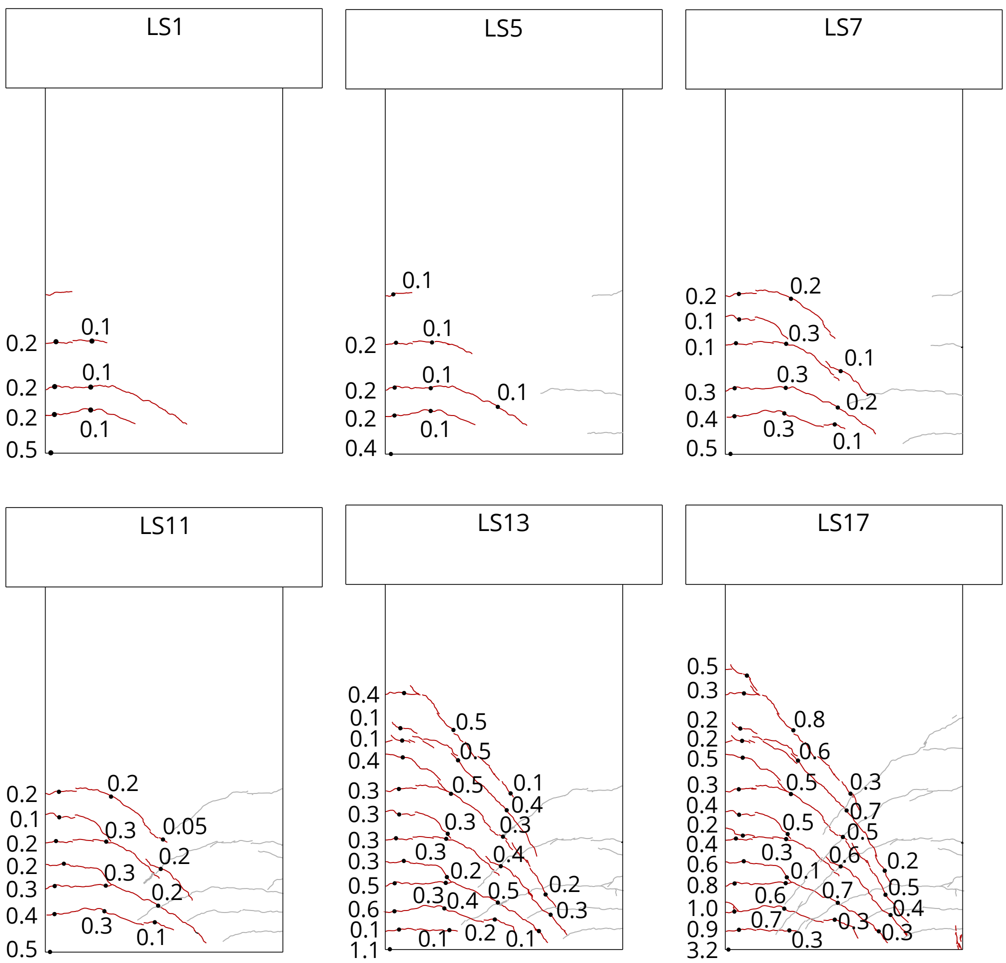

a) Positive envelope

Figure 3-23. CW1 crack patterns and crack widths in mm

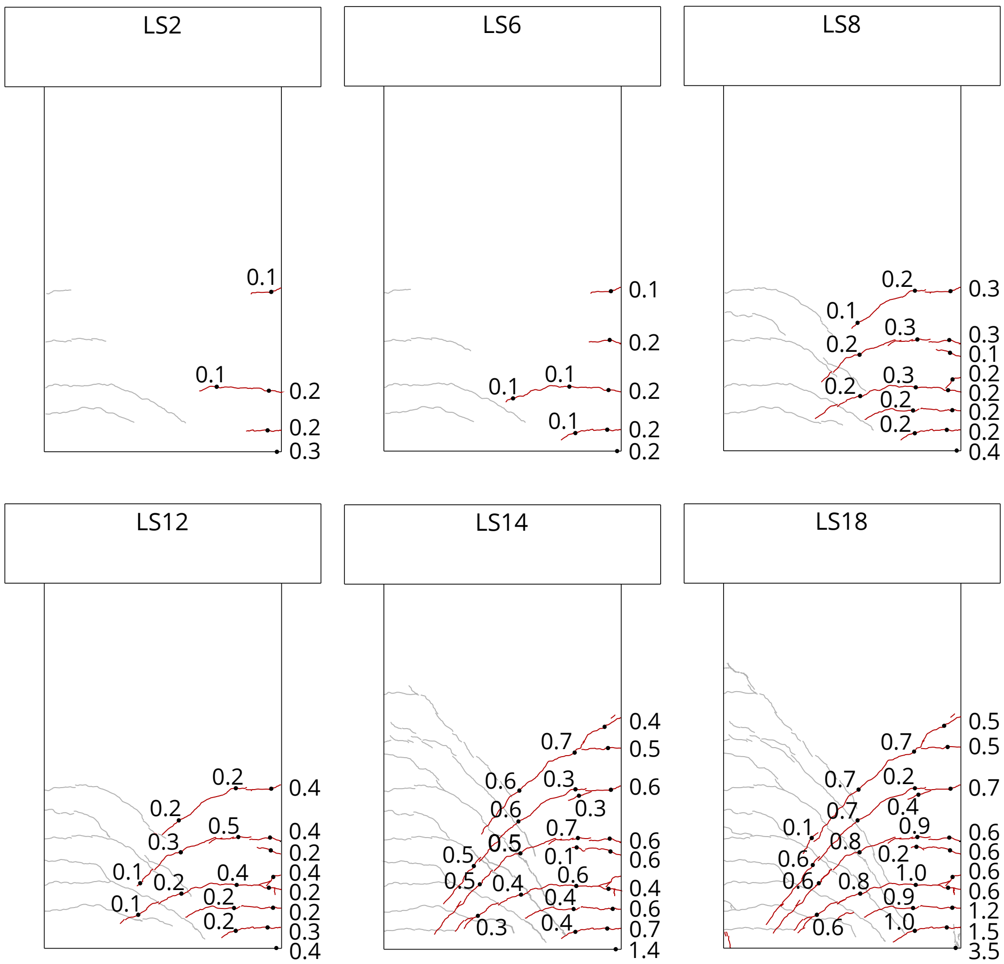

b) Negative envelope

Figure 3-23. CW1 crack patterns and crack widths in mm (continued)

The longitudinal strains on the side faces of wall CW1 measured using the chains of displacement transducers are shown in Figure 3-24. The positive strain represents the face of the wall in tension while the negative strain corresponds to the compressed side of the wall. Consistent with the cracking patterns, the largest deformations were measured in the region near the base crack. This strain measurement also includes the anchorage deformations due to the pullout of the rebars in tension, therefore it does not represent the actual rebar strain at that location. According to these measurements, the yielding of the longitudinal reinforcement propagated up to a height of about 1,25 m from the base in the positive direction of loading and 1.5 m in the negative direction.

The strains in the longitudinal rebars, along the envelope of the response in each loading direction, measured using the strain gauges in the base section are shown in Figure 3-25. The strains are evaluated as a mean value of the strain measured with the two gauges placed at the same distance along the depth of the section. The first yielding of the longitudinal reinforcement occurred in the second set of cycles (LS7 and LS8), at a top displacement of 7.5 mm and corresponding drift ratio of 0.3%. After load stages LS13 and LS14, the strain gauge data deviates from the expected trend and are assumed not to represent the reliable measurements. The erroneous values are likely a consequence of the accumulation of plastic strain in the rebars due to the cyclic loading history.

The test data is further used to evaluate the behavior of the shear reinforcement. The horizontal strain measurements near failure in Figure 3-26 were evaluated on the concrete surface using the optical measuring equipment, i.e. LED scanners and DIC system. In Figure 3-26a, the strain profiles along each row of the LED markers were calculated from the relative movement of the adjacent markers, divided by the distance between the markers (i.e. 233 mm). The values shown in the plot represent the maximum value of the strain measured along each row of markers. Figure 3-26b shows the local horizontal strains generated using the data from the DIC system. It can be seen that the strains are concentrated at the location of the cracks, and are significantly larger than those in Figure 3-26a.

The horizontal strains obtained from both the LED and DIC systems indicate that the stirrups yielded in the regions of shear cracking. The maximum LED and DIC strains reached respectively 5.9 mε and 20 mε, while the yield strain of the stirrups was $\varepsilon_{yv} = 2.6$ mε. However, it should be noted that, because of the local slip between the stirrups and concrete in the vicinity of the cracks, the local stirrup strain in the crack differs from the strains measured with the optical systems on the concrete surface. As the LED system uses a relatively large averaging length and the DIC system a very small length, the strains shown in Figure 3-26a and Figure 3-26b provide the lower and upper bound estimate of the actual stirrup strain in the cracks, respectively.

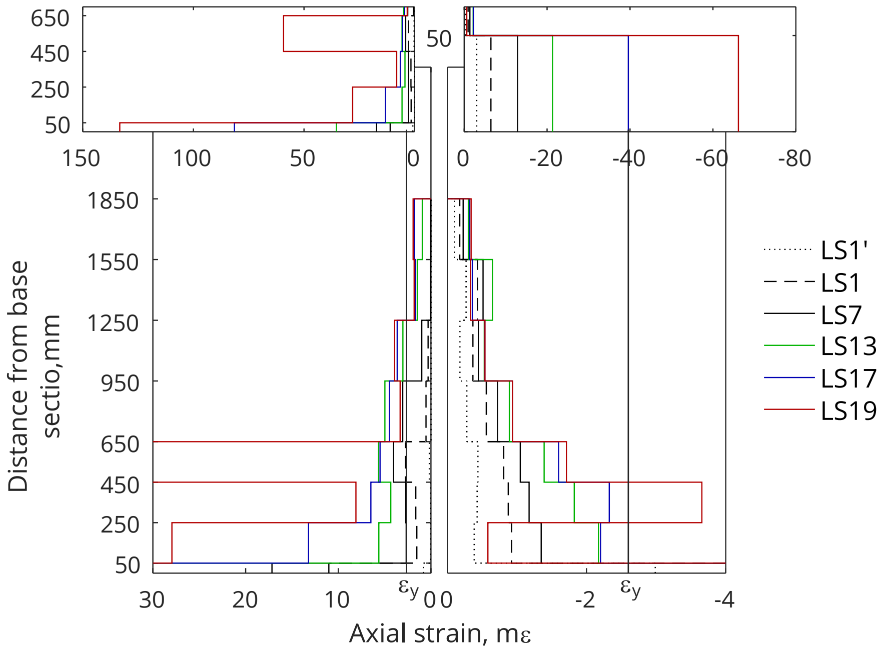

a) Positive envelope

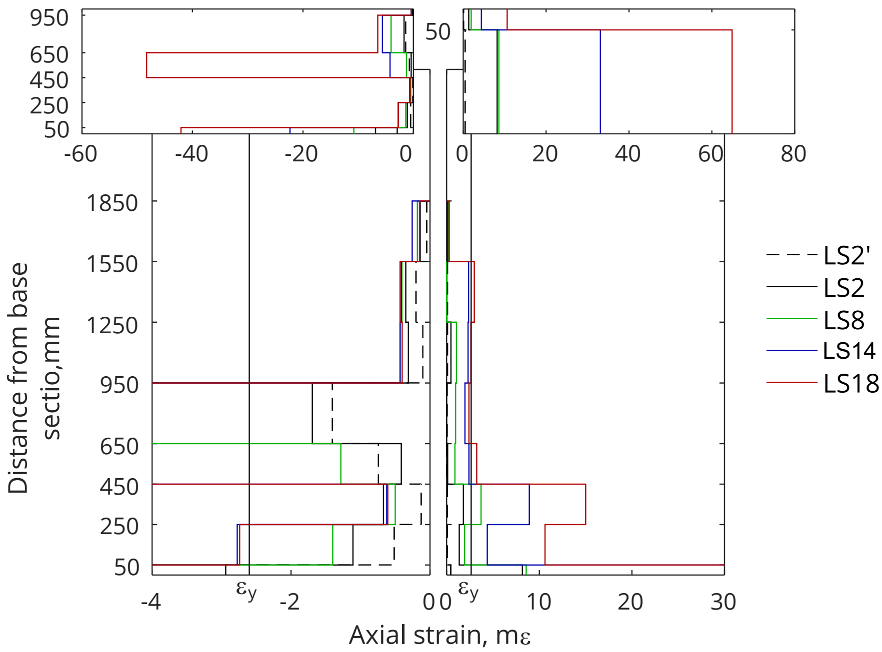

b) Negative Envelope

Figure 3-24. CW1 axial strains

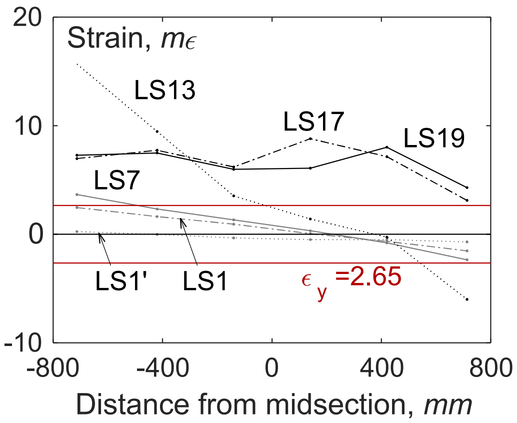

a) Positive envelope

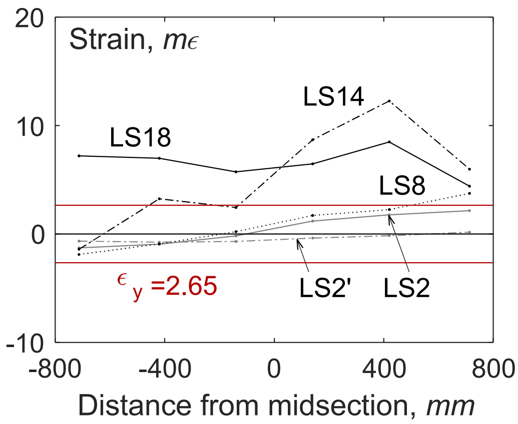

b) Negative envelope

Figure 3-25. CW1 strain gauge measurements

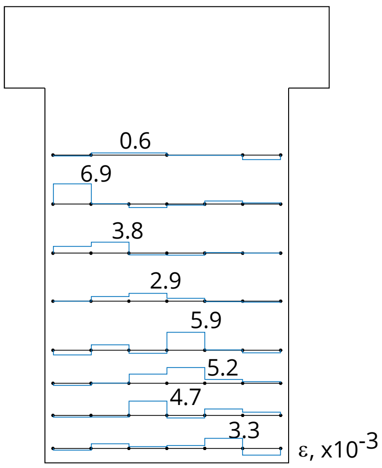

a) Horizontal strains from LED scanners

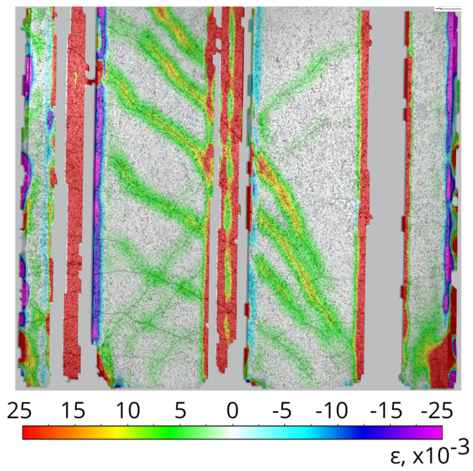

b) Horizontal strains from DIC system

Figure 3-26. CW1 horizontal strains near failure (LS19)

The strain in stirrups is further evaluated with the bond model (Sigrist, 1995), as described in the previous section (§3.3.1). The results from this approach for ϕ8 bars (the stirrups) and ϕ12 bars (the longitudinal reinforcement) are shown in Figure 3-27. As before, the results for ϕ12 can be validated by using the measured opening of the base crack, as well as the strain gauge measurements performed on the longitudinal reinforcement in the crack. The stress in the bar in the crack is obtained from the measured strain by using the experimental stress-strain curves for the steel (Figure 3-5). From Figure 3-27, it can be seen that the bond model gives a good estimate of the crack that causes yielding in the ϕ12 rebars when compared to the measured values for each loading direction. The bond model estimates the yielding of the ϕ8 stirrups at a crack width of about 0.4 mm, which corresponds to the equivalent opening of an inclined 45° crack of approximately 0.3 mm. The measured crack widths in Figure 3-23 indicate the stirrups yielded when the specimen was loaded to 95% V_{fl} or at LS13 and LS14.

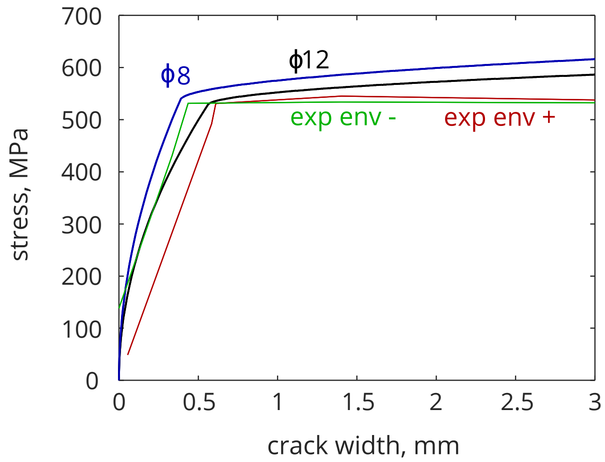

Figure 3-27. Comparison of predicted stress in rebar at crack location against experimental values for the base crack opening

Finally, the recordings of the movement of LED markers allow the visualization of the deformed shapes of specimen CW1 throughout the test. Figure 3-28 shows the evolution of the deformed shape along the envelope of the response and the deformed shape at the last step of the envelope in each direction (LS18 and LS19). For better visualization of the deformed shapes, the displacements of the markers were magnified 15 times. From the visual evaluation of the deformed shapes, it appears that the horizontal sections remain plane throughout the envelope of the response and that there is a very small distortion to the shape of the quadrilaterals defined by the LED markers. Detailed discussion and analysis of these deformation patterns are presented in §3.4.2.

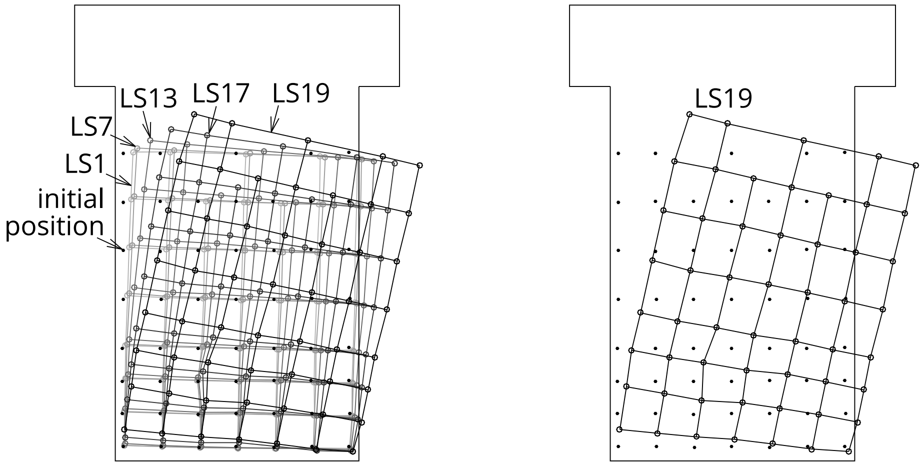

a) Positive envelope

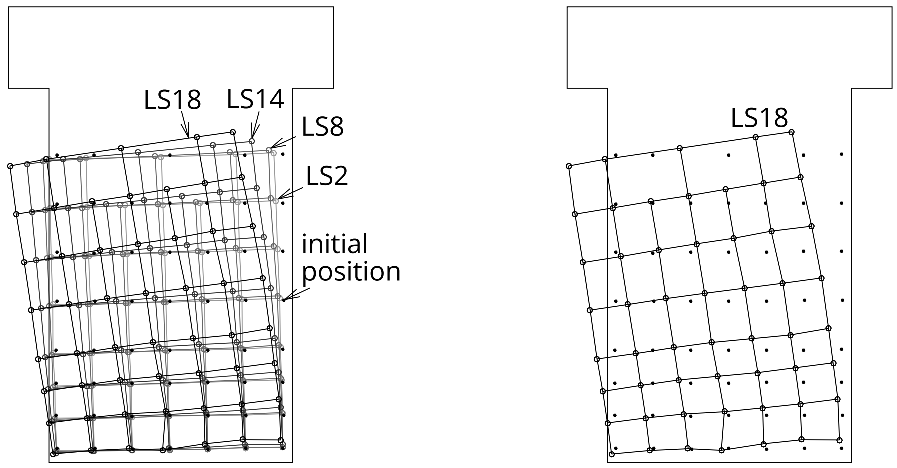

b) Negative envelope

Figure 3-28. CW1 deformed shape (magnification x15)

3.3.3 Specimen CW2

The global response of specimen CW2 in terms of the top lateral displacement versus lateral load relationship is shown in Figure 3-29. This specimen was subjected to an axial compression force of 2650 kN, corresponding to about 21% of the compressive capacity of the concrete section, bhf_c'. The maximum lateral load sustained by this wall was measured at 884 kN in the positive direction, and 875 kN in the reverse direction. The maximum displacement at failure Δ_u was 27.4 mm, which corresponds to the drift ratio of approximately 1.1%. As before, the maximum displacement or drift ratio at failure was adopted to correspond to a 20% drop in the maximum load experienced by the specimen.

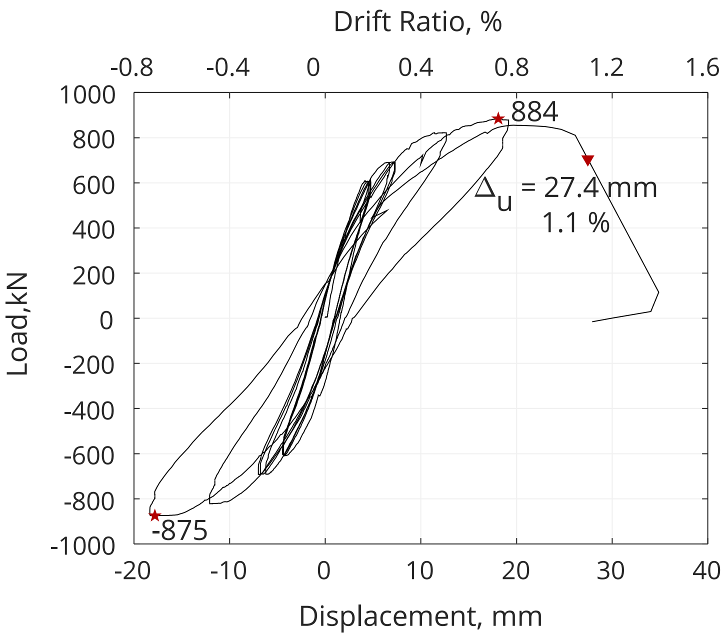

Figure 3-29. CW2 global response

The hysteretic response of specimen CW2 is similar to that of the specimen CW1, and it resembles the response of a "bridge pier under high axial load" as described by Priestley et al. (2007). Such a response is characterized by relatively narrow hysteretic loops that are usually observed in members with axial load or prestressed concrete members. The axial compression closed the cracks leaving relatively small residual displacements upon unloading. There is almost no evident yield plateau in the global response of the specimen, and the failure occurred at a relatively low drift ratio.

Specimen CW2 failed in flexure due to the crushing of the concrete in vicinity of the base section as shown in Figure 3-30. The failure caused a sudden drop in the lateral resistance of the wall. The crushing of the concrete was accompanied by the buckling of four layers of longitudinal bars below the second stirrup, which also caused the opening of the bottom stirrup. The condition of the crushed zone of the specimen after removal of the detaching concrete debris is shown in Figure 3-30.

Figure 3-31 shows the envelope of the response of wall CW2 and the peaks of each loading stage (LS). The circles connected with a thick black line define the envelope of the response, while the intermediate loading steps are marked with the red triangles. It can be observed that there was virtually no strength degradation between the cycles and the load fully recovered in the consecutive cycles. In this respect, it is worth noting that the first yielding of the longitudinal reinforcement occurred at a displacement of about 6.6 mm or the drift ratio of about 0.26%.

Figure 3-30. CW2 failure

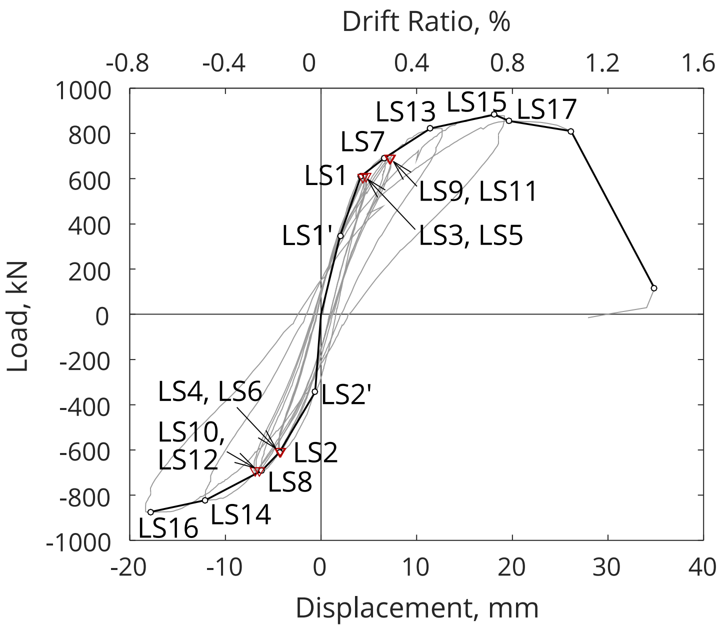

Figure 3-31. CW2 loading history

The cracking patterns and the measured crack widths at several loading stages in each loading direction are shown in Figure 3-32. In the two first sets of cycles corresponding to the lateral force of 70% and 80% of V_{fl} (LS1 to LS12), several flexural cracks formed in the lower third portion of the test region. The cracks were initially horizontal and started inclining towards the middle of the section with the increasing loading. In the following load cycles (LS13 and LS14), when the specimen was loaded up to 95% of V_{fl}, several new cracks formed higher up in the test regions propagating at an angle of about 45 ° . A vertical splitting crack also appeared at the compressed side of the base section, indicating the onset of crushing of the concrete. In the last two cycles before the failure (LS15 and LS16), the existing cracks extended and widened, and no new cracks were observed. Due to the high axial compression, cracking in the wall was limited to the bottom half of the test region. The largest crack width observed throughout the test was the opening of the base crack, with the width evaluated using the DIC system measured at 2.5 mm just before failure (LS17). The widest inclined crack was measured at 0.6 mm.

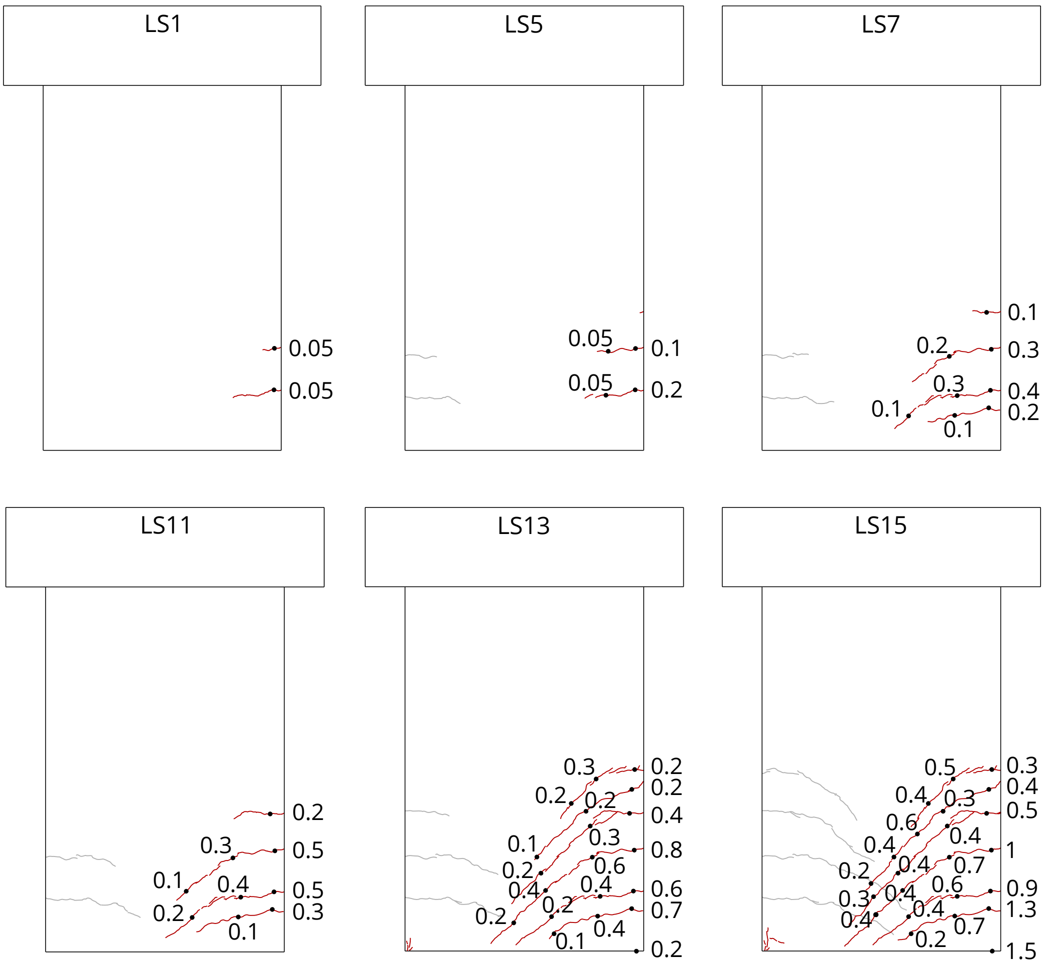

a) Positive envelope

Figure 3-32. CW2 crack patterns and crack widths in mm

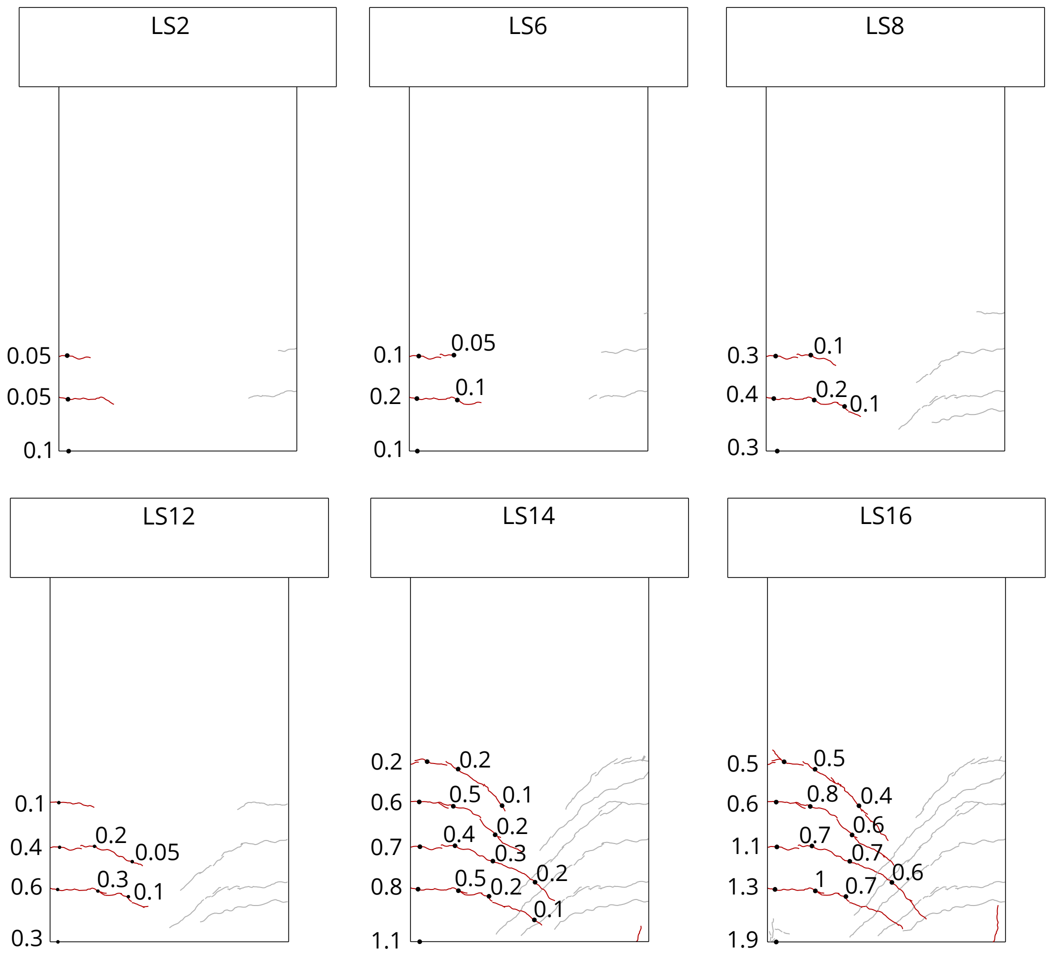

b) Negative Envelope

Figure 3-32. CW2 crack patterns and crack widths in mm (continued)

The longitudinal strains measured on the side faces of wall CW2 using the chains of displacement transducers are shown in Figure 3-33. The positive strain represents the face of the wall in tension while the negative strain corresponds to the compressed side of the wall. Consistent with the cracking patterns, the largest deformations on the tension side in each direction of loading were measured in the region near the base section. It is noted that the strain measurement at the level of the base crack includes the strain penetration deformations, therefore it does not represent the actual rebar strain at that location. According to these measurements, the yielding of the reinforcement is limited to a height of 650 mm from the base section.

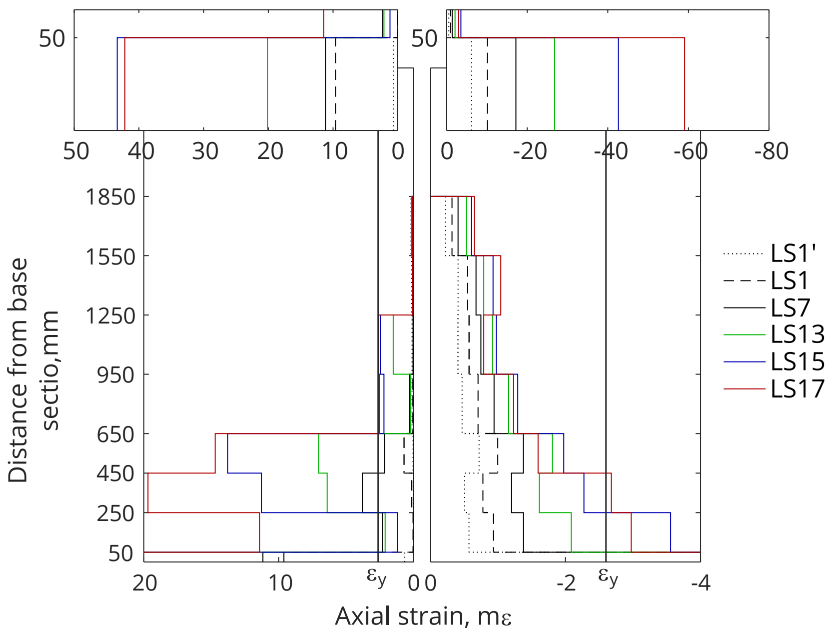

a) Positive envelope

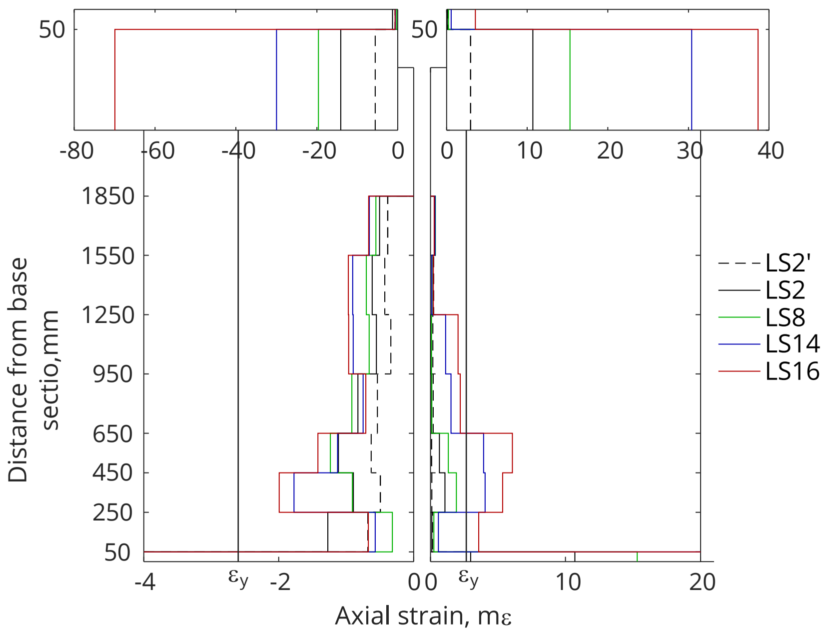

b) Negative envelope

Figure 3-33. CW2 axial strains

The strains in the longitudinal rebars, along the envelope of the response in each loading direction, measured using the strain gauges in the base section are shown in Figure 3-34. The strains are evaluated as a mean value of the strain measured with the two gauges placed at the same distance along the depth of the section.

The measurements show that the reinforcement was at the onset of yielding at LS7, at the top displacement of 6.6 mm and corresponding drift ratio of 0.26%. After load stages LS13 and LS14, the strain gauge data deviates from the expected trend and are assumed not to represent reliable measurements. The erroneous values are likely a consequence of the accumulation of plastic strain in the rebars due to cyclic loading history.

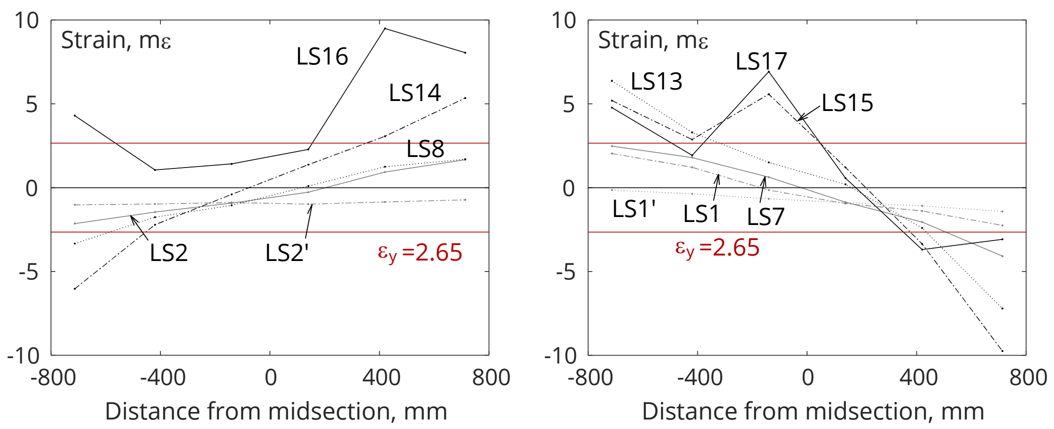

a) Positive envelope

b) Negative envelope

Figure 3-34. CW2 strain gauge measurements

The test data is further used to investigate the behavior of the shear reinforcement. The estimates of the horizontal strains near failure are shown in Figure 3-35. The strains were obtained from the optical measuring equipment, LED scanners and DIC system. In Figure 3-35a, the strain profiles along each row of the LED markers were calculated from the relative movement of the adjacent markers, divided by the distance between the markers (i.e. 233 mm). The values shown in the plot represent the maximum value of the strain measured along each row of markers. Figure 3-35b shows the local horizontal strains generated using the data from the DIC system. It can be seen that the strains are concentrated at the location of the cracks, and are significantly larger than those in Figure 3-35a.

The horizontal strains obtained from both the LED and DIC systems indicate that the stirrups yielded in the regions of shear cracking. The maximum LED and DIC strains reached respectively 3.3 mε and 9 mε, while the yield strain of the stirrups was $\varepsilon_{yv} = 2.6$ mε. As explained before, it should be noted that, because of the local slip between the stirrups and concrete in the vicinity of the cracks, the local stirrup strain in the crack differs from the strains measured with the optical systems on the concrete surface. As the LED system uses a relatively large averaging length and the DIC system a very small length, the strains shown in Figure 3-35a and Figure 3-35b provide the lower and upper bound estimate of the actual stirrup strain in the cracks, respectively.

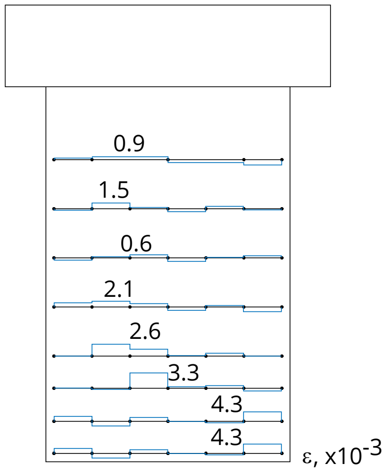

a) Horizontal strains from LED scanners

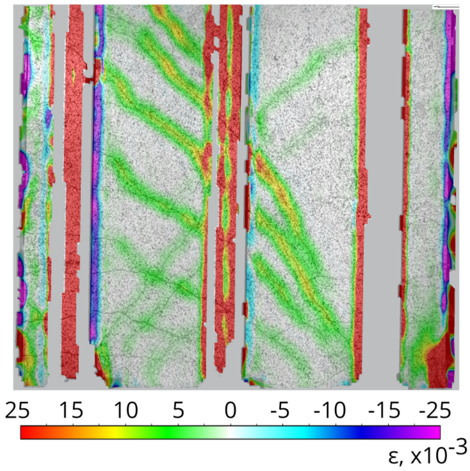

b) Horizontal strains from DIC system

Figure 3-35. CW2 horizontal strains near failure (LS17)

Similar to walls CW0 and CW1, the bond model by Sigrist (1995) was used to obtain the estimate of the crack opening that causes the yielding of stirrups. Since specimens CW1 and CW2 had similar concrete strength, the crack width that causes yielding of the ϕ8 stirrups is 0.4 mm, which corresponds to the equivalent opening of an inclined 45° crack of approximately 0.3 mm. The measured crack widths in Figure 3-32 indicate that the yielding in stirrups first occurred when the specimen was loaded to 95% of V_{fl}, or at LS13 and LS14.

Finally, the measurements performed using the LED system allow the visualization of the deformed shapes of specimen CW2 throughout the test. Figure 3-36 shows the evolution of the deformed shape along the envelopes of the response and the deformed shape at the last step of the envelope in each direction. For better visualization of the deformed shapes, the displacements of the markers were magnified 15 times. From the visual evaluation of the deformed shapes, it appears that the horizontal sections remain plane throughout the envelope of the response and that there is a very small distortion to the shape of the quadrilaterals defined by the LED markers. Detailed discussion and analysis of the deformation patterns are presented in §3.4.2.

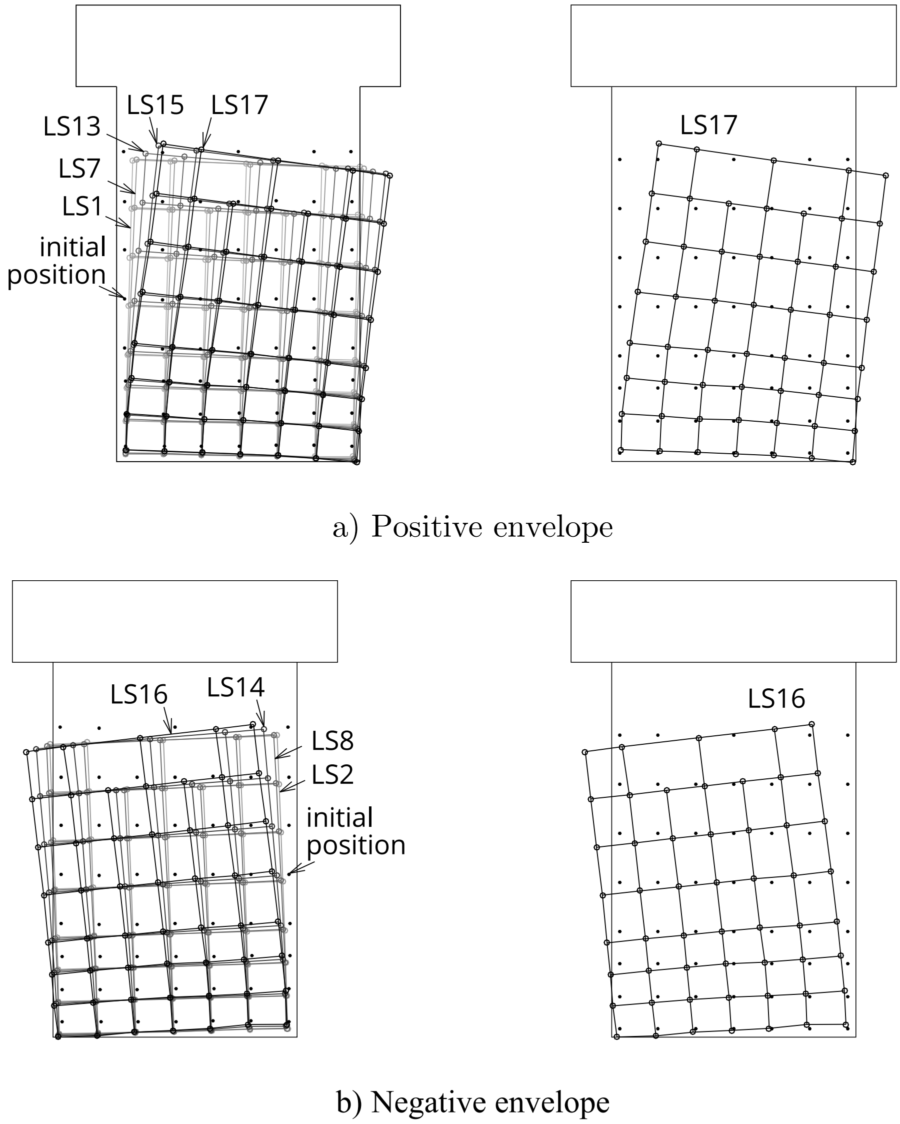

Figure 3-36. CW2 deformed shape (magnification x15)

3.4 Analysis of results

3.4.1 Effect of axial load

The global force-displacement relationship of the three walls are compared in Figure 3-37. The complete hysteretic response of each wall is shown in Figure 3-37a while Figure 3-37b compares the envelopes of the response. Table 2 contains the most important values from the envelopes: the maximum load V_{max} sustained by the specimens, the yield displacement Δ_y, the ultimate displacement Δ_u and corresponding drift ratio δ_u, and the flexural capacity predictions V_{fl}. The ultimate displacement and drift ratio at failure were adopted to correspond to a 20% drop in the maximum load experienced by the specimen.

The main test variable was the level of the axial loads applied to specimens CW0, CW1, and CW2, corresponding to 0, 10%, and 21% of the compressive strength of the concrete section *bhf'c*, respectively. As expected, the increasing axial compression force resulted in a significant increase in the lateral resistance. All three specimens exhibited significant yielding of the longitudinal reinforcement and their failure was dominated by flexure. The resistance attained by each wall was in a good agreement with the flexural strength predictions V_{fl} obtained based on the classical sectional analysis using program Response2000 (Bentz, 2000). In terms of displacement/drift ratio capacity, the trend is the opposite as the increasing compression on the wall resulted in reduced displacements at failure. For specimens CW1 and CW2, as the axial load was approximately doubled from 1315 kN to 2650 kN, the lateral load resistance increased by 29%, and the displacement capacity decreased by 45%.

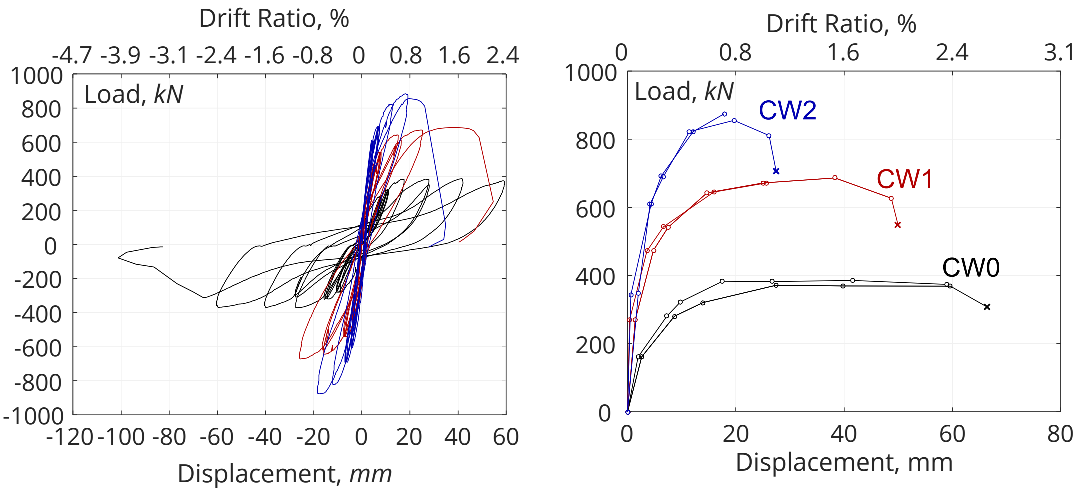

a) Hysteretic response

b) Envelopes

Figure 3-37. Lateral load versus top displacement (drift ratio) response of test walls

From the full response of the walls in Figure 3-37a, it can be seen that the application of the axial load also affected the shape of the hysteretic loops. In the case of specimens CW1 and CW2, the presence of axial load ensured that the cracks close well upon unloading, leaving very little residual displacements. On the contrary, the absence of compression force on wall CW0 caused the elongated hysteretic loops due to the "pinching effect" caused by the sliding deformations in the base. These deformations occur upon the load reversals and increase with the accumulation of inelastic deformations in the longitudinal rebars. They are reflected in the force-displacement response as the reduction in the reloading stiffness at the low level of applied lateral force.

Table 3-4. Summary of main test results

Specimen	CW0	CW1	CW2
V_{max}, kN	-386	686	884
Δ_y, mm	6.4	7.5	6.6
Δ_u, mm	-66.3	50.0	27.4
δ_u, %	2.6	2.0	1.1
V_{fl}, kN	405	639	829

In terms of cracking, all three walls developed fan-shaped cracking patterns. Initially the walls developed horizontal flexural cracks near the base section, followed by the propagation of inclined flexure-shear cracks higher up in the test region. The effect of axial load on the cracking patterns and crack widths (slip) near failure of walls CW0, CW1, and CW2 is illustrated in Figure 3-38. It can be seen that the extent of the propagation of cracking is significantly decreased with the bigger compression on the wall. Wall CW0 had the cracks propagating across the whole clear height of the test region, while walls CW1 and CW2 had cracked up to about two-thirds and one-half of the height, respectively. This is an expected result as the axial compression decreases the tensile stresses due to flexure, and therefore limits the extent of cracking. Consistent with this result, the opening of the cracks was larger with lower axial loads. Just before the failure occurred, the opening of the base crack reached about 19 mm, 6.4 mm, and 2.5 mm in specimens CW0, CW1, and CW2, respectively. In addition, there was a notable difference in the width of the inclined cracks, ranging up to 1.9 mm for wall CW0, 0.8 mm for wall CW1, and 0.6 mm for wall CW2. In the case of wall CW0, a substantial amount of slip on the crack was observed with values of up to about 0.7 mm. The widths of the flexural cracks, measured near the tensile boundary of the wall above the base crack, did not differ greatly between the tests.

The axial strains from the chains of displacement transducers near failure of the three walls are compared in Figure 3-39. Consistent with the cracking patterns and failure modes, the biggest tensile and compressive strains are concentrated in the areas close to the base section. The tensile strains are diminishing with the increasing axial load. It is estimated that the yielding of the reinforcement propagated up to a height of 1550 mm, 1250 mm, and 650 mm from the base of walls CW0, CW1, and CW2, respectively. The compressive strains also exceeded the yield strain of the reinforcement but in a smaller region near the base section. The maximum values of the compressive strains also show that near failure the edge concrete was well in the post-peak regime.

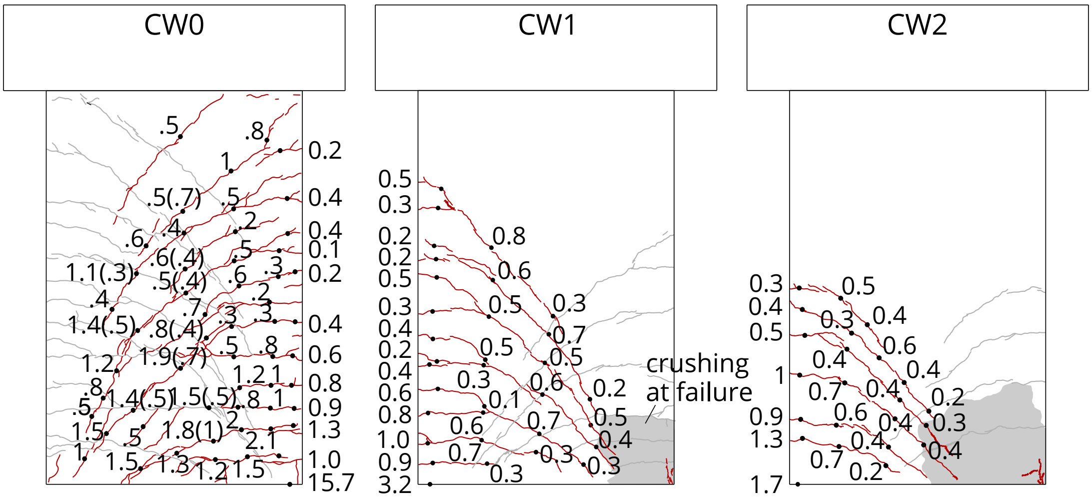

Figure 3-38 Comparison of cracking patterns and crack widths (slip) in mm at loading stages prior to failure for walls CW0 (LS21), CW1 (LS17), and CW2 (LS15)

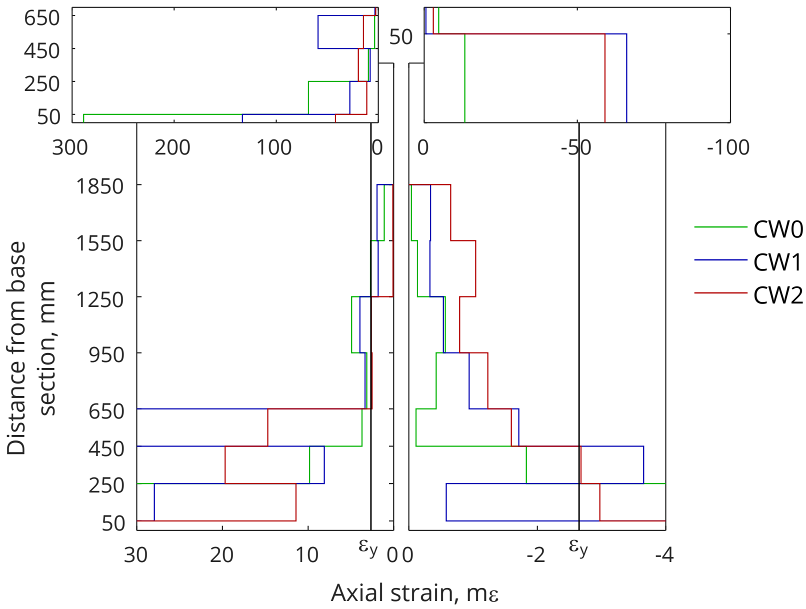

Figure 3-39. Strains from chains of displacement transducers for specimens CW0 (LS23), CW1 (LS17), and CW2 (LS15) near failure

The comparison of the horizontal strains obtained from the DIC system near the failure of the three specimens is shown in Figure 3-40. The vertical bands of high strains in CW1 and CW2 are due to disturbances of the view of the cameras caused by the test setup (Figure 3-6), and therefore they need to be neglected as artificial. Apart from this effect, the horizontal strains are concentrated along the inclined cracks and provide an estimate of the strain in the shear reinforcement in the cracks. As discussed earlier, considering the imperfect bond between rebars and concrete, the actual strain in the stirrups is somewhat smaller than the strains at the crack locations evaluated from the DIC system. The three DIC plots show a trend of decreasing horizontal strains between the specimens with increasing axial load. In the case of specimen CW0, the maximum strains were of the order of 30 mε, which is about 11.5 times the yield strain of the stirrups. For specimens CW1 and CW2, the maximum horizontal strains across the cracks were estimated to be about 20 and 8 mε or about 8 and 3 times higher than the yield strain of the stirrups, respectively.

All three specimens failed in flexure-dominated modes at the critical base section. Specimen CW0 failed due to rupture of the longitudinal tensile bars that had buckled in compression in the previous loading cycle. In contrast, specimens CW1 and CW2 failed by crushing of the concrete in the compressed “toe” of the wall. The crushing of the concrete was accompanied by the buckling of the longitudinal rebars and opening of the stirrups in the failed regions. The depth of the crushed compression zones and the number of buckled bars was larger in the specimen with a higher axial load. Within the failed zones, two layers of compression reinforcement buckled in wall CW1 while four layers buckled in wall CW2. The crushed zones are depicted with grey shading in Figure 3-38. Even though the specimens failed in flexural failure modes, they failed in an abrupt manner, i.e. the occurrence of failure mechanism caused a sudden drop of lateral resistance.

Even though the specimens had characteristics that make them susceptible to shear failures, such as a low aspect ratio and a relatively small amount of transverse reinforcement, diagonal tension failures did not occur. The measured horizontal deformations shown in Figure 3-40 indicate that all the walls attained yielding in the stirrups across the shear cracks. However, the primary shear resisting mechanisms, i.e. aggregate interlock, stirrups, and the compression zone, were sufficient to suppress the diagonal tension failure. The increasing compression on the walls increased the shear resistance as evidenced by the reduced shear cracking and the smaller displacements in the cracks. At the same time, the increased demand on the compression zone due to higher axial load significantly reduced the global deformation capacity of the walls.

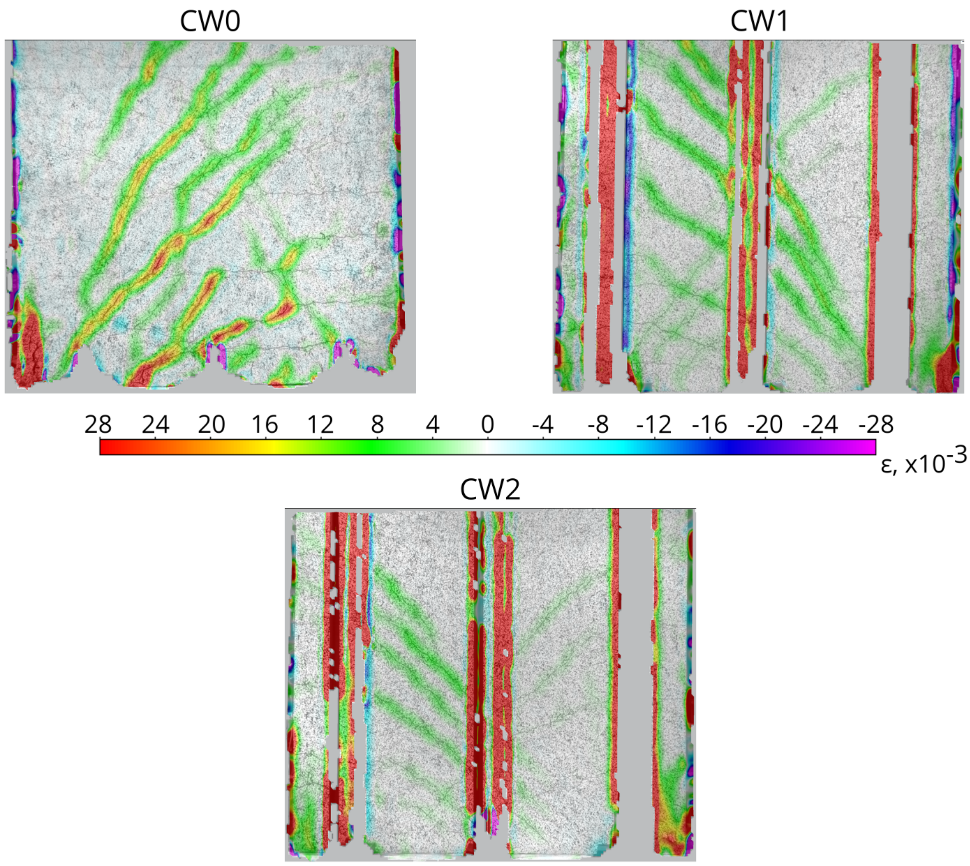

Figure 3-40 Horizontal strains from DIC system prior to failure for specimens CW0, CW1, and CW2

3.4.2 Analysis of deformations

In addition to the comparison of the various local deformations measured in the test specimens, it is also of interest to analyze how these deformations contribute to the drift of the walls. Such an analysis is performed in this section by considering three distinct deformation modes as illustrated in Figure 3-41. These modes include flexural, shear, and sliding deformations.

The flexural deformations occur as a consequence of the rotation of the horizontal sections (Figure 3-41a). The rotations of the sections were calculated at the level of each row of LED markers, using the vertical displacements of the outer columns of markers. The rotation of the top section located at the level of the lateral load was measured with the inclinometer attached to the top block of the specimens (Figure 3-8). The relative horizontal displacement between two rows of LED markers (sections) is evaluated using the following expression:

$$\Delta_{fl,k} = \frac{\theta_i + \theta_{i+1}}{2} dh_k \tag{3-1}$$

where index k indicates the number of the rectangle defined between the two adjacent sections. The top displacement due to flexure Δ_{fl} is obtained by summing up the contribution of each rectangle $\Delta_{fl,k}$ along the height of the wall.

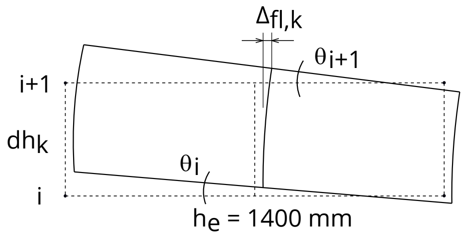

a)Flexural deformation

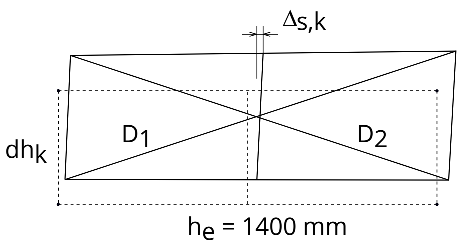

b) Shear deformation

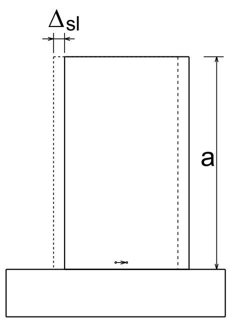

c) Sliding deformations

Figure 3-41. Deformation components

The shear deformations represent the change of the 90-degree angles of the rectangular elements defined by two adjacent rows of LED markers (Figure 3-41b). They are calculated from the change of lengths D_1 and D_2 of the diagonals in each rectangular element, which are in turn evaluated from the displacements of the four corner markers of the rectangle. Based on these simple geometrical considerations, the shear displacement in rectangle k is evaluated using the expression:

$$\Delta_{s,k} = \frac{(D_1^2 + D_2^2)}{4h_e} \tag{3-2}$$

The top displacement due to shear Δ_s is obtained by summing up the contribution of each rectangle $\Delta_{s,k}$ along the height of the wall. The shear deformations estimated in this way assumes a constant curvature over the height of the rectangle dh_k. When the curvature is constant, D_1 and D_2 are not affected by the curvature.

The sliding deformations represent the horizontal rigid body movement of the wall with respect to the foundation, see Figure 3-41c. The sliding displacement Δ_{sl} was evaluated by averaging the horizontal displacements of the two middle LED markers belonging to the bottom row of markers. The sliding was also measured using the displacement transducers attached at a height of about 50 mm from the bottom section on each side of the wall. However, these measurements contain the deformations due to the expansion of the concrete cover in compression, as well as the deformation along the whole length of the section. For these reasons, the measurements from the LED scanners were found more suitable for estimating this mode of deformation. In the cases where the information from the LED markers was not available, it was supplemented by the displacements obtained with the DIC system at the same location.

Finally, the total top horizontal displacement of the walls is calculated by summing up the flexural and shear deformations of each rectangle of targets and adding the sliding deformation at the base:

$$\Delta_{top} = \sum_{1}^{\max k} (\Delta_{fl,k} + \Delta_{s,k}) + \Delta_{sl} = \Delta_s + \Delta_{fl} + \Delta_{sl} \qquad (3\text{-}3)$$

Using Eqs. (3-1)– (3-3) the contribution of each deformation pattern to the top drift ratio was calculated for each of the three test specimens. Figure 3-42 compares the top drift ratios obtained from the assumed deformation patterns against the experimentally measured values at all load stages up to failure. It can be seen that the predicted top drift ratios are in a very good agreement with the measured values for all three walls and therefore the deformations experienced by the specimens can be effectively described using the assumed deformation modes. The plots also show that the most significant contribution to the top drift is due to flexure and that the contributions of the shear and sliding deformations decrease with increasing axial load.

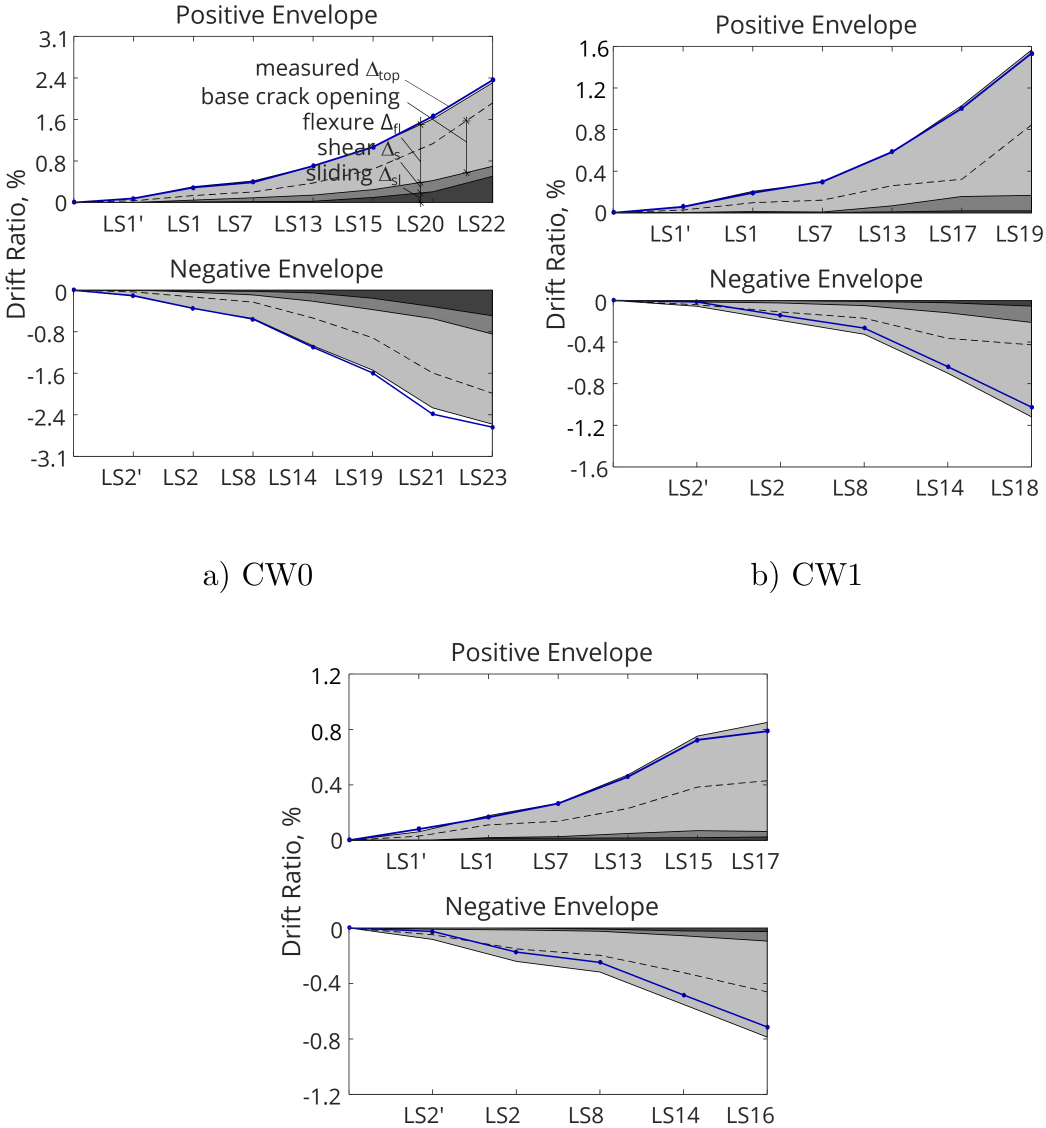

a) CW0 b) CW1

c) CW2

Figure 3-42. Contribution of deformation components to total horizontal displacement for each specimen

The cracking patterns and the strain measurements showed that the biggest deformations were observed at the level of the base crack. The portion of the flexural deformations arising from the base crack opening is highlighted with the dashed lines in Figure 3-42. The top displacement due to the base crack opening is calculated by multiplying the rotation of the bottom row of LED markers with their distance to the axis of lateral load application. Not surprisingly, the base crack opening represents the major portion of the flexural deformations. Near failure, the percentage of contribution of the base crack opening to the total drift was up to 43 % for walls CW1 and CW2, and 44% for wall CW0. The base crack opening also includes the deformation due to strain penetration in the foundation block, i.e. the deformations in the reinforcing steel below the level of the base section. Since the strain penetration was not directly measured, it can be assumed that at least one half of the contribution of the base crack opening arises from the strain penetration.

As mentioned above, the contribution of the shear deformations diminished with the increasing axial compression on the walls. In the loading stages after yielding of longitudinal reinforcement this contribution was evaluated to be about 13.6%, 10.6%, and 6.4% for walls CW0, CW1, and CW2, respectively.

Finally, the sliding deformations were significant only in the case of specimen CW0, where the absence of axial load was the leading cause for the accumulation of plastic strains in the tension reinforcement. The sliding increased progressively along the load-displacement envelope and it reached a value of about 21% in the last two loading steps. Specimens CW1 and CW2 exhibited negligible values of sliding displacement.

4 Macro-Kinematic Modeling

This chapter focuses on the kinematics-based modeling of short reinforced concrete walls. In §4.1, an SDOF kinematic approach is proposed for evaluating the behavior of flexure-dominated walls under seismic actions. In §4.2, the modeling of shear-dominated walls is based on the three-parameter kinematic theory (3PKT) (Mihaylov et al. 2016), which is extended to account for the effects of barbells, strain penetration in the foundation, cracking above the critical shear cracks, and stirrup ruptures.

4.1 Single degree-of-freedom (SDOF) kinematic approach for flexure-dominated short walls

4.1.1 SDOF kinematics of short walls

An interesting observation about the kinematics of the CW test walls can be made from the measured deformations patterns shown in Figure 4-1. The arrows in the figure represent the vectors of displacements of the selected points on the wall surface measured using the DIC system near failure. What appears as a grey shading in the plots is the complete vector displacement field estimated by this measuring technique. From this visual representation of the displacement vectors, it appears that the walls rotate around a point at the base of the specimens. The center of rotation shown for each wall in Figure 4-1 was estimated from the vector displacement field, by averaging the horizontal coordinates of the points with horizontal vectors. These points are approximately aligned on a straight vertical line passing through the center of rotation.

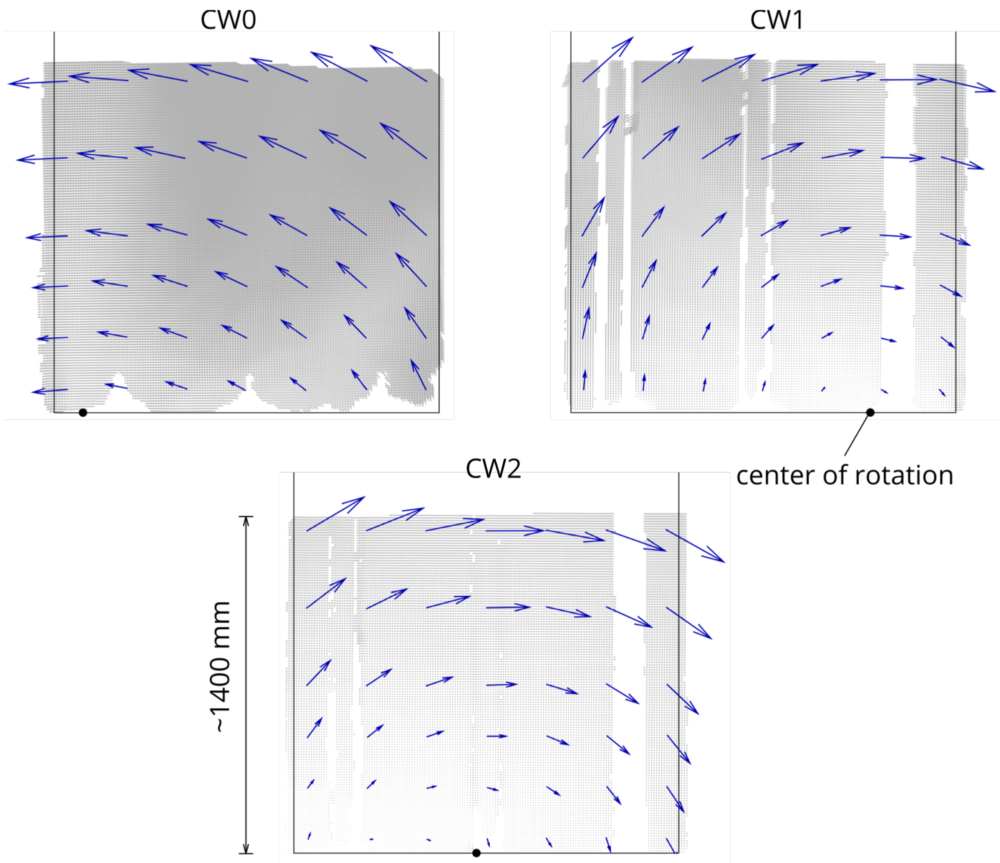

Figure 4-1. Displacement fields of walls CW0, CW1, and CW2 near failure measured using DIC system

Based on these experimental observations, a simple kinematic model that describes the global displacement filed in walls is proposed, refer to Figure 4-2. The global deformed shape in the kinematic model is idealized as a function of a single degree of freedom (SDOF) – the rotation of the rigid block around a point at the base section of the wall. The rigid block assumption is justified, and later on validated, with the test observations. Most of the deformations in walls are limited to the fan-shaped cracked region and there are relatively negligible deformations in the uncracked region which can be assumed as rigid.

Displacements δ_{xi} and δ_{yi}, in the x- and y-direction, respectively, of an arbitrary point (x_i, y_i) on the rigid block can be estimated using the following expressions:

$$\delta_{xi} = \vartheta \, y_i \tag{4-1}$$

$$\delta_{yi} = \vartheta \, (x_{cr} - x_i) \tag{4-2}$$

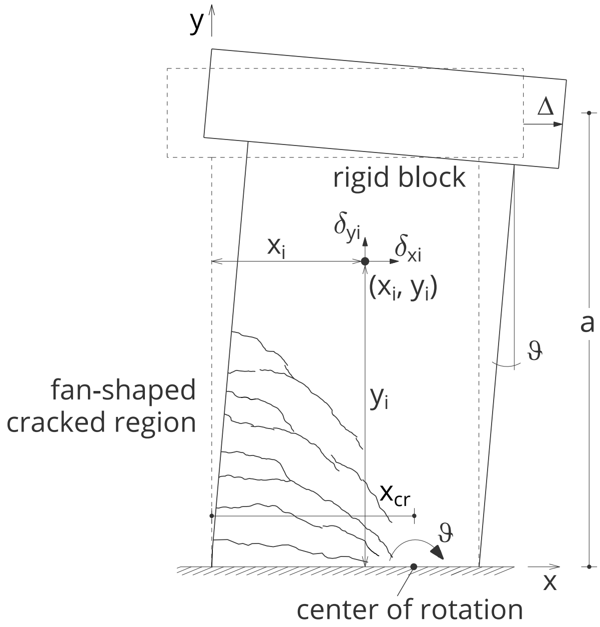

Figure 4-2. SDOF kinematic model

The top horizontal displacement Δ is expressed as a function of the rotation ϑ and is obtained as follows:

$$\Delta = \delta_{xi}(y = a) = \vartheta\ a \tag{4-3}$$

The assumed kinematics shown is validated using the measured displacements of the grid of LED markers on the CW wall specimens. An optimization procedure, which minimizes the distances between the predicted and measured marker locations, was used to obtain the rotational DOF (ϑ) corresponding to the best fit between the predicted and measured displacement fields. Figure 4-3 shows comparisons between these two displacement fields for walls CW0, CW1, and CW2 at maximum resistance. The figure also compares the measured top displacement Δ_{exp} with the top displacement corresponding to the fitted (optimized) displacement field from the optimization calculation Δ_{opt}. Since one of the main assumptions of the kinematic model is that the deformations in the rigid block are negligible compared to those in the cracked region, the optimization procedure was performed only with the LED markers located above the steepest shear cracks shown with diagonal dashed lines in Figure 4-3. The center of the rotation at the base section was evaluated as the location where the measured vertical displacement of the bottom row of LED markers is zero.

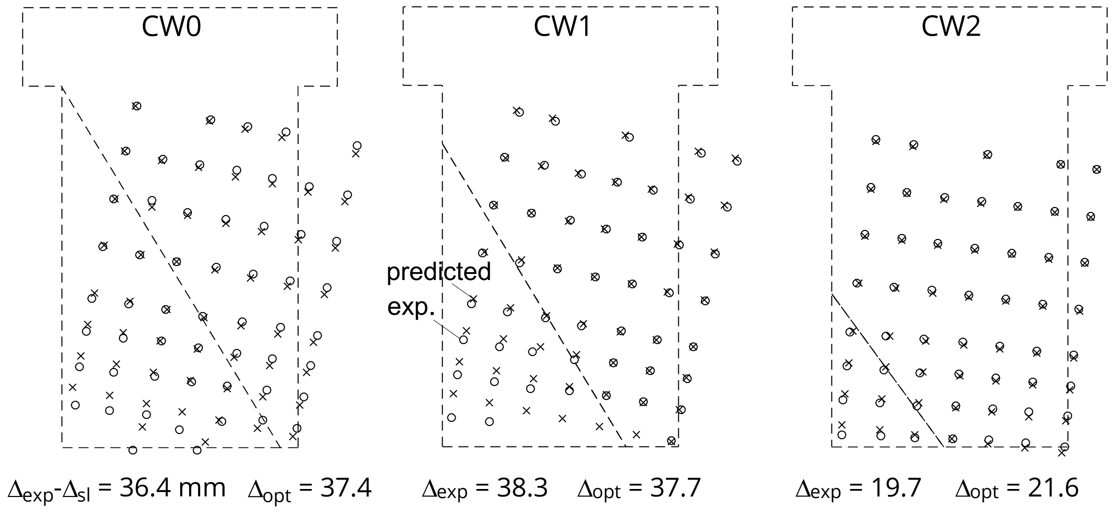

Figure 4-3. Comparison of measured and fitted displacement fields based on the SDOF kinematics for wall CW0, CW1, and CW2 at V_{max} (x15 magnification)

The comparisons of the measured and optimized deformation patterns shown in Figure 4-3 demonstrate that a simple kinematic description using the SDOF kinematics can effectively predict the displacements of the assumed rigid block in all the specimens. An excellent comparison of displacements was achieved for walls CW1 and CW2. In the case of wall CW0, the comparison was performed on the displacement field corrected for the observed sliding displacements that do not contribute to the deformation pattern described by the kinematics. It can be seen from Figure 4-3 that the measured displacements field of wall CW0 is placed somewhat higher than the predicted pattern. This is due to the measurement errors of the LED scanner system, that affected the vertical displacements of the targets in the case of wall CW0. More specifically, only in this test, the vertical displacements were observed to gradually "drift" with time even when the wall was unloaded. In addition, since the kinematics only considers the rigid body rotation, the discrepancies in the displacement patterns can be observed in the cracked regions of all three walls. Finally, it should be noted that the agreement between the predicted and measured displacement patterns has been observed to remain consistent along the entire envelopes of the response of the CW walls.

4.1.2 General formulation of mechanical model

The SDOF kinematic model is used as a basis for a complete mechanical model that can predict the load-displacement envelope of wall piers. A schematic representation of the mechanical model and its main relationships are shown in Figure 4-4. It can be seen from the figure that the wall is idealized as consisting of two distinct regions: a fan-shaped cracked region and a rigid block. The three sets of equations in the figure express the generic hypotheses for the description of the behavior of a cantilever wall pier subjected to vertical and horizontal loading.

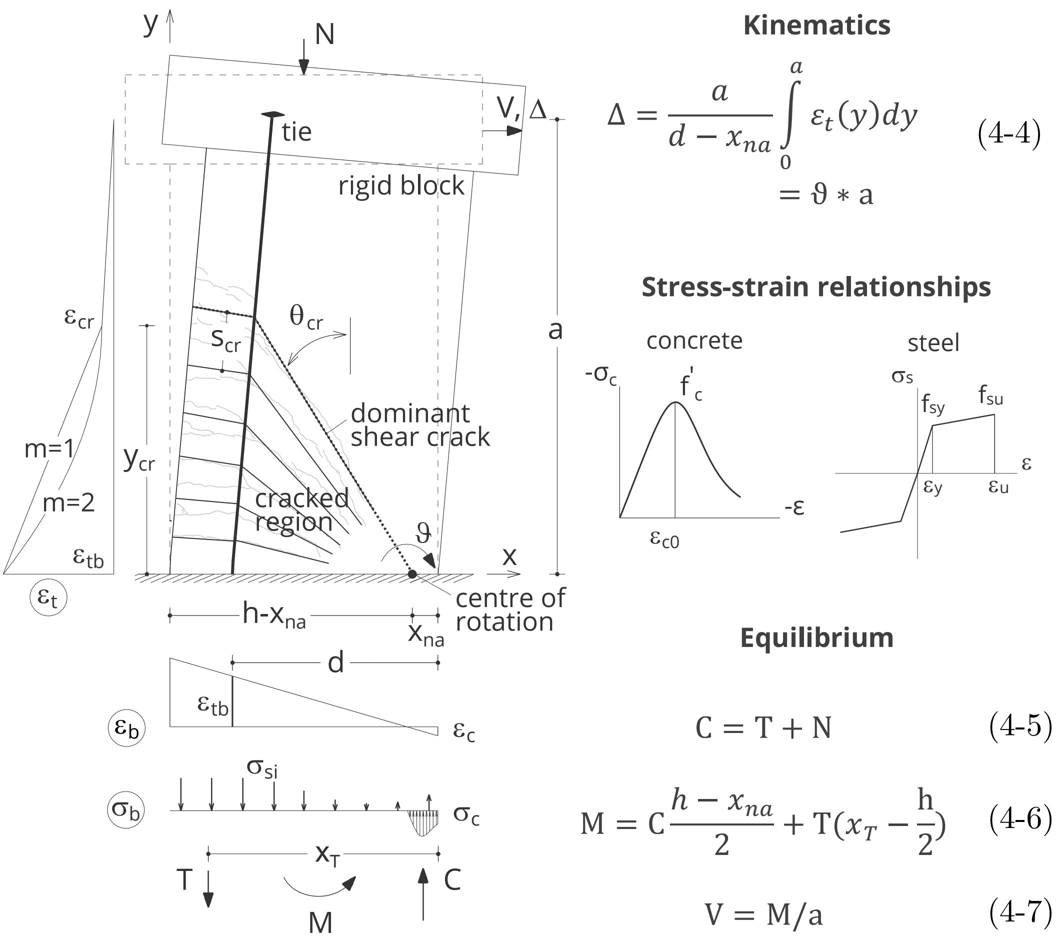

Figure 4-4. SDOF mechanical model

The SDOF kinematic model assumes that the behavior along the base section can be described using classical sectional analysis, which implies a linear strain compatibility condition. The linear strain profile along the base section ε_b can be defined using two variables, e.g. the maximum strain at the compressive edge ε_c and the neutral axis depth x_{na}. For a given value of the strain ε_c and known stress-strain curves of the steel and concrete, the neutral axis depth can be evaluated by satisfying the equilibrium condition given by Eq. (4-5). The tension (T) and compression force (C) couple are determined by integrating the stresses in the concrete σ_c and reinforcement σ_{si} along the base section. This in turn allows the calculation of the moment M and the corresponding lateral force V from Eqs. (4-6) and (4-7), respectively.

The link between the behavior at the level of the base section and the global behavior of the wall is established through an assumed strain profile in the reinforcement tie ε_t. The tie represents the longitudinal reinforcement in tension, whose centroid is located at a distance d from the compressive edge of the wall corresponds to the centroid of the reinforcement in one-half of the section. It is further assumed that the rigid block rotates around the neutral axis of the base section, and therefore the center of the rotation of the SDOF kinematic model is located at a distance x_{na} from the extreme compressed fiber. In this way, the relationship between the global displacement and the strain along the length of the tie is expressed with Eq. (4-4). For a known value of the rotation ϑ, the displacement of any point of the rigid block can be estimated using Eqs. (4-1) and (4-2).

Consistent with the experimental observations, the model assumes that cracking in the wall develops in a fan-shaped cracking pattern and propagates along the length of the tie up to the cracking height y_{cr}. As the load on the wall increases, the cracking propagates higher up the member the cracks become steeper (flexure-shear cracks). The cracking height y_{cr} can be estimated from the cracking moment of the concrete section M_{cr} as follows:

$$M_{cr} = \left(f_{tc} + \frac{N}{bh}\right)\frac{bh^2}{6} \tag{4-8}$$

$$y_{cr} = \min\left(a - \frac{M_{cr}}{V}, d\ cot\theta_{cr}\right),\ \ V > \frac{M_{cr}}{a} \tag{4-9}$$

where,

$f_{tc} = 0.33 f_c'^{2/3}$	Tensile strength of concrete
I_g	Gross moment of inertia of concrete section
θ_{cr}	Inclination of the dominant shear crack

As shown in Eqs. (4-9), it is also assumed that the cracking height is limited by the propagation of the dominant shear crack. The inclination of this crack θ_{cr} is determined from a shear strength calculation according to the AASHTO code shear provision (AASHTO 2007; Bentz et al. 2006). This assumption is adopted to account for the effect of shear-flexure cracking on the propagation of the deformations in the tie and is discussed in detail in the following section. The fan-shaped cracked region can be approximately described by connecting the height of cracking along the tie to the center of rotation by a straight line (radial crack). The concrete between the radial cracks can be seen as a series of rigid radial struts pinned at the center of rotation and connected to the tie. The horizontal and vertical displacements of any point along a strut can be obtained as the rotation of the strut is multiplied by the vertical and horizontal distances to the center of rotation, respectively. The strut rotation is in turn obtained by integrating the strain profile in the tie below the strut, and by dividing the result by d-x_{na}.

The spacing of the cracks along the tie s_{cr} can be estimated based on the Model Code 90 (CEB-FIP, 1990), as a function of longitudinal rebar diameter d_b and the effective reinforcement ratio of the tension zone $\rho_{l,eff}$:

$$s_{cr} = 0.28 d_b \rho_{l,eff} \tag{4-10}$$

where $\rho_{l,eff}$ is equal to the area of the reinforcement in one-half of the section divided by $bh/2$. For a known strain profile in the reinforcement tie, it is possible to estimate the crack widths along the tie by integrating the tributary area of the tensile strains belonging to each crack.

Before cracking, the initial linear branch of the force-displacement curve is obtained from a Timoshenko beam theory using uncracked sectional properties:

$$\Delta = V\left(\frac{a^3}{3E_cI_g} + \frac{1.2a}{0.4E_cbh}\right) \tag{4-11}$$

To model the nonlinear behavior after cracking, the generic formulation of the SDOF approach described above is further extended to the nonlinear constitutive modeling of its components. This is done through considerations of different phenomena observed in walls under seismic-type loading, which makes this approach adequate for predicting the envelope of the cyclic behavior of walls.

4.1.3 Constitutive modeling

4.1.3.1 Strain profile in reinforcement tie

The deformations developing in the cracked regions of walls depends on the propagation of inclined flexure-shear cracks, the amount of transverse reinforcement, and the properties of the longitudinal reinforcing steel (Fardis, 2009; Priestley et al., 2007). The inclined shear-flexure cracking, often observed in short wall members, causes the propagation of tensile strains higher along the tensile boundary. In the literature, this phenomenon is often referred to as the tension shift. The tensile forces tend to diminish over a certain distance until they can be transferred by the compression struts (Park and Paulay, 1975; Fardis, 2009). Larger stirrup ratios in the member enable the forces to be transferred over a shorter distance reducing the effect of the tension shift. In terms of properties of the reinforcing steel, a high ratio of the ultimate strength to yield strength of the longitudinal rebar steel (f_u/f_y) allows the propagation of the deformations further away from the critical base section. On the contrary, low f_u/f_y ratios cause the concentration of the strains near the critical section. It is also noted that if a major diagonal shear crack develops before flexural yielding in the base, the strains in the tie cease to increase above the crack as no further cracking is observed.

The vertical strain profiles in the tie of the SDOF mechanical model is described by using a set of simplifying assumptions. In most cases, the strain profile can be represented with a bilinear relationship shown in Figure 4-4. This relationship is defined between the point of load application, the cracking strain ε_{cr} at the cracking height, and the strain at the base section ε_{bt}. This is supported by several studies where an approximately linear variation was observed in the tension regions of test specimens (Dazio et al, 2009; Hines et al., 2004). The effect of shear cracking is considered to be limiting the propagation of deformations to the cracked region below the dominant shear crack, which is taken into account in Eq. (4-9). According to this equation, the height of cracking y_{cr} cannot exceed the vertical projection of the major shear crack $d{\cdot}cot(\theta_{cr})$, where θ_{cr} is the angle of the crack.

To account for the effect of the f_u/f_y ratio of the longitudinal reinforcement, the distribution of strains over the cracked length of the tie can be represented with the following expression:

$$\varepsilon_t(y) = (\varepsilon_{tb} - \varepsilon_{cr})\left(1 - \frac{y}{y_{cr}}\right)^m + \varepsilon_{cr}, \;\; y \leq y_{cr} \qquad (4\text{-}12)$$

where,

ε_{tb}	Strain in tie at critical section
m	Modification factor for vertical strain profile based on f_u/f_y
ε_{cr}	Cracking strain in concrete

y_{cr} Cracking height

Factor m is a function of f_u/f_y that is assumed to follow the relationship proposed in Figure 4-5. This factor controls the shape of the strain profile within height y_{cr} which varies from parabolic for f_u/f_y=1 (m=2) to linear for f_u/f_y≥1.2 (m=1). These two limit cases are illustrated in Figure 4-5. The parabolic pattern accounts for the localization of the strains in the base section when the reinforcing steel exhibits limited strain hardening, while the linear pattern represents more distributed plastic deformations along the reinforcement with a significant strain hardening behavior.

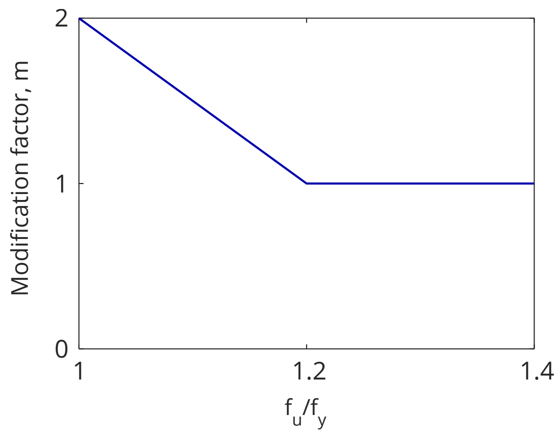

Figure 4-5. Modification factor m as a function of f_u/f_y

The effect of factor m on the predicted response of wall WSH1 reported by Dazio et al. (2009) is shown in Figure 4-6. Using the proposed relationship, the m factor is evaluated at 1.35. It can be seen from the load-displacement curves that m=1.35 results in a slightly less ductile response than m=1 due to the localization of strains. It can also be seen that the predicted response represents a good envelope of the measured hysteretic response of the test specimen.

4.1.3.2 Behavior of steel reinforcement in tension

The adopted stress-strain relationship for modeling the response of reinforcing steel is the bilinear relationship illustrated in Figure 4-4 (elastic-plastic with strain hardening). The occurrence of rupture in the longitudinal reinforcement in tension is one of the flexural failure modes often observed in walls. In modeling the response of the reinforcement subjected to cyclic loading, it is not appropriate to use a value of fracture strain ε_{su} obtained from monotonic tensile tests on rebars. The reason is that the breaking strain depends on the maximum compressive strain in the rebars from the previous cycle of loading. Due to the effects of cycling loading, the longitudinal reinforcement in compression is likely to buckle with the increasing inelastic deformations as observed in the CW tests. It has been shown in a study by Restrepo-Posada (1992) that the buckling of the rebars can cause microscopic cracks at the compression side of the rebar. This can lead to premature failure once the rebar is reloaded in tension. Based on these considerations, it is assumed in the analysis that the rupture in rebars occurs at 60% of the maximum fracture strain ($0.6\varepsilon_{su}$) (Priestley et al. 2007).

The fracture of rebars was the failure mode governing the behavior of walls WSH1 (Dazio et al., 2009) and R1 (Oesterle et al., 1976). These walls were analyzed using the mechanical model, and their measured and predicted responses are compared in Figure 4-6. During the test on wall WSH1, the fracture of the web rebars was observed before the wall failed by the rupture of the boundary reinforcement. The prediction shows that the rupture strains in the web and boundary rebars are accurately captured. In the case of wall R1, the failure in the test occurred as a consequence of the effects of cycling and the buckling of the rebars in the last cycle. The overall behavior of both walls is well captured by the analysis. The properties of walls WSH1 and R1 are summarized in Table 4-3 and Table 4-2, respectively.

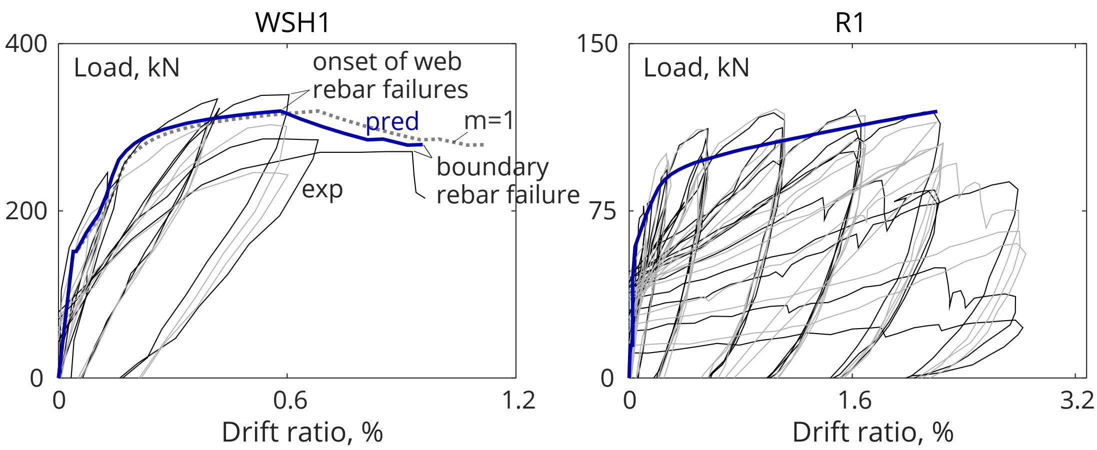

Figure 4-6. Comparison of measured and predicted response of walls WH1 (Dazio et al., 2009) and R1 (Oesterle, et al., 1976) that failed due to rupture of longitudinal rebars

4.1.3.3 Modeling of concrete and reinforcement in compression

4.1.3.3.1 Walls with non-seismic detailing

In the SDOF model, the modeling of concrete in compression is based on the stress-strain relationship proposed by Popovics (1973), see the curve labeled "basic" in Figure 4-7. This relationship has been described by Collins and Mitchel (1991) using the following relationships:

$$\sigma_c = -f_c' n \frac{\frac{\varepsilon}{\varepsilon_{c0}}}{n - 1 + \left(\frac{\varepsilon}{\varepsilon_{c0}}\right)^{nk}} \tag{4-13}$$

$$n = 0.8 + \frac{f_c'}{17} \tag{4-14}$$

$$k = 0.67 + \frac{f_c'}{62} \tag{4-15}$$

$$E_c = 3220\sqrt{f_c'} + 6900, MPa \tag{4-16}$$

$$\varepsilon_{c0} = -\frac{f_c'}{E_c \frac{n}{n-1}} \tag{4-17}$$

where,

σ_c	Concrete stress
f'_c	Concrete cylinder strength
n, k	Coefficients
E_c	Modulus of elasticity
ε_{c0}	Concrete strain at peak stress

This relationship is further modified to more realistically represent the behavior of the concrete in the compression zone of walls. The lateral deformation in the concrete at the boundary between the rigid foundation and the wall are restrained, causing a biaxial compression state in the concrete in the region of the base section. This state increases the concrete strength and therefore an enhancement factor of 1.25 is adopted for f_c based on a relationship by Kupfer et al. (1969). In the modified concrete stress-strain law, it is also assumed that the concrete completely loses its resistance at the large strains. This modification is adopted to more realistically capture the sudden drop in resistance after the crushing in the concrete occurs. The proposed modified concrete relationship and the basic stress-strain curve as per Popovics (1973) are compared in Figure 4-7.

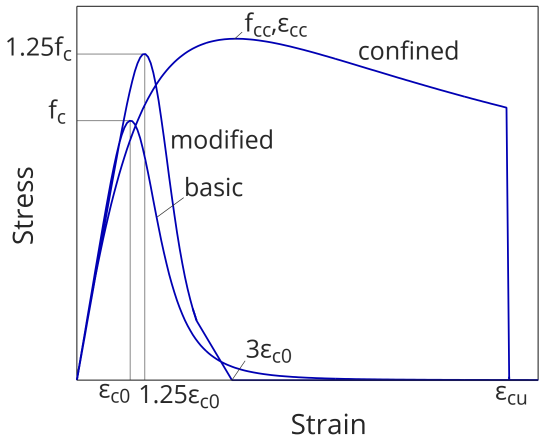

Figure 4-7. Behavior of concrete in compression in the SDOF approach

The presence of a biaxial stress state can also be seen from the crushed failure zones in walls CW1 and CW2 (Figure 3-21 and Figure 3-30). The crushing in concrete occurred at a certain distance above the base section which indicates that it was triggered at a distance where the confining effect was diminished.

Another phenomenon, nearly always observed in the response walls, is the buckling of the longitudinal rebars in compression. An important variable that affects buckling is the amount and detailing of the transverse reinforcement in the boundary elements. An often-used parameter to describe buckling is the slenderness ratio of the rebar s_v/d_b (Bresler & Gilbert, 1961), expressed as the ratio of the stirrup spacing and the bar diameter. Apart from the local buckling of rebars within a single stirrup spacing, a global buckling can also occur over a length of multiple stirrup spacings (Massone & Lopez, 2013). Buckling can also be related to the loading history, i.e. it depends on the tensile strain previously reached in the rebar (Moyer & Kowlasky, 2003). The occurrence of buckling is considered a significant limit state tht will often require the removal and replacement of the member (Priestley et al, 2007).

The buckling of reinforcement is taken into account in the SDOF mechanical model by modifying the constitutive law of the rebars in compression using the model proposed by Dhakal & Maekawa (2002). The model takes into account the effects of the slenderness ratio and the yield strength of steel on the reduction of strength of the rebar in compression. The effect of the slenderness ratio on the stress-strain response of steel is illustrated in Figure 4-8.

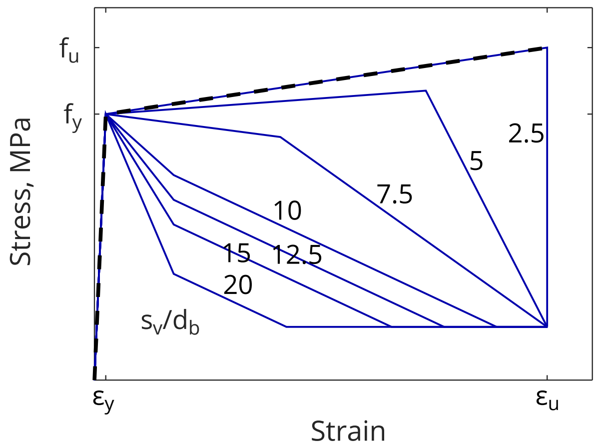

Figure 4-8. Buckling of rebars in compression

Figure 4-9 shows the predictions of the mechanical model applied to two test specimens without seismic detailing, i.e. walls WSH4 (Dazio et al. 2009) and VK1 (Bimschas, 2010). To observe the effects of buckling, two response predictions were generated for each wall, with and without bar buckling taken into account. Given that the failure in the concrete and the buckling in the longitudinal reinforcement occurs simultaneously, it can be seen that the effect of buckling has a relatively low impact on the response predictions. In the test of wall VK1, the failure occurred due to crushing of the compression zone near the base section which further triggered the formation of wide diagonal cracks. Wall WSH4 failed in a similar manner, by crushing of the unconfined concrete in the compression zone near the base section. In both cases, the failure modes and the complete global response of the walls are captured well by the model. The main properties of specimens WSH4 and VK1 are shown in Table 4-2.

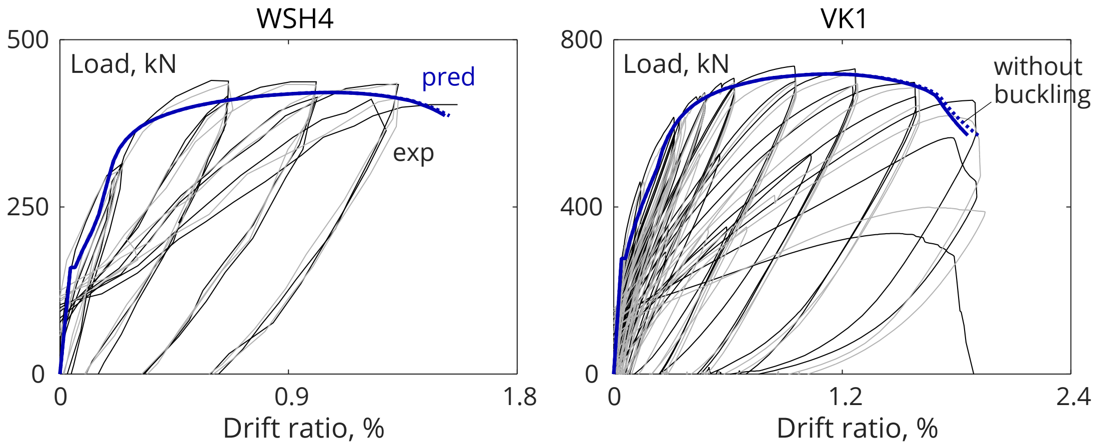

Figure 4-9. Comparison of experimental and predicted response of walls WSH4 (Dazio et al., 2009) and VK1 (Bimschas, 2000) failed due to concrete crushing

4.1.3.3.2 Walls with seismic detailing

In seismic design, the concrete in the boundary zones of walls is confined by transverse reinforcement that is properly detailed and provided with sufficiently tight spacing. The stress-strain response of the confined concrete in the SDOF approach is modeled according to the model by Mander et al. (1988), see the curve labeled "confined" in Figure 4-7. The confinement is taken into account considering the lateral confining pressure perpendicular to the plane of the wall. The confined concrete strength f'_{cc} and the corresponding strain ε_{cc} is calculated from the following expression:

$$f'_{cc} = f'_c\left(-1.254 + 2.254\left(1 + \frac{7.94 f_{ltp}}{f'_c}\right)^{0.5} - \frac{2 f_{ltp}}{f'_c}\right) \quad (4\text{-}18)$$

$$\varepsilon_{cc} = \varepsilon_{c0}\left(1 + 5\left(\frac{f'_{cc}}{f'_c} - 1\right)\right) \quad (4\text{-}19)$$

where,

f_{ltp}	Effective lateral pressure perpendicular to wall (Mander et al.,1988)
f'_c	Concrete cylinder strength
ε_{c0}	Concrete strain at peak strength, see Eq. (4-17)

Due to the effect of the biaxial stress state discussed in the previous section, it is considered that the minimum increase in the peak strength and strain corresponds to the enhancement factor of 1.25. Therefore, if the provided volumetric ratio of the confining reinforcement does not provide an increase in the confined concrete strength of at least 25%, the concrete is assumed to have the modified stress-strain relationship defined in §4.1.3.3.1.

As shown in Figure 4-7, the stress-strain curve of confined concrete has a sudden drop of resistance at a strain of ε_{cu}. This strain corresponds to the fracture of the transverse reinforcement that confines the concrete core, and can be estimated as follows (Priestley et al, 2007):

$$\varepsilon_{cu} = 0.004 + 1.4\rho_s f_{yv}\varepsilon_{uv}/f'_{cc} \quad (4\text{-}20)$$

where,

ρ_s Volumetric ratio of transverse reinforcement

f_{yv} Yield strength of confining reinforcement

ε_{uv} Breaking strain of confining reinforcement

f'_{cc} Confined concrete strength

It is noted by Priestley et al. (2007) that Eq. (4-20) is approximate and it tends to overestimate the effective ultimate strain under combined actions of moment and axial compression by a factor of about 1.3 to 1.6.

In the case of walls with confining reinforcement, the buckling of the longitudinal rebars is considered to be a significant limit state that can trigger the failure in the wall. As discussed, buckling is a complex mechanism that can be related to the loading history or the lateral instability of the compression zone. Given that the approach for buckling described in §4.1.3.3.1 does not consider the effects of cycling, it is not suitable for capturing the buckling in walls with seismic detailing. In part, the reason is that the failure strain of the confined concrete ε_{cu} is unconservative. Therefore, the failure criterion for buckling is simply modeled based on an empirical criterion from the literature. It is adopted in the analysis that the failure due to buckling is determined from the damage controlled curvature φ_{ls} proposed by Priestley et al. (2007):

$$\varphi_{ls} = \varphi_s + \frac{16d_b - s}{16d_b - s_{b,max}}(12\varphi_y - \varphi_s) \tag{4-21}$$

$$s_{b,max} = (3 + 6(f_u/f_y - 1))d_b \tag{4-22}$$

$$\varphi_s = 0.0175h \tag{4-23}$$

where,

φ_s Serviceability limit state curvature for cantilever walls (Priestley et al., 2007)

s Stirrup spacing

d_b Longitudinal rebar diameter

φ_y Yield curvature

$s_{b,max}$ Minimum stirrup spacing

Figure 4-10 shows the predictions of the mechanical model applied to two test specimens with seismic detailing, i.e. wall WSH5 by Dazio et al. (2009) and RW1 by Thomsen & Wallace (1995) (for wall properties refer to Table 4-3). Wall WSH5 had boundary zones reinforced with hoops and cross ties resulting in a volumetric reinforcement ratio of 1.1%. Even though wall WSH5 failed due to rupture of the rebars on the tension side of the section, the failure was accompanied by crushing of the concrete and buckling of the rebars on the compression side. In the prediction, the ultimate strain in confined concrete was reached for wall WSH5. The model predicts a buckling limit state to cause the failure of wall RW1. This prediction is consistent with the observed failure mode: the occurrence of buckling in the experiment in the last load cycle was reported to have caused a drop in the lateral resistance (Thomsen & Wallace, 1995).

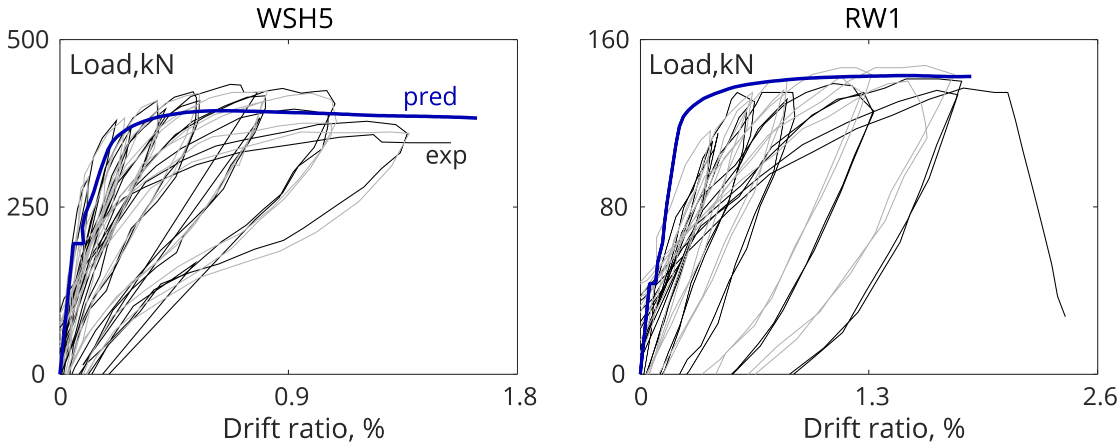

Figure 4-10. Comparison of experiment and response predictions of specimens WSH5 (Dazio et al., 2009) and RW1 (Thomsen & Wallace, 1995) with confined boundaries

4.1.3.4 Pullout of reinforcement

Thus far, the SDOF mechanical model assumes a fixed condition along the base section of the walls that ignores the anchorage deformations (strain penetration). The strains along the rebar anchored in a concrete foundation drop to zero over a certain development length. The pullout displacement of the bar can be estimated by integrating the strain profile below the base section. The strain penetration deformations are considered by using the bond model proposed by Sigrist (1995). The calculation of the pullout displacement Δ_{po} of a rebar anchored in a concrete foundation using this model is presented in section §4.2.4. The pullout displacement in the SDOF model is calculated at the location of the reinforcing tie and it causes a top displacement calculated as follows:

$$\Delta_{top,po} = \frac{\Delta_{po}}{d - x_{na}} a \tag{4-24}$$

where the effective depth d defines the position of the tie relative to the compressive edge, x_{na} neutral axis depth, and a shear span. The contribution of the pullout displacement is accounted for in the global response by adding it to the top displacement from the analytical model at each step of the envelope.

It is noted that the examples shown above do not include pullout deformations at the level of the base. The maximum contribution of the pullout deformations to the top horizontal displacement predicted by the approach for these walls is between 5% and 9%.

4.1.4 Model validation

4.1.4.1 CW test series

This section is intended to validate the proposed analytical model using the experimental data acquired from the CW test series (Chapter 3). The comprehensive experimental measurements are utilized to perform a detailed comparison between the observed behavior and the predictions of the proposed modeling approach.

The global response predictions of walls CW0, CW1, and CW2 are compared to the envelopes of the measured force-displacement relationships in Figure 4-11. In modeling of the response of the concrete in compression, the parameters of the concrete model by Popovics (1973) were slightly modified to best fit the response measured from the compression tests on concrete cylinders. For wall CW0, the best fit was obtained using a modulus of concrete (E_c) of 18500 MPa, and parameters $n = 2.15$ and $k = 1.1$. For walls CW1 and CW2, the adopted values of E_c, n, and k were 25000 MPa, 2.75, and 1.2, respectively. The main analysis results in terms of the predicted resistance and ultimate displacement capacity of all the walls are summarized and compared to the experiments in Table 4-1. Figure 4-11 shows that there is a good agreement between the predicted and the measured global response of all three specimens. In terms of the failure modes, the analysis predicted that all three walls failed due to the loss of the resistance in the concrete compression zone. This coincides with the failure mode observed in tests on walls CW1 and CW2. Even though wall CW0 failed by rupturing of the tensile reinforcement, its response is well predicted. Spalling of concrete in the compression zones was observed at both sides of the section near the end of the test. From the results, it is evident that the proposed kinematic approach adequately captures the effects of axial load on the global behavior consistent with the test observations on CW walls.

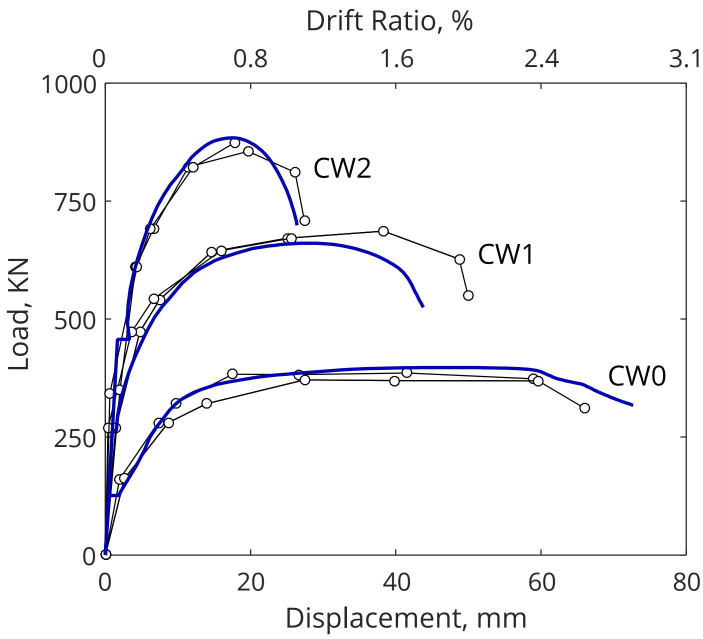

Figure 4-11. Global response predictions of walls CW0, CW1, CW2

Table 4-1. Measured and predicted response CW walls

Wall ID	V_{max} kN	V_{pred} kN	$\Delta_{u,exp}$ mm	$\delta_{u,exp}$ %	$\Delta_{u,pred}$ mm	$\delta_{u,pred}$ %	V_{exp}/V_{pred}	$\delta_{u,exp}/\delta_{u,pred}$
CW0	386	397	66.3	2.60	72.7	2.85	0.97	0.91
CW1	686	661	50	1.96	43.8	1.72	1.04	1.14
CW2	884	884	27.4	1.07	26.4	1.04	1.00	1.04

The principal assumptions of the proposed approach that define the global response of walls are the relationships between the top displacement and rotational DOF, as well as the shape of the strain profile in the reinforcement tie. In Figure 4-12, these assumptions are tested by comparing the equivalent measured quantities with the model predictions at each step of the envelope of the response of all three test specimens.

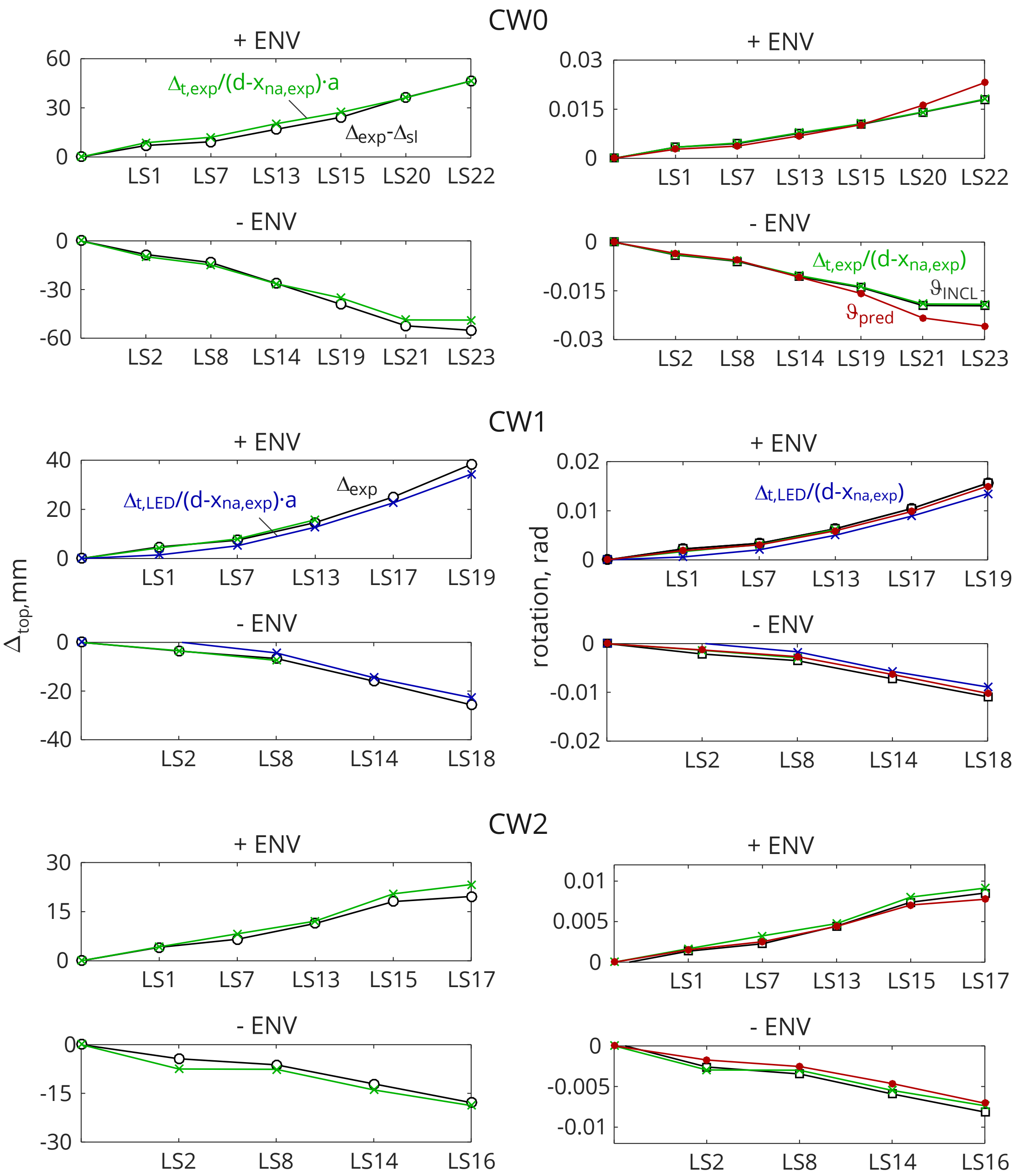

Figure 4-12. Validation of principal model assumptions

The left-hand side of Figure 4-12 compares the top horizontal displacement of the walls obtained in two different ways: the direct measurements performed in the test, and the result from Eqn. (4-4) of the mechanical model used with measured $\Delta_{t,exp}$ and x_{na}. Displacement $\Delta_{t,exp}$ is the total elongation of the vertical tie expressed with the integral in Eqn. (4-4), and it was obtained from the measured vertical displacement of the top block using the displacement transducers vdispL and vdispR. The neutral axis depth $x_{na,exp}$ was estimated from the optical measurements as described in §4.1.1. For wall CW0, the comparisons are made with the displacement envelope corrected by subtracting the sliding displacement of the base section since this deformation mode is not explicitly taken into account in the mechanical model. In the case of wall CW1, one of the sensors measuring the vertical displacements of the top block in the specimens failed during the experiment, and thus $\Delta_{t,exp}$ was alternatively estimated from the data acquired using LED scanners ($\Delta_{t,LED}$). The right-hand side of Figure 4-12 compares the rotation measured using the inclinometer on top of the block ($\vartheta_{\mathrm{INCL}}$), the rotation obtained from the mechanical model using measured $\Delta_{t,exp}$ and $x_{na,exp}$ (i.e. $\Delta_{t,exp}/(d\text{-}x_{na,exp})$), and the rotation predicted by the SDOF approach ($\vartheta_{\mathrm{pred}}$). The comparisons in Figure 4-12 successfully validate the main assumptions of the mechanical model and show a good agreement between the measured and predicted values. The mechanical model overestimated the rotation of the top block at the last few loading stages of wall CW0 without an axial load. This is not evident in the prediction of the global force-displacement response in Figure 4-11 because the overestimated rotation compensates for the sliding deformations observed in the test.

As the SDOF mechanical model predicts entire deformed shapes of the walls, these predictions are compared in Figure 4-13 against the displacement measurements from the LED and DIC systems used in the CW tests. The comparison in the figure corresponds to the displacement at the maximum measured resistance of the walls. Since the model does not take into accounts the sliding deformations, the envelope of wall CW0 was corrected by subtracting the sliding mode. The displacements of the points on the rigid block were obtained using the predicted rotational DOF and Eqs. (4-1) and (4-2). The displacements of the points in the cracked region of the walls, i.e. below the top inclined crack, were obtained from the rotation of the radial struts calculated by integrating the vertical strain profile in the reinforcement tie below the respective strut. The cracked region in Figure 4-13 is distinguished by the dashed lines connecting the cracked height along the tie to the estimated neutral axis depth. The contribution of the rotation due to the pullout displacement from the foundation was also considered in calculating the displacements of the targets on the rigid block and the fan. The biggest discrepancy between the predicted and measured displacement patterns is observed in the lower portions of the cracked region of walls CW0 and CW1, and it is a consequence of the underestimated pullout deformations localized at the base crack. A globally good agreement is also observed in the comparisons of predicted and measured deformation patterns at each step of the response envelopes of the three walls presented in Appendix B.

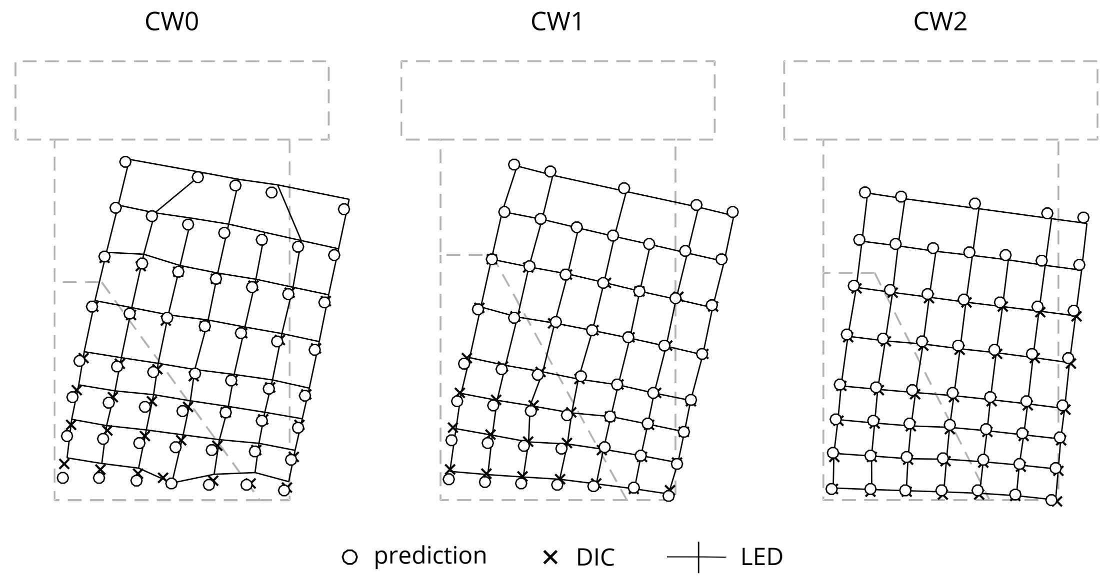

Figure 4-13. Comparison of complete displacement field measured with LED and DIC system against predicted displacement fields for walls CW0, CW1, and CW2 at V_{max}

In the validation of the SDOF approach, the response at the local level of behavior is further considered by comparing the predicted and measured vertical strain profiles, stirrup strains, and crack widths. Figure 4-14 compares the strains predicted along the reinforcement tie to the strains measured along the tensile edge of the walls using chains of displacement transducers (DT) and the LED scanner. The comparisons are performed at the drift corresponding to the maximum resistance observed in the tests. The average horizontal strains along the web of the walls were predicted along the envelope of the response at the location of the sensor ddef_3, and are compared to the measured values in Figure 4-15. Additionally, the proposed approach is validated by using the measured crack widths as shown in Figure 4-16. For the purpose of comparison, the discrete crack spacing in the model was assumed to correspond to crack distances measured in the tests. The crack widths were estimated by integrating the tributary area of the predicted strain profile belonging to the respective crack. As the cracks predicted along the reinforcement tie are compared to the cracks measured at the tensile face of the wall, the predicted crack profile was multiplied by the ratio h/d=1.3.

The SDOF approach predictions of the local deformations capture the experimentally observed trends with good accuracy. The predictions of the local deformations are essential in predicting the structural limit states that are related to the extent of damage in the structural components under seismic actions. This demonstrates the suitability of such simplified procedures towards the application in performance-based design and assessment procedures.

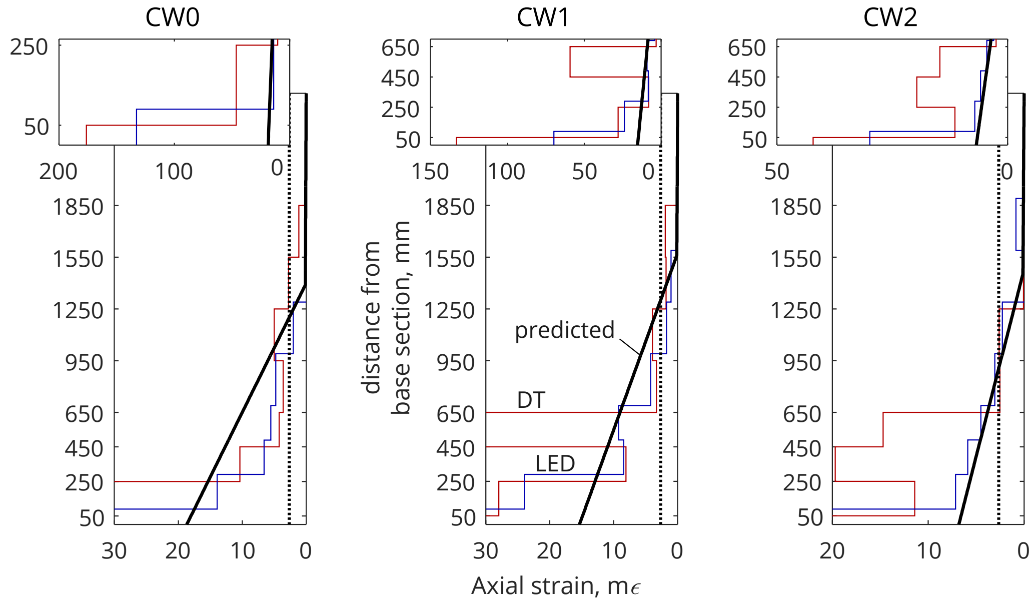

Figure 4-14. Comparison of measured and predicted axial strains at V_{max} of CW test walls

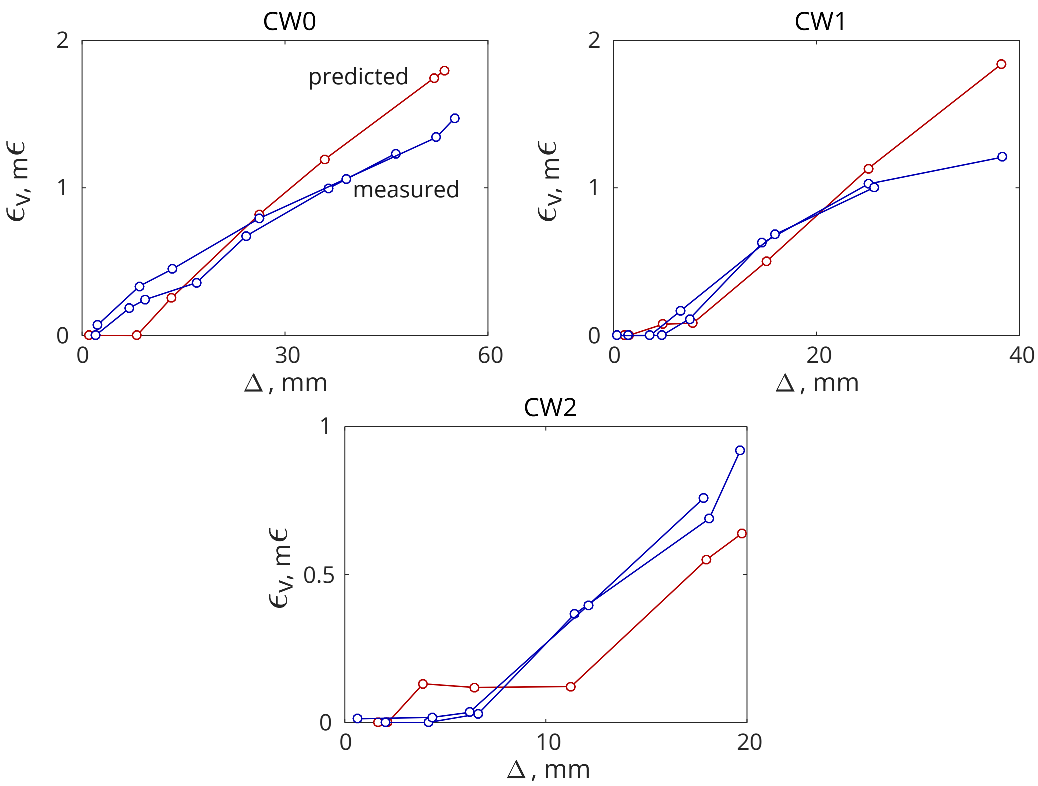

Figure 4-15. Comparison of measured and predicted average horizontal web strains along the envelopes of the response of CW wall specimens

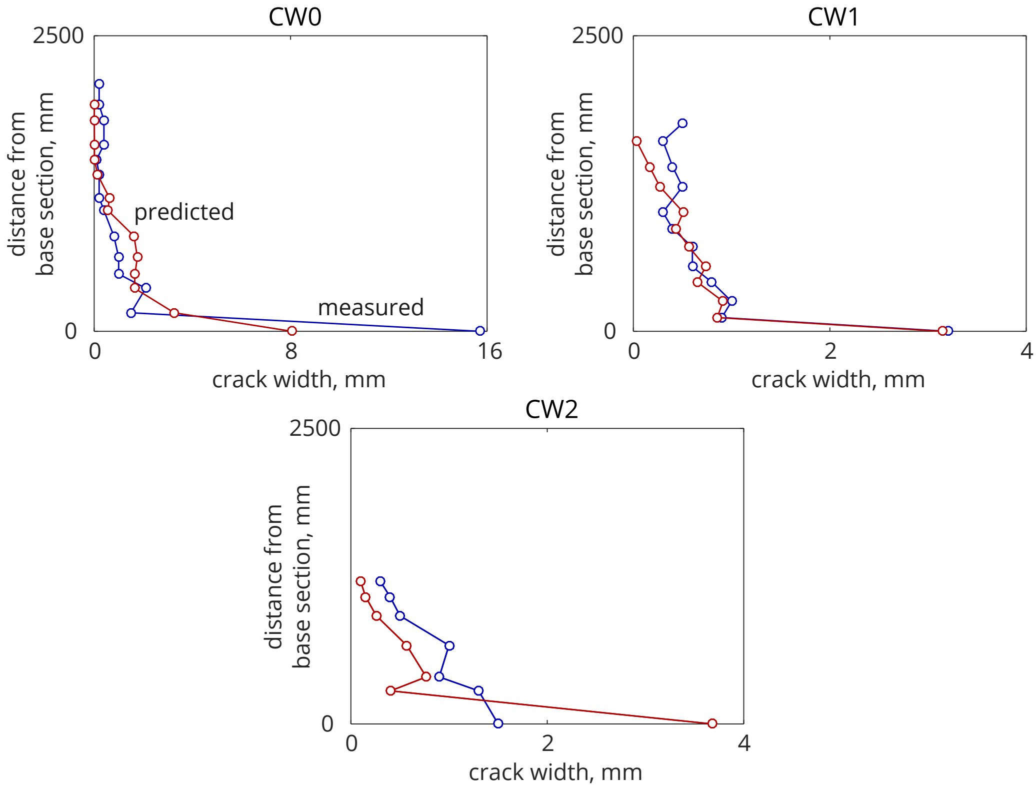

Figure 4-16. Comparison of measured and predicted crack widths at the loading stages prior to the failure of CW walls

4.1.4.2 Validation with database of tests from the literature

A part of the methodology adopted for this study is to perform an extensive evaluation of the proposed approach with test walls with a range of different properties. Apart from the detailed validation of the proposed model on the CW test series discussed in the previous section, the validation is extended to the test series available in the literature. The properties of all the test specimens considered in the validation of the SDOF mechanical model are summarized in Table 4-2 and Table 4-3. The complete set of tests used for validation consists of 42 walls.

Since there is a large number of experimental studies available in the literature, a set of criteria were imposed in order to narrow down the available information. Considering the aspect of practical application, the specimens considered had a depth of the section h larger or equal to 1 m. In terms of geometry and reinforcement detailing, the wall test database is limited to rectangular walls without lap splices and diagonal reinforcement.

The test database is also bounded by a range of parameters where the main assumptions of the model are applicable. For example, very short (squat) walls with aspect ratios less than about 1.0 exhibit the significant effects of shear in the behavior. Therefore, the aspect ratios of walls considered in the validation database range from 0.9 up to a maximum of 3.1. Since the proposed approach is suited for flexure-dominated walls, another limitation is considered in terms of failure modes. The proposed procedure does not consider the pure shear failures that occurred before the yielding of the longitudinal reinforcement. The test walls that have failed in shear and were not included in the database are walls 72 and 73 (Hirosawa, 1985).

The expected behavior of the walls with seismic detailing, i.e. with confining reinforcement in the boundary elements, can be distinguished from the walls with simple detailing. The walls with simple detailing generally fail in a brittle manner while the walls with seismic detailing are expected to exhibit a more ductile behavior. Therefore, the validation is shown on a subset of walls with non-seismic (Table 4-2) and seismic detailing (Table 4-3).

Several specimens that had confining reinforcement with a relatively large spacing were considered within the subset of walls with non-seismic detailing. This is considered in case the confining model estimates less than 5% increase in the concrete compression strength for the given configuration of confining hoops and stirrups. This kind of confinement can be neglected since it does not effectively enhance the concrete properties to improve the response of the wall. The behavior of the concrete in compression in such walls is modeled with the modified concrete stress-strain relationship proposed in §4.1.3.3.1. On this basis, the confinement was neglected in the response predictions of two wall specimens, SW1-6 (Zhao et al., 2002) and wall WR-20 (Oh et al., 2002).

Table 4-2. Properties of walls non-seismic detailing

Wall ID	h mm	b mm	a mm	a/h	ρ_l %	ρ_v %	f_{yl} MPa	f_{ul} MPa	f_{yv} MPa	f'_c MPa	N/bhf'_c %
CW0[a]	1500	230	2550	1.7	0.79	0.15	530	640	540	25.1	0.0
CW1[a]	1500	230	2550	1.7	0.72	0.15	530	640	540	38.1	10
CW2[a]	1500	230	2550	1.7	0.72	0.15	530	640	540	36.6	21
VK1[b]	1500	350	3300	2.2	0.82	0.08	515	630	518	35	7.5
VK3[b]	1500	350	3300	2.2	1.23	0.08	515	630	518	34	7.7
VK6[c]	1500	350	4300	2.9	1.23	0.08	521	609	528	44.4	5.9
VK7[c]	1500	350	3300	2.2	1.23	0.22	521	609	528	30	8.7
S4[d]	1180	100	1320	1.1	1.02	1.01	574	764	574	32.9	6.7
S9[d]	1180	100	1320	1.1	1.02	0.00	560	762	-	29.2	7.5
S10[d]	1180	100	1320	1.1	2.00	1.01	496	716	496	31	7.2
SW1[e]	3050	203	2867	0.9	0.67	0.67	462	703	462	24.8	0
WSH4[f]	2000	150	4600	2.3	0.82	0.25	576	675	519	40.9	5.7
R1[g]	1905	102	4572	2.4	0.49	0.27	512	765	522	44.8	0
WR0[h]	1500	200	3000	2.0	0.74	0.31	449	617	342	27.6	10
WR20[h]	1500	200	3000	2.0	0.74	0.31	449	617	342	27.6	10
SW6-1[i]	1000	125	2200	2.2	0.60	0.36	352	505	299	30.8	30

[a]Chapter 3
[b]Bimschas (2010)
[c]Hannewald et al. (2013)
[d]Maier and Thürlimann (1985)
[e]Luna et al. (2015)
[f]Dazio et al. (2009)
[g]Oesterle et al. (1976)
[h]Oh et al. (2002)
[i]Zhang et al. (2010)

Table 4-3. Properties of walls with seismic detailing

Wall ID	h mm	b mm	a mm	a/h	ρ_{lb} %	f_{ylb} MPa	f_{ulb} MPa	ρ_s %	f_{yvb} MPa	f_{uvb} MPa	ρ_{lw} %	f_{yl} MPa	f_{ul} MPa	ρ_{vw} %	f_{yv} MPa	f'_c MPa	N/bhf'_c %
TW1[a]	1220	152	2440	2.0	3.7	475	635	2.5	440	490	0.18	515	635	0.27	515	47	2.0
TW2[a]	1220	152	2440	2.0	8.3	475	635	2.4	440	490	0.38	515	635	0.62	440	49	7.3
TW3[a]	1220	152	1830	1.5	3.7	475	635	2.5	440	490	0.21	515	635	0.33	515	49	7.7
TW4[a]	1220	152	1830	1.5	7.0	475	635	2.4	440	490	0.46	515	635	0.74	440	56	6.4
TW5[a]	1220	152	1830	1.5	7.0	475	635	2.4	440	490	0.38	515	635	0.62	440	58	1.6
WSH1[b]	2000	150	4600	2.3	1.8	547	620	1.2	584	601	0.27	584	601	0.25	584	45	5.1
WSH2[b]	2000	150	4600	2.3	1.8	583	747	1.2	485	535	0.27	485	535	0.25	485	40.5	5.7
WSH3[b]	2000	150	4600	2.3	2.0	601	725	1.1	489	552	0.48	569	700	0.25	489	39.2	5.8
WSH5[b]	2000	150	4600	2.3	0.9	584	714	1.1	562	615	0.24	519	559	0.25	519	38.3	12.8
WSH6[b]	2000	150	4600	2.3	1.7	576	675	1.5	519	559	0.57	584	714	0.25	519	45.6	10.8
76[c]	1700	160	1700	1.0	5.6	384	422	2.6	423	465	0.53	415	457	1.20	423	15	13.3
77[c]	1700	160	1700	1.0	5.6	384	422	2.6	423	465	0.53	415	457	1.20	423	18.7	10.7
80[c]	1700	160	1700	1.0	2.6	389	428	2.6	423	465	0.53	415	457	1.20	423	15	13.3
81[c]	1700	160	1700	1.0	2.6	389	428	2.6	423	465	0.53	415	457	1.20	423	18.7	10.7
R2[d]	1905	102	4572	2.4	3.0	450	708	4.3	535	691	0.27	535	691	0.31	535	46.4	0.0
WR10[e]	1500	200	3000	2.0	1.3	449	617	2.4	342	445	0.43	342	445	0.31	342	36.2	10.0
WR20[e]	1500	200	3000	2.0	1.3	449	617	1.2	342	445	0.43	342	445	0.31	342	34.2	10.0
MSW1[f]	1200	100	1800	1.5	1.7	585	673	1.5	610	702	0.57	610	702	0.57	610	24.5	0.0

Table 4-3. Properties of walls with seismic detailing (continued)

Wall ID	h mm	b mm	a mm	a/h	ρ_{lb} %	f_{ylb} MPa	f_{ulb} MPa	ρ_s %	f_{yvb} MPa	f_{uvb} MPa	ρ_{lw} %	f_{yl} MPa	f_{ul} MPa	ρ_{vw} %	f_{yv} MPa	f'_c MPa	N/bhf'_c %
MSW2[f]	1200	100	1800	1.5	1.3	585	673	1.3	610	702	0.27	610	702	0.28	610	24.5	0.0
MSW3[f]	1200	100	1800	1.5	1.3	585	673	1.3	610	702	0.27	610	702	0.28	610	24.5	7.0
LSW1[f]	1200	100	1200	1.0	1.7	585	673	2.4	610	702	0.57	610	702	0.57	610	24.5	0.0
LSW2[f]	1200	100	1200	1.0	1.3	585	673	2.1	610	702	0.27	610	702	0.28	610	24.5	0.0
LSW3[f]	1200	100	1200	1.0	1.3	585	673	2.1	610	702	0.27	610	702	0.28	610	24.5	7.0
RW1[g]	1219	102	3810	3.1	3.3	434	641	1.2	434	483	0.28	448	586	0.33	448	31.6	10.2
RW2[g]	1219	102	3810	3.1	3.3	434	641	1.7	434	483	0.28	448	586	0.33	448	34.5	8.8
SW6_3[h]	1000	125	2200	2.2	1.9	352	505	1.4	299	411	0.38	299	411	0.36	299	26.46	30.0
A2C[i]	1300	200	2700	2.1	2.4	425	603	3.5	450	670	0.55	448	675	0.59	452	671	0

[a]Tran and Wallace (2012)
[b]Dazio et al. (2009)
[c]Hirosawa (1975)
[d]Oesterle et al. (1976)
[e]Oh et al. (2002)
[f]Salonikios (1999)
[g]Thomsen (1995)
[h]Oh et al. (2002)
[i]Zhang et al. (2010)

4.1.4.2.1 Walls with non-seismic detailing

The 16 walls with non-seismic reinforcement detailing consisted of walls with uniformly distributed reinforcement and with concentrated reinforcement at the wall boundaries. The aspect ratio a/h of the walls ranges between 0.9 and 2.9, the reinforcement ratios varied between 0.49% and 2 % for the longitudinal rebars ρ_l, and between 0 and 1 % for the stirrups ρ_v. The walls were subjected to axial compression loads with normalized values N/bhf'_c varying from 0% up to 30%. The characteristics of all the walls with non-seismic detailing are summarized in Table 4-2.

Figure 4-17 compares the experimental and predicted load-displacement response envelopes of all test walls with non-seismic reinforcement detailing. The main results of the validation of the SDOF kinematic approach on the subset of unconfined walls, in terms of ratios of the predicted and measured values of the maximum resistance and drift capacity, are summarized in Table 4-4. The model predicts the failure in walls due to the crushing of the concrete in compression or rupture of the reinforcement in tension. The failure drift from the experiment is adopted to correspond to a drop of the lateral capacity of 20% and is compared to the equivalent value predicted by the model. In cases where the tests were stopped before the load dropped by 20%, the predicted and measured drift capacities correspond to the maximum drop of load reported in the test. It can be seen that the global response of the walls with non-seismic detailing is predicted with good accuracy, featuring an average of experimental-to-predicted ratio for the resistance of 1.03 and a coefficient of variation (COV) of 5.6%, while the ratios for the drift capacity have an average of 1.01 and a COV of 18.6%.

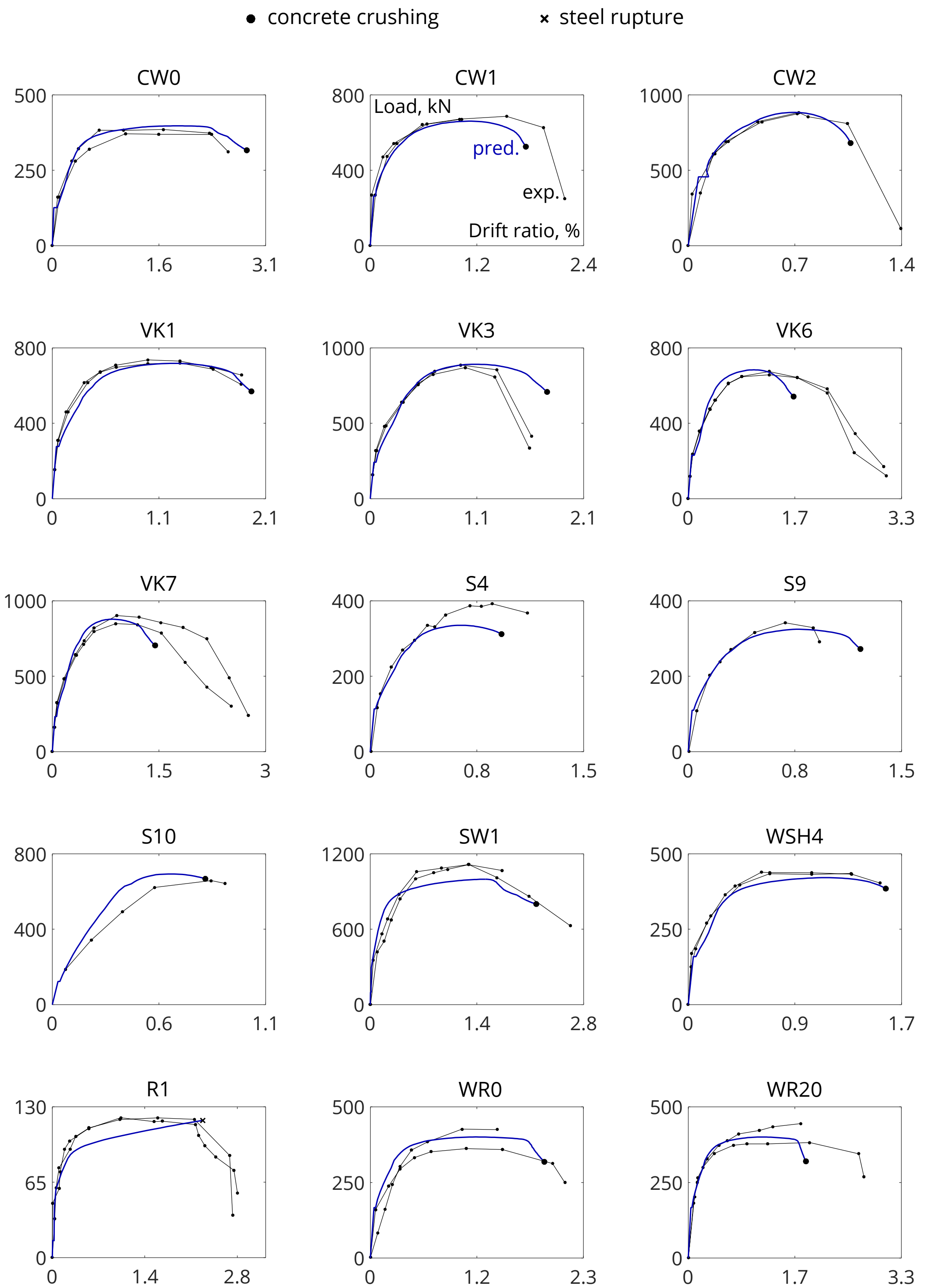

Figure 4-17. Experimental and predicted response envelopes of walls with non-seismic detailing

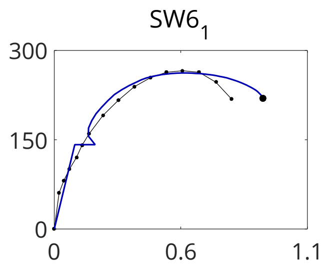

Figure 4-17. Experimental and predicted response envelopes of walls with non-seismic detailing (continued)

Table 4-4. Predicted and measured force and displacement capacity of walls with non-seismic reinforcement detailing

		Experiment			Prediction			Comparison	
Wall ID	a/h	V_{exp} kN	Δ_{exp} mm	δ_{exp} %	V_{pred} kN	Δ_{pred} mm	δ_{pred} %	V_{exp}/V_{pred}	$\Delta_{exp}/\Delta_{pred}$
CW0	1.7	386	66.3	2.60	397	72.7	2.85	0.97	0.91
CW1	1.7	686	50.0	1.96	661	43.8	1.72	1.04	1.14
CW2	1.7	884	27.4	1.07	884	26.4	1.04	1.00	1.04
VK1	2.2	737	62.7	1.90	718	64.5	1.97	1.03	0.97
VK3	2.2	887	44.5	1.35	892	57.4	1.76	0.99	0.78
VK6	2.9	675	96.3	2.24	684	73.1	1.71	0.99	1.32
VK7	2.2	903	54.8	2.25	878	47.0	1.47	1.03	1.17
S4	1.1	392	14.7	1.12	335	12.2	0.92	1.17	1.21
S9	1.1	342	10.6	0.80	325	16.1	1.22	1.05	0.66
S10	1.1	658	12.1	0.92	693	10.8	0.82	0.95	1.12
SW1	0.9	1114	57.1	1.99	998	62.7	2.19	1.12	0.91
WSH4	2.3	439	72.0	1.57	419	74.9	1.60	1.04	0.96
R1	2.4	121	107.3	2.35	122	112.6	2.46	0.99	0.95
WR0	2.0	427	49.7	1.66	401	57.1	1.90	1.06	0.87
WR20	2.0	443	73.2	2.44	401	55.2	1.84	1.11	1.33
SW6-1	2.2	266	17.8	0.81	262	20.6	0.94	1.01	0.86
							Avg.	1.03	1.01
							CoV, %	5.61	18.64

4.1.4.2.2 Walls with seismic detailing

The database of walls with seismic detailing consists of 27 wall specimens with the main properties as listed in Table 4-3. The aspect ratios a/h of these walls vary from 1 to 3.1, the longitudinal web reinforcement ratios ρ_l are between 0.18% and 0.57%, and the stirrup ratios ρ_v are between 0.27% and 1.2%. In the boundary zones, the walls had the longitudinal reinforcement ratios ρ_{lb} between 0.9% and 8.3%, and the volumetric ratios of the confining hoops and stirrups ρ_s up to 4.3%. The walls featured axial compression load ratios (N/bhf'_c) from 0% to 30%.

Figure 4-18 compares the experimental and predicted global response envelopes of all test walls with seismic reinforcement detailing. The main results of the validation of the SDOF kinematic approach on this subset of walls, in terms of ratios of the measured and predicted values of maximum resistance and drift capacity, are summarized in Table 4-5. As before, the drift capacity is defined by the displacement corresponding to a 20% drop in the lateral resistance. If the post-peak of the measured displacement envelope was not available, the comparisons were made at a percentage of the load drop corresponding to the maximum measured drift ratio. It can be seen that the force capacity of the test walls is accurately predicted with an average experimental-to-prediction ratio of 0.99 and CoV of about 9.8%. A lesser accuracy and higher variability were achieved in the drift capacity predictions, featuring an average experimental-to-prediction ratio of 1.04 and CoV of about 28.1%.

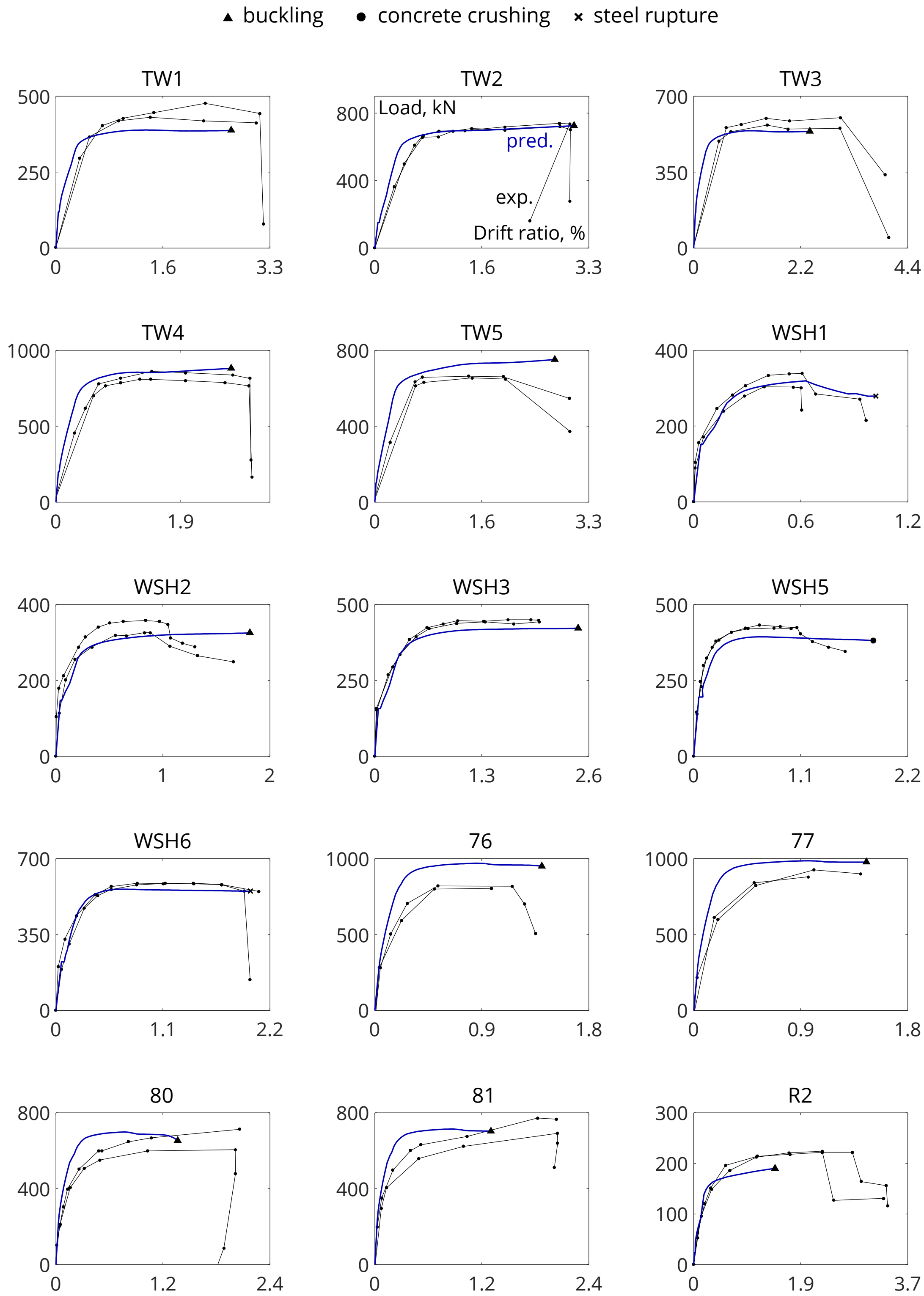

Figure 4-18. Experimental and predicted response envelopes of walls with seismic detailing

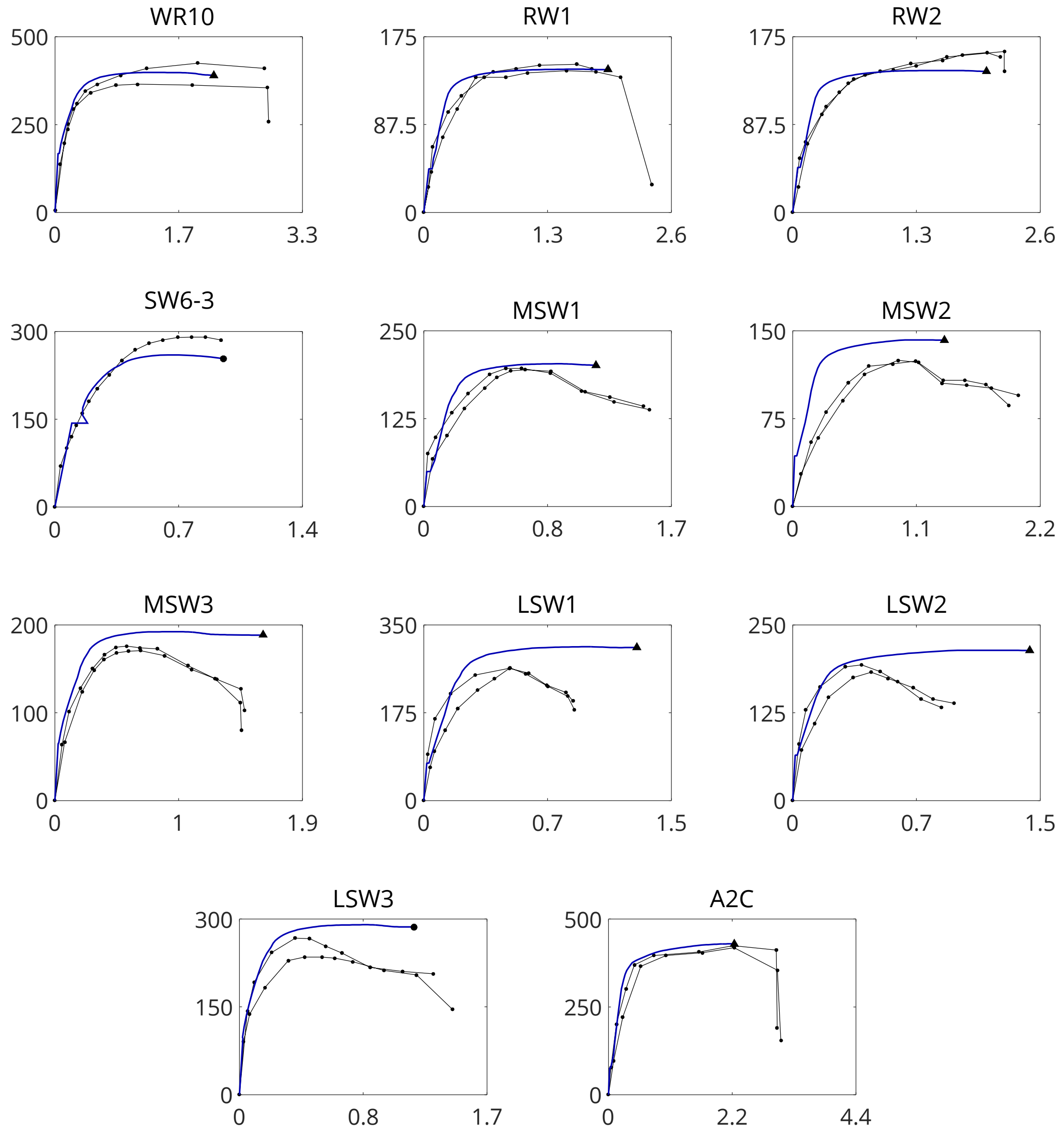

Figure 4-18. Experimental and predicted response envelopes of walls with seismic detailing (continued)

Table 4-5. Predicted and measured force and displacement capacity of walls with seismic detailing

		Experiment			Prediction			Comparison	
Wall ID	a/h	V_{exp} kN	Δ_{exp} mm	δ_{exp} %	V_{pred} kN	Δ_{pred} mm	δ_{pred} %	V_{exp}/V_{pred}	$\Delta_{exp}/\Delta_{pred}$
TW1	2.0	477	76.6	3.14	404	67.7	2.77	1.18	1.13
TW2	2.0	740	73	2.99	766	77.4	3.17	0.97	0.94
TW3	1.5	601	60.4	3.30	559	44.8	2.45	1.07	1.35
TW4	1.5	862	54.4	2.97	935	50.6	2.76	0.92	1.08
TW5	1.5	664	44.3	2.42	822	52.2	2.85	0.81	0.85
WSH1	2.3	339	42.7	0.93	319	46.8	1.02	1.06	0.91
WSH2	2.3	358	58.5	1.27	325	81.5	1.77	1.10	0.72
WSH3	2.3	450	92.1	2.00	426	113.9	2.48	1.06	0.81
WSH5	2.3	433	70.8	1.54	394	79.8	1.74	1.10	0.89
WSH6	2.3	587	94.7	2.06	559	90.8	1.97	1.05	1.04
76	1.0	820	21.3	1.25	970	23.5	1.38	0.85	0.90
77	1.0	926	23.4	1.38	986	24.7	1.46	0.94	0.95
80	1.0	713	33.5	1.97	699	22.9	1.35	1.02	1.46
81	1.0	772	34.1	2.01	714	22.0	1.29	1.08	1.55
R2	2.4	222	137	3.00	230	77.0	1.68	0.96	1.78
WR10	2.0	425	86	2.87	399	64.1	2.14	1.07	1.34
MSW1	1.5	197	20.9	1.16	203	21.2	1.18	0.97	0.99
MSW2	1.5	125	33.0	1.83	142	24.9	1.39	0.88	1.32
MSW3	1.5	176	22.1	1.23	192	29.8	1.65	0.91	0.74
LSW1	1.0	265	9.9	0.83	309	15.3	1.27	0.86	0.65
LSW2	1.0	193	8.4	0.70	214	17.3	1.44	0.90	0.49
LSW3	1.0	268	11.3	0.94	290	14.1	1.17	0.92	0.80
RW1	3.1	141	82.2	2.16	145	76.7	2.01	0.98	1.07
RW2	3.1	160	85.5	2.24	141	80.2	2.10	1.13	1.07
SW6-3	2.2	290	20.1	0.91	260	20.4	0.93	1.12	0.98
A2C	2.1	425	81.5	3.02	456	61.0	2.26	0.93	1.34
							Avg.	0.99	1.04
							CoV, %	9.8	28.1

4.1.4.2.3 Discussion of results

Figure 4-19 shows the variation of the ratios of the measured and experimental force and drift capacities with respect to the main properties of the wall specimens considered in the database. These properties include the aspect ratio of the walls, the axial load ratio, the longitudinal reinforcement ratios, the transverse reinforcement ratios, and the volumetric ratio of confining reinforcement. The plots are used to verify whether the model exhibits bias with respect to the properties of the modeled wall specimens. In most of the cases, it can be seen that the response predictions in terms of resistance and drift capacity are uniformly scattered around the average across the entire horizontal axes of the plots. A slight bias is identified in the conservative predictions of the drift capacity of walls with volumetric steel ratios higher than about 3.

The basis for the development of the SDOF kinematic approach for short walls are the experimental observations from the CW test series, which are representative of walls with non-seismic detailing in existing structures. Considering that the failure mechanisms in such walls are modeled in more detail, the approach is better suited for the analysis of walls with non-seismic detailing as compared to the walls with seismic detailing. Comparisons of the predicted and measured envelopes of walls with simple detailing in §4.1.4.2.1 has shown that that the mechanical model evaluated very well the response of nearly all the walls considered.

The validation of the SDOF approach against the dataset of walls with simple detailing has shown that the predictions of behavior in terms of the force resistance and the initial stiffness are very well captured. Minor discrepancies in the initial stiffness can be attributed to the underestimated strain penetration deformations or the additional displacement in the experimental envelopes due to flexibility in the test setup. In terms of failure modes, the analysis predicts failures in walls due to rupture of the reinforcement in tension and crushing of the concrete in the compression zone. The latter failure mode was exhibited by the majority of the walls in the dataset, and this was adequately predicted by the model. In the case of wall CW0, the failure occurred due to rupture of the longitudinal reinforcement, while the SODF model predicted a loss of lateral resistance without rupture. Specimen S9, which had no stirrups, reached its full flexural capacity, but it failed due to the opening of shear cracks along the diagonal of the wall. Therefore, the analysis overpredicted the drift capacity in this case as this type of failure is not considered by the model. In addition, specimens VK1 and VK3 also failed by crushing in the compression zones, which triggered the opening of wide shear cracks. In these cases, the observed failure mode was flexural, but it can also be interpreted as a ductile shear failure due to the presence of wide shear cracks. Since this type of shear failure is triggered by the crushing of the concrete in compression, the behavior is captured by the approach with reasonable accuracy. The drift capacities of the walls with non-seismic reinforcement were also well captured, but with a higher scatter compared to the strength predictions. This is likely due to the two major approximations of the SDOF approach, i.e. the simplified modeling of the strain distribution along the reinforcement tie and the simplified considerations of the effects of shear cracking.

The formulation of the SDOF kinematic approach considers the effects of increased concrete strength and ductility in compression due to confining reinforcement in the boundary elements (§4.1.3.3.2). For walls with such reinforcement, the analysis can predict failures due to the crushing of concrete, buckling of rebars in compression, and rupture of rebars in tension.

The evaluation of the response predictions against experimental envelopes of walls with seismic detailing (§4.1.4.2.2) has shown very good agreement in terms of the predictions of the maximum force resistance of all the walls. The discrepancies in the initial stiffness that can be observed are likely due to the underestimated strain penetration in the foundation. Most of the walls in this dataset have failed due to crushing of the concrete and simultaneous buckling of the longitudinal rebars in compression. This failure mode is adequately captured by the analysis using the adopted curvature-based buckling failure criterion (§4.1.3.3.2). However, the drift capacity predictions exhibit higher scatter when compared to those of walls with simple detailing. It is noted that walls with seismic detailing are characterized by a ductile behavior which introduces more pronounced effects of cyclic loading in their response. Another reason for the higher scatter is that the failure due to rebar buckling in compression is considered in a simple manner with the empirical failure criterion in the SDOF approach. The modeling of such failures can be addressed by implementing failure criteria based on the physical models for rebar buckling instead. From Figure 4-19, it can be seen that the SDOF approach predicts slightly unconservative drift capacities in walls with small volumetric steel ratios and conservative drift capacities in walls with very large amounts of confining hoops and stirrups.

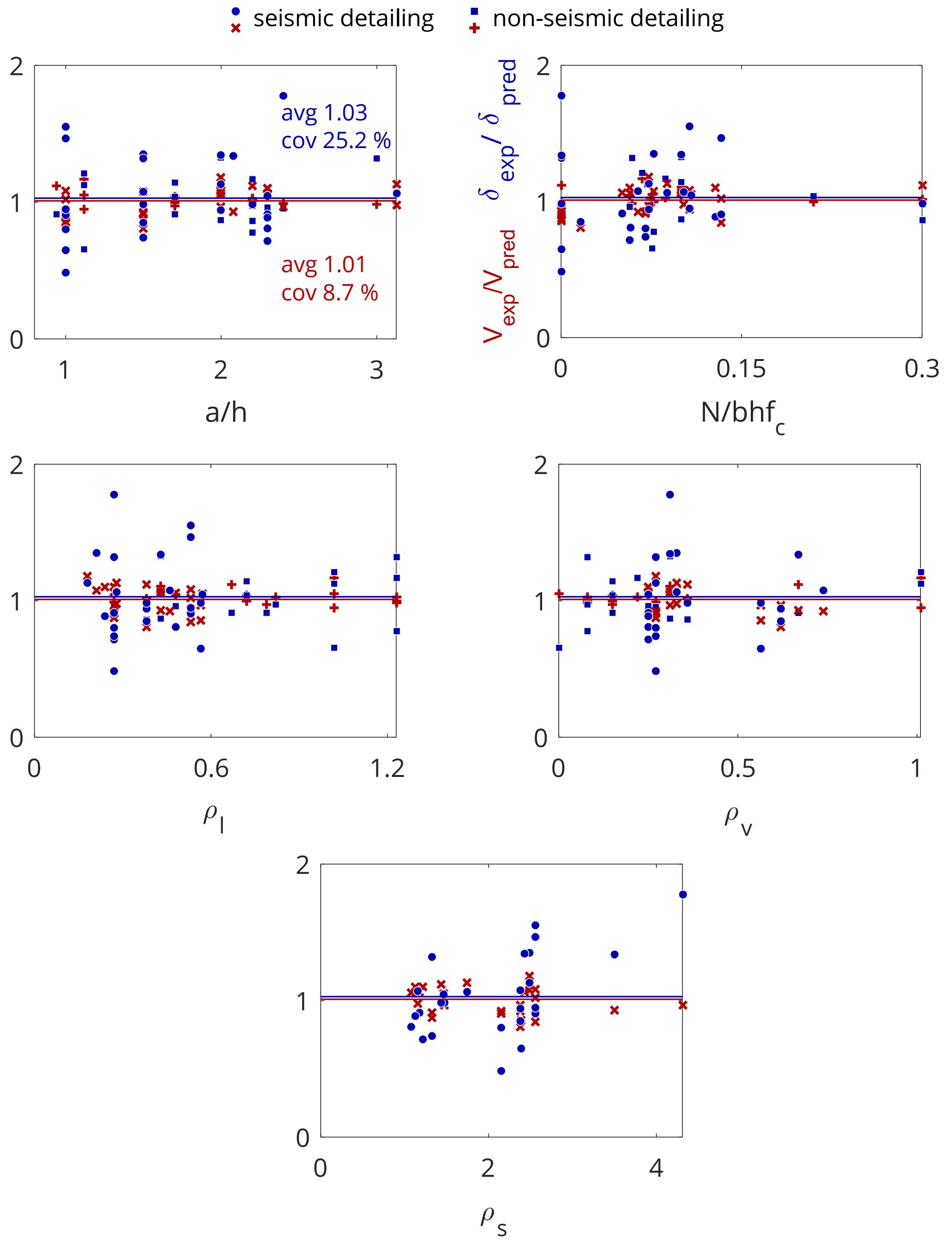

Figure 4-19. Sensitivity of maximum resistance and displacement capacity predictions with respect to main parameters of test specimens

4.2 Three-parameter kinematic theory (3PKT) for shear-dominated short walls

4.2.1 Summary of 3PKT formulation

4.2.1.1 Kinematics of shear-dominated walls

The three-parameter kinematic theory is built on a kinematic model that describes the deformation patterns (or displacement field) of fully-cracked rectangular cantilever walls. The model has been formulated based on measured deformed shapes of test specimens that failed in shear, under the combined action of lateral and vertical loads (Bimschas, 2010).

As shown in Figure 4-20, the kinematic model consists of three basic deformation patterns, each of which is a function of a single degree of freedom (DOF). These deformation patterns are marked by a straight critical shear crack inclined at angle α_1 with respect to the vertical axis. Angle a_1 is obtained from a shear-strength calculation according to the AASHTO (2007) provisions, but cannot be smaller than the angle of the diagonal of the wall α. The critical crack divides the kinematic model into two distinct regions: a rigid block above the crack and a fan of struts below the crack (Figure 4-20). The struts from the fan are pinned at the toe of the wall (point A) and are connected to a vertical tie on the flexural tension side of the section. This tie represents the vertical reinforcement A_s in the tension one-half of the section.

As shown in Figure 4-20, the first basic deformation pattern is associated with the average strain $\varepsilon_{t,avg}$ along the tension reinforcement (tie). Namely $\varepsilon_{t,avg}$ is the first degree of freedom of the kinematic model. As the tie elongates and $\varepsilon_{t,avg}$ increases, the fan of struts spreads and the rigid block rotates about the toe of the wall. The rotation of the block results in the widening of the critical crack. This deformation pattern can be associated with flexure.

The second deformation pattern is characterized by a lateral displacement Δ_c of the rigid block with respect to the fan (Figure 4-20b). This displacement occurs along the critical diagonal crack resulting in the widening of the crack as well as the slip on the crack. At the bottom of the wall DOF Δ_c results in concentrated compressive deformations in what will be referred to as the critical loading zone (CLZ). As evident from Figure 4-20b, the deformation pattern expressed with displacement Δ_c can be associated with shear.

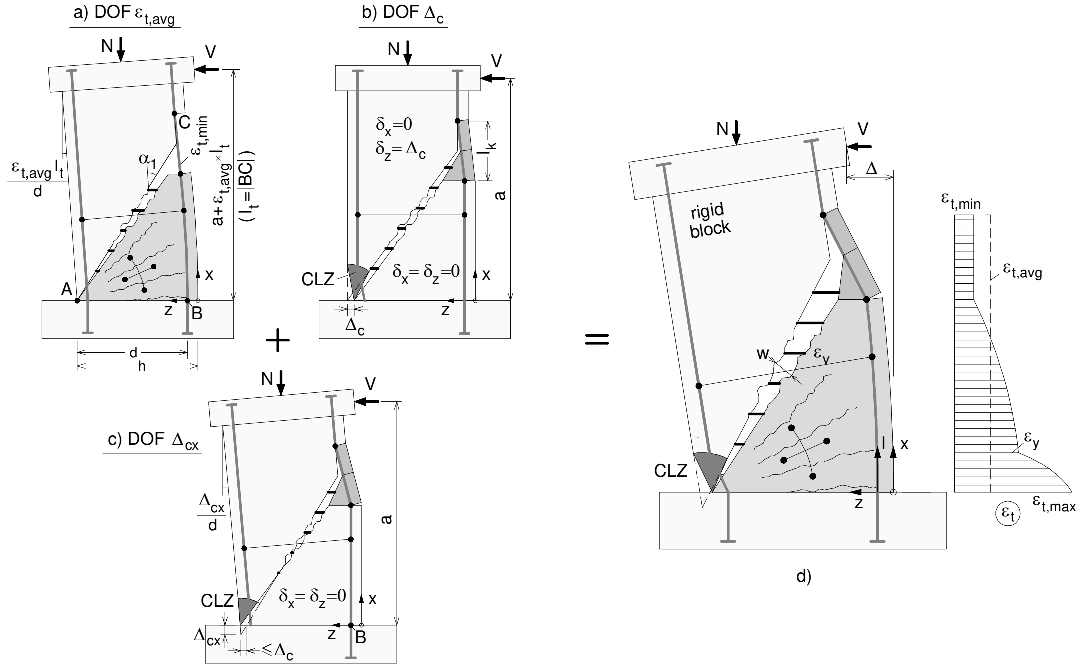

Figure 4-20. Three-parameter kinematic model for shear-dominated walls

The third DOF of the kinematic model is the downward displacement Δ_{cx} of the compression edge of the wall (Figure 4-20c). This displacement is accommodated in the CLZ of the wall and causes a rotation of the rigid block about point B at the bottom of the tie. The rotation can result in a contact between the rigid block and the fan at the bottom of the critical crack if DOF Δ_c is not sufficiently large. As evident from Figure 4-20c, DOF Δ_{cx} can be associated with the action of the vertical load N which drives the rigid block downwards.

When the three deformation patterns are superimposed, they produce the complete deformation pattern of the wall (Figure 4-20d). More precisely, the horizontal and vertical displacements of each point from the wall are expressed as the sum of the displacements from the three basic deformation patterns. Based on small-displacement kinematics, the resulting expressions for the displacement field of the wall are:

- Below the critical crack

$$\delta_x(x,z) = \varepsilon_{t,avg}x \tag{4-25}$$

$$\delta_z(x,z) = \frac{\varepsilon_{t,avg} x^2}{h-z} \tag{4-26}$$

- Above the critical crack

$$\delta_x(x,z) = \frac{\varepsilon_{t,avg} l_t}{d}(h-z) + \frac{\Delta_{cx}}{d}(h-d-z) \tag{4-27}$$

$$\delta_z(x,z) = \left(\frac{\varepsilon_{t,avg} l_t}{d} + \frac{\Delta_{cx}}{d}\right)x + \Delta_c \ , \tag{4-28}$$

where,

d	Effective length of the section
h	Total length of the section
l_t	Cracked length along the flexural reinforcement (tie)

These expressions represent conditions for compatibility of deformations which are used to simplify the complex behavior of shear-dominated walls. A detailed discussion on the derivation of these equations can be found elsewhere (Mihaylov et al., 2016).

4.2.1.2 Load-bearing mechanisms

To determine DOFs $\varepsilon_{t,avg}$, Δ_c, and Δ_{cx} under a vertical load and lateral displacement at the top of the wall, it is necessary to combine the compatibility equations with constitutive relationships for the load-bearing mechanisms in the wall. In the 3PKT these mechanisms are modeled with nonlinear springs "attached" to the kinematic model (Figure 4-21). Some of the mechanisms (springs) connect the rigid block to the fan, while the rest represent the interaction between the rigid block and the foundation in the CLZ. The mechanisms across the critical diagonal crack include the aggregate interlock shear F_{ci}, tension in the shear reinforcement F_s, contact forces F_{cn} and F_{ct} between the rigid block and the fan in the vicinity of the critical loading zone, dowel action F_d of the flexural reinforcement along length l_k at the top of the critical crack, and tension in the flexural reinforcement $F_{t,min}$ within l_k. The interaction between the rigid block and foundation includes the forces resulting from the principal compression in the critical loading zone F_{CLZ1} and F_{CLZ2}, as well as the vertical force F_{sc} in the compression reinforcement.

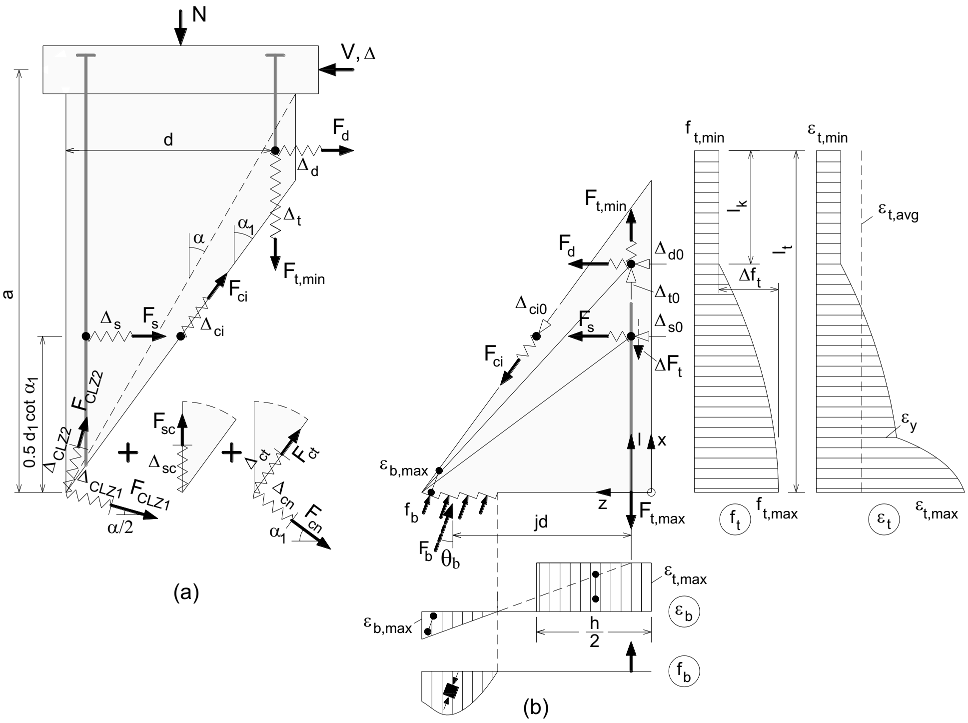

Figure 4-21. Load-bearing mechanisms in shear-dominated walls according to the 3PKT (Mihaylov et. al, 2016)

For a given set of DOFs $\varepsilon_{t,avg}$, Δ_c, and Δ_{cx}, the kinematic conditions in Eqs. (4-25) to (4-28) are used to determine the deformations in the springs, and these deformations are in turn used to determine the forces in the springs by using appropriate constitutive relationships. The deformations and nonlinear behavior of the springs are summarized in Figure 4-22.

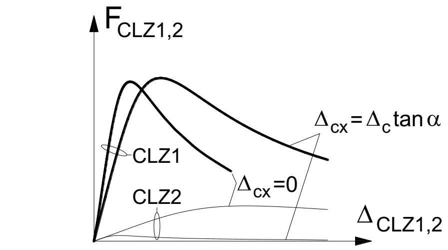

$$\Delta_{CLZ,1} = \boldsymbol{\Delta_c} \cos\frac{\alpha}{2} - \boldsymbol{\Delta_{cx}} \sin\frac{\alpha}{2}$$

$$\Delta_{CLZ,2} = \boldsymbol{\Delta_c} \sin\frac{\alpha}{2} + \boldsymbol{\Delta_{cx}} \cos\frac{\alpha}{2}$$

a) Inclined compression in CLZ

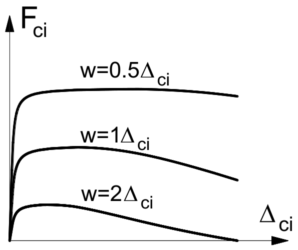

$$\Delta_{ci} = \boldsymbol{\Delta_c} \sin\alpha_1 + \boldsymbol{\Delta_{cx}} \cos\alpha_1 - \Delta_{ci0} \geq 0$$

$$\mathrm{w} = \left[\frac{(\boldsymbol{\varepsilon_{t,min}} l_k)}{2\sin\alpha_1}\frac{h}{d} + \boldsymbol{\Delta_c}\cos\alpha_1 + \right.$$
$$\left. + \frac{\boldsymbol{\Delta_{cx}}}{d}\left(\frac{h}{2\sin\alpha_1} - d\sin\alpha_1\right)\right]\frac{1}{n_{cr}}$$

b) Aggregate interlock

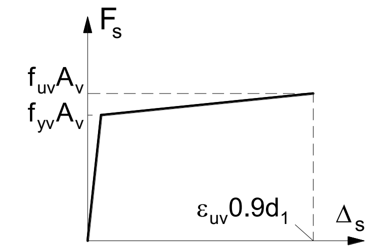

$$\Delta_s = \left(\frac{\boldsymbol{\varepsilon_{t,avg}} l_t}{d} + \frac{\boldsymbol{\Delta_{cx}}}{d}\right) 0.5 d_1 \cot\alpha_1 + \boldsymbol{\Delta_c} - \Delta_{s0}$$

c) Transverse reinforcement

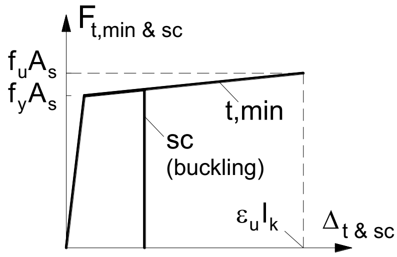

$$\Delta_t = \boldsymbol{\varepsilon_{t,min}} l_k = \boldsymbol{\varepsilon_{t,avg}} l_t - \Delta_{t0}$$

$$\Delta_{sc} = \boldsymbol{\Delta_{cx}}$$

d) Vertical reinforcement

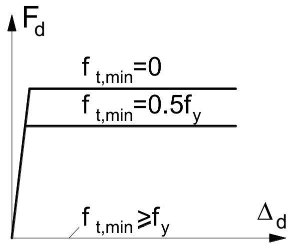

$$\Delta_d = \left(\frac{\boldsymbol{\varepsilon_{t,avg}} l_t}{d} + \frac{\boldsymbol{\Delta_{cx}}}{d}\right) l_t + \boldsymbol{\Delta_c} - \Delta_{d0}$$

e) Dowel action

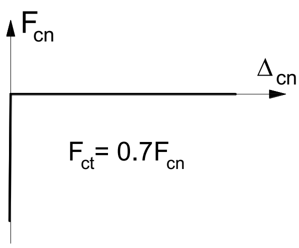

$$\Delta_{cn} = \boldsymbol{\Delta_c} \cos\alpha_1 - \boldsymbol{\Delta_{cx}} \sin\alpha_1$$

$$\Delta_{ct} = \boldsymbol{\Delta_c} \sin\alpha_1 + \boldsymbol{\Delta_{cx}} \cos\alpha_1$$

f) Contact between rigid block and fan

Figure 4-22. Deformations and constitutive relationships of the nonlinear springs along the critical diagonal crack

4.2.1.3 Overview of solution procedure and failure modes

By using the compatibility conditions and constitutive relationships for the load-bearing mechanisms in the wall, the forces in the springs and fan can be computed for a given set of DOFs $\varepsilon_{t,avg}$, Δ_c, and Δ_{cx}. If the lateral displacement Δ at the top of the wall is imposed, the number of unknown DOFs is reduced to only two. These two DOFs are determined to ensure the vertical and moment equilibrium of the forces acting on the rigid block. These forces include the external vertical load N and the spring forces F_i. In addition, the horizontal equilibrium of the block is used to calculate the lateral load on the wall V corresponding to the imposed displacement Δ. Due to the nonlinear behavior of the springs and fan, the equilibrium conditions are solved through an iterative procedure based on the secant stiffness approach. Despite the iterative procedure, the complete load-displacement analysis (V-Δ response) of a wall takes only a few seconds on a typical computer due to the small number of DOFs used in 3PKT formulation.

Finally, as can be seen from Figure 4-21, there are two potential failure planes defined in the 3PKT: the critical diagonal crack and the base section of the wall. The wall can fail in shear along the critical crack either prior to or after the yielding of the flexural reinforcement. Failure in the base section can either occur by rupture of the reinforcement or by crushing of the concrete in the compression zone under the combined action of bending and shear.

4.2.1.4 Range of applicability of the 3PKT

As the 3PKT is developed for short shear-dominated walls, it is necessary to define a limit between such members and walls controlled by flexure. A wall is considered short and shear-dominated if it has an aspect ratio $a/h \leq 3.0$, and if the 3PKT predicts that the shear reinforcement spring F_s yields before the flexural reinforcement in the base section. In other words, the results from the analysis are considered valid if the flexural reinforcement remains elastic or yields after the stirrups. The applicability of the 3PKT is also limited to walls under normalized axial compression $n=N/bhf_c'$ smaller than 0.20. Higher stress levels are relatively rare in practice and typically cause shear failures upon diagonal cracking. As the 3PKT assumes that the wall is fully cracked, it is not suitable for modeling such failures. Additional limitations include concrete compressive strength ≤60 MPa, no lap-splice failures, and no out-of-plane-instability. Finally, even though the 3PKT was originally developed for rectangular walls, this part of the study will explore the possibility to also apply it to walls with barbells.

4.2.2 Rectangular short walls with aspect ratios *a/h*=2-3

The three-parameter kinematic theory was initially validated with tests performed by Bimschas (2010). This experimental study included loading to failure of three large-scale cantilever walls with an aspect ratio a/h=3.3m/1.5m=2.2. The specimens were designed to represent existing bridge piers with low amount of transverse reinforcement (stirrup ratio ϱ_v=0.08%). The vertical reinforcement was uniformly distributed across the section with a ratio ϱ_l=0.82% or 1.23%. The goal of the experimental campaign was to investigate the potential for premature shear failures and loss of axial capacity of wall-type piers under seismic loading. The test specimens were therefore subjected to cyclic lateral displacements with increasing amplitude and a constant axial load with n≈0.07. This experimental campaign was extended by Hannewald et al. (2013) to include more slender walls (a/h=3.0) and walls with larger shear reinforcement ratio (ϱ_v=0.22%). The main properties of four walls from the two studies are summarized in Table 4-6. (VK series).

Table 4-6. Properties of test specimens

Rectangular Walls

Wall ID	b *mm*	h *mm*	d *mm*	a/h	ρ_l %	ρ_v %	f_y *MPa*	f_{yv} *MPa*	f_c' *MPa*	$\frac{N}{bhf_c'}$	V_{max} *kN*
VK1	350	1500	1190	2.2	0.82	0.08	515	518	35.0	0.071	737
VK3	350	1500	1160	2.2	1.23	0.08	515	518	34.0	0.073	887
VK6	350	1500	1160	3.0	1.23	0.08	521	528	44.4	0.056	675
VK7	350	1500	1160	2.2	1.23	0.22	521	528	30.0	0.082	903
Wall 2	100	2000	1585	0.33	0.80	0.26	435	425	22.0	0	680
SW5	203	3050	2287	0.33	1.00	1.00	462	462	29.7	0	3190
SW6	203	3050	2287	0.33	0.67	0.67	462	462	26.2	0	2460
SW9	203	3050	2287	0.54	1.50	0.67	462	462	29.7	0	2880
SW10	203	3050	2287	0.54	1.50	0.33	462	462	31.7	0	2380

Walls with Barbells

Wall ID	b *mm*	h *mm*	b_b *mm*	h_b *mm*	a/h	ρ_{lb} %	ρ_{vb} %	ρ_{lw} %	ρ_{vw} %	f_y *MPa*	f_{yv} *MPa*	f_c' *MPa*	$\frac{N}{bhf_c'}$	V_{max} *kN*
U1.5	100	1670	200	150	1.5	3.43	0.22	0.16	0.16	465	472	17.6	0	342
U2.0	100	1250	200	150	2.0	3.73	0.22	0.16	0.16	465	472	26.5	0	274
LW1	80	3500	250	250	0.65	1.29	0.57	0.28	0.28	515	365	27.3	0	660
WF-12	120	3500	300	500	0.51	1.89	1.29	0.20	0.20	571	364	13.9	0	1180
WF-15	150	3500	300	500	0.51	1.89	1.29	0.86	0.86	571	443	22.6	0	2122

The complete hysteretic load-displacement response of wall VK1 is shown in Figure 4-23a, while the envelope responses of the other three specimens are presented in Figure 4-23b. The lateral displacements are expressed in terms of drift ratio $\delta=\Delta/a$, %. It can be seen that all specimens exhibited a plastic plateau caused by the yielding of the flexural reinforcement at the base of the wall. However, while the specimens showed certain ductility, their drift ratio capacity was limited by sudden shear failures along diagonal cracks. This type of shear failure is governed by the complex interaction between shear, flexure, and axial load. At the same time, the accurate prediction of such failures is very important for the assessment of existing structures with limited ductility. If the assessment is based on a conservative model that neglects the available ductility, this can result in costly and disruptive retrofit measures. As evident from Figure 4-23, the 3PKT method captured well the entire behavior of the walls, including the yield plateau and the drift ratio capacity determined by the sudden drop of lateral resistance.

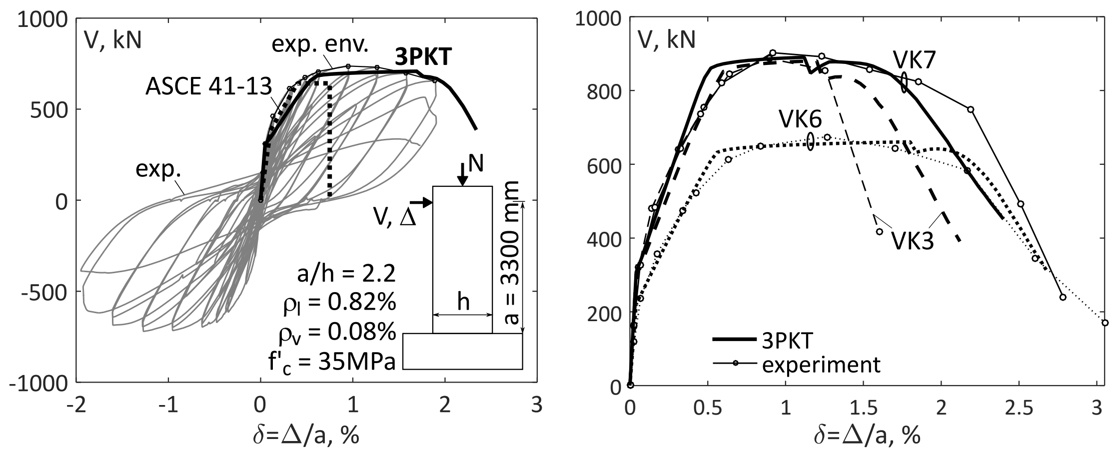

a) Hysteretic response of specimen VK1

b) Envelope response of specimens VK3,6,7

Figure 4-23. Measured and predicted response of test specimens from VK series (tests by Bimschas, 2010 and Hannewald, 2013)

For comparison, Figure 4-23a also shows the load-displacement envelope calculated according to the ASCE 41-13 (2014) provisions. As the calculated flexural capacity of the wall is smaller than its shear capacity, the peak shear force is determined by flexure and agrees well with the experiment. At the same time, as the code commentary states that the response of walls with $a/h \leq 2.5$ is better approximated by a backbone curve for members controlled by shear, the drift ratio values are determined based on this assumption. As evident from the plot, this simple approach significantly underestimates the displacement capacity of wall VK1. Similar observations also apply to walls VK3, 6, and 7.

Given the adequate load-displacement predictions of the 3PKT, it is of interest to use this method to better understand the mechanism of shear failures in short walls, and in particular failures occurring after the yielding of the flexural reinforcement. As the applied shear does not increase significantly after yielding, some of the shear resisting mechanisms must degrade with increasing deformations in order to trigger a shear failure. This is demonstrated in Figure 4-24a which shows the predicted components of shear resistance in wall VK1 and how these components vary with an increasing drift ratio. The shear forces V_i correspond to the horizontal components of the forces in the springs attached to the rigid block. More precisely, shear V_{ci} corresponds to force F_{ci}, shear V_s to F_s, V_d to F_d, V_{CLZ} to F_{CLZ1} and F_{CLZ2}, and V_{cf} corresponds to F_{cn} and F_{ct} (Figure 4-21). It can be seen that the transverse reinforcement is predicted to yield at a drift ratio of about 0.4% (component V_s) and maintains a constant shear resistance until the end of the analysis. It can also be seen that the main mechanism exhibiting degradation is the critical loading zone. Shear component V_{CLZ} reaches its peak approximately halfway along the yield plateau of the global V-δ response and decreases gradually as the drift ratio increases. In order to maintain a constant shear force within the yield plateau, the decrease of V_{CLZ} is compensated by an increased demand on the aggregate interlock mechanism (component V_{ci}). This subtle internal redistribution of shear forces is the key to capturing the eventual shear failure. According to the 3PKT method, it is the aggregate interlock that is finally overloaded and triggers the failure. Following the sudden drop of resistance, the analysis continues until the damaged critical loading zone and aggregate interlock are not able to support the vertical load N. This last point from the analysis at $\delta\approx 2.4\%$ marks the complete failure of the wall characterized by a sudden downwards sliding of the rigid block along the critical crack.

Further insight into this failure is provided in Figure 4-24b which shows the displacements of the two faces of the critical crack parallel to the crack. These displacement components are evident from the expression for the crack slip Δ_{ci} in Figure 4-22b. The displacement above the crack $\Delta_c sin a_1 + \Delta_{cx} cos a_1$ increases with increasing drift ratio in proportion to the strain in the critical loading zone ε_{CLZ}. At the same time, the displacement below the crack Δ_{ci0} increases as well in proportion to the strain $\varepsilon_{b,max}$ in the compression zone of the fan. It is therefore the difference between these two displacements that determines the slip in the crack and controls the shear failure. The reason for the redistribution of the shear forces after flexural yielding is strain $\varepsilon_{b,max}$ which is mainly caused by flexure and increases within the plastic plateau of the global response. This creates a tendency for less slip and less aggregate interlock on the crack. As a result, the rigid block must slide downwards in order to "find" a new equilibrium position. As the block moves downwards, the CLZ enters the post-peak regime and the increased slip on the crack generates larger aggregate interlock stresses until the interlock mechanism breaks down.

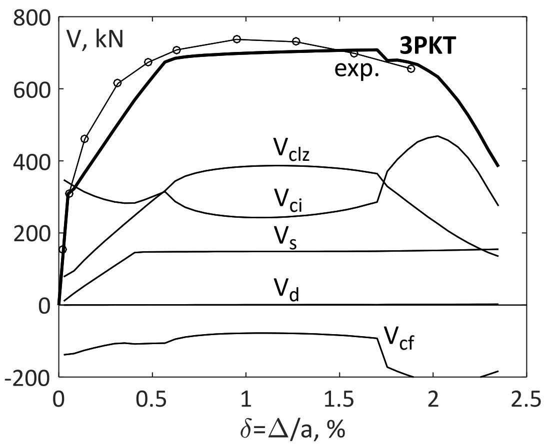

a) Predicted components of shear resistance

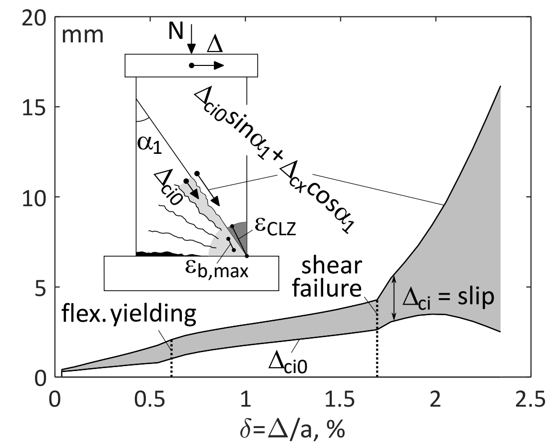

b) Predicted sliding deformations along the critical diagonal crack

Figure 4-24. Mechanism of failure along diagonal cracks in shear-dominated walls according to the 3PKT method applied to specimen VK1 (test by Bimschas, 2010)

4.2.3 Rectangular squat walls with a/h≤1.0

4.2.3.1 Test by Wirandinata (1985)

While the 3PKT was formulated mainly on the basis of experimental data from moderately short walls, it is also of interest to apply this method to squat shear walls that work predominantly in shear. Such a wall with an aspect ratio a/h=0.33 was tested by Wirandinata (1985) (Wall 2 in Figure 4-25a and Table 4-6.). The specimen had a 2000 mm-long section that featured end zones with concentrated vertical reinforcement and confining hoops. The ratio of the total vertical reinforcement was ϱ_l=0.80% while the horizontal reinforcement ratio was ϱ_v=0.26%. Cyclic lateral displacements with increasing amplitude were applied at the top of the wall via a stiff concrete block. Apart from the weight of the block, no vertical load was applied on the test specimen.

The envelopes of the measured load-displacement response of Wall 2 in both loading directions are shown in Figure 4-25b. It can be seen that this specimen did not exhibit a yield plateau, and therefore its flexural reinforcement remained mostly elastic. It was reported that only the extreme rows of reinforcement yielded near the peak load, and this was followed by sliding of the wall along a horizontal crack at the base. The thick line in Figure 4-25b shows that the load-displacement response produced by the 3PKT method follows closely the experimental curves. As for specimen VK1, the figure also shows the predicted components of shear resistance and how they vary with increasing lateral displacement. It can be seen that similar to the more slender wall, the two dominant shear mechanisms are the compression in the CLZ and the aggregate interlock across the critical crack. The CLZ is predicted to fail at a drift ratio of only 0.2%, and then the shear is redistributed towards the less stiff aggregate interlock mechanism. The peak shear resistance of the wall occurs when shear component V_{CLZ} is decreasing and V_{ci} is increasing. This is different from wall VK1 whose failure was triggered by the breakdown of the aggregate interlock mechanism. Due to the very flat slope of the critical crack (Figure 4-25a), the horizontal web reinforcement is predicted to have a negligible contribution to the shear resistance similar to the dowel action of the vertical reinforcement.

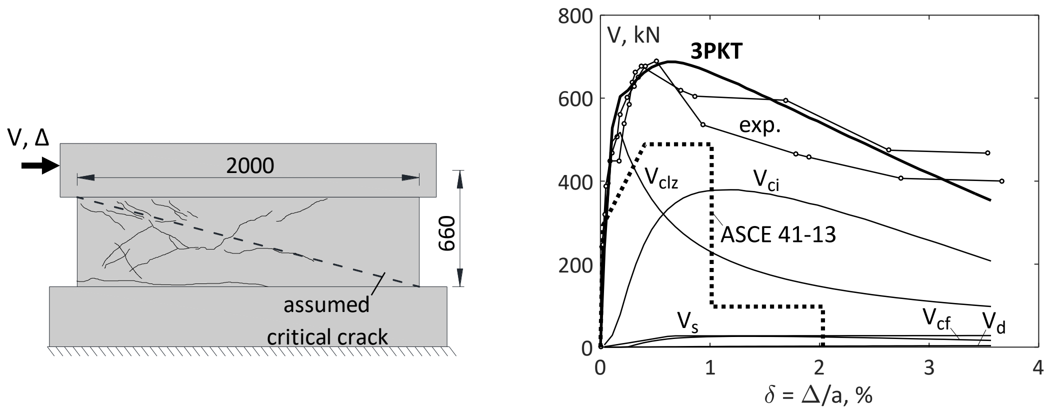

a) Test setup and observed crack pattern near failure b) Measured and predicted response

Figure 4-25. Test specimen Wall 2 (Wirandinata, 1985)

These adequate predictions can be somewhat surprising considering that the 3PKT method does no account for sliding deformations at the base of the wall.

However, due to the flat slope of the critical diagonal crack, the behavior along this crack is similar to that along the base crack. According to the 3PKT, the sliding along the critical crack is triggered by the crushing of the critical loading zone. This is in agreement with the test observation that, after Wall 2 reached its peak resistance, the crushing of the compression zones was followed by significant sliding deformations at the base (Wirandinata, 1985).

Figure 4-25b also shows the envelope response produced on the basis of the ASCE 41-13 (2014) provisions. Because Wall 2 has an aspect ratio smaller than 1.5, it is classified as a shear-controlled wall, and this determines its peak resistance and drift ratio values at the key points along the backbone curve. As evident from the plot, the code provisions are very conservative both in terms of strength and displacement capacity.

4.2.3.2 Effect of wall dimensions

Another more recent experimental program on squat walls was performed by Luna et al. (2015) and Luna (2016). This study involved testing to failure of large-scale walls with aspect ratios varying between 0.33 and 0.94. The test specimens were subjected to cyclic lateral displacements without a vertical load. The first wall studied here is specimen SW6 as it was similar to Wall 2 (Figure 4-26). Compared to Wall 2, this specimen had the same aspect ratio of 0.33, it was about 50% larger (h=3050 mm) and featured slightly different boundary conditions. While Wall 2 was loaded by a rigid concrete block, specimen SW6 was loaded through steel brackets and plates which were post-tensioned to either side of the wall. In terms of vertical reinforcement, SW6 had a slightly smaller vertical ratio (0.67% vs. 0.80%) and a significantly larger horizontal reinforcement ratio (0.67% vs. 0.26%). It should also be noted that the vertical reinforcement of SW6 was uniformly distributed across the length of the section. The remaining properties of the two walls can be compared in Table 4-6.

The reported failure mode of wall SW6 was diagonal compression. It was observed that the loss of lateral resistance was due to crushing of the concrete at the toes of the wall. Similar to Wall 2, this specimen exhibited sliding at the base after reaching the peak shear force.

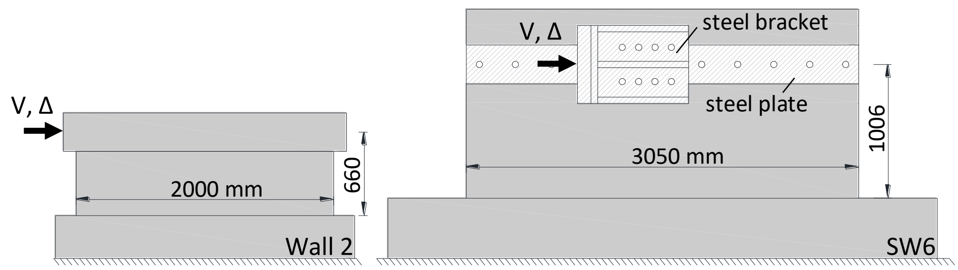

Figure 4-26. Tests Wall 2 and SW6 – geometry and loading apparatuses

The measured load-displacement envelopes of the two walls in the two loading directions are compared in Figure 4-27a. For the sake of more direct comparisons, the lateral forces are normalized by the gross concrete area of the section and the compressive strength of the concrete. It can be seen that specimen SW6 had very different responses in the two loading directions compared to the rather symmetrical behavior of Wall 2. This unsymmetrical response is explained with the fact that SW6 was not restrained against out-of-plane displacements, and exhibited a certain unsymmetrical twist about a vertical axis. If the peak resistances in the two directions are averaged, it appears that SW6 was weaker than Wall 2 in terms of normalized shear stress at failure V_{max}/bhf_c'.

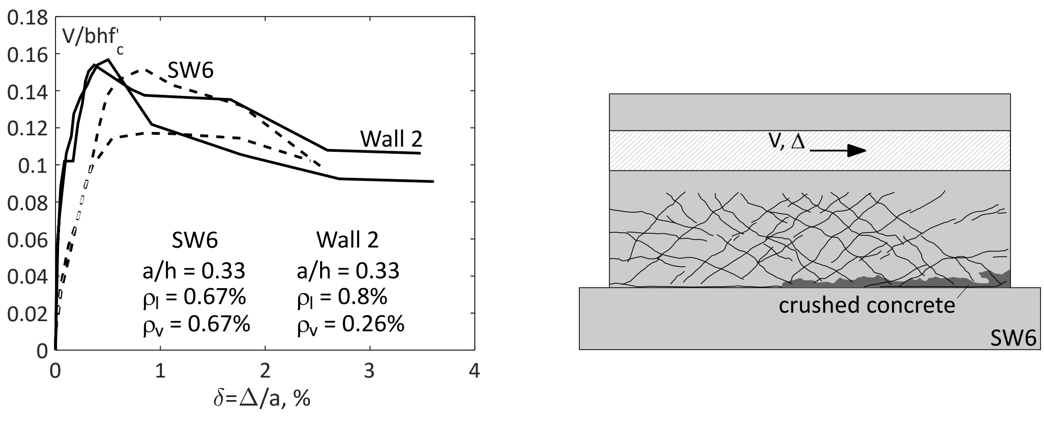

a) Measured response compared to Wall 2

b) Observed crack pattern at failure

Figure 4-27. Test specimen SW6 (Luna et. al, 2015)

Another important observation is that the two walls differed significantly in terms of stiffness. It can be seen from Figure 4-27a that SW6 was significantly less stiff than Wall 2, even though it had a stronger concrete (f_c'=26.2 MPa vs. 22.0 MPa).

The authors of test SW6 evaluated the stiffness of the wall based on the ASCE 43-05 (2005) and ASCE 41-06 (2007) provisions and found that the predictions were respectively 1.56 and 2.38 times larger than the measured stiffness. This discrepancy was explained mainly with microcracking caused by the large foundation block which restrained the shrinkage deformations in the wall (Luna et al., 2015).

By default, the 3PKT uses a modulus of elasticity of concrete calculated from the compressive strength according to $E_c=3320\sqrt{f_c'}+6900$, MPa (Carrasquillo et al., 1981). However, to account for the actual condition of the concrete prior to the test, specimen SW6 was analyzed with one-half of this value as recommended in Luna (2016). The complete load-displacement response predicted on this basis is shown in Figure 4-28a together with the predicted components of shear resistance. It can be seen that the 3PKT captures well the average peak and post-peak response in the two loading directions, but underestimates the deformations in the pre-peak regime.

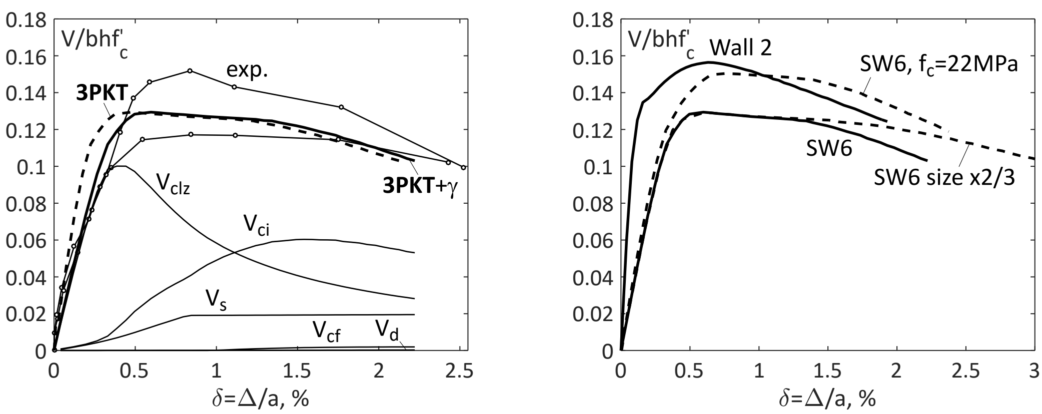

a) Specimen SW6 – effect of shear deformations above the wall diagonal

b) 3PKT predictions – effect of size and concrete compressive strength

Figure 4-28. Measured and predicted responses of test specimens SW6 and Wall 2

The predicted stiffer response is explained with the way that specimen SW6 was loaded. As mentioned earlier, the lateral load on the wall was not applied through a stiff concrete block, but through bolted steel plates. It can be assumed that this test apparatus applies an approximately uniform load along the wall, and does not completely restrain the horizontal deformations at the level of the load. As a result, shear cracks propagated in the presumed rigid block as evident from the crack diagram in Figure 4-27b. This crack pattern differs from that of Wall 2 where the orientation of the cracks was closer to that assumed in the kinematic model (Figure 4-25a). To account for this effect in a simple manner, it is suggested to increase the predicted drift ratios with the shear deformations in the concrete block estimated as:

$$\gamma = 100\frac{1.2V}{G_c bh} \tag{4-29}$$

where the shear modulus G_c of concrete is assumed equal to $0.4E_c$. As evident from the difference between the thick dashed and solid lines in Figure 4-28, these additional drift ratios improve the 3PKT prediction in the pre-peak regime.

Finally, it is of interest to use the 3PKT to explain the apparent difference in normalized shear strength between walls SW6 and Wall 2. One possible hypothesis is the size effect in shear, considering that SW6 was 1.53 times larger than Wall 2. According to Figure 4-28b however, decreasing the size of wall SW6 with a factor of 2/3 increases the ductility of the wall, but does not influence the shear strength. Instead, the 3PKT predicts that the main reason for the strength difference between the two walls is the difference in concrete strength. If wall SW6 is analyzed with the concrete strength of Wall 2 (f_c'=22 MPa), the predicted peak resistances of the specimens become almost identical. This shows that, even though the walls are squat and work predominantly in diagonal compression, the shear resistance does not scale linearly with the compressive strength of the concrete.

4.2.3.3 Effects of aspect ratio and amount of reinforcement

To further validate the 3PKT approach and to study the effects of other test variables, it is of interest to analyze the rest of the squat walls tested by Luna et al. (2015) to which the model is applicable. As discussed earlier, the 3PKT applies to walls for which the shear reinforcement spring F_s is predicted to yield before the yielding of the flexural reinforcement. Figure 4-29 shows the measured and predicted responses of the walls for which this condition is met (see the properties of the walls in Table 4-6.).

Specimens SW5 and SW6 had an aspect ratio of 0.33 and differed only in terms of reinforcement ratios ϱ_l and ϱ_v (ϱ_l=ϱ_v=1.0% for SW5 vs. 0.67% for SW6). It can be seen from Figure 4-29 that the 50% larger reinforcement ratio of SW5 resulted in a relatively modest increase of shear strength and a more significant reduction of drift ratio capacity. The drift ratio capacity δ_u is defined here as the drift ratio at a 20% drop of lateral resistance. For the sake of comparisons, the 3PKT load-displacement curves are terminated at the predicted δ_u. The 3PKT captures reasonably well the responses of specimens SW5 and SW6, even though it overestimates the drift capacity of SW5.

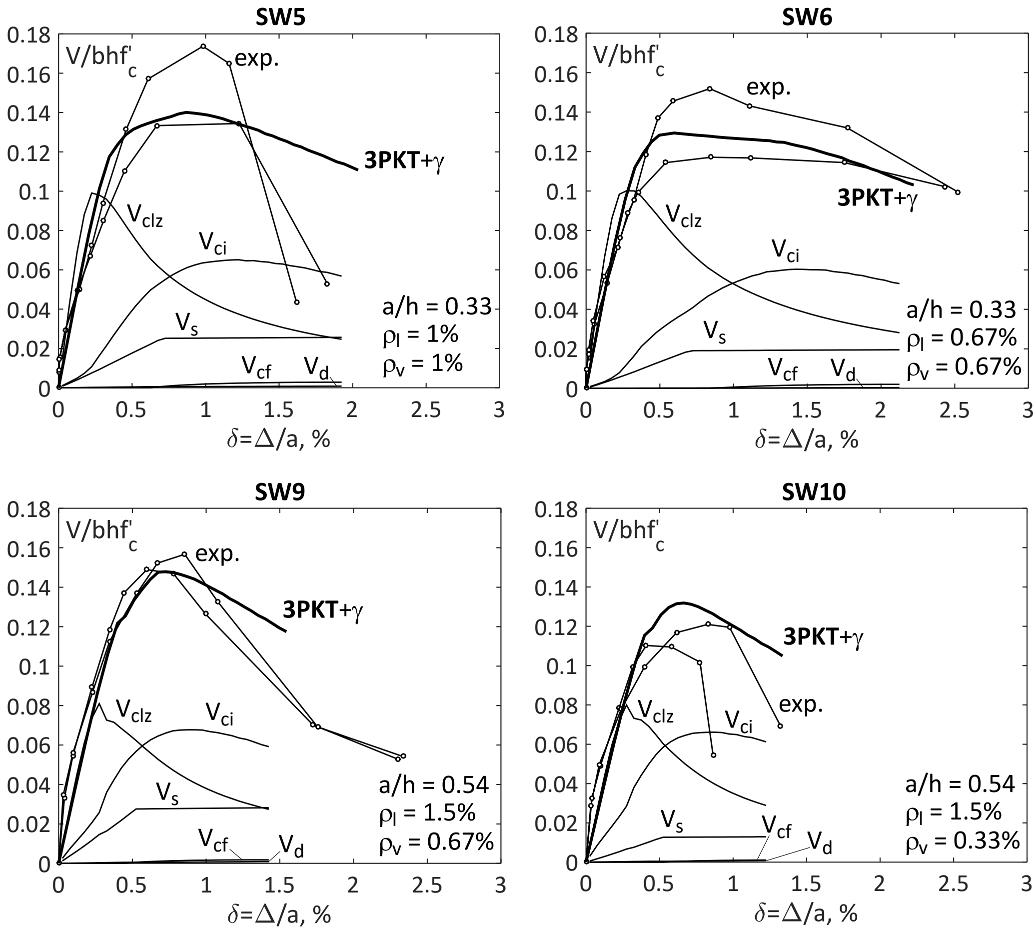

Figure 4-29. Effect of aspect ratio and amount of reinforcement on the shear response of squat walls – tests SW5,6,9,10 (Luna et al., 2015)

Specimens SW9 and SW10 had an aspect ratio of 0.54 and differed only in the amount of shear reinforcement (ϱ_v=0.67% for SW9 vs. 0.33% for SW10). As compared to the shorter walls, the trend in drift ratio capacity is reversed: a 50% increase of shear reinforcement resulted in a slight decrease of measured drift ratio capacity. These subtle trends are captured by the 3PKT which accounts for the complex interactions of the shear mechanisms in the walls.

In addition to the complete load-displacement responses, the 3PKT method is used to predict the deformation patterns of walls SW5-6 and SW9-10. These patterns are expressed by Eqs. (4-25)-(4-28) as functions of the degrees of freedom of the kinematic model $\varepsilon_{t,avg}$, Δ_c, and Δ_{cx} which are predicted at each drift level.

In Figure 4-30 the results from Eqs. (4-25)-(4-28) are compared to displacement measurements performed on a grid of targets (Luna et al., 2013). The predicted deformed shape of the grid is shown with dots while the measured deformations are depicted with a mesh of quadrilaterals. The comparisons are performed at the drift ratios corresponding to the peak measured load in the "positive" loading direction. It can be seen that the 3PKT produced reasonable predictions for the shorter walls and captured very well the deformation patterns of the taller specimens. While the rotations of the rigid block of specimens SW5 and SW6 are slightly underestimated by the model, an excellent agreement is observed for walls SW9 and SW10 in terms of both the rotation and translations of the block. The visible discrepancy along a horizontal line of targets in specimen SW10 is likely due to an error in measurements as the horizontal shift in the mesh of quadrilaterals is not consistent with the crack diagrams and photos provided by Luna (2016).

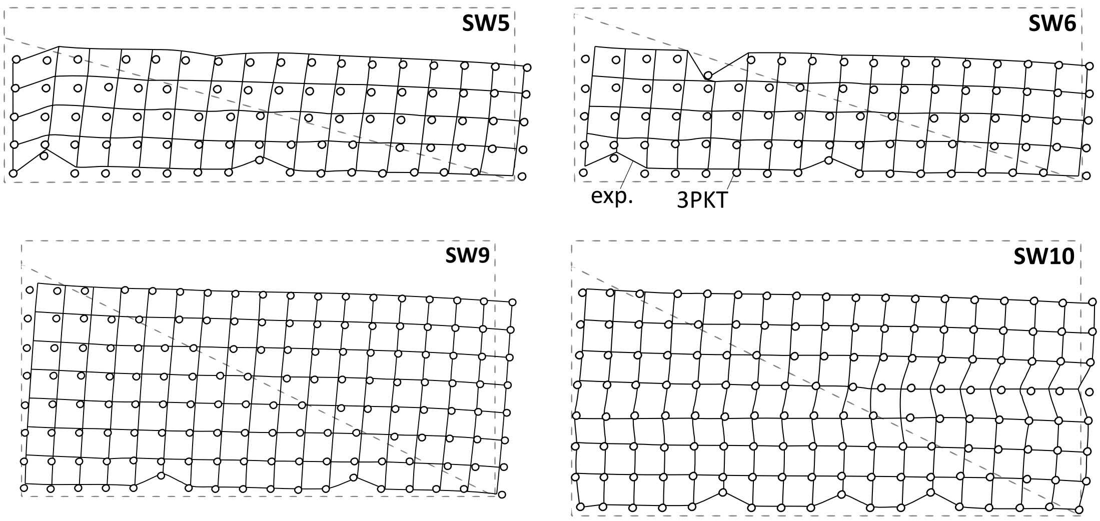

Figure 4-30. Measured (mesh) and predicted (dots) deformation patterns at peak load – tests SW5, 6, 9, 10 (Luna et al., 2015)

4.2.3.4 Comparisons with walls with a/h=2-3

As the predicted DOFs of the kinematic model $\varepsilon_{t,avg}$, Δ_c, and Δ_{cx} can be associated respectively with flexure, shear, and axial load, they can be used to compare the behavior of squat walls with a/h≤1.0 to that of walls with a/h=2-3. Such a comparison is performed by evaluating the contribution of each DOF to the total drift ratio of the wall. The relationships between the drift ratio and DOFs are expressed from Eq. (4-28) by substituting x=a and dividing the result by the height of the wall:

$$\delta(\varepsilon_{t,avg}) = \frac{\varepsilon_{t,avg} l_t}{d} \tag{4-30}$$

$$\delta(\Delta_c) = \frac{\Delta_c}{a} \tag{4-31}$$

$$\delta(\Delta_{cx}) = \frac{\Delta_{cx}}{d} \tag{4-32}$$

In addition to these drift ratios, the analysis of the squat walls from the SW series also included the shear deformations γ above the critical diagonal crack expressed with Eq. (4-29).

Figure 4-31 compares the drift ratio components calculated for wall SW9 with a/h=0.54 and wall VK6 with a/h=3.0. The values are normalized with respect to the total drift ratio, and therefore add up to unity at each drift level. It can be seen that the two plots differ significantly. The peak behavior of the squat wall is dominated by DOF Δ_c while that of the taller specimen is governed by $\varepsilon_{t,avg}$ (see drift components at V_{max}). The second largest drift contribution at peak load comes from the shear deformations γ in the squat wall and DOF Δ_{cx} in the taller wall. These dominant components are consistent with the test observations that wall SW9 performed mostly horizontal sliding along the critical crack while VK6 exhibited significant flexural yielding. In the post-peak regime of wall SW9, the sliding deformations associated with Δ_c become even more dominant. In test VK6, following the shear failure at the end of the plastic plateau, the contribution of Δ_{cx} increased and that of $\varepsilon_{t,avg}$ decreased rapidly. This shows a significant downward sliding of the rigid block along the critical crack due to the action of the axial load on wall VK6.

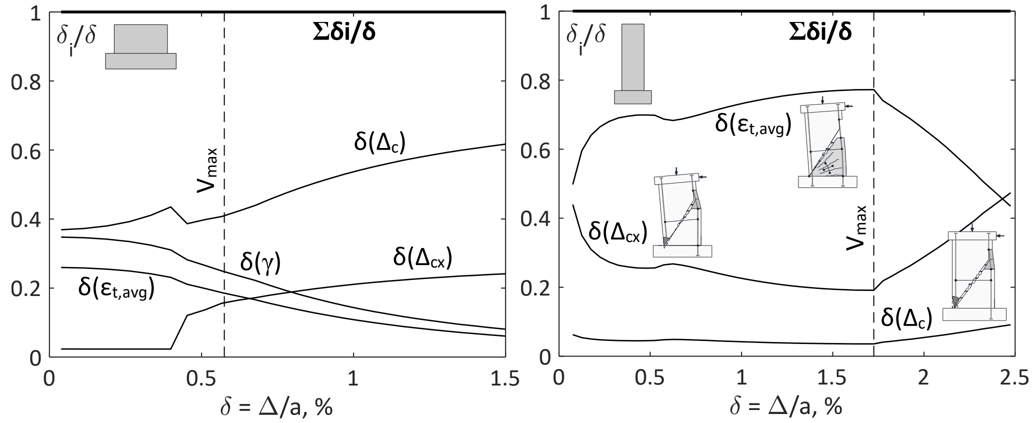

a) Squat wall SW9 with a/h=0.54 b) Short wall VK6 with a/h=3.0

Figure 4-31. Predicted evolution of the DOFs of the 3PKT in squat and short walls

4.2.4 Short walls with barbells

As mentioned earlier, the three-parameter kinematic theory was developed for short shear-dominated walls with rectangular sections. However, because in practice it is also common to encounter walls with barbells, this section focuses on an effort to extend the 3PKT to such members.

Some general considerations on the effect of barbells can be made on the basis of the 3DOF kinematic model in Figure 4-20. The main assumption of the model is that the concrete block above the critical diagonal crack has negligible deformations as compared to the toe of the wall and the fan below the critical crack. The presence of barbells is likely to strengthen this assumption as they stiffen the flexural compression side of the wall. The flexural tension side, on the other hand, is assumed cracked, and therefore the concrete in the barbells can be neglected, while the reinforcement in the barbells should be included in the vertical tie of the model. In addition, the tension barbell can have a certain effect on the control of the shear cracks in the web of the wall. As evident from the expression for w in Figure 4-22b, the crack width derived from the kinematics of the wall is divided by the number of the major diagonal cracks n_{cr}. A stiff tension barbell can increase n_{cr} as compared to rectangular walls, and therefore reduce the crack width. Another important consideration is the effect of the compression barbell on the behavior of the critical loading zone. As the barbell is wider than the web, it can increase the resistance of the CLZ. On the other hand, if the barbell represents a relatively small portion of the length of the wall section h, crushing of the concrete can occur in the web in the vicinity of the barbell. In this latter case, the CLZ can be modeled with a width equal to that of the web as in rectangular sections.

To test these assumptions, the 3PKT is applied to two shear critical walls with barbells tested by Mestyanek (1985). The walls had a constant height a=2.5 m and different section lengths resulting in aspect ratios a/h of 1.5 and 2.0 (walls U1.5 and U2.0 in Table 4-6). The widths of the web and barbell were respectively b=100 mm and b_b=200 mm, while the length of the barbell was h_b= 150 mm. The ratio h_b/h equaled 0.090 for U1.5 and 0.12 for U2.0. The walls were subjected to cyclic lateral displacements without a vertical load.

The failure modes of walls U1.5 and U2.0 are shown in Figure 4-32 with photos taken after failure. Both specimens failed along critical diagonal cracks with minor yielding of the flexural reinforcement in the base section. The left photograph in the figure shows the critical loading zone of the shorter wall which spread in the barbell and web. Kinking and buckling of the reinforcement was observed in this zone. It was also reported that a non-negligible portion of the drift ratio of the walls resulted from strain penetration in the foundation block along the anchorage length of the tension reinforcement (bar pullout). As the original 3PKT does not account for this effect, it is of interest to include the bar pullout deformations in the model.

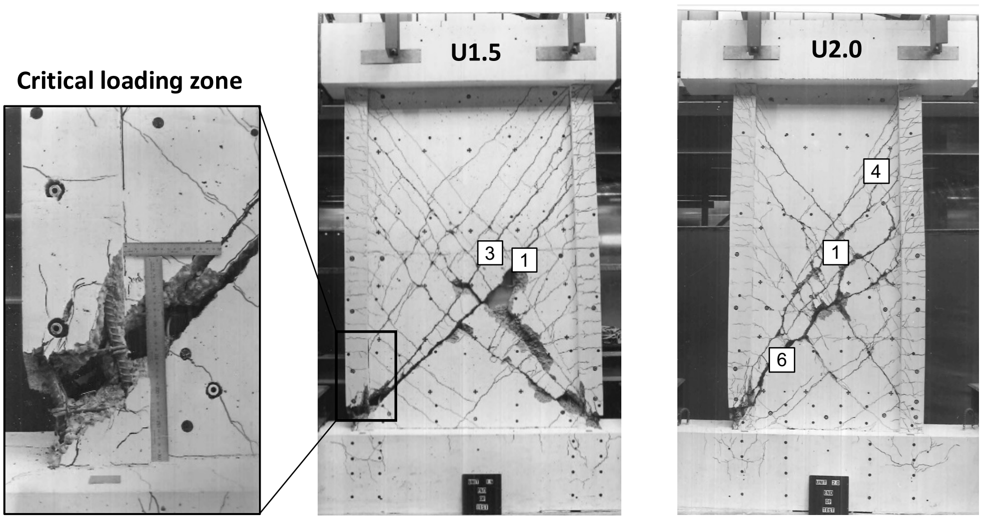

Figure 4-32. Observed failure modes of test specimens U1.5 and U2.0 (photos courtesy of Mestyanek, 1985)

The pullout displacement of a bar sufficiently anchored in a concrete block can be evaluated by using a model proposed by Sigrist (1995). In this model, the anchorage length is divided into two parts: l_1 near the top surface of the foundation where the reinforcement has yielded, and l_0 below l_1 where the reinforcement is elastic. The bond stress between the bar and the concrete is assumed constant in each zone with values of f_{ct} within l_1 and $2f_{ct}$ within l_0, where $f_{ct} \approx 0.33\sqrt{f_c}$ is the tensile strength of the concrete. Considering also the equilibrium of the bar, the following expressions are derived for the vertical pullout displacement at the top surface of the foundation as a function of the strain in the bar $\varepsilon_{t,max}$ at the same location:

$$\Delta_{po} = \frac{1}{2}\left(\varepsilon_{t,max} + \frac{f_y}{E_s}\right) l_1 + \frac{1}{2} min\left(\varepsilon_{t,max}, \frac{f_y}{E_s}\right) l_0 \tag{4-33}$$

$$l_1 = max\left(f_{t,max} - f_y, 0\right) \frac{d_b}{4f_{ct}} \tag{4-34}$$

$$l_0 = min\left(f_{t,max}, f_y\right) \frac{d_b}{8f_{ct}} \ , \tag{4-35}$$

where $f_{t,max}$ is the stress in the bar obtained from the strain $\varepsilon_{t,max}$ by using a bi-linear stress-strain relationship for the reinforcement. If $f_{t,max}$ is smaller than the yield strength of the bar f_y, length l_1 is zero and the pullout displacement is given only by the second term of Eq. (4-33). The pullout displacement Δ_{po} is transformed into a drift ratio as follows:

$$\delta_{po} = \frac{\Delta_{po}}{d - c} \ , \tag{4-36}$$

where c is the depth of the compression zone in the base section. Both the depth c and strain $\varepsilon_{t,max}$ are obtained from the 3PKT analysis at each load step (Figure 4-21). Drift ratio δ_{po} is added to the drift ratios from the 3PKT analysis.

With this additional drift ratio, the 3PKT is applied to walls U1.5 and U2.0. To minimize the modifications of the original approach, the test specimens were modeled as rectangular walls with a section width equal to the width of the web (b=100 mm). The only difference with rectangular walls is that the tension reinforcement A_s includes also the bars in the barbells located outside the web.

Figure 4-33 shows the measured and predicted load-displacement response of the walls. It can be seen that the walls did not exhibit a yield plateau and their lateral resistance decreased quickly in the post-peak regime. It can also be seen that the 3PKT captured well the entire response, including the residual capacity near the end of the tests. The additional drift ratio due to bar pullout accounted for about 8.5% of the drift ratio at peak load which is consistent with the average experimental value of about 11% reported in Mestyanek (1986). According to the predicted components of shear resistance, a major change of behavior occurred at a drift ratio of about 0.6% when the vertical reinforcement in the CLZ is predicted to buckle as observed in the tests (Figure 4-32). In the 3PKT the buckling is taken into account by a sudden drop of the resistance of spring F_{sc} as indicated in the F_{sc}-Δ_{cs} diagram in Figure 4-22d. For walls such as U1.5 and U2.0 without significant confinement of the compression zones, the buckling is estimated to occur when the concrete cover spalls off at a compressive strain in the CLZ Δ_{cx}/l_{b1e}=0.004. Upon buckling, the shear carried in the critical loading zone V_{CLZ} is predicted to decrease and that resisted by the aggregate interlock V_{ci} to increase.

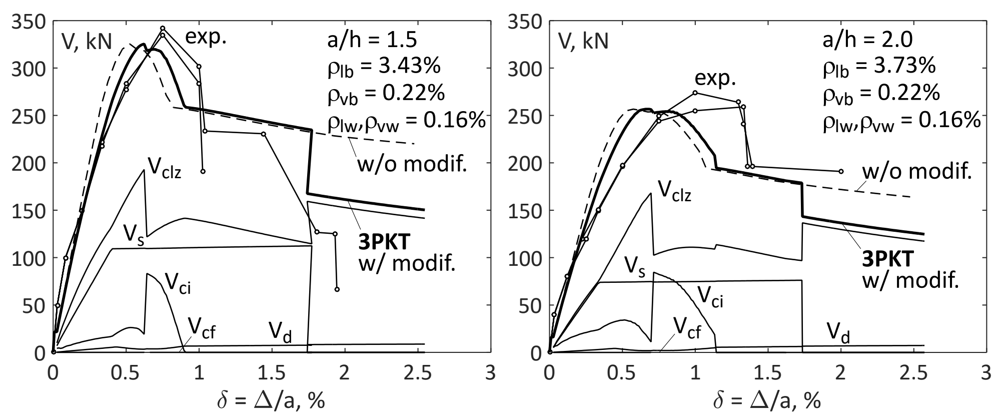

a) Specimen U1.5 b) Specimen U2.0

Figure 4-33. Measured and predicted responses of walls with barbells (tests by Mestyanek, 1986)

Another sudden change of behavior occurred in the post-peak regime of wall U1.5 when the stirrups ruptured at $\delta\approx1.75\%$. Such ruptures are caused by strain localization in the critical crack which is difficult to model accurately. Because the original 3PKT uses the average strain along the stirrups Δ_s/d (Figure 4-22c), it does not capture strain localization. To improve the predictions, it is proposed to estimate the width of the critical crack which results in stirrup rupture and to compare this width to the width calculated at each load step. More precisely, it is necessary to compare the rupture width to the movement in the crack parallel to the stirrups. This movement w_s can be expressed with the crack width w and slip Δ_{ci} which are readily available from the kinematic model (Figure 4-22b):

$$w_s = w \cos\alpha_1 + \Delta_{ci} \sin\alpha_1 \ , \tag{4-37}$$

where α_1 is the angle of the critical crack. If w_s exceeds the rupture value $w_{s,max}$, the shear contribution of the stirrups V_s is brought to zero. The crack movement $w_{s,max}$ is estimated based on an empirical relationship derived from pullout tests of small-diameter bars (Shima, 1987):

$$w_{s,max} = 0.094\left(f_{uv} - f_{yv}\right)\left(\varepsilon_{uv} - \frac{f_{yv}}{E_s}\right)\frac{d_{bv}}{(f_c/20)^{2/3}} \ , \tag{4-38}$$

where f_{uv} is the tensile strength of the stirrups, f_{yv} is the yield strength, and d_{bv} is the stirrup diameter. This relationship does not account for the presence of other cracks in the vicinity of the critical crack, and therefore should be viewed as approximate. It can be seen however from Figure 4-33 that this approach resulted in reasonable predictions of the stirrup ruptures in walls U1.5 and U2.0. It should be noted that when the stirrup rupture and strain penetration were taken into account in the analysis of the walls from the VK and SW series, they had a negligible effect on the predicted displacement capacity as compared to the U series.

In addition to walls U1.5 and U2, it is also of interest to model the behavior of shorter barbell walls. Such walls were tested by Hwang et al. (2004) and Hsiao et al. (2008) and their properties are summarized in Table 4-6 (see walls LW1, WF-12, and WF-15). These walls had a length h of 3500 mm and a/h ratios of either 0.51 or 0.65. The main difference between the walls was the web thickness (from 80 mm for LW1 to 150 mm for WF-15) and the amount of web reinforcement (approx. 0.24% for LW1 and WF-12, and 0.86% for WF-15). As a result of these differences, the walls featured different failure modes: diagonal tension in LW1, web crushing in WF-12, and sliding shear failure in the base section of WF-15.

Figure 4-34 compares the measured and predicted responses of the three squat barbell walls. It can be seen from the thick solid lines that the kinematics-based approach captures reasonably well the complete behavior of walls LW1 and WF-12, while significantly underestimates the displacement capacity of wall WF-15.

As in the squat rectangular walls, the critical loading zones fail first followed by the aggregate interlock mechanism as sliding deformations occur along the critical crack. All three specimens featured barbells with heavy confinement reinforcement (hoops) which was neglected in the modeling of the behavior of the CLZ. This is because the compression in the critical loading zones of squat walls is oriented at flat angles with respect to the confining reinforcement, and therefore it does not effectively engage the hoops.

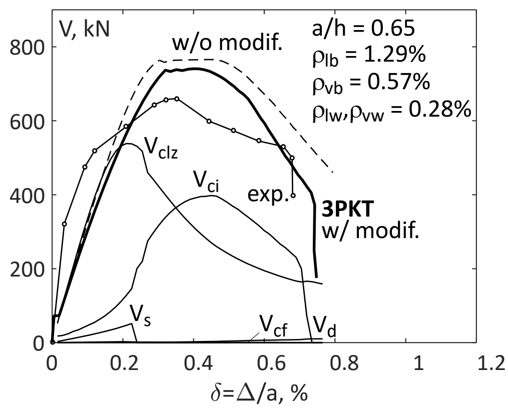

a) Specimen LW1

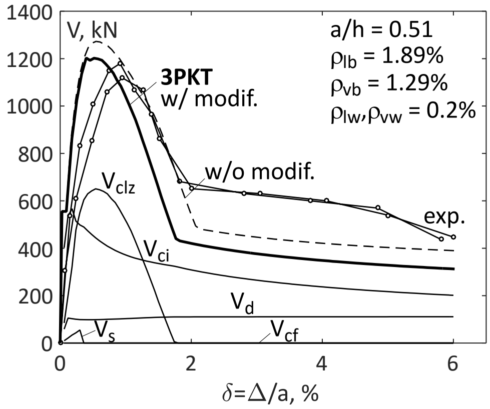

b) Specimen WF-12

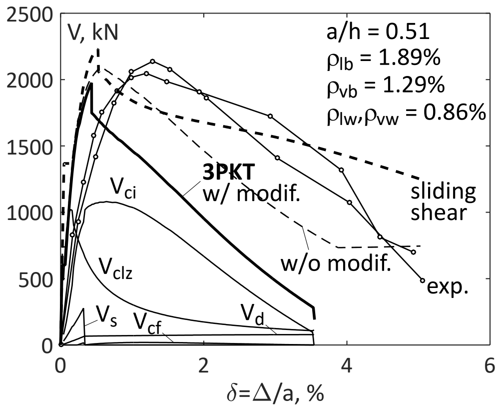

c) Specimen WF-15

Figure 4-34. Measured and predicted responses of squat walls with barbells [tests by Hwang et al., 2004 and Hsiao et al., 2008]

To better understand the discrepancies between the measured and predicted post-peak response of wall WF-15, the model is also applied with a small modification in the input data consistent with the observed sliding shear failure. Instead of a critical crack running along the diagonal of the specimen as in the original analysis, the crack is introduced as nearly horizontal at angle α_1=80°. As evident from the thick dashed line in Figure 4-34c, this results in significant sliding deformations along the crack and a more plastic behavior dominated by the aggregate interlock. This prediction agrees better with the test results and illustrates the need for further enhancement of the kinematics-based approach to automatically capture both diagonal tension and sliding shear failure modes.

The analysis of the barbell walls shown in Figure 4-33 and Figure 4-34 also illustrates the effect of bar pullout and stirrup rupture on the behavior of the test specimens. This effect becomes evident by comparing the predictions of the complete approach (thick continuous lines “w/ modif.”) to those of the original approach (thin dashed lines “w/o modif.”). In the case of walls U1.5 and U2, the behavior is affected mainly by the bar pullout which increases the drift capacity. As the stirrup rupture occurred late in the post-peak response, it had no effect neither on the drift capacity nor on the strength of the member. In contrast, in the case of wall WF-12, the bar pullout effect was negligible while the stirrup rupture was predicted to occur early reducing the peak resistance. These two cases are used as a basis of a parametric analysis to investigate the effect of bar pullout and stirrups rupture on walls with variable aspect ratios and amounts of shear reinforcement.

Figure 4-35a shows how the drift capacity of wall U1.5 would change if the height of the wall subjected to shear a was decreased or increased. The plot also shows the different deformation contributions to the drift capacity as they vary with the a/h ratio. It can be seen that the drift capacity of squat walls is dominated by the degree of freedom $\varDelta_c$, while the contribution of the pullout deformations δ_{po} is negligible. However, as a/h is increased from 0.5 to 3, drift $\delta(\varDelta_c)$ diminishes while the contribution of the bar pullout increases to about 11% of the total drift. In addition to δ_{po}, the contributions of DOFs $\varepsilon_{t,avg}$ and $\varDelta_{cx}$ also increase with the a/h ratio, and this results in an approximately constant drift capacity in the range of a/h from 1 to 3 (δ_u≈0.9%).

Figure 4-35b shows how the shear strength of walls similar to wall WF-12 is influenced by the stirrup ratio and stirrup ruptures. If stirrup ruptures are neglected (thin dashed line), as the stirrup ratio is increased from 0 to 1.5%, the shear strength increases by 40%. In comparison, if stirrup ruptures are considered, the increase of shear strength is smaller at 28%. It should be noted however that in both cases the effect of the shear reinforcement is limited by sliding shear failures that occur at the base of the wall. This upper bound on the shear resistance is indicated with a horizontal line obtained with the kinematics-based approach with a critical crack set at an angle a_1 of 80° as done earlier for specimen SW-15.

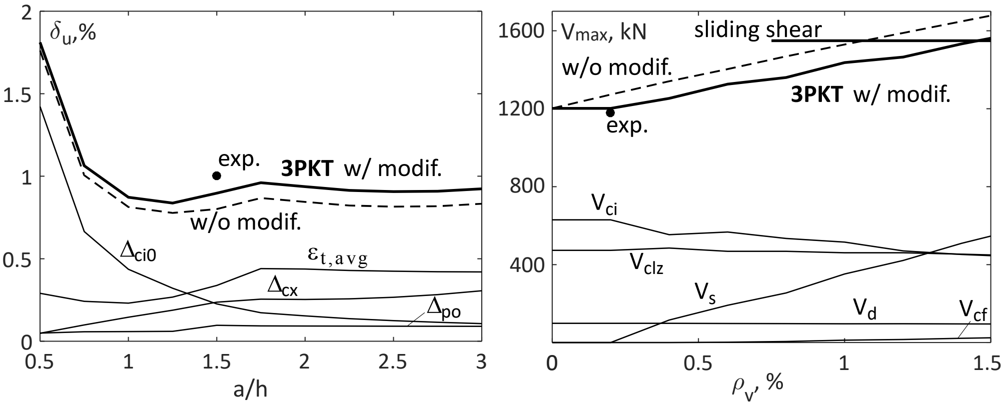

a) Specimen U1.5 b) Specimen WF-12

Figure 4-35. Parametric analyses on the effect of bar pullout and stirrups rupture (tests by Mestyanek, 1986 and Hwang et al, 2004)

Finally, because tests U1.5 and U2.0 included the measurement of crack widths in the web of the walls, it is of interest to compare these measurements to the 3PKT predictions. This comparison is performed in Figure 4-36 where the shear force is plotted as a function of the crack width. The experimental points labeled w_i correspond to crack width measurements at different locations on the web as labeled in Figure 4-32. In test U1.5, the measurements were performed on two diagonal cracks 1 and 3 which were located very close to each other. Even though the walls had a ratio of web reinforcement of only 0.16%, the close cracks indicate adequate crack control which can be explained in part with the presence of stiff barbells. As the 3PKT does not account for the effect of barbells on the number of major cracks n_{cr}, its prediction for wall U1.5 is compared to the sum of w_1 and w_3. In wall U2.0, on the other hand, crack measurements w_1, w_4 and w_6 were performed at remote locations, and for this reason they are not added up. In general, the two plots in Figure 4-36 show that the 3PKT captures well the trend in the experimental data, and the predictions improve near failure when the deformations tend to concentrate in a single crack. In practice, if the width of the cracks is measured onsite, the V-w plots produced by the 3PKT method can be used to evaluate whether the wall is near failure. Therefore, this approach can be useful in the assessment of walls that have sustained damage during strong earthquakes.

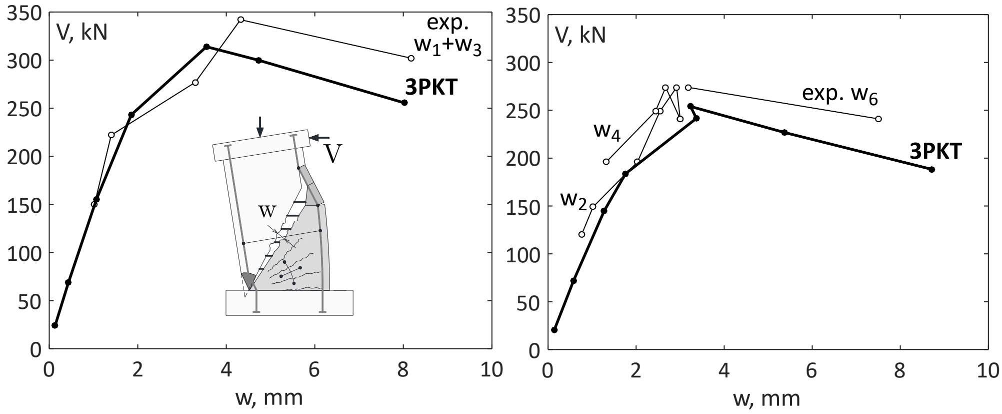

a) Specimen U1.5 b) Specimen U2.0

Figure 4-36. Measured and predicted crack widths in walls with barbells (tests by Mestyanek, 1986)

4.2.5 Modeling of CW test walls

4.2.5.1 Global response predictions

In this section, the CW wall specimens from the experimental study from Chapter 3 are modeled using the 3PKT approach. Figure 4-37 compares the global response predictions for walls CW0 and CW1 generated using the approach to their measured responses. It can be seen from the figure that the global drift versus force relationship of wall CW0 is adequately predicted by the 3PKT. The analysis predicts the failure by rupture of the rebars consistent with the test observations. However, the analysis also indicates that the yielding of the stirrups occurred after the yielding of the longitudinal reinforcement. This means that this wall is not considered as shear-dominated by the approach and is outside of its applicability range defined in §4.2.1.4. The analysis of wall CW1 predicted a shear-dominated response with the rigid block sliding along the critical crack at failure. In the test, wall CW1 failed due to crushing of the compression zone at the critical base section. As a result, the drift capacity of the wall CW1 is largely underestimated by the 3PKT.

The 3PKT could not generate a response prediction for wall CW2. The reason is that the high axial load could not be equilibrated by the force-resisting mechanisms of the rigid block. This wall is also outside of the range of applicability of the 3PKT which is limited to compressive forces smaller than 20% of the compressive capacity of the concrete section (CW2 was loaded with 21% of bhf'_c).

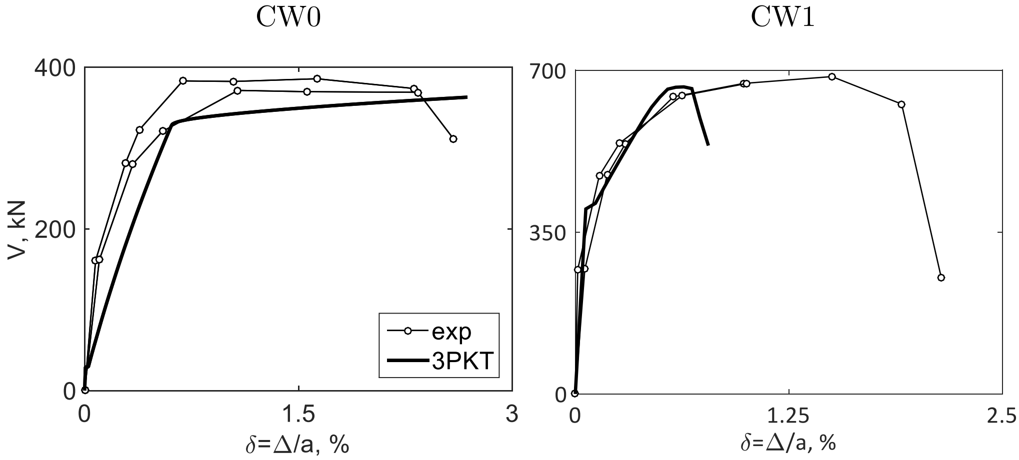

Figure 4-37. Measured versus predicted global response of walls CW0 and CW1

4.2.5.2 Analysis of 3PKT kinematics

As discussed earlier, the 3PKT postulates a simple kinematic description of the deformation patterns in shear-dominated short walls using three DOFs. It is therefore of interest to also test this assumption with the available measurements from the flexure-dominated CW wall tests. To achieve this, the measurements of the horizontal displacement (Δ), rotation (θ), and downward displacement (Δ_{cx}) of the top block of the specimens were used. Displacement Δ_{cx} is defined at the compression edge of the wall and is obtained from the readings of the two vertical displacement transducers vdisp_R and vdisp_L shown in Figure 3-8. Assuming that the top block remains undeformed, a linear interpolation is used between these two readings to obtain Δ_{cx}. The same two transducers are used to determine the rotation of the top block θ, or equivalently θ can be obtained from the inclinometer attached to the block (INCL in Figure 3-8). Finally, the horizontal displacement Δ at the top of the wall is evaluated by averaging the measurements of the horizontal displacement transducers hdisp_1 and hdisp_2 (Figure 3-8). These quantities are equivalent to the DOFs of the assumed rigid block, and are directly related to the DOFs used in the formulation of the approach using the following relationships (Mihaylov et al., 2016):

$$\varepsilon_{t,avg} = (\theta d - \Delta_{cx})/l_t \tag{4-39}$$

$$\Delta_c = \Delta - \theta a \tag{4-40}$$

where l_t is the cracked length along the longitudinal tension reinforcement below the major inclined crack. This length is evaluated as $\mathrm{d}\cot\alpha_1$, where α_1 is the angle of the crack with respect to the vertical axis. Angle α_1 is estimated from the crack diagrams of specimens CW0, CW1, and CW2 at 33°, 45°, and 50°, respectively.

Following this procedure, the contributions of DOFs $\varepsilon_{t,avg}$, Δ_c, and Δ_{cx} to the top displacement of walls CW0, CW1, and CW2 were determined along the envelope of response of the test specimens, see Figure 4-38. The response envelope of wall CW0 was corrected for the measured sliding displacements given that this deformation mode is not considered by the 3PKT kinematics. In all the specimens, $\varepsilon_{t,avg}$ and Δ_{cx} are the highest contributors to the total horizontal displacement. It can also be seen that there is a negative contribution of DOF Δ_c to the top displacement. As the 3PKT formulation imposes that this quantity should be positive (Figure 4-20), this observation points out that there is a physical limitation to the 3PKT kinematics in capturing the deformed shapes of flexure-dominated walls. Figure 4-39 compares the deformation patterns measured on walls CW1 and CW2 at maximum load with the deformation patterns predicted by the 3PKT kinematics. It can be seen that the effect of negative horizontal displacement is reflected in the overlapping of the rigid block and the fan.

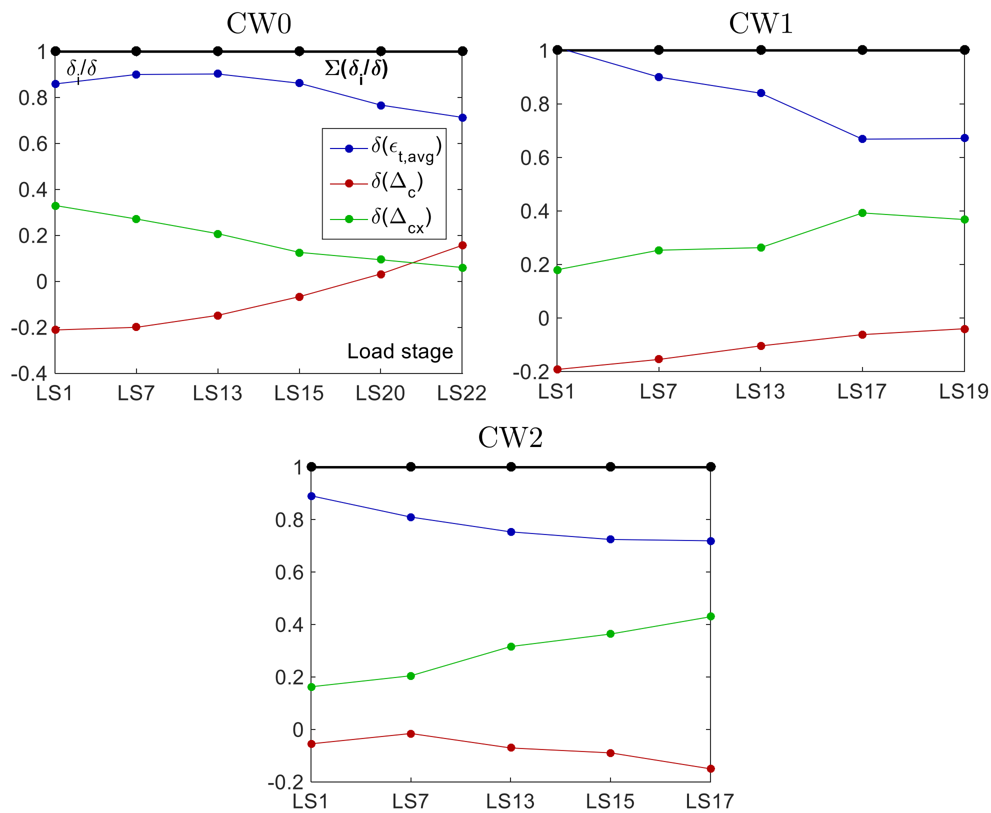

Figure 4-38. Analysis of 3PKT kinematics based on measurements for test walls CW0, CW1, and CW2

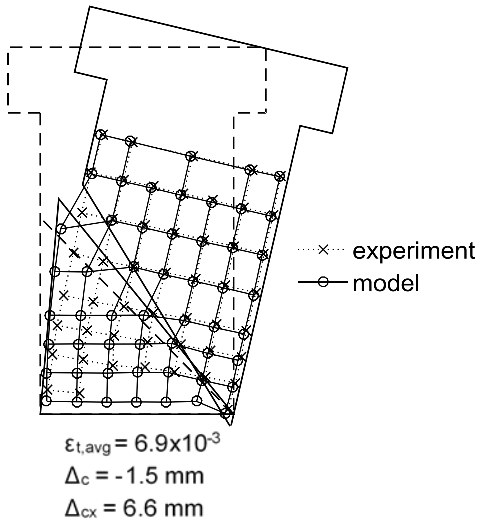

Figure 4-39. Comparisons of measured displacements and displacements predicted by the 3PKT kinematics of walls CW1 (left) and CW2 (right) at V_{max}

4.2.6 Summary and conclusions

In this chapter, the complete behavior of shear-dominated short walls was evaluated based on a three-parameter kinematic theory. The original 3PKT method for rectangular sections was summarized and was extended to account for the effects of barbells, strain penetration in the foundation, cracking above the critical shear cracks, and stirrup ruptures. Aside from these considerations, the validation of the approach was extended to available test data of squat walls.

Table 4-7 summarizes the main experimental and predicted results for the 14 walls studied in §4.2.2-4.2.4. It lists the drift ratio capacity of the walls δ_u, the corresponding lateral displacement Δ_u, and the lateral resistance V_{max}. Based on the 3PKT method, the average experimental-to-predicted ratio for the drift ratio capacity is 1.00 with a coefficient of variation COV=20.3%, excluding the very conservative prediction for specimen WF-15 due to pure sliding shear failure. For the lateral resistance, the corresponding values are 1.04 and 9.6%. These results show that the 3PKT method with only three DOFs can produce adequate predictions of both strength and displacement capacity of shear-dominated walls. For comparison, the ASCE 41-13 (2014) provisions produce reasonably conservative lateral resistances with an average experimental-to-predicted ratio of 1.19 but significantly underestimate the drift ratio capacity with an average ratio of 1.77. It can also be seen that the code provisions result in significantly more scattered predictions than the 3PKT method. This shows that, in cases where the conclusion from a seismic evaluation of an existing structure is sensitive to the drift ratio capacity of the walls, and where a conservative model can result in unnecessary costly retrofit measures, it is worthwhile performing a more detailed analysis based on the 3PKT method. While this method features an iterative solution procedure, it uses a straightforward input without open parameters and requires limited computation time as compared to nonlinear FEMs.

The 3PKT was also used to model test specimens CW0, CW1, and CW2 described in Chapter 3. It was identified that it has limitations in predicting the response of flexure-dominated short walls. The analysis of the kinematic assumptions in the 3PKT showed that the flexural behavior in walls is not adequately captured by this approach. For this reason, the kinematic modeling of the flexure-dominated was revisited in the previous section §4.1.

Table 4-7. Measured and predicted shear strength and drift capacity of test specimens

		Experiment			ASCE 41-13			3PKT			Exp./ ASCE		Exp./ 3PKT	
Wall ID	a/h	Δ_u mm	δ_u %	V_{max} kN	Δ_u mm	δ_u %	V_{max} kN	Δ_u mm	δ_u %	V_{max} kN	δ_u	V_{max}	δ_u	V_{max}
VK1	2.2	62.7	1.90	737	24.8	0.75	642*	73.4	2.23	710	2.53	1.15	0.85	1.03
VK3	2.2	44.6	1.35	887	24.8	0.75	726	55.9	1.69	880	1.80	1.22	0.80	1.00
VK6	3.0	101	2.24	675	28.8	0.64	668*	106.0	2.35	661	3.50	1.01	0.95	1.01
VK7	2.2	74.3	2.25	903	24.8	0.75	763*	64.4	1.95	890	3.00	1.18	1.15	1.01
Wall 2	0.33	11.9	1.80	680	6.6	1.00	489	12.5	1.90	688	1.80	1.39	0.95	0.99
SW5	0.33	13.8	1.37	3190	10.1	1.00	2802	19.7	1.96	2573	1.37	1.14	0.70	1.26
SW6	0.33	22.8	2.27	2460	10.1	1.00	2632	21.8	2.16	2104	2.27	0.93	1.05	1.21
SW9	0.54	19.4	1.18	2880	16.5	1.00	2757	24.4	1.48	2714	1.18	1.04	0.80	1.04
SW10	0.54	17.8	1.08	2380	16.5	1.00	1812	12.2	1.28	2594	1.08	1.31	0.84	0.91
U1.5	1.5	25.0	1.00	342	25.0	1.00	301	21.6	0.87	325	1.00	1.14	1.15	1.05
U2.0	2.0	33.8	1.35	274	25.0	1.00	201	27.2	1.24	256	1.35	1.36	1.24	1.07
LW1	0.65	15.1	0.66	660	22.7	1.00	651	12.8	0.56	743	0.66	1.01	1.17	0.89
WF-12	0.51	26.2	1.46	1180	18	1.00	969	19.2	1.07	1204	1.46	1.70	1.37	0.98
WF-15	0.51	49.5	2.75	2122	18	1.00	2072	12.8	0.71	1962	2.75	1.02	3.88	1.08
										Avg.	1.77**	1.19	1.00**	1.04
										COV, %	47.3**	11.7	20.3**	9.6

*Values based on flexural resistance; the rest correspond to shear resistance

**Without considering WF-15 that exhibited pure shear sliding

5 Finite element modeling of walls

5.1 Overview

Finite element analysis of the behavior of short wall represents the most complex method considered within the framework of this thesis. The software used for performing the analyses is VecTor2 (version date 5/3/2018), developed by VecTor Analysis Group (2018) at the University of Toronto. VecTor2 is a 2D finite element code for static and dynamic nonlinear analysis specialized in reinforced concrete. The basis of the calculations in VecTor2 are two well-known theories for the behavior of reinforced concrete: Modified Compression Field Theory (MCFT) (Vecchio & Collins, 1986) and Disturbed Stress Field Model (DSFM) (Vecchio, 2000).

The objective of this chapter is to investigate the suitability of the finite element procedure implemented in VecTor2 for the evaluation of the behavior of short walls under horizontal actions. A mesh sensitivity study and the effect of key modeling assumptions of the behavior of reinforced concrete are first analyzed on selected test specimens. The results of the analyses are discussed and compared to experimental observations in terms of global response, crack patterns, and failure modes. These analyses are considered as a benchmark as they give a good overview of how the finite element model performs when applied to short walls. Additionally, a database of 59 test specimens with diverse properties is modeled with the numerical approach. The response predictions are compared against the experimental observations in terms of the global force-displacement response.

5.2 General modeling assumptions

VecTor2 has many constitutive models representing different phenomena related to the behavior of reinforced concrete. The choice of input options could produce countless possibilities, thus the effect of each of many input options or their different combinations was not investigated. Instead, the default input options were chosen with a few exceptions discussed later on.

The calculations in VecTor2 are based on the two rotating smeared crack models simulating the behavior of reinforced concrete: Modified Compression Field Theory (MCFT) (Vecchio & Collins, 1986) and Disturbed Stress Field Model (DSFM) (Vecchio, 2000). The MCFT uses the constitutive relationships derived from a series of experimental campaigns performed on reinforced concrete panel (membrane) elements under combined shear and axial stresses. Apart from general equilibrium calculations on a membrane element, this theory also considers local stress calculations across the cracks using an aggregate interlock model. The DSFM represents an extension of the MCFT, and it incorporates the calculation of slip displacements in the cracks. As a consequence, principal stress and strain directions are no longer aligned in the DSFM. The local stress conditions and slip deformations on the cracks are evaluated using an aggregate interlock model proposed by Walraven (1981).

The stress-strain behavior of concrete in compression, including the pre-peak and post-peak response, is modeled based on a relationship for normal strength concrete proposed by Popovics (1973). While this is not the default model, it is selected because of its accurate description of test data as well as for consistency with the macro-kinematic modeling in Chapter 4. The presence of increased concrete strength due to confinement is taken into account according to the Kupfer/Richart model (Vecchio, 1992). The effects of compression softening in the concrete are considered using the Vecchio 1992-A model (Wong & Vecchio, 2002). The cracking strength of the concrete under tension is evaluated with the Mohr-Columb criterion with an angle of friction of 37° (Wong & Vecchio, 2002). The tension stiffening effect, which represents the tensile stresses in the concrete after cracking, is evaluated using the Modified Bentz model (Vecchio, 2000) The reinforcement is modeled as a smeared material, and therefore the simulations do not explicitly account for phenomena such as buckling of reinforcement, dowel action, or bond effects. This approach, as opposed to using discrete truss elements for the reinforcement, was selected to simplify the modeling.

5.3 Modeling of walls

Figure 5-1 shows typical finite element models of wall tests (CW test series and wall 82 by Hirosawa, 1975). The walls were discretized using four-node quadrilateral plane stress elements with two translational degrees of freedom per node. As the accuracy of these elements decreases with deviation from a square shape (Wong & Vecchio, 2002), the aspect ratio in all the models is kept as close to unity as possible. To simplify the modeling, the wall models were assumed to be clamped at the level of the base section, and the nodes at the base were restrained from any movement. Therefore, the models did not account for strain penetration in the foundation blocks.

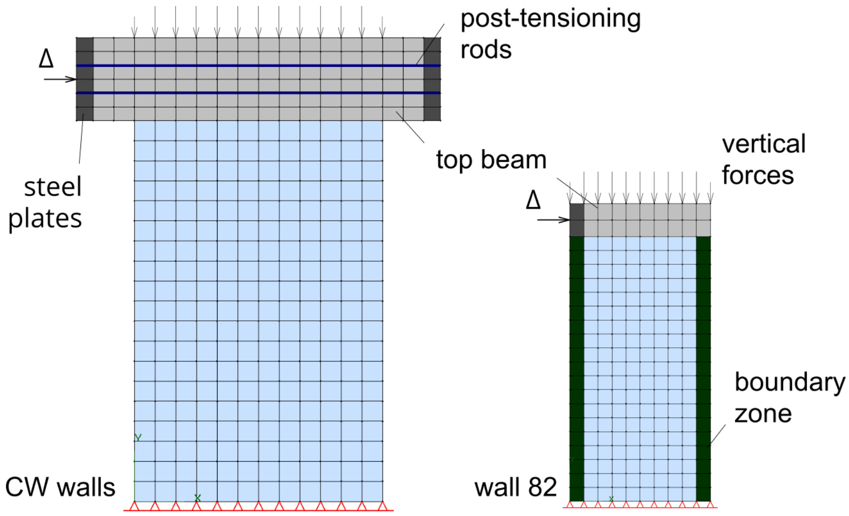

Figure 5-1. FEM models of CW walls and wall 82 (by Hirosawa, 1975)

As mentioned earlier, the reinforcement in the models was introduced as smeared. The different colors in the wall models in Figure 5-1 represent the concrete with different amounts of reinforcement. In cases of concentrated reinforcement in boundary elements such as in wall 82 in the figure (Hirosawa, 1985), the reinforcement ratio was calculated separately for the boundary zones and the web of the specimen. Confining hoops and ties in the boundary elements were included as both horizontal in-plane and out-of-plane reinforcement. In this way, tri-dimensional confinement was taken into account.

The axial compressive forces were uniformly distributed over the nodes of the top face of the models. The horizontal loading was applied as a monotonically-increasing displacement assigned to the node belonging to the axis of load application. As opposed to modeling with applying forces, the displacement-controlled analysis allows capturing the post-peak response of the wall. In the case of the CW walls, the steel plates were stiff enough to prevent localized deformations at the node of the load application. If steel plates were not present, a column of elements was made essentially rigid by increasing their modulus of elasticity and strength (wall 82). Monotonic analyses were preferred to cyclic analyses in order to allow for a large number of comparisons with measured envelope responses.

5.4 Benchmark analyses

The test specimens modeled in this section include wall VK3 (Bimschas, 2010), wall 82 (Hirosawa, 1975), and the CW test specimens. These walls are used as benchmark cases because they exhibited different behavior and give a good overview of the outcome of nonlinear finite element simulations of short walls. The benchmark analyses investigate the effects of the mesh size and the basic formulations of the behavior of concrete elements, i.e. MCFT and DSFM, on the response predictions. The results of the analyses were compared to the experimental observations in terms of force-displacement response, cracking patterns, and failure modes.

5.4.1 Wall VK3

The first benchmark finite element analysis was performed on wall VK3 by Bimschas (2010). The wall had a rectangular section with a depth of 1500 mm and an aspect ratio of 2.2. It was designed to represent an existing bridge pier with detailing deficiencies, featuring a very low amount of transverse reinforcement (0.08%) and a longitudinal reinforcement ratio of 0.82%. The wall was subjected to a constant axial force of 1315 kN, which corresponds to 7.4% of the compressive capacity of the concrete section. The lateral load was introduced as imposed cyclic displacements at the top of the wall reproducing seismic loading.

Specimen VK3 was modeled using three different meshes corresponding to 15, 20, and 30 elements across the section depth. For each mesh size, the predictions were generated using both the MCFT and DSFM formulations. Figure 5-2 compares the predicted global force-displacement response against the positive and negative envelopes of the experimental response. The top two plots show the mesh sensitivity obtained with the MCFT and DSFM formulations, while the bottom three plots compare the two formulations for each of the three mesh sizes.

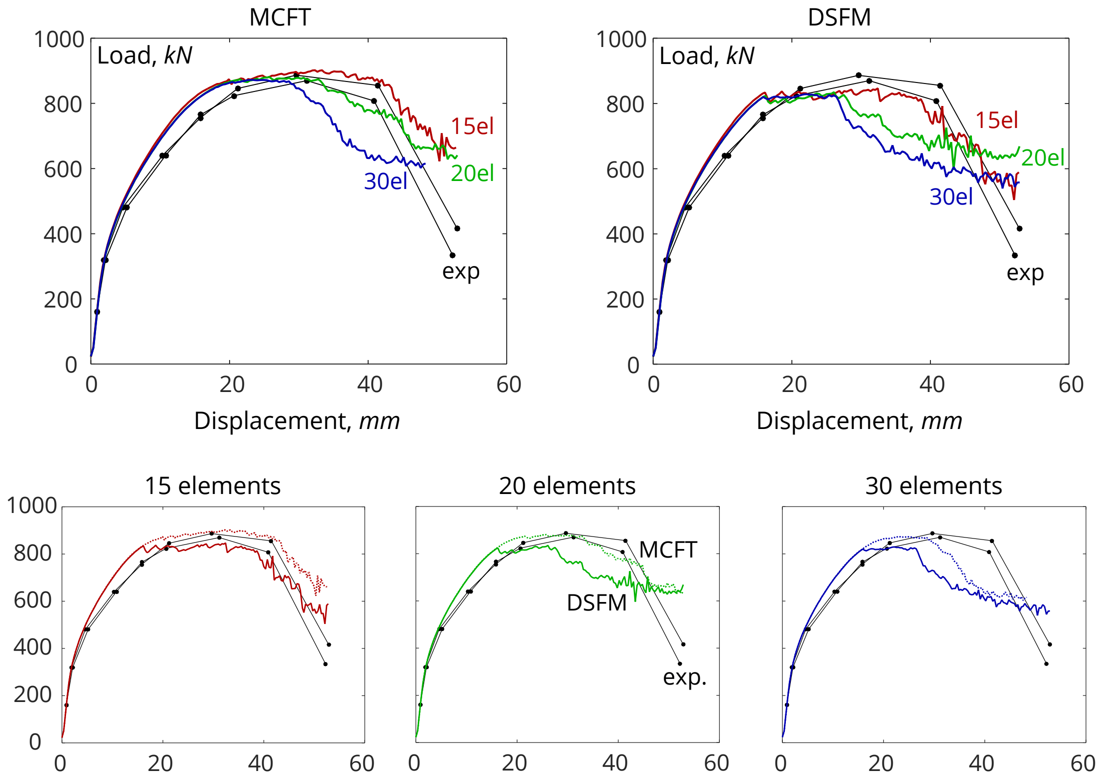

Figure 5-2. Finite element predictions of wall VK3

From Figure 5-2, it can be observed that the mesh sensitivity is pronounced in the post-peak range of the response. The same trend is observed for both the DSFM and MCFT formulations, where a smaller mesh size causes a drop in lateral resistance at smaller displacements. This is a consequence of the localization of deformations in a line of critical elements, meaning that the deformations in the smaller elements cause smaller global top displacements. The predicted lateral resistance is also shown to be decreasing with a smaller mesh size. However, this effect is relatively minor (a maximum difference of about 3%). The average experimental-to-predicted ratio for the peak resistance obtained with the MCFT and DSFM for all three meshes is 1.00 and 1.06, respectively.

From the comparisons between the DSFM and MCFT predictions for each mesh size, it can be seen that there is a clear separation point where the two curves diverge. The point of separation occurs with the yielding in the stirrups in the case of DSFM, which is when the slip deformations start to be significant. Also, upon yielding of the transverse reinforcement, it can be seen that there is an instability in the predictions reflected as “wiggling” of the response curve. The reason for this is that at stages of large damage the numerical convergence criteria are not met in all finite elements.

The failure mode of VK3 can be defined as a ductile shear failure. The wall exhibited significant yielding of the flexural reinforcement but eventually failed in shear along wide diagonal cracks. A photograph at the end of the test of VK3 is shown in Figure 5-3. The figure also shows the cracking and deformation patterns at the maximum load predicted by the MCFT and DSFM formulations using 20 elements across the section. In the case of the DSFM prediction, there are wider cracks in the regions of shear cracking compared to the MCFT, which occurs due to slip deformations on the shear cracks. In both cases, the analysis captured well the crack patterns and the failure mode observed in the experiment.

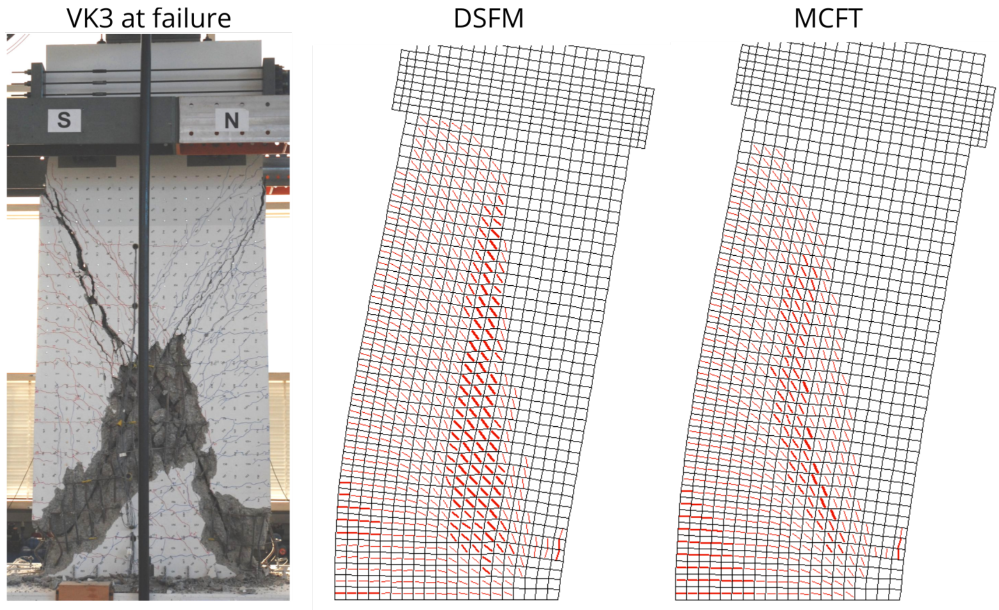

Figure 5-3. Comparison of experimental and predicted cracking patterns of wall VK3 (Bimschas, 2010) at peak load

5.4.2 Wall 82 results

Specimen 82 (Hirosawa, 1975) had an 850 mm by 160 mm rectangular section and an aspect ratio of 2.0. The wall featured heavily reinforced boundaries with a local longitudinal reinforcement ratio of 9.9%, confined with closely spaced stirrups with a volumetric ratio of about 2.5%. The longitudinal and transverse web reinforcement was uniformly distributed with a ratio of 0.53% and 1.20%, respectively. The wall was subjected to a constant axial force of 272 kN, which corresponds to 9.4% of the compressive capacity of the concrete section. The lateral load on this wall was applied in a quasi-static cyclic manner.

As before, the effect of mesh size on the response predictions was investigated using three different meshes, corresponding to 10, 20, and 30 elements across the section depth. A slightly different number of elements was used than in the case of VK3 because of the geometrical constraints imposed by the presence of boundary elements. The global response predictions obtained from the finite element analyses of wall 82 for the three mesh sizes and each formulation (MCFT and DSFM) are shown in Figure 5-4.

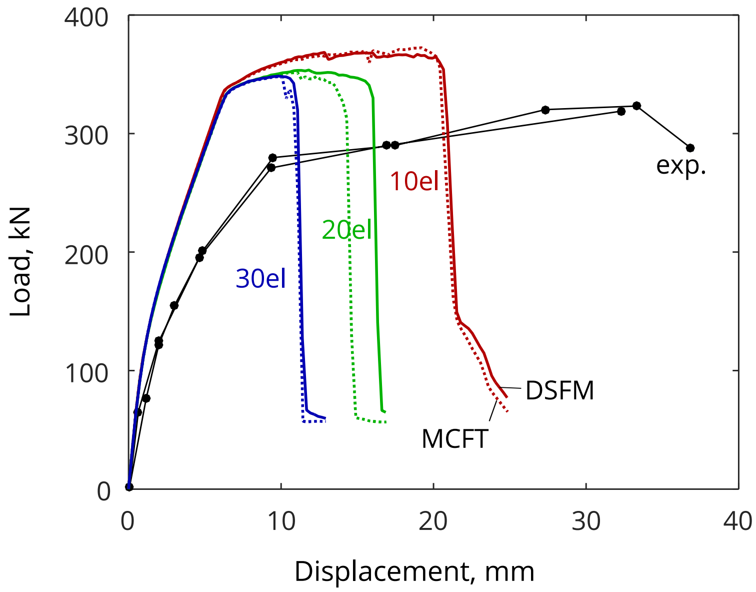

Figure 5-4. Finite elements predictions of wall 82

Figure 5-4 shows a clear mesh sensitivity both in terms of peak resistance and displacement capacity. The models significantly overestimate the stiffness of the wall and overpredict its strength by about 9% on average. The difference between the predicted and measured strength can be explained with the degradation of concrete strength or bar buckling in the compression zone due to the effects of cyclic loading in the test. The discrepancy in the initial stiffness indicates that there might have been deformations due to strain penetration or deformations in the test setup in the measured response which are not considered by the analysis. The ratio of experimental to predicted shear force produced by the MCFT formulation with meshes of 10, 20, and 30 elements is 0.87, 0.92, and 0.93, respectively. These values are almost identical to the case of the DSFM formulation. The displacement response predictions are affected to a greater extent by the mesh size effect. From the mesh of 10 to 30 elements, the predictions of the failure drift decrease by about 50%. Overall, the predicted displacement capacity of the wall is greatly underestimated compared to the experimental values. From Figure 5-4, it can be seen that the difference between the predictions of the MCFT and DSFM formulations for the same mesh size is not significant.

The analyses did not predict yielding of the transverse reinforcement, meaning that there were no significant slip deformations in the cracks.

The sudden drop in the lateral load resistance in the response predictions was caused by a shear-compression failure of the finite elements in the base section. The failure caused the localization of deformations in the compressed elements, which further spread to the adjacent elements in the bottom row. This caused the wall to “slide” in the base within the descending branch of the post-peak response as shown in Figure 5-5. The plots depict the predicted cracking diagrams from the model with 20 elements and DSFM formulation, as well as the experimentally observed cracking and damage. The crack patterns and the failure mode of the specimen were well captured by the analysis. Since there were no significant slip deformations in the cracks, the cracking pattern predicted by the MCFT formulation is nearly identical.

Similar to the observation in the case of wall VK3, the localization of the deformations in critical elements introduce the mesh size effect in the response predictions. It was also observed that, when approaching the peak resistance and in the post-peak range of the response, the convergence criteria were not met in all the elements. Even if the numerical instability was not as apparent in the global response as in the case of wall VK3, it was detected in the response of specific elements.

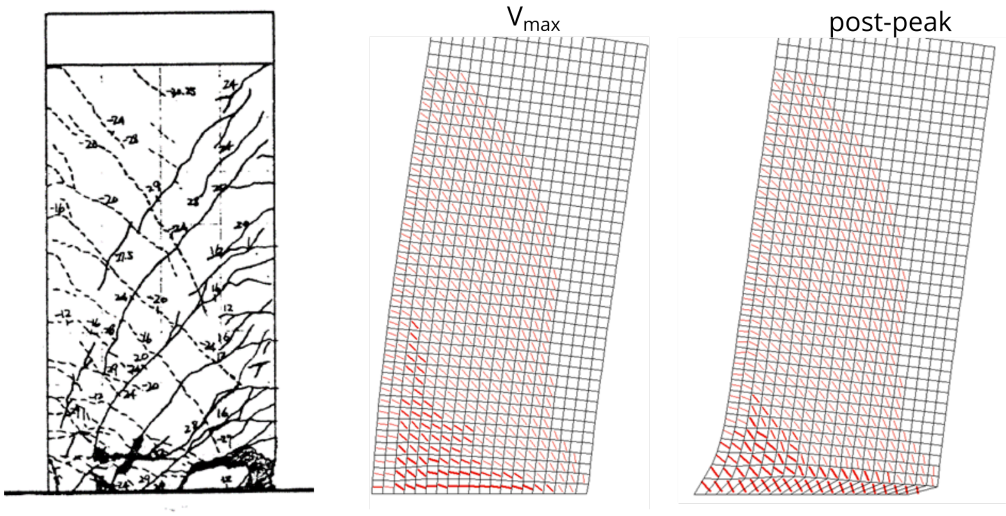

Figure 5-5. Experimental vs predicted cracking and failure of wall 82 (test by Hirosawa, 1975)

5.4.3 CW series

As discussed earlier, walls CW0, CW1, and CW2 had uniformly distributed reinforcement with a longitudinal ratio of 0.79% in wall CW0 and 0.72% in walls CW1 and CW2. Equally spaced stirrups resulted in a transverse reinforcement ratio of 0.15%. Walls CW0, CW1, and CW2 were subjected to axial loads corresponding to 0, 10%, and 21% of compression strength of the concrete section bhf'_c, respectively.

The comparisons of the predicted and measured envelopes for all three walls are shown in Figure 5-6. The walls were modeled with a mesh of 20 elements per section using the MCFT and DSFM formulations. Based on the results of the analyses of a dataset of walls discussed later in the text, this was found to be the number of elements per section that produces the most accurate strength predictions. As it was shown in section 3.4.2, all the specimens had a significant contribution of the opening of the base crack to the top lateral displacement, which includes the contribution from the strain penetration in the foundation block. Since the finite element models do not consider the strain penetration deformations and assume a fixed boundary condition at the level of the base crack, the predicted global responses are compared to the experimental envelopes corrected for the estimated strain penetration displacements. In the corrected envelopes, it is assumed that one-half of the contribution of base crack opening to the top lateral displacement is due to strain penetration from the foundation block.

For wall CW0, the finite element models based on the MCFT and DSFM produce similar predictions of the lateral resistance, overestimating the measured resistance by about 10%. The displacement capacity is significantly overestimated when compared to the experimental envelopes. In the case of walls CW1 and CW2, the analyses accurately predicted the lateral resistance. In terms of displacement capacity, the DSFM formulation predictions are in good agreement with the corrected experimental envelopes, while the MCFT formulation significantly overestimates the displacements at failure. Similar to the observations in the previous benchmark analyses, there is a pronounced wiggling in the global response in the post-peak regime due to convergence issues. The observed numerical instability in the response limits the confidence in predictions of the displacement capacity.

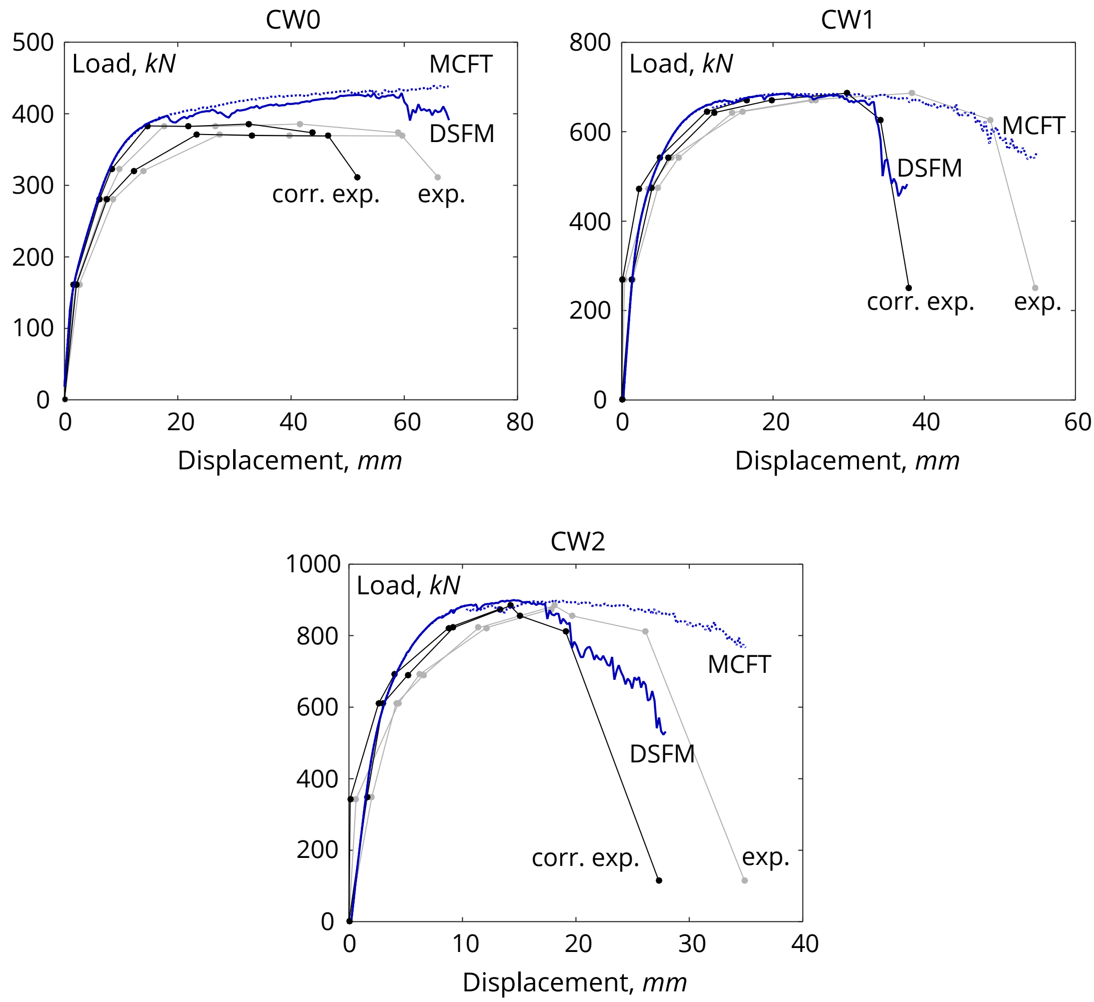

Figure 5-6. Finite element predictions of walls CW0, CW1, and CW2

The predicted crack and deformation patterns obtained from the DSFM simulations of the CW walls are compared to the experimental patterns in Figure 5-7. It can be seen that the extent of cracking is very well predicted by the models. For all three walls, the DSFM formulation predicted a resistance degradation in the elements along the shear cracks which led to a loss in lateral resistance. Even though the DSFM predicted better the global response, the failure modes predicted by the MCFT formulation are in a better agreement with the test observations. According to the MCFT analyses, all the walls failed by crushing of concrete at the compression “toe” of the walls, which was the observed failure mode in tests CW1 and CW2. In the case of CW0, the analysis did not predict the rupture in the longitudinal rebars observed in the test. Even though the MCFT results are not shown in Figure 5-7, the extent of cracking was equally well predicted by the MCFT formulation as the DSFM formulation.

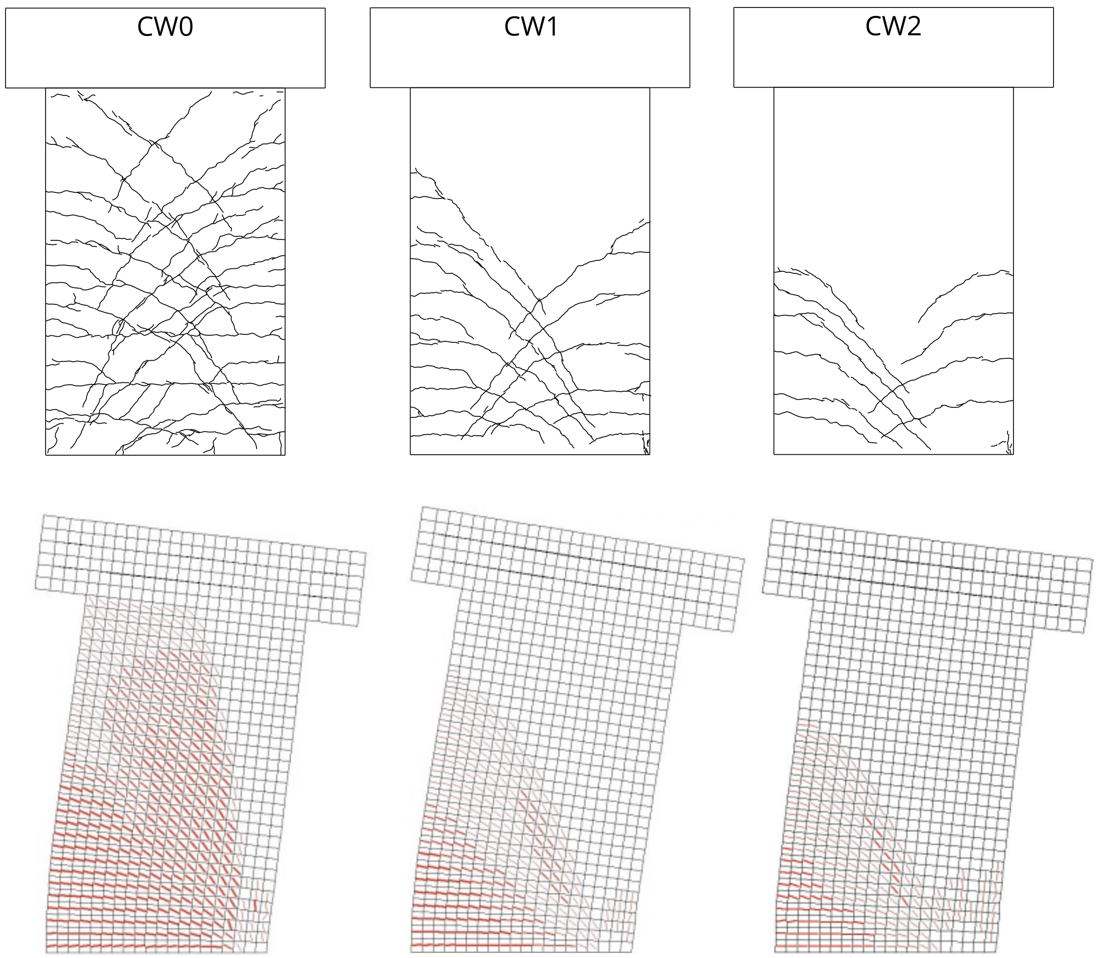

Figure 5-7. Comparison of experimental and predicted cracking diagrams at maximum resistance of CW tests

5.5 Analysis of database of test specimens

This section investigates the suitability of the finite element method implemented in VecTor2 for assessing the behavior of walls with diverse properties. To achieve this objective, a database of 59 test specimens from 10 different test series was modeled and analyzed using the nonlinear finite element method.

Table 5-1 summarizes the properties of the FE models of the database of wall tests. The database includes all the specimens from the test series used for the validation of the original 3PKT approach (Mihaylov et al., 2016). In addition, the CW test specimens are added to this database. The depth of section h of the walls varies from 0.65 m to 3 m, and their aspect ratio a/h from 0.3 to 3. In terms of reinforcement, the specimens feature longitudinal reinforcement ratios ρ_l from 0.18% to 2.5% and transverse reinforcement ratios ρ_v from 0% to 1.5%. The longitudinal reinforcements ratios ρ_{lb} and volumetric ratios of stirrups ρ_s in walls with concentrated longitudinal reinforcement and confining reinforcement in the boundary zones vary from 1.3% to 9.9% and from 0.64% to 4.91%, respectively. The concrete strengths f'_c of walls range from 14 MPa to 56 MPa, and the axial compression load ratios N/bhf'_c range from 0% and 21.4%. All walls were tested under reversed cyclic lateral loads, except for the walls by Maier & Thürlimann (1985) and Lefas et al. (1990) which were loaded monotonically.

Based on analyses of a large number of wall specimens, it was observed that a mesh size of 20 elements across the section produces the most adequate predictions in terms of lateral resistance, and therefore this size was used for the modeling of all walls from the database. In terms of material modeling formulations, the benchmark analyses did not show clearly whether MCFT or DSFM performed better. However, the DSFM formulation was selected for the database analyses as it accounts for sliding deformations in the cracks.

Figure 5-8 compares the global force-displacement predictions from the nonlinear finite element analyses to the experimental curves of all 59 specimens in the database. The values of the maximum force resistance predicted by the analyses are summarized and are compared to the measured values in Table 5-1. The force resistance experimental-to-predicted ratios V_{exp}/V_{pred} are plotted in Figure 5-9 as a function of the aspect ratio of the walls a/h.

It can be concluded from Table 5-1 that the nonlinear element analyses have accurately predicted the resistance of the walls, producing a slightly unconservative average V_{exp}/V_{pred} ratio of 0.98 and a coefficient of variation of 9.1%. As evident from Figure 5-9, the VecTor2 predictions tend to be more unconservative for squat walls with aspect ratios smaller than approximately 1.0. From the comparison of the global responses in Figure 5-8, it can also be observed that the maximum force resistance predicted by the analysis tends to occur at a smaller drift than measured in the tests. This indicates that the modeling approach exhibits discrepancies in the predictions on the global and local level of the response with respect to the experimental observations. In terms of strength and initial stiffness predictions, the discrepancies can be attributed in part to the modeled loading and support conditions, respectively. While the simulations were performed under monotonic loading, all the tests but those by Meier and Thurlimann (1985) and Lefas et al. (1990) featured reversed cyclic loading. Furthermore, while the model neglects the strain penetration in the foundation, these deformations were present in all the test specimens, in addition to potential rigid-body movements of the foundation in some of the tests.

Regarding the predictions of the displacement capacity, essential from the point of view of the assessment of structures subjected to seismic actions, it is observed that the VecTor2 analyses produce inadequate estimates of the global failure drifts compared to the experimental data. Most of the comparisons in Figure 5-8 show that the observed global displacement capacity is greatly underestimated by the model. This is mainly a consequence of the localization of deformations in the critical elements, generally located in the compression zone near the base section. As shown in the examples of the benchmark analyses, the effect of localization also introduces a significant mesh size dependency in the response predictions. In addition, there is the presence of convergence problems with increasing inelastic deformations, which is usually seen as “wiggling” in the global response. Even if the later cannot be always observed in the global response, it is present at a local level, i.e. in the response of specific elements. This convergence issue renders the determination of the failure drifts very subjective. Therefore, from the standpoint of the practical assessment of wall piers, failure drifts obtained in this manner cannot be considered as reliable. Similar observations related to the discussed issues of VecTor2 response predictions were reported in the study by Almeida et al. (2014).

Table 5-1. Summary of tests modeled inVecTor2

Test Series	Wall ID	h m	a/h	ρ_{be} %	ρ_s %	ρ_l %	ρ_v %	f'c MPa	$\frac{N}{bhf'_c}$ %	V_{pred} kN	$\frac{V_{exp}}{V_{pred}}$
CW series	CW0	1.5	1.7	/	/	0.79	0.15	25.1	0	429	0.90
	CW1	1.5	1.7	/	/	0.72	0.15	38.8	10	686	1.00
	CW2	1.5	1.7	/	/	0.72	0.15	36.1	21	900	0.98
Bimschas (2010)	VK1	1.5	2.2	/	/	0.82	0.08	35	7.5	712	1.03
	VK3	1.5	2.2	/	/	1.23	0.08	34	7.7	835	1.06
Hannewald et al. (2013)	VK6	1.5	3	/	/	1.23	0.08	44.4	5.9	674	1.00
	VK7	1.5	2.2	/	/	1.23	0.22	30	8.7	910	0.99
Tran et al. (2002)	TW1	1.22	2	3.7	2.5	0.18	0.27	48	2.0	376	1.04
	TW2	1.22	2	8.3	2.4	0.38	0.62	48	7.3	277	1.24
	TW3	1.22	1.5	3.7	2.5	0.21	0.33	48	7.7	644	1.02
	TW4	1.22	1.5	7.0	2.4	0.46	0.74	56	6.4	455	1.05
	TW5	1.22	1.5	7.0	2.4	0.38	0.62	56	1.6	759	0.97
Lefas et al. (1990)	SW11	0.75	1.1	3.1	1.2	2.4	1.1	41.8	0.0	631	0.95
	SW12	0.75	1.1	3.1	1.2	2.4	1.1	42.9	10.2	912	0.95
	SW13	0.75	1.1	3.1	1.2	2.4	1.1	32.5	20.8	763	0.87
	SW14	0.75	1.1	3.1	1.2	2.4	1.1	33.7	0.0	257	0.99
	SW15	0.75	1.1	3.1	1.2	2.4	1.1	34.6	10.2	323	1.02
	SW16	0.75	1.1	3.1	1.2	2.4	1.1	41.4	21.2	310	1.07
	SW17	0.75	1.1	3.1	1.2	2.4	0.37	38.6	0.0	243	1.09
	SW21	0.65	2.1	3.3	0.9	2.5	0.8	34.2	0.0	288	1.09
	SW22	0.65	2.1	3.3	0.9	2.5	0.8	40.5	10.6	356	1.00
	SW23	0.65	2.1	3.3	0.9	2.5	0.8	38.2	21.2	245	1.02
	SW24	0.65	2.1	3.3	0.9	2.5	0.8	38.6	0.0	117	1.10
	SW25	0.65	2.1	3.3	0.9	2.5	0.8	36.0	21.4	143	1.06
	SW26	0.65	2.1	3.3	0.9	2.5	0.8	24.1	0.0	157	1.15
Hirosawa (1985)	72	1.7	1.0	5.7	0.64	0.53	0.30	17.6	11.4	120	1.01
	73	1.7	1.0	5.7	0.64	0.53	0.30	21.2	9.4	152	0.98
	74	1.7	1.0	5.7	1.28	0.53	0.60	21.2	9.4	108	1.15
	75	1.7	1.0	5.7	1.28	0.53	0.60	14	14.3	841	0.98
	76	1.7	1.0	5.7	2.55	0.53	1.20	15	13.3	884	0.96
	77	1.7	1.0	5.7	2.55	0.53	1.20	18.7	10.7	975	0.85
	78	1.7	1.0	2.5	1.28	0.53	0.60	21.2	9.4	895	0.92
	79	1.7	1.0	2.5	1.28	0.53	0.60	14	14.3	930	0.88

Table 5-1. Summary of tests modeled inVecTor2 (continued)

Test Series	Wall ID	h m	a/h	ρ_{be} %	ρ_s %	ρ_l %	ρ_v %	f'c MPa	$\frac{N}{bhf'_c}$ %	V_{pred} kN	$\frac{V_{exp}}{V_{pred}}$
Hirosawa (1985)	80	1.7	1.0	2.5	2.55	0.53	1.20	15	13.3	979	0.95
	81	1.7	1.0	2.5	2.55	0.53	1.20	18.7	10.7	710	0.98
	82	1.7	1.0	9.9	2.46	0.53	0.60	21.2	9.4	664	0.96
	83	1.7	1.0	9.9	2.46	0.53	0.60	18.2	11.0	695	1.03
	84	1.7	1.0	8.4	4.91	0.53	1.20	18.2	11.0	717	1.08
	85	1.7	1.0	8.4	4.91	0.53	1.20	21.2	9.4	354	0.91
Luna et al. (2015)	SW1	3	0.9	/	/	0.67	0.67	24.8	0	349	0.97
	SW2	3	0.5	/	/	1.0	1.0	48.3	0	319	1.01
	SW3	3	0.5	/	/	0.67	0.67	53.8	0	323	1.04
	SW4	3	0.5	/	/	0.33	0.33	29.0	0	1110	1.00
	SW5	3	0.3	/	/	1.0	1.0	29.6	0	2598	0.97
	SW6	3	0.3	/	/	0.67	0.67	26.2	0	1799	1.16
	SW7	3	0.3	/	/	0.33	0.33	26.2	0	1064	0.95
	SW8	3	0.5	/	/	1.5	1.5	24.1	0	3842	0.83
	SW9	3	0.5	/	/	1.5	0.67	29.6	0	2833	0.87
	SW10	3	0.5	/	/	1.5	0.33	31.7	0	1708	0.82
	SW11	3	0.5	1.5	1.5	0.67	0.67	34.5	0	2863	0.97
	SW12	3	0.5	2	2	0.33	0.33	34.5	0	2887	1.00
Wiradinata (1985)	Wall1	2	0.6	1.4	1.1	0.56	0.22	22	0	2796	0.85
	Wall2	2	0.3	1.4	1.1	0.56	0.22	22	0	2334	0.81
Oh et al. (2002)	WR0	1.5	2.0	1.3	/	0.32	0.28	32.9	10.0	2022	0.92
	WR10	1.5	2.0	1.3	2.4	0.32	0.28	36.2	10.0	572	1.01
	WR20	1.5	2.0	1.3	1.2	0.32	0.28	34.2	10.0	830	0.83
Maier and Thurlimann (1985)	S4	1.2	1.1	/	/	1.02	1.01	32.9	6.7	458	0.93
	S9	1.2	1.1	/	/	1.02	/	29.2	7.5	503	0.84
	S10	1.2	1.1	/	/	2.0	1.01	31	7.2	489	0.91
										Avg.	0.98
										COV, %	9.1

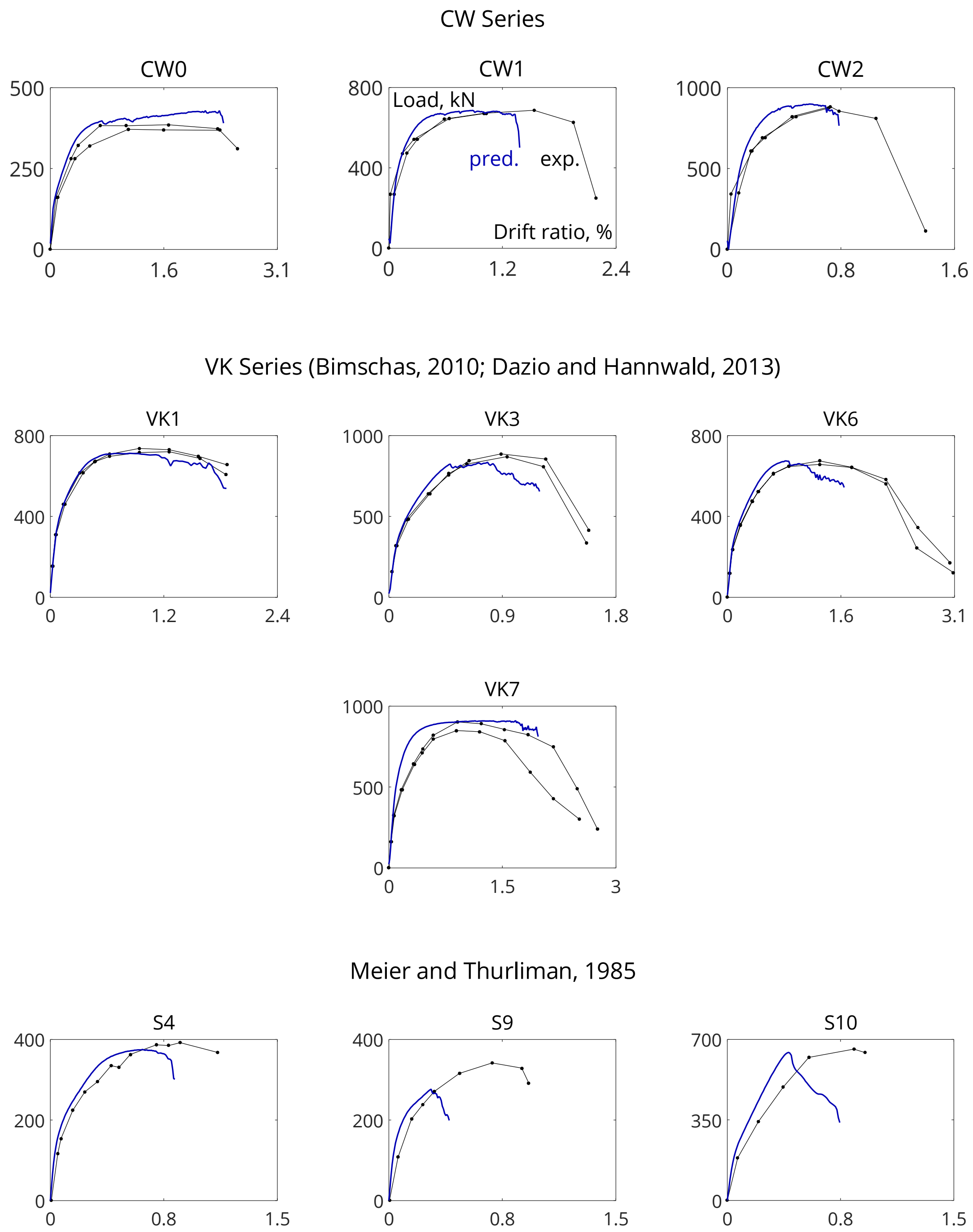

Figure 5-8. VecTor2 predictions of lateral resistance versus drift ratios of a database of 59 test specimens

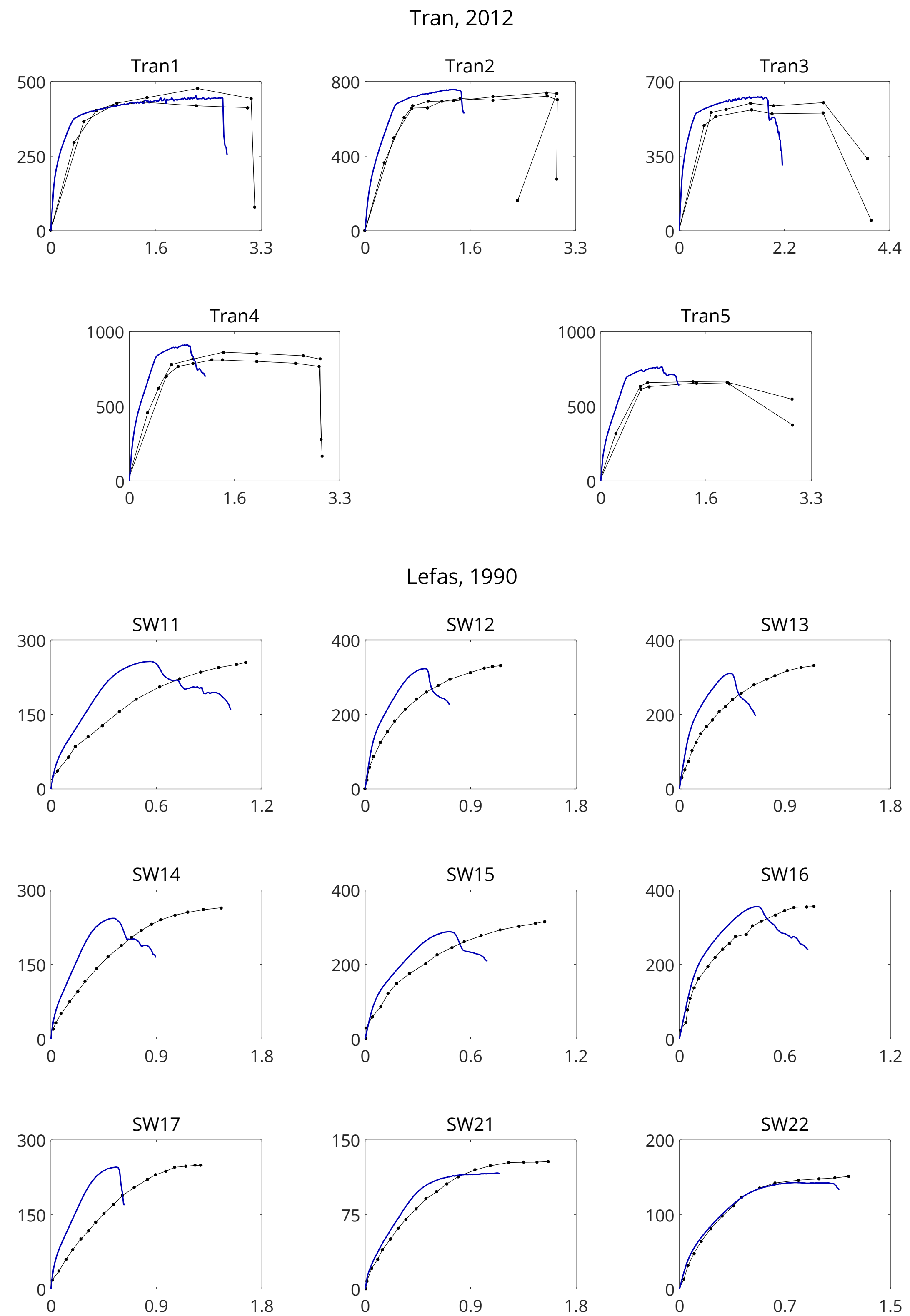

Figure 5-8. VecTor2 predictions of lateral resistance versus drift ratios of a database of 59 test specimens (continued)

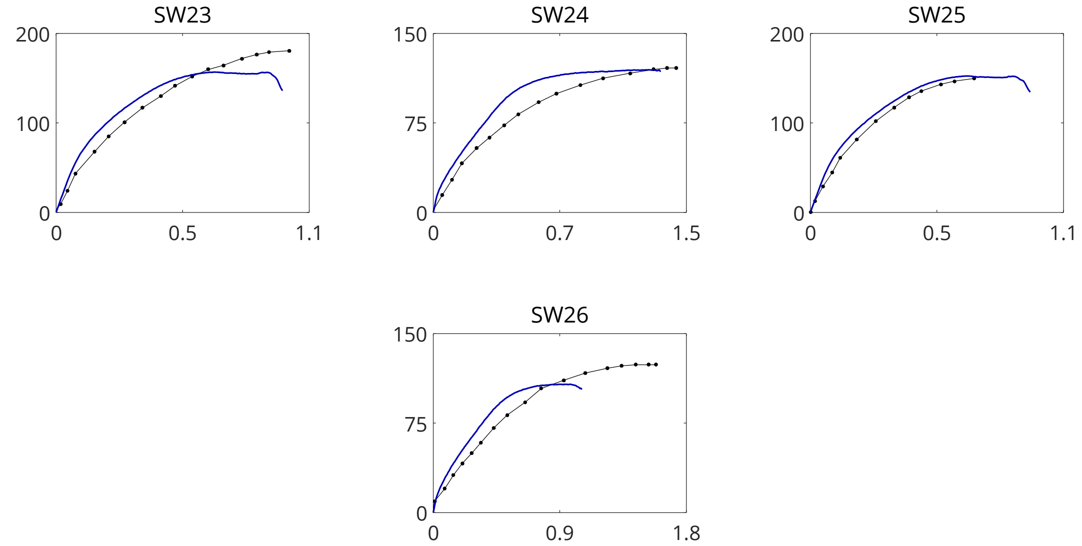

Hirosawa, 1985

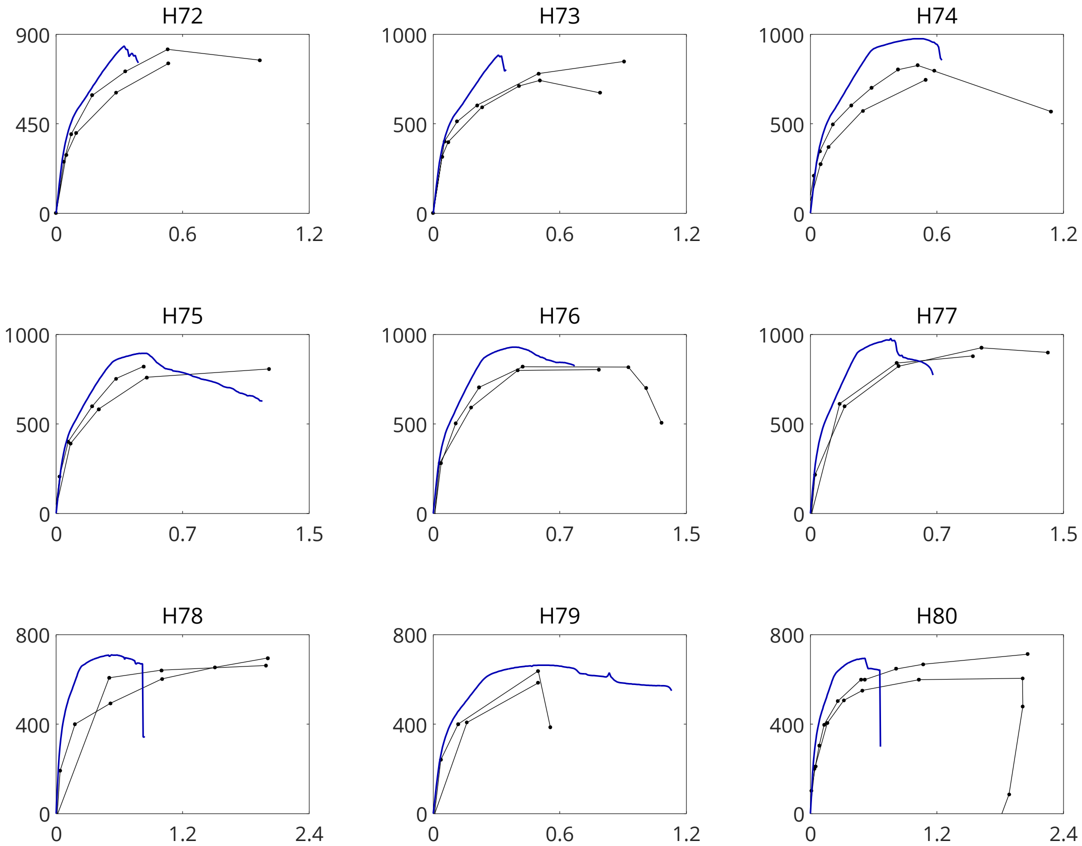

Figure 5-8. VecTor2 predictions of lateral resistance versus drift ratios of a database of 59 test specimens (continued)

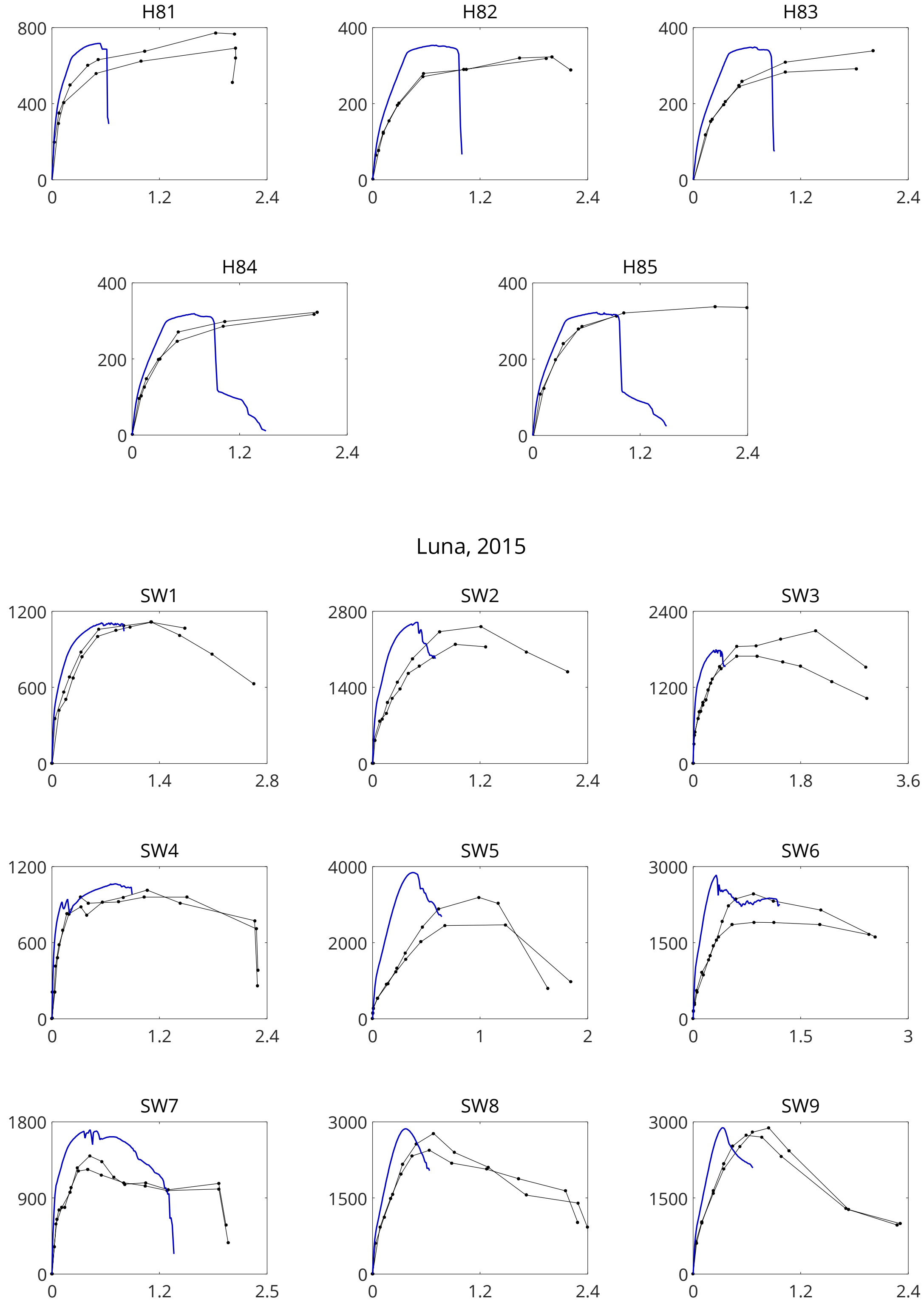

Figure 5-8. VecTor2 predictions of lateral resistance versus drift ratios of a database of 59 test specimens (continued)

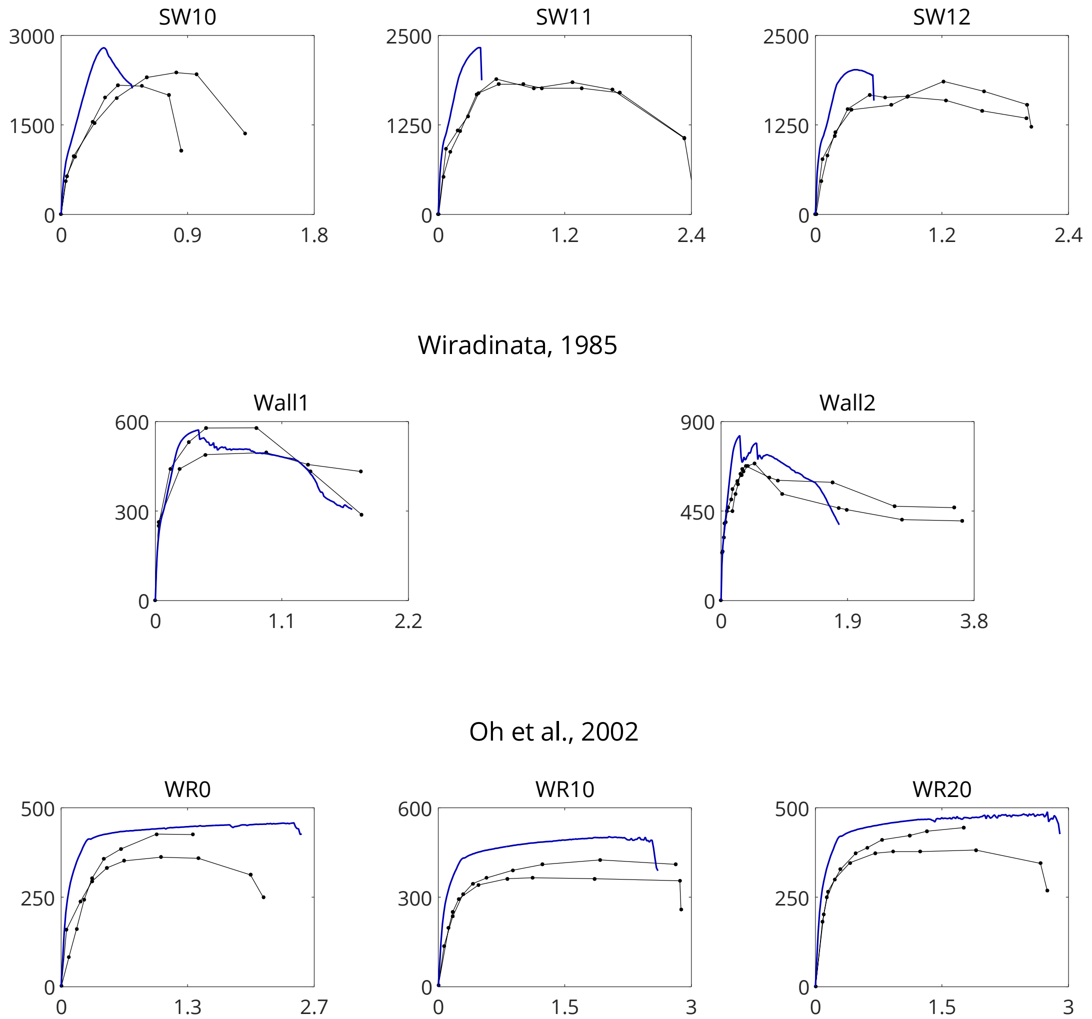

Figure 5-8. VecTor2 predictions of lateral resistance versus drift ratios of a database of 59 test specimens (continued)

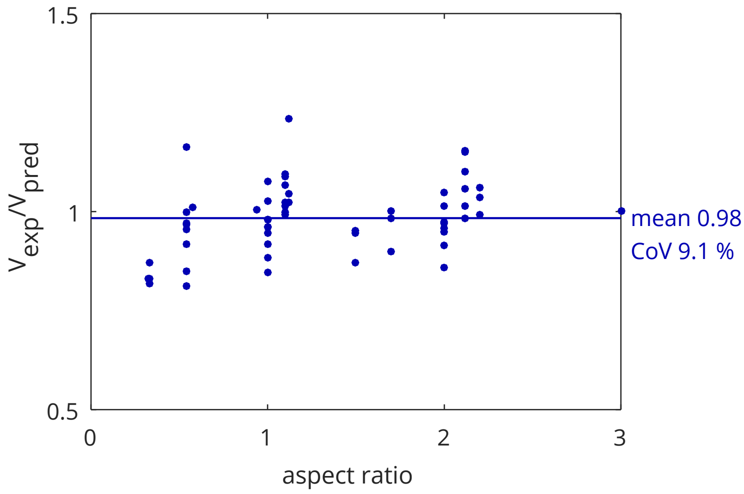

Figure 5-9. Statistics of VecTor2 strength predictions for a database of 59 wall tests

6 Conclusions and outlook

6.1 Summary and conclusions

The study of the behavior and modeling of short walls under seismic loading is encompassed within the framework of this thesis through the following three main parts:

1) Experimental study performed on three large-scale short walls

2) Development and validation of efficient and reliable (low fidelity) macro-kinematic based models for predicting the local and global behavior of flexure- and shear-critical walls

3) Evaluation and guidance for practical application of a nonlinear finite element approach (high fidelity) implemented in software Vector2

6.1.1 Experimental study

The experimental study in §3 was performed by testing to failure of three large-scale short walls under the combined actions of vertical loading and quasi-static cyclic horizontal loading. The walls had an aspect ratio h/d of 1.7 and were lightly reinforced in shear to represent walls from existing construction. The main test variable was the level of axial compression: wall specimens CW0, CW1, and CW2 were loaded to 0%, 10%, and 21% of compressive strength of the concrete section, respectively. Apart from conventional hard-wired measurements, modern optical measuring techniques (LED scanners and DIC system) were used to obtain detailed measurements of the complete deformation patterns developing across the surface of the walls.

All three walls exhibited flexure-dominated behavior. Wall CW0 failed due to rupture of the longitudinal reinforcement in tension, while CW1 and CW2 failed due to crushing of the concrete in compression. Even though the specimens were lightly reinforced in shear and the test data indicated that the stirrups yielded in all three walls, shear failure did not develop. As a consequence of increasing the axial load on the wall, an expected increase in the lateral force resistance was observed. The opposite trend was observed in terms of the drift ratio at failure which was significantly reduced with the increasing compression load.

The flexure-dominated behavior was confirmed from the analysis of the deformations measured across the surface of the walls. It was shown that the flexural deformation mode, and particularly the opening of the base crack, has the highest contribution to the top displacement. The contribution of shear deformations was shown to be less relevant with the increasing axial load. In wall CW0, significant sliding deformations were also observed near failure due to the effects of cycling and absence of axial compression load.

6.1.2 Macro-kinematic modeling

The observations from the experiments were used as a basis for developing the SDOF kinematic approach in §4.1 for predicting the cyclic load-displacement envelope of flexure-dominated short walls. In this approach, the wall is idealized as consisting of two distinct regions: a fan-shaped cracked region and a rigid block. The deformations in the wall are expressed as a function of a single DOF, i.e. the rotation of the rigid block around the neutral axis of the base section. The behavior along the critical base section is modeled based on the classical sectional analysis. The link between the kinematics and the behavior of the critical base section is established through modeling of the deformations in the assumed cracked region with simplified considerations of the effects of shear cracking. Through constitutive modeling, the approach considers various physical aspects of behavior observed in walls, rendering the approach suitable for capturing their cyclic response envelopes.

The SDOF approach was subjected to an extensive validation against the test data of the CW test series. The main assumptions of the proposed approach are validated and show a good agreement with the test observations. In terms of the global response, predicted and measured force-displacement response envelopes were compared, as well as the deformed shapes along the entire envelopes of the response. Furthermore, the predictions of local response were validated with the corresponding measurements of the flexural reinforcement strains, strains in the stirrups, and crack widths. The approach predictions at the global and local level showed a good overall agreement with the test data. The SDOF approach was further validated against the database of wall tests from the literature, including walls with non-seismic and seismic reinforcement detailing. The approach was developed primarily for the analysis of walls with non-seismic detailing, and it was shown that it can successfully capture the response of such walls with varying properties. While the response of walls with seismic detailing is also well captured in many cases, it is noted that the modeling of such members requires further investigation. The range of applicability of the SDOF mechanical model is clearly defined with respect to the limitations of its main hypotheses and the properties of the test specimens considered in the validation.

In its essence, the SDOF procedure represents a proof of the concept that simplified kinematic models coupled with realistic physical modeling of force-resisting mechanisms can accurately predict the response of short walls at both global and local level. This is essential for the accurate evaluation of the limit states of short walls which are dependent on the extent of damage under seismic actions. Finally, this shows the prospects towards the implementation of such procedures in PBEE seismic design and assessment procedures.

The modeling of shear-dominated short walls in this thesis is based on the three-parameter-kinematic approach (3PKT; Mihaylov et al., 2016). The 3PKT uses a three-degree-of-freedom kinematic model to describe the deformation patterns in diagonally-cracked walls with rectangular sections. In the kinematic model, the wall is divided into two parts - a rigid block and a fan of struts - separated by the diagonal crack. The DOFs of the kinematic model are predicted by combining the kinematic conditions with equations for equilibrium and constitutive relationships for the load-bearing mechanisms in walls. The mechanisms of shear resistance across the diagonal crack are modeled with nonlinear springs to capture the pre-peak and post-peak behavior of the wall. The base section of the wall is also modeled to account for yielding of the reinforcement and crushing of the concrete.

The original 3PKT approach is extended in §4.2 to account for additional physical aspects of the behavior of walls, including the effects of barbells, strain penetration in the foundation, cracking above the critical shear cracks, and stirrup ruptures. The validation of the approach is further extended with the available test data of squat walls and walls with barbell-shaped sections. It was shown that the approach produces promising results in predicting the strength and displacement capacity of shear-dominated walls. In the discussion of the results, the 3PKT is also used to give insight into different phenomena observed in the behavior of short walls. Finally, the validation of the 3PKT against the test data from the CW wall series showed limitations of this approach to predict the response of flexure-dominated walls, which are addressed with the SDOF kinematic approach.

6.1.3 Finite element modeling

In comparison to the kinematic modeling, a more complex nonlinear finite element analysis approach implemented is software VecTor2 was applied to short walls. VecTor2 is a 2D finite element code for static and dynamic nonlinear analysis of concrete structures based on the Modified Compression Field Theory (MCFT, Vecchio & Collins, 1986) and Disturbed Stress Field Method (DSFM, Vecchio, 2000). The objective was to investigate the suitability of this approach for practical application for predicting the response of short walls.

The evaluation of this approach consisted of modeling a database of test walls from the literature. The walls were analyzed under constant vertical compression load and monotonically increasing horizontal displacement, which allows capturing of the complete envelope of the response of walls, including the post-peak regime. Initially, several benchmark analyses were performed on selected test walls to investigate the effects of the mesh size and basic formulations of the behavior of concrete elements, i.e. the MCFT and DSFM. The response predictions of the walls in the database were then generated using a mesh size of 20 elements across the section of walls and the DSFM formulation.

The results of the analyses showed that the finite element approach produces adequate strength prediction of short walls. On the other hand, the approach was shown to be inadequate for predicting the displacement capacity of walls. The limitations of this approach to accurately predict the displacement capacity of walls were attributed to a pronounced effect of the mesh size, the occurrence of localization of deformations, as well as numerical instability issues.

6.2 Recommendations for further research

In future research on developing the macro-kinematic models, it is of interest to develop a more general approach that can accurately predict the behavior of short walls with varying properties. Given that the SDOF mechanical model shows promising results in modeling flexural behavior in walls, it can be used as a basis for further development.

Initially, the modeling of the flexure-dominated walls can be further refined within the SDOF mechanical model. This can be achieved by focusing on detailed physical modeling of the main simplifications in the approach. In particular, the modeling of the deformations in the cracked region and the effects of the tension shift mechanism can be improved. In addition, the rebar buckling in walls with confined boundary zones can be extended by considering physical models from the literature that address this failure mechanism.

The following step towards a more general approach would be to introduce the more detailed modeling of the effects of shear in the SDOF approach. In this context, it is useful to consider the concepts implemented in the 3PKT approach. The kinematics can be extended to account for the shear deformation mode. With the adequate modeling of the development of cracking in walls and shear resisting mechanisms, the procedure can be extended to consider shear failure mechanisms, i.e. diagonal tension, ductile shear, and diagonal compression failures. The emphasis should be on the modeling of the shear-flexure interaction that allows capturing the transition between different modes of behavior in walls. It is noted that such a procedure should be developed with the intent to provide consistent predictions on the global and local level with respect to the adopted material models and their limit states. This is essential for accurately capturing structure limit states that are dependent on the extent of damage in the structural members under seismic actions. Such a unified approach would be suitable for a wider range of applications within the performance-based seismic design and assessment procedures.

Given the evidence that the cyclic loading can have a significant impact on the behavior of walls, it is necessary to further investigate this effect on the different modes of behavior exhibited by walls. This can be addressed by implementing hysteretic relationships in modeling of the behavior of resisting mechanisms. This would allow the analysis of the complete cyclic behavior of walls and would provide further insight into the cyclic behavior and cyclic degradation of the force-resisting mechanisms that can play an important role, especially in the response of ductile walls. Such development would also allow the implementation of the macro-kinematic procedures towards more complex analyses, such as nonlinear time-history analyses.

Bibliography

AASHTO. (2007). *AASHTO LRFD bridge design specifications, 4th Ed.* Washington, DC.

Almeida, P., Tarquini, D., & Beyer, K. (2014). Modelling Approaches for Inelastic Behaviour of RC Walls: Multi-level Assessment and Dependability of Results. *Archives of Computational Methods in Engineering, 23*(1), 69-100.

ASCE 41-06. (2007). *Seismic Rehabilitation of Existing Buildings.* Reston, Virginia: American Society of Civil Engineers.

ASCE 41-13. (2014). *Seismic Evaluation and Retrofit of Existing Buildings.* Reston, Virginia: American Society of Civil Engineers.

ASCE 43-05. (2005). *Seismic Design Criteria for Structures, Systems, and Components in Nuclear Facilities.* Reston, Virginia: American Society of Civil Engineers.

ASCE 7-16. (2017). *Minimum design loads and associated criteria for buildings and other structures.* Reston, Virginia: American Society of Civil Engineers.

Bazant, Z. P., & Oh, B. H. (1995). Microplane model for progressive fracture of concrete and rock. *Journal of Engineering Mechanics, 111*(4), 559-582.

Bentz, C. E., Vecchio, F. J., & Collins, P. M. (2006). Simplified Modified Compression Field Theory for Calculating Shear Strength of Reinforced Concrete Elements. *ACI Structural Journal, 103*(4), 614-624.

Bentz, E. (2000). *Sectional Analysis of Reinforced Concrete Members.* University of Toronto, Department of Civil Engineering, Toronto.

Bimschas, M. (2010). *Displacement-based seismic assessment of existing bridges in regions of moderate seismicity.* Ph.D. thesis, Institute of Structural Engineering, Swiss Federal Institute of Technology Zurich, Zurich.

Bimschas, M., Chatzi, E., & Marti, P. (2015). Inelastic deformation analysis of RC bridge piers, part 2: Application and verification. *ACI Structural Journal, 112*(3), 277-286.

Biskinis, D., & Fardis, M. N. (2010). Flexure-controlled ultimate deformations of members with continuous or lap-spliced bars. *Structural Concrete, 78*(3), 171-178.

Bresler, B., & Gilbert, H. P. (1961). Tie Requirements for Reinforced Concrete Columns. *ACI Structural Journal, 58*(11), 555-570.

Carrasquillo, R. L., Nilson, A. H., & Slate, F. O. (1981). Properties of high strength concrete subject to short-term loads. *ACI Structural Journal, 78*(3), 171-178.

CEB-FIP. (1990). *CEB-FIP model code 1990.* Lausanne, Switzerland: Comité Euro-International du Béton.

CEN, Eurocode 2. (2002). *Design of concrete structures.* Brussels: European Committee for Standardization.

CEN, Eurocode 8. (2005). *Design of structures for earthquake resistance.* Brussels: European Committee for Standardization.

Chen, S., & Kabeyasawa, T. (2000). Modeling of reinforced concrete shear wall for nonlinear analysis. *Proceedings of the 12th World Conference on Earthquake Engineering.* Auckland.

Collins, P. M., & D., M. (1991). *Prestressed Concrete Structures.* Englewood Cliffs (NJ, USA): Prentice Hall.

Dazzio, A., Beyer, K., & Bachmann, H. (2009). Quasi-static cyclic tests and plastic hinge analysis of RC structural walls. *Engineering Structures, 31*(7), 1556-1571.

Dhakal, P. R., & Maekawa, K. (2002). Modeling for Postyield Buckling of Reinforcement. *ASCE Journal of Structural Engineering, 128*(9), 1139-1147.

Elwood, J. (2013). Performance of concrete buildings in the 22 February 2011 Christchurch earthquake and implications for Canadian codes. *Canadian Journal of Civil Engineering, 40*(3), 759-776.

Fardis, N. M. (2009). *Seismic Design, Assessment and Retrofitting of Concrete Buildings.* Springer Netherlands.

Günay, M., & Mosalam, K. (2012). PEER Performance Based Earthquake Engineering Methodology, Revisited. Lisboa: 15th World Conference on Earthquake Engineering.

Ghorbani-Renani, I., Velev, N., Tremblay, R., Palermo, D., Massicotte, B., & Léger, P. (2009). Modeling and Testing Influence of Scaling Effects on Inelastic Response of Shear Walls. *ACI Structural Journal*, 358-367.

Hannewald, P., Bimschas, M., & Dazio, A. (2013). *Quasi-static cyclic tests on RC bridge piers with detailing deficiencies.* Swiss Federal Institute of Technology ETH, Zurich.

Herbrand, M., Adam, V., Classen, M., Kueres, D., & Heggar, J. (2017). Strengthening of Existing Bridge Structures for Shear and Bending with Carbon Textile-Reinforced Mortar. *Materials, 10*, 1099.

Hines, M. E., Restrepo, I. J., & Seible, F. (2004). Force-Displacement Characterization of Well-Confined Bridge Piers. *ACI Structural Journal, 101*(4), 537-548.

Hirosawa, M. (1975). *Past experimental results on reinforced concrete shear walls and analysis on them (in Japanese).* Building Research Institute, Ministry of Construction, Tsukuba, Japan.

Hsiao, F. P., Wang, J. C., & Chiou, Y. J. (2008). Shear strengthening of reinforced concrete framed shear walls using CFRP strips. *14th World Conference on Earthquake Engineering.* Beijing, Chine.

Hwang, S. J., Tu, Y. S., Yeh, Y. H., & Chiou, T. C. (2004). Reinforced concrete partition walls retrofitted with carbon fiber reinforced polymer. *ANCER*

Annual Meeting: Networking of Young Earthquake Engineering Researchers and Professionals. Honolulu, Hawaii.

I., L. D., Kotsovos, D. M., & N., A. N. (1990). Behavior of Reinforced Concrete Structural Walls: Strength, Deformation Characteristics, and Failure Mechanism. *ACI Structural Journal*, Title No. 87-S3.

Kaba, S. A., & Mahin, S. A. (1984). *Refined modelling of reinforced concrete columns for seismic analysis.* Berkely: University of California.

Kagermanov, A., & Ceresa, P. (2016). Physically-based cyclic tensile model for reinforced concrete membrane elements. *Journal of Structural Engineering, 142*(12).

Kam, Y. W., Pampanin, S., & Elwood, K. (2011). Seismic Performance of Rreinforced Concrete Buildings in the 22 February Christchurch (Lyttelton) Earthquake. *Bulletin of The New Zealand Society for Earthquake Engineering*, Vol. 44, No. 4.

Kani, G. N. (1964). The Riddle of Shear Failure and Its Solution. *Journal of the American Concrete Institute, 61*(4), 441-467.

Kupfer, H., Hilsdorf, H. K., & Rusch, H. (1969). Behaviour of concrete under biaxial states of stress. *Am. Concrete Inst. Journal & Proceedings, 66*(8), 656-666.

Li, B., Maekawa, K., & Okamura, H. (1994). Contact density model for stress transfer across cracks in concrete. *Journal of the Faculty of Engineering, University of Tokyo, 40*(1), 9-52.

Luna, B. N. (2016). *Seismic Response of Low Aspect Ratio Reinforced Concrete Walls for Buildings and Safety-Related Nuclear Applications.* University at Buffalo, Department of Civil, Structural and Environmental Engineering, Buffalo, New York.

Luna, B. N., Rivera, J. P., & Whittaker, A. S. (2015). Seismic behavior of low-aspect-ratio reinforced concrete shear walls. *ACI Structural Journal, 112*(5), 593-603.

Luna, B. N., Rivera, J. P., Rocks, J. F., Goksu, C., Weinreber, S., & Whittaker, A. S. (n.d.). University at buffalo—low aspect ratio rectangular reinforced concrete shear wall—specimen SW1, SW2, SW3, SW4, SW5, SW6, SW7, SW8, SW9, SW10, SW11, SW12. *Network for Earthquake Engineering Simulation (Distributor).*

Maier, J., & Thürlimann, B. (1985). *Bruchversuche an Stahlbetonscheiben.* Zurich: Swiss Federal Institute of Technology ETH.

Mander, J. B., Priestley, M. J., & Park, R. (1988). Theoretical stress-strain model for confined concrete. *Journal of Structural Engineering, 114*(8), 1804-1826.

Massone, L. M., Orakcal, K., & Wallace, J. W. (2006). Shear-flexure interaction for structural walls. *ACI Special Publications, SP-236-07*, 127-150.

Massone, M. L., & Lopez, E. E. (2013). Modeling of reinforcement global buckling in RC elements. *Engineering Structures, 59*, 484-494.

Mazars, J., Kotronis, P., & Davenne, L. (2002). A new modelling strategy for the behavior of shear walls under dynamic loading. *Earthquake Engineering and Structural Dynamics, 31*(4), 937-954.

Mestyanek, J. M. (1986). *The earthquake resistance of reinforced concrete structural walls of limited ductility.* University of Canterbury, Christchurch, New Zealand.

Mihaylov, I., Hannewald, P., & Beyer, K. (2016). Three-Parameter Kinematic Theory for Shear-Dominated Reinforced Concrete Walls. *Journal of Structural Engineering, 142*(7).

Moehle, J., & Deierlein, G. G. (2004). A Framework Methodology for Performance-Based Earthquake Engineering. Vancouver: 13th World Conference on Earthquake Engineering.

Moyer, J. M., & Kowalsky, J. M. (2003). Influence of Tension Strain on Buckling of Reinforcement in Concrete Columns. *ACI Structural Journal, 100*(1), 75-85.

Oesterle, G. R., Fiorato, E. A., Johal, S. L., Carpenter, E. J., Russell, G. H., & Corley, G. W. (1976). *Earthquake Resistant Structural Walls - Tests of Isolated Walls.*

Oh, Y.-H., Han, W. S., & Lee, L.-H. (2002). Effect of boundary element details on the seismic deformation capacity of structural walls. *Earthquake Engng Struct. Dyn.*, 1583-1602.

Orakcal, K., Wallace, J. W., & Conte, J. P. (2004). Nonlinear modeling and analysis of slender reinforced concrete walls. *ACI Structural Journal, 101*(5), 688-699.

Palermo, V., Tsionis, G., & Sousa, M. L. (2018). *Building stock inventory to assess seismic vulnerability across Europe.* EUR 29257 EN, Publications Office of the European Union, Luxembourg.

Panagiotou, M., Restrepo, J. I., Schoettler, M., & Kim, G. (2012). Nonlinear cyclic truss model for reinforced concrete walls. *ACI Structural Journal, 109*(2), 205-214.

Park, H., & Eom, T. (2007). Truss model for nonlinear analysis of RC members subject to cyclic loading. *Journal of Structural Engineering, 133*(10), 1351-1363.

Park, R., & Paulay, T. (1975). *Reinforced Concrete Structures.* John Wiley & Sons, Inc.

Petrangeli, M., Pinto, P. E., & Ciampi, V. (1999). Fiber element for cyclic bending and shear of RC structures. I: Theory. *Journal of Engineering Mechanics, 125*(9), 994-1001.

Popovics, S. (1970). A review of stress-strain relationships for concrete. *ACI Structural Journal, 67*(3), 243-248.

Popovics, S. (1973). A numerical approach to the complete stress-strain curve of concrete. *Cement and Concrete Research, 3*(5), 583-599.

Priestley, M. J., Calvi, G. M., & Kowalsky, M. J. (2007). *Displacement-Based Seismic Design of Structures.* Pavia, Italy: IUSS Press.

Priestley, M., & Paulay, T. (1992). *Seismic design of reinforced concrete and masonry buildings.* John Wiley & Sons, Inc.

Restrepo-Posada, I. J. (1992). *Seismic behavior of bonnections between precast concrete elements.* University of Canterbury, Christchurch.

Salonikios, N. T., Kappos, J. A., Tegos, A. I., & Penelis, G. G. (1999). Cyclic Load Behavior of Low-Slenderness Reinforced Concrete Walls: Design Basis and Test Results. *ACI Structural Journal*, Title No. 96-S73.

Shima, H., Chou, L., & Okamura, H. (1987). Micro and macro models for bond in RC. *Journal of the Faculty of Engineering, University of Tokyo, 39*(2), 133-194.

Sigrist, V. (1995). *Zum Verformungsvermögen von Stahlbetonträgern.* Federal Institute of Technology ETH, Zurich.

Thomsen, H. J., & J., W. W. (1995). *Displacement-Based Design of Reinforced Concrete Walls: An Experimental Investigation of Walls with Rectangular and T-Shaped Cross-Sections.* Clarkson University, Department of Civil and Environmental Engineering.

Tran, T. A., & Wallace, W. J. (2004). Experimental Study of Nonlinear Flexural and Shear Deformations of Reinforced Concrete Structural Walls. Lisbon: 15 WCEE.

Vecchio, F. (2000). Disturbed stress field model for reinforced concrete: Formulation. *ASCE Journal of Structural Engineering, 126*(9), 1070-1077.

Vecchio, F. J. (1992). Finite Element Modeling of Concrete Expansion and Confinement. *ASCE Journal of Structural Engineering, 118*(9), 2390-2406.

Vecchio, F., & Collins, M. (1986). The Modified Compression-Field Theory for Reinforced Concrete Elements Subjected to Shear. *ACI Structural Journal, 19*(16), 219-231.

VecTor2. (2018). VecTor Analysis Group (http://vectoranalysisgroup.com). Toronto: University of Toronto.

Wallace, W. J., Massone, M. L., Bonelli, P., Dragovich, J., Lagos, R., Luders, C., & Moehle, J. (2012). Damage and Implications for Seismic Design of RC Structural Wall Buildings. *Earthquake Spectra*, S281-s299.

Walraven, J. C. (1981). Fundamental analysis of aggregate interlock. *Journal of Structural Engineering, 107*(11), 2245-2270.

Wiradinata, S. (1985). *Behaviour of squat walls subjected to load reversals.* University of Toronto, Department of Civil Engineering, Toronto, Canada.

Wong, P. S., & J., V. F. (2002). *VecTor2 and FormWorks User's Manual.* University of Toronto.

Zhang, H., Lu, X., & Wu, X. (2010). Experimental Study and Numerical Simulation of the Reinforced Concrete Walls with Different Stirrup in the Boundary Element. *Journal of Asian Architecture and Building Engineering*, 447-454.

Appendices

Appendix A: Test Data

Measuring devices

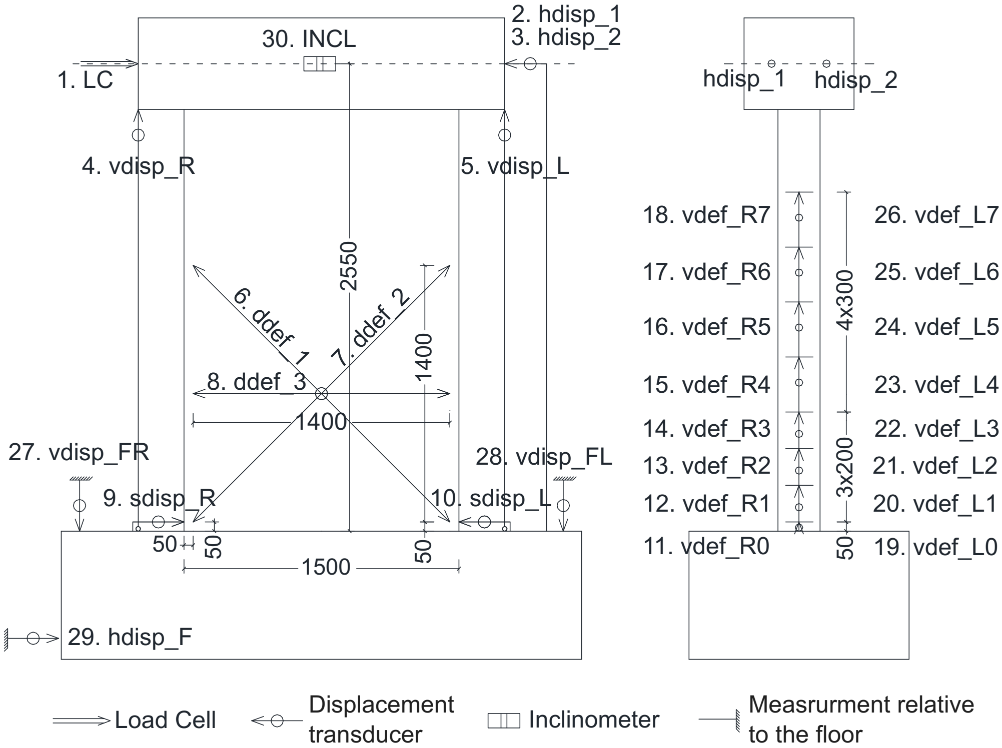

Grid of markers for LED scanners

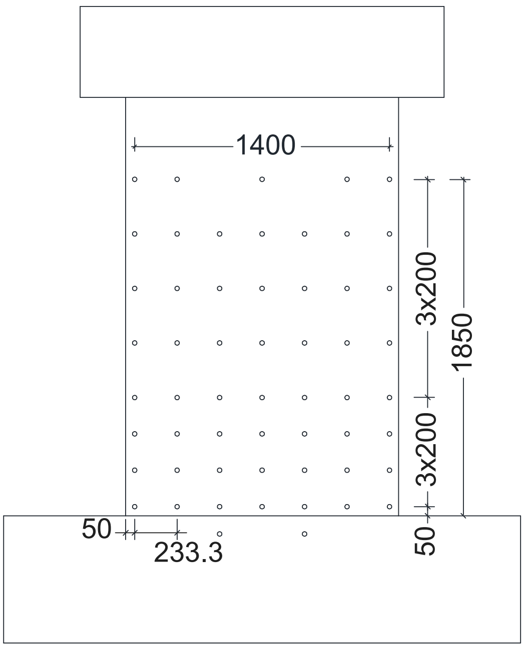

Appendix A.1: Wall CW0

Global response

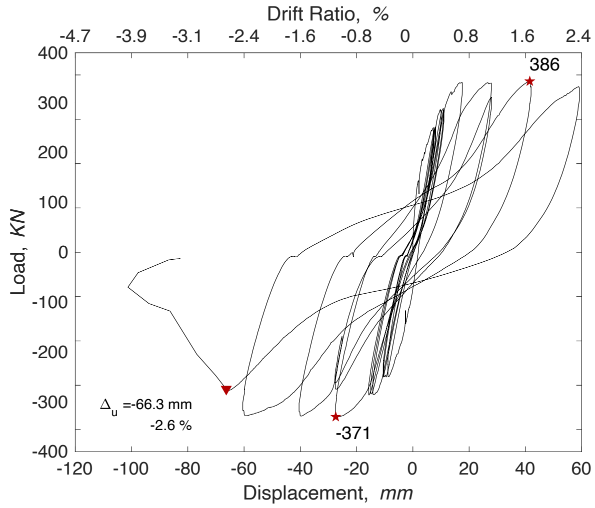

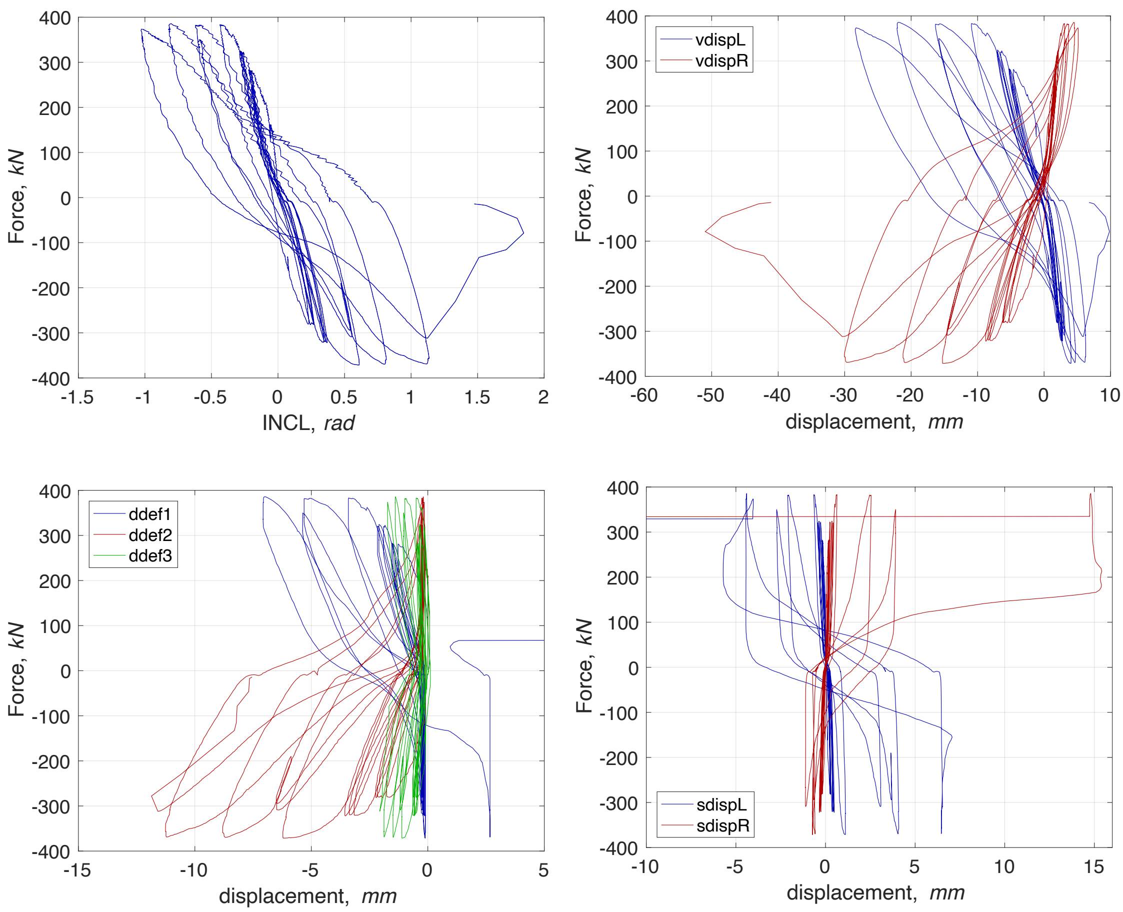

Table A-1. Wall CW0 data summary

Load Stage	LC kN	Δ^* mm	INCL rad	vdisp _L mm	vdisp _R mm	ddef1 mm	ddef2 mm	ddef3 mm	sdisp _R mm	sdisp _L mm
LS1'	161	2.0	-0.054	-1.11	0.61	-0.18	0.01	0.00	0.04	-0.04
LS1	281	7.3	-0.195	-4.63	1.73	-1.28	-0.12	-0.26	0.16	-0.16
LS2'	-162	-2.6	0.079	0.62	-1.65	-0.18	-0.45	-0.10	-0.04	0.10
LS2	-280	-8.6	0.227	1.91	-5.12	-0.21	-1.66	-0.47	-0.17	0.25
LS3	282	7.9	-0.214	-5.16	1.75	-1.49	-0.25	-0.45	0.19	-0.19
LS4	-281	-9.5	0.244	2.00	-5.53	-0.28	-1.94	-0.57	-0.19	0.27
LS5	283	8.1	-0.212	-5.25	1.70	-1.53	-0.26	-0.41	0.20	-0.20
LS6	-282	-10.5	0.271	2.15	-6.20	-0.27	-2.22	-0.48	-0.21	0.29
LS7	322	9.8	-0.257	-6.38	2.06	-1.84	-0.25	-0.34	0.25	-0.27
LS8	-321	-13.9	0.338	2.57	-8.00	-0.20	-3.08	-0.63	-0.26	0.38
LS9	324	10.8	-0.283	-7.02	2.15	-2.10	-0.26	-0.34	0.36	-0.36
LS10	-320	-14.8	0.353	2.68	-8.37	-0.17	-3.32	-0.55	-0.32	0.44
LS11	321	11.0	-0.280	-7.08	2.13	-2.16	-0.26	-0.16	0.43	-0.43
LS12	-322	-15.6	0.369	2.77	-8.77	-0.14	-3.54	-0.58	-0.34	0.48
LS13	383	17.5	-0.438	-10.93	3.08	-3.40	-0.23	-0.50	0.64	-0.66
LS14	-371	-27.4	0.609	4.05	-15.25	-0.11	-6.21	-1.11	-0.73	1.11
LS15	382	26.7	-0.593	-15.72	3.51	-5.07	-0.25	-0.94	2.47	-2.07
LS16	-309	-27.2	0.549	3.06	-14.44	-0.25	-6.40	-1.17	-1.10	3.05
LS17	350	28.0	-0.592	-15.82	3.33	-5.37	-0.26	-1.04	3.91	-2.73
LS18	-294	-27.5	0.540	2.92	-14.31	-0.25	-6.48	-1.18	-0.66	3.68
LS19	-370	-39.8	0.802	4.65	-20.92	-0.12	-8.69	-1.49	-0.58	4.05
LS20	386	41.6	-0.804	-21.95	4.52	-7.02	-0.19	-1.39	14.79	-4.40
LS21	-369	-59.6	1.118	6.14	-29.72	2.67	-11.22	-1.88	-	6.46
LS22	374	59.0	-1.027	-28.29	5.10	-	-0.16	-1.73	-	-4.04
LS23	-312	-65.9	1.124	5.91	-30.37	-	-11.59	-2.06	-	-

$^*\Delta$ =0.5*(hdisp_1 + hdisp_2)

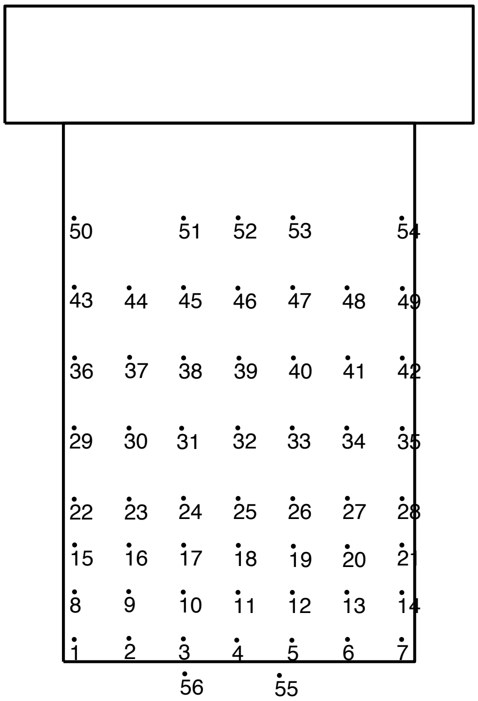

LED grid numbering

Table A-2. Relative displacements of LED grid of wall CW0

Relative horizontal displacements, mm

LED no.	LS1'	LS1	LS2'	LS2	LS7	LS8	LS13	LS14	LS15	LS19	LS20	LS21	LS22	LS23
1	0.15	0.44	0.05	-0.16	0.79	-0.33	1.28	-1.22	2.70	-4.33	7.14	-9.21	15.30	-11.02
2	0.10	0.30	-0.10	-0.33	0.43	-0.57	0.87	-1.50	2.40	-4.67	6.33	-9.13	9.85	-
3	0.17	0.32	-0.09	-0.36	0.28	-0.50	0.92	-1.36	2.33	-4.19	6.47	-8.07	12.65	-13.40
4	-0.01	0.41	-0.26	-0.19	0.59	-0.61	0.80	-1.25	2.65	-0.81	5.44	-7.16	12.97	-10.73
5	0.15	0.41	-0.01	-0.21	0.61	-0.36	1.05	-1.12	2.95	-3.25	7.71	-6.16	15.35	-9.70
6	0.20	0.51	-0.02	-0.25	0.51	-0.38	1.00	-0.99	3.05	-2.85	9.29	-6.18	17.42	-9.27
7	0.24	0.32	-0.29	-0.33	0.43	-0.43	1.17	-1.09	3.21	-3.30	8.23	-6.36	16.43	-9.19
8	0.19	0.64	-0.15	-0.59	0.75	-1.29	1.50	-3.20	3.67	-7.35	9.03	-13.50	16.55	-19.31
9	0.24	0.69	-0.13	-0.55	1.02	-0.97	1.88	-2.95	4.14	-7.09	8.43	-12.48	17.12	-17.66
10	0.22	0.64	-0.13	-0.56	1.00	-0.98	1.78	-2.50	4.16	-6.34	9.83	-11.77	18.21	-17.24
11	0.23	0.78	-0.04	-0.46	1.00	-0.86	1.83	-2.43	4.18	-6.13	9.90	-10.96	18.46	-16.16
12	0.23	0.70	-0.12	-0.56	0.97	-0.96	1.77	-2.40	4.18	-5.98	9.86	-11.25	18.53	-16.33
13	0.26	0.72	0.08	-0.34	1.01	-0.71	2.18	-1.91	5.00	-4.82	11.14	-9.16	19.90	-13.53
14	0.30	0.76	0.09	-0.35	0.98	-0.63	2.25	-1.81	4.93	-4.54	10.90	-9.25	20.05	-13.43
15	0.35	1.04	-0.32	-1.06	1.39	-2.15	2.67	-5.11	5.43	-9.97	11.91	-17.05	21.37	-22.81

16	0.34	1.01	-0.29	-1.04	1.33	-2.07	2.52	-5.22	5.40	-10.02	11.90	-17.11	21.07	-22.88
17	0.37	1.09	-0.42	-0.99	1.64	-1.72	3.07	-4.47	5.98	-9.34	12.75	-16.48	22.31	-22.23
18	0.43	1.23	-0.25	-1.03	1.57	-1.42	3.10	-3.69	6.18	-8.21	12.81	-15.16	22.32	-20.82
19	0.43	1.10	-0.19	-0.91	1.57	-1.45	3.02	-3.82	6.28	-8.31	13.31	-15.00	23.26	-20.53
20	0.27	1.30	-0.27	-0.93	1.64	-1.35	3.29	-3.59	6.77	-7.78	13.47	-14.30	23.27	-19.49
21	0.42	1.13	-0.31	-0.93	1.83	-1.23	3.36	-3.31	6.63	-7.61	13.85	-14.66	23.70	-19.71
22	0.39	1.41	-0.47	-1.61	1.80	-3.12	3.58	-7.07	7.01	-12.65	14.38	-21.04	24.48	-26.87
23	0.45	1.39	-0.53	-1.70	1.94	-3.05	3.71	-7.08	7.22	-12.71	14.55	-20.96	24.78	-26.69
24	0.53	1.43	-0.47	-1.49	1.98	-2.55	3.76	-6.07	7.41	-11.65	14.74	-20.22	25.12	-25.98
25	0.48	1.47	-0.57	-1.37	2.08	-2.40	3.96	-6.08	7.48	-11.60	14.83	-19.71	25.21	-25.52
26	0.48	1.64	-0.42	-1.38	2.38	-2.24	4.20	-5.24	8.04	-10.52	15.93	-18.23	26.68	-24.09
27	0.57	1.90	-0.43	-1.29	2.43	-2.07	4.80	-5.30	8.66	-10.36	16.72	-18.29	27.55	-23.86
28	0.56	1.65	-0.19	-1.34	2.49	-2.13	4.77	-5.06	8.78	-10.24	16.84	-18.26	27.58	-23.60
29	0.78	2.28	-0.82	-2.68	2.96	-4.65	5.51	-10.14	10.06	-16.88	18.98	-26.85	30.67	-32.65
30	0.77	2.39	-0.85	-2.74	3.12	-4.71	5.83	-10.16	10.51	-16.82	19.00	-26.99	30.62	-32.74
31	0.81	1.97	-0.75	-2.64	2.72	-4.42	5.43	-9.61	9.92	-16.24	19.58	-26.22	31.16	-32.01
32	0.87	2.66	-0.68	-2.31	3.77	-3.82	6.67	-8.75	11.62	-15.15	20.57	-24.82	32.33	-30.69
33	0.83	2.70	-0.63	-2.23	3.63	-3.55	6.66	-8.24	11.52	-14.50	20.72	-24.13	32.72	-29.91
34	0.89	2.73	-0.55	-2.06	3.63	-3.40	6.94	-7.90	11.95	-14.23	20.90	-23.76	32.80	-29.48
35	0.87	2.64	-0.75	-2.16	3.75	-3.36	6.91	-7.81	11.82	-18.79	20.98	-23.42	31.32	-30.85
36	1.04	3.21	-1.21	-3.81	4.33	-6.45	7.75	-13.36	13.01	-21.09	23.71	-32.80	36.59	-38.70
37	1.01	3.46	-0.91	-3.61	4.97	-6.15	8.38	-12.97	13.95	-24.04	23.96	-32.84	36.18	-38.48
38	1.15	3.43	-1.09	-3.82	4.59	-6.18	8.28	-13.23	13.63	-21.10	24.00	-32.42	36.75	-38.28
39	1.16	3.59	-1.12	-3.68	5.00	-5.83	8.74	-12.57	14.20	-20.21	24.31	-31.73	37.31	-37.52
40	1.08	3.65	-1.07	-3.62	4.97	-5.77	9.10	-12.10	14.83	-19.50	25.05	-30.90	38.16	-36.77
41	1.06	3.70	-0.98	-3.45	5.11	-5.35	9.28	-11.54	14.94	-19.29	25.35	-30.25	38.18	-36.19
42	1.18	3.53	-1.09	-3.39	4.88	-5.36	9.12	-11.68	14.67	-19.11	24.97	-30.54	37.91	-36.41
43	1.36	4.56	-1.55	-4.96	5.97	-8.15	10.53	-16.48	16.87	-25.30	28.85	-38.33	42.97	-44.22
44	1.36	4.54	-1.51	-4.95	6.03	-8.06	10.53	-16.53	16.84	-25.11	28.82	-38.39	42.74	-44.27
45	1.44	4.64	-1.59	-4.95	6.25	-8.00	10.80	-16.40	17.32	-24.91	28.87	-38.05	42.91	-44.03
46	1.45	4.77	-1.47	-4.90	6.39	-8.05	11.43	-16.33	17.84	-24.96	29.24	-38.12	43.22	-43.98
47	1.40	4.66	-1.49	-4.93	6.36	-7.62	11.38	-15.80	17.92	-24.31	29.00	-37.28	43.09	-43.20
48	1.61	4.68	-1.49	-4.79	6.55	-7.52	11.40	-15.28	18.16	-23.98	29.06	-36.64	43.34	-42.66
49	1.43	4.66	-1.72	-4.80	6.23	-7.35	11.42	-15.15	17.73	-23.49	29.22	-36.49	43.19	-42.76
50	1.73	5.79	-1.90	-6.05	7.69	-9.79	13.32	-19.71	20.75	-29.43	33.70	-44.12	49.41	-49.95
51	1.77	5.73	-1.93	-5.94	7.80	-9.60	13.65	-19.21	20.95	-28.69	33.95	-44.03	49.50	-49.84
52	1.69	5.76	-1.95	-6.13	7.80	-9.78	13.61	-19.69	20.81	-29.60	33.65	-43.72	48.75	-49.70
53	1.67	5.82	-1.88	-6.04	7.80	-9.65	14.28	-19.32	21.73	-29.03	34.43	-43.16	49.72	-48.87
54	1.93	5.85	-1.65	-5.91	7.77	-9.14	13.63	-19.36	20.85	-28.89	33.90	-42.62	49.05	-47.85
55	0.00	0.15	-0.01	-0.01	0.18	-0.07	0.21	0.01	0.24	0.00	0.37	0.12	0.37	0.09
56	0.04	0.14	0.04	-0.01	0.11	-0.04	0.15	-0.05	0.18	-0.05	0.22	0.12	0.37	0.14

Relative vertical displacements, mm

LED no.	LS1'	LS1	LS2'	LS2	LS7	LS8	LS13	LS14	LS15	LS19	LS20	LS21	LS22	LS23
1	0.52	1.39	0.62	0.45	2.83	0.98	4.80	1.20	7.28	1.70	11.95	1.52	19.12	3.40
2	0.44	1.13	0.65	0.69	2.41	1.40	4.11	2.32	6.13	3.38	9.22	4.17	11.98	20.01
3	0.38	0.96	0.77	0.95	2.22	1.75	3.56	3.01	5.06	4.43	7.40	5.94	9.66	6.76
4	0.19	0.24	-0.01	0.10	0.21	0.24	0.88	1.17	1.84	6.24	1.45	4.01	4.03	5.99
5	0.23	0.77	1.01	1.39	1.90	2.35	2.83	4.27	3.85	6.23	5.17	8.46	5.98	9.25
6	0.10	0.39	1.01	1.51	1.53	2.58	2.18	4.93	2.85	7.46	5.62	11.37	6.17	12.78
7	0.07	0.15	1.20	1.75	1.22	2.93	1.48	5.78	1.70	9.43	1.81	16.39	1.75	19.64
8	0.67	1.85	0.49	0.24	3.36	0.66	5.96	0.74	9.49	1.23	14.74	1.19	20.42	1.58
9	0.54	1.54	0.63	0.68	2.96	1.36	5.11	2.52	8.04	3.98	11.95	6.55	16.06	7.43
10	0.41	1.30	0.80	1.12	2.76	1.96	4.56	3.62	6.97	5.75	10.30	7.91	13.42	8.65
11	0.31	1.03	0.93	1.44	2.41	2.51	3.77	4.81	5.68	7.27	8.26	10.05	10.47	10.69
12	0.23	0.71	1.08	1.78	1.97	2.95	3.00	5.99	4.45	9.10	6.30	13.20	7.84	13.92
13	0.14	0.47	1.23	1.87	1.64	3.11	2.47	6.15	3.46	9.23	4.71	13.81	5.60	15.08
14	0.01	0.04	1.30	2.06	1.02	3.43	1.19	7.12	1.48	11.19	1.76	17.58	1.70	20.07
15	0.87	2.25	0.43	0.04	3.76	0.44	6.65	0.50	10.54	0.97	16.05	1.09	21.71	1.50
16	0.76	1.90	0.70	0.80	3.43	1.68	5.84	2.92	9.03	4.40	13.58	5.76	17.87	6.29
17	0.60	1.72	0.93	1.27	3.26	2.33	5.37	4.45	8.11	6.76	11.99	9.37	15.67	10.15
18	0.42	1.34	1.19	1.80	2.82	2.93	4.44	5.57	6.47	8.52	9.39	12.17	12.07	12.91
19	0.24	0.87	1.34	2.20	2.19	3.52	3.30	7.16	4.98	10.83	7.22	15.85	9.18	16.64
20	0.11	0.49	1.64	2.56	1.69	4.11	2.57	8.47	3.62	12.65	4.85	18.67	5.89	19.63
21	-0.06	-0.10	1.77	2.97	0.90	4.71	1.09	10.04	1.42	15.08	1.68	22.57	1.72	23.99
22	0.93	2.61	0.41	0.04	4.29	0.44	7.39	0.48	11.39	1.04	17.16	1.15	22.80	1.68
23	0.75	2.15	0.70	0.79	3.80	1.68	6.43	2.91	9.87	4.35	14.58	5.77	19.22	6.36
24	0.59	1.75	0.91	1.28	3.23	2.31	5.37	4.41	8.10	6.69	11.98	9.40	15.65	10.18
25	0.45	1.34	1.14	1.78	2.73	3.14	4.42	6.17	6.48	9.17	9.35	12.97	12.06	13.68
26	0.29	1.08	1.49	2.37	2.45	3.74	3.55	7.30	5.23	10.99	7.34	15.98	9.33	16.72
27	0.09	0.47	1.68	2.82	1.69	4.48	2.55	9.19	3.54	13.65	4.89	20.01	5.94	20.94
28	-0.09	-0.15	1.83	3.27	0.79	5.21	0.92	10.98	1.26	16.15	1.49	23.94	2.15	25.37
29	1.07	3.27	0.34	-0.12	5.12	0.25	8.59	0.24	12.81	0.82	18.59	0.96	24.21	1.54
30	0.87	2.70	0.69	0.75	4.43	1.60	7.29	2.82	10.81	4.26	15.60	5.68	20.24	6.26
31	0.61	2.03	0.89	1.58	3.37	2.66	5.63	4.82	8.46	7.04	12.64	9.50	16.36	10.18
32	0.46	1.68	1.28	2.20	3.22	3.54	5.01	6.61	7.30	9.60	10.32	13.54	13.10	14.31
33	0.24	1.06	1.53	2.71	2.38	4.22	3.65	8.10	5.35	11.82	7.39	16.86	9.37	17.59
34	0.05	0.43	1.84	3.31	1.56	5.15	2.46	10.17	3.54	14.71	4.62	21.05	5.65	21.92
35	-0.15	-0.29	2.08	4.05	0.66	6.29	0.82	12.53	1.20	16.03	1.34	26.05	-1.64	23.48
36	1.07	3.61	0.31	-0.24	5.51	0.14	9.20	0.14	13.43	0.68	19.19	0.90	24.75	1.48
37	1.10	3.42	1.29	1.48	6.00	2.96	9.54	4.53	13.27	3.18	18.22	8.75	22.88	9.28
38	0.64	2.42	0.98	1.54	4.17	2.91	6.54	5.17	9.42	7.42	13.54	10.12	17.36	10.67
39	0.47	1.82	1.31	2.46	3.42	3.88	5.25	7.05	7.50	10.02	10.44	13.93	13.17	14.63

40	0.23	1.14	1.63	3.25	2.58	4.96	4.06	9.08	5.72	12.76	7.73	17.87	9.63	18.66
41	0.00	0.36	2.00	3.68	1.50	5.63	2.23	10.78	3.25	15.28	4.27	21.72	5.23	22.54
42	-0.18	-0.38	2.30	4.70	0.59	7.11	0.71	13.27	1.01	18.65	1.14	26.31	1.20	27.19
43	1.13	4.11	0.27	-0.32	6.12	0.01	9.94	-0.03	14.15	0.45	19.17	0.68	24.87	1.24
44	0.98	3.41	0.57	0.59	5.05	1.49	8.37	2.56	12.02	3.98	16.05	5.37	20.54	5.93
45	0.71	2.80	1.04	1.62	4.63	2.94	7.10	5.25	9.91	7.53	13.68	9.96	17.33	10.42
46	0.46	1.90	1.30	2.51	3.68	4.26	5.79	7.65	8.09	10.71	11.33	14.63	14.27	15.21
47	0.26	1.19	1.68	3.55	2.65	5.43	4.19	9.72	5.87	13.49	7.68	18.63	9.51	19.24
48	0.11	0.24	1.85	3.92	1.36	5.99	2.15	11.30	3.22	15.79	4.24	22.31	5.35	22.98
49	-0.21	-0.46	2.19	5.02	0.45	7.46	0.52	13.87	0.97	19.47	0.96	26.93	1.03	27.67
50	1.03	4.00	0.30	-0.25	6.03	0.15	9.88	0.21	14.20	0.72	18.97	0.67	24.14	1.13
51	0.73	2.73	0.91	1.61	4.72	3.01	7.58	5.40	10.82	7.83	13.26	10.10	16.76	10.68
52	0.48	1.98	1.23	2.48	3.74	4.04	5.82	7.13	8.13	9.91	10.34	13.96	13.32	14.49
53	0.24	1.14	1.57	3.43	2.48	5.60	4.03	10.18	5.77	13.81	7.94	18.88	9.55	19.46
54	-0.17	-0.22	2.49	5.69	0.72	8.47	0.87	14.42	0.93	19.46	1.97	27.16	1.88	28.21
55	0.19	0.50	0.79	0.93	1.54	1.64	2.06	2.13	2.28	2.54	2.63	2.67	2.68	2.65
56	0.17	0.45	0.62	0.72	1.28	1.27	1.70	1.65	1.86	1.99	2.22	2.15	2.28	2.14

Appendix A.2: Wall CW1

Global response

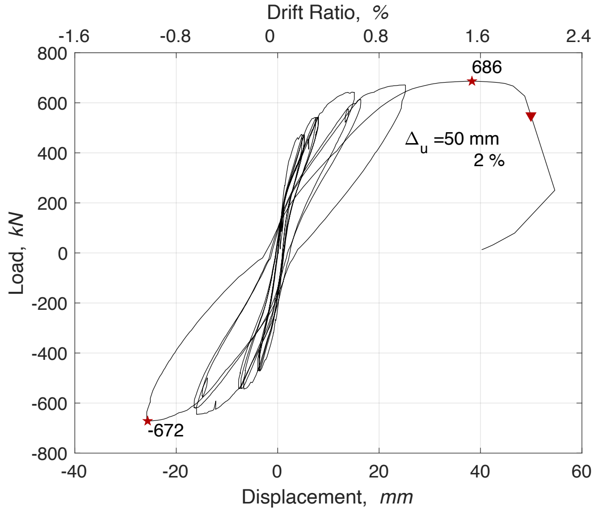

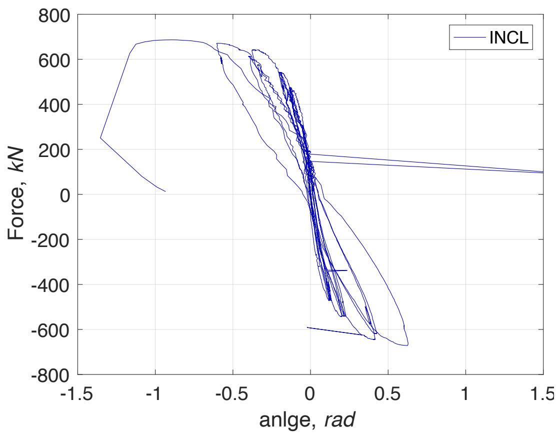

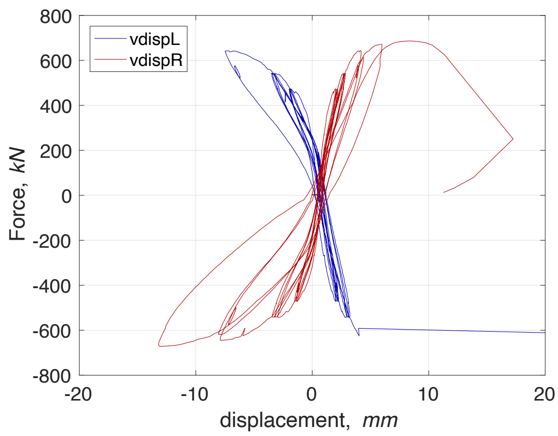

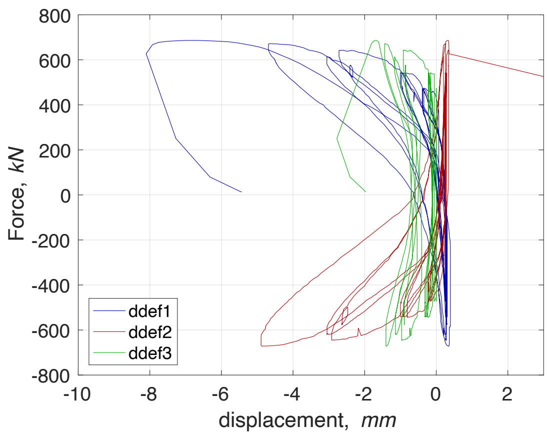

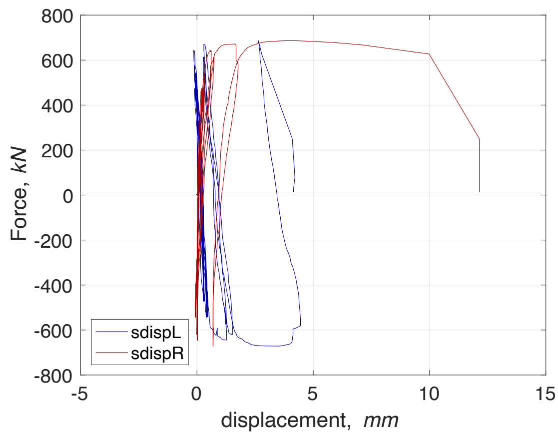

Table A-3. Wall CW1 data summary

Load Stage	LC kN	Δ^* mm	INCL rad	vdisp _L mm	vdisp _R mm	ddef1 mm	ddef2 mm	ddef3 mm	sdisp _R mm	sdisp _L mm
LS1'	270	1.42	-0.037	-0.10	1.01	0.07	0.19	0.00	0.08	0.01
LS1	474	4.77	-0.128	-1.90	2.01	-0.34	0.25	0.00	0.21	-0.10
LS2'	-270	-0.36	0.035	0.99	0.16	0.15	0.22	0.00	0.02	0.15
LS2	-472	-3.58	0.121	2.02	-1.34	0.25	-0.17	0.00	-0.04	0.28
LS3	473	5.24	-0.135	-1.98	2.17	-0.38	0.25	0.00	0.24	-0.08
LS4	-470	-3.57	0.122	2.10	-1.31	0.26	-0.17	0.00	-0.04	0.29
LS5	471	5.24	-0.135	-1.94	2.18	-0.39	0.25	0.00	0.25	-0.05
LS6	-471	-3.88	0.133	2.22	-1.47	0.27	-0.21	-0.05	-0.06	0.31
LS7	541	7.48	-0.194	-3.24	2.68	-0.86	0.26	-0.16	0.31	-0.10
LS8	-543	-6.62	0.199	2.89	-2.92	0.27	-0.80	-0.24	-0.08	0.41
LS9	543	8.06	-0.204	-3.48	2.83	-1.00	0.27	-0.21	0.32	-0.09
LS10	-541	-7.07	0.211	3.06	-3.11	0.29	-0.89	-0.27	-0.07	0.44
LS11	541	7.84	-0.194	-3.34	2.77	-0.94	0.29	-0.21	0.32	-0.04
LS12	-542	-7.37	0.217	3.12	-3.25	0.30	-0.95	-0.30	-0.07	0.46
LS13	643	14.65	-0.363	-7.23	4.12	-2.62	0.35	-0.88	0.59	-0.13
LS14	-645	-15.92	0.413	-	-7.87	0.28	-2.91	-0.96	0.01	1.26
LS15	613	16.39	-0.400	-	4.41	-3.05	0.20	-1.16	0.73	0.28
LS16	-619	-16.10	0.416	-	-7.88	0.25	-3.00	-1.12	0.00	1.48
LS17	672	25.08	-0.598	-	5.96	-4.66	0.26	-1.44	1.63	0.30
LS18	-672	-25.64	0.625	-	-13.11	0.35	-4.87	-1.40	0.69	3.53
LS19	686	38.32	-0.895	-	8.34	-6.85	0.32	-1.69	4.03	2.64

$^*\Delta$ =0.5*(hdisp_1 + hdisp_2)

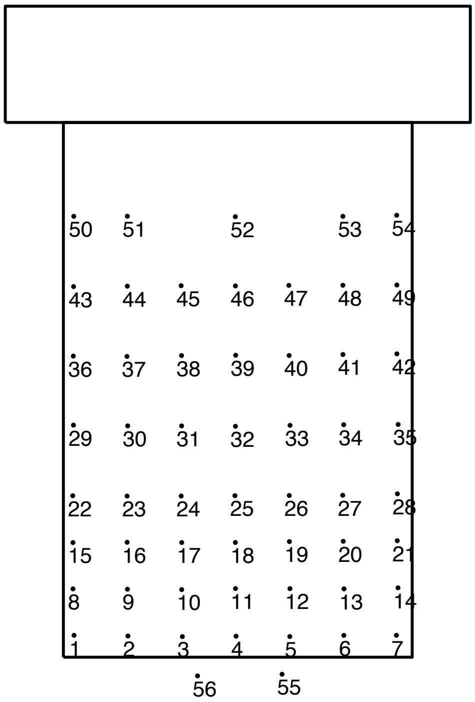

LED grid numbering

Table A-4. Relative displacements of LED grid of wall CW1

Relative horizontal displacements, mm

LED no.	LS1'	LS1	LS2'	LS2	LS7	LS8	LS13	LS14	LS17	LS18	LS19
1	0.18	0.33	-0.04	-0.17	0.33	-0.30	0.65	-0.64	-0.01	-0.01	0.62
2	0.20	0.47	-0.05	-0.23	0.58	-0.35	0.71	-0.77	-	-	-
3	0.29	0.56	0.00	-0.17	0.56	-0.22	0.79	-0.57	-	-	-
4	0.35	0.42	0.21	-0.08	0.49	-0.21	0.68	-0.55	-	-	-
5	0.30	0.57	0.09	-0.06	0.65	-0.15	0.90	-0.42	-	-	-
6	0.37	0.60	0.08	-0.08	0.75	-0.10	1.07	-0.29	-	-	-
7	0.26	0.39	0.05	0.03	0.64	0.08	0.99	0.07	1.35	-0.33	1.31
8	0.26	0.76	-0.16	-0.47	0.84	-0.90	1.24	-1.98	2.09	-3.17	3.57
9	0.39	0.69	0.04	-0.45	1.00	-0.80	1.44	-1.81	2.16	-3.10	3.41
10	0.32	0.69	-0.02	-0.38	0.93	-0.85	1.39	-1.76	2.21	-2.88	3.26
11	0.28	0.86	0.06	-0.37	1.09	-0.61	1.80	-1.06	2.94	-1.82	4.35
12	0.28	0.65	0.18	-0.38	0.98	-0.50	2.00	-0.98	2.94	-1.69	4.12
13	0.36	1.03	0.08	-0.31	1.02	-0.66	1.89	-1.07	3.55	-1.82	4.60
14	0.42	0.96	0.00	-0.33	1.11	-0.61	2.09	-1.14	3.47	-1.81	4.82
15	0.20	1.07	-0.13	-0.65	1.43	-1.42	2.16	-3.27	3.52	-5.10	5.71

16	0.32	0.96	-0.15	-0.67	1.23	-1.23	1.96	-3.11	3.46	-5.01	5.52
17	0.24	-0.21	-0.11	-0.52	-0.46	-1.02	0.01	-3.07	1.72	-5.11	3.90
18	0.41	1.07	-0.15	-0.73	1.40	-1.20	2.18	-2.68	4.11	-4.42	6.20
19	0.45	1.13	-0.04	-0.62	1.56	-1.07	2.98	-2.11	5.05	-3.49	7.41
20	0.50	1.10	-0.03	-0.58	1.77	-1.01	3.03	-2.02	5.27	-3.60	7.69
21	0.52	1.20	-0.02	-0.62	1.65	-0.99	3.02	-1.88	5.30	-3.55	7.79
22	0.32	1.31	-0.54	-1.32	1.82	-1.81	2.98	-4.59	5.70	-7.36	9.47
23	0.37	1.37	-0.09	-0.98	1.77	-1.84	2.93	-4.57	5.48	-6.97	9.08
24	0.59	1.41	-0.17	-1.07	1.99	-1.86	3.49	-4.34	6.01	-6.98	9.48
25	0.49	1.51	-0.26	-0.98	1.88	-1.85	3.23	-4.29	5.90	-6.94	9.23
26	0.43	1.53	-0.12	-0.89	2.11	-1.71	4.07	-3.47	6.94	-5.82	10.60
27	0.53	1.47	-0.16	-1.04	2.00	-1.61	4.00	-3.27	7.06	-5.44	10.60
28	0.64	1.63	-0.17	-1.09	1.96	-1.64	3.89	-3.26	6.92	-5.44	10.39
29	0.52	1.90	-0.39	-1.63	2.71	-2.97	4.71	-6.64	8.70	-10.40	13.97
30	0.54	1.94	-0.45	-1.76	2.73	-2.92	4.88	-6.61	8.66	-10.40	14.00
31	0.61	2.08	-0.25	-1.64	2.91	-2.80	5.40	-6.50	9.17	-10.32	14.41
32	0.64	2.01	-0.27	-1.66	2.82	-2.67	5.83	-5.98	9.72	-9.89	15.08
33	0.63	2.04	-0.34	-1.51	2.94	-2.69	5.72	-5.60	9.94	-9.10	15.35
34	0.69	1.98	-0.19	-1.45	3.07	-2.63	5.67	-5.34	9.88	-8.75	15.34
35	0.75	2.10	-0.39	-1.58	2.82	-2.55	5.79	-5.24	10.07	-8.55	15.30
36	0.68	2.52	-0.50	-2.20	3.75	-3.87	6.95	-8.41	11.53	-13.33	18.53
37	0.64	2.60	-0.60	-2.27	3.67	-3.80	7.04	-8.50	12.18	-13.34	19.10
38	0.88	2.50	-0.47	-2.14	3.90	-3.88	7.57	-8.34	12.92	-13.25	20.00
39	0.89	2.64	-0.35	-2.21	3.70	-3.72	7.61	-8.22	12.94	-13.28	19.89
40	0.79	2.56	-0.51	-2.26	3.68	-3.81	7.45	-8.38	12.77	-13.18	19.76
41	0.74	2.48	-0.57	-2.30	3.73	-3.81	7.42	-8.44	12.85	-13.34	19.84
42	0.79	2.52	-0.39	-2.12	3.81	-3.64	7.46	-7.74	13.30	-12.28	19.87
43	0.89	3.24	-1.07	-2.76	4.54	-4.74	8.75	-10.29	14.94	-16.67	23.02
44	0.90	3.13	-0.67	-2.94	4.58	-4.97	9.37	-10.71	16.01	-16.60	24.62
45	0.71	3.13	-0.87	-2.88	4.69	-4.90	9.55	-10.71	16.29	-16.56	24.68
46	0.96	3.17	-0.83	-2.90	4.75	-4.94	9.30	-10.52	15.95	-16.56	24.44
47	0.96	3.13	-0.73	-2.85	4.67	-4.84	9.19	-10.53	15.68	-16.56	24.39
48	1.10	3.39	-0.60	-2.80	4.85	-4.81	9.48	-10.42	16.17	-16.50	24.66
49	0.97	3.17	-0.77	-2.80	4.82	-5.07	9.32	-10.65	16.15	-16.72	24.79
50	-	-	-0.86	-3.40	5.64	-5.81	11.28	-12.36	19.53	-19.37	29.28
51	1.12	4.01	-0.93	-3.40	5.69	-5.89	10.84	-12.76	19.21	-19.68	29.18
52	1.19	4.03	-0.85	-3.48	5.68	-6.08	11.34	-12.91	19.34	-19.94	29.48
53	0.95	3.75	-1.15	-3.70	5.84	-6.17	11.18	-13.05	18.88	-19.84	29.38
54	0.84	3.59	-1.05	-3.62	5.20	-5.81	10.45	-12.83	18.73	-20.30	28.98
55	0.34	0.36	0.15	-0.08	0.47	-0.01	0.47	0.05	0.56	0.04	0.58
56	0.22	0.29	0.08	-0.02	0.38	0.07	0.43	-0.03	0.62	2.96	0.38

Relative vertical displacements, mm

LED no.	LS1'	LS1	LS2'	LS2	LS7	LS8	LS13	LS14	LS17	LS18	LS19
1	-0.20	0.31	-0.66	-0.99	0.34	-1.38	1.07	-2.00	0.01	0.01	6.27
2	-0.29	0.08	-0.62	-0.78	0.04	-1.00	0.53	-0.98	-	-	-
3	-0.39	-0.16	-0.61	-0.64	-0.28	-0.70	0.13	-0.40	-	-	-
4	-0.46	-0.28	-0.59	-0.38	-0.46	-0.46	-0.28	-0.01	-	-	-
5	-0.47	-0.47	-0.48	-0.15	-0.59	-0.11	-0.44	0.61	-	-	-
6	-0.51	-0.67	-0.37	0.12	-0.87	0.24	-0.87	1.45	-	-	-
7	-0.54	-0.88	-0.27	0.23	-1.27	0.35	-1.68	1.50	-2.35	3.07	-3.37
8	-0.16	0.69	-0.69	-1.12	0.87	-1.58	2.09	-2.36	5.72	-3.06	11.06
9	-0.27	0.35	-0.60	-0.85	0.50	-1.08	1.43	-1.07	4.21	-0.92	8.39
10	-0.35	0.03	-0.56	-0.60	0.07	-0.62	0.77	-0.01	2.64	0.84	5.65
11	-0.43	-0.11	-0.51	-0.33	-0.06	-0.28	0.52	0.26	2.06	1.47	4.44
12	-0.51	-0.46	-0.43	-0.11	-0.47	0.09	0.03	1.21	0.87	3.08	2.19
13	-0.57	-0.76	-0.40	0.14	-0.92	0.56	-0.91	2.16	-0.72	4.78	-0.39
14	-0.62	-1.04	-0.29	0.42	-1.41	0.92	-1.99	3.09	-2.72	6.41	-3.70
15	-0.09	1.05	-0.75	-1.25	1.36	-1.73	2.99	-2.65	6.98	-3.37	12.75
16	-0.23	0.65	-0.66	-0.92	0.88	-1.18	1.99	-1.21	5.12	-1.06	9.74
17	-0.38	0.28	-0.55	-0.56	0.44	-0.59	1.43	0.22	3.96	1.26	7.59
18	-0.41	-0.09	-0.53	-0.31	-0.02	-0.03	0.56	1.09	2.17	2.78	4.48
19	-0.48	-0.44	-0.45	0.05	-0.45	0.35	0.19	1.75	1.23	3.97	2.63
20	-0.57	-0.73	-0.35	0.39	-1.01	0.87	-0.98	2.88	-0.77	5.91	-0.60
21	-0.63	-1.13	-0.24	0.82	-1.53	1.44	-2.14	4.01	-2.96	7.77	-4.05
22	-0.11	1.22	-0.75	-1.29	1.73	-1.86	3.70	-2.77	8.17	-3.55	14.60
23	-0.20	0.82	-0.64	-0.96	1.18	-1.25	2.72	-1.32	6.28	-1.21	11.36
24	-0.32	0.38	-0.61	-0.63	0.74	-0.63	1.92	0.12	4.71	1.15	8.60
25	-0.41	-0.03	-0.51	-0.29	0.13	0.01	0.97	1.40	2.79	3.14	5.44
26	-0.51	-0.44	-0.42	0.07	-0.48	0.58	0.21	2.25	1.41	4.72	2.91
27	-0.60	-0.84	-0.35	0.42	-1.08	0.86	-1.05	2.98	-0.88	6.10	-0.67
28	-0.71	-1.24	-0.27	0.80	-1.68	1.57	-2.34	4.41	-3.15	8.41	-4.22
29	-0.08	1.36	-0.87	-1.49	2.35	-2.06	4.66	-3.01	9.33	-3.77	15.86
30	-0.22	0.83	-0.75	-1.05	1.33	-1.36	2.98	-1.46	6.65	-1.32	11.81
31	-0.39	0.36	-0.66	-0.72	0.81	-0.71	2.30	0.05	5.21	1.12	9.24
32	-0.49	-0.09	-0.55	-0.29	0.13	-0.01	1.44	1.58	3.51	3.43	6.24
33	-0.54	-0.56	-0.48	0.06	-0.57	0.65	0.14	2.70	1.27	5.20	2.70
34	-0.64	-0.94	-0.38	0.43	-1.23	1.16	-1.21	3.72	-1.12	7.09	-0.92
35	-0.79	-1.41	-0.27	0.82	-1.90	1.87	-2.61	5.01	-3.48	9.16	-4.62
36	-0.06	1.34	-1.01	-1.70	2.33	-2.29	5.17	-3.31	10.00	-4.08	16.38
37	-0.28	0.79	-0.90	-1.27	1.54	-1.59	3.92	-1.71	7.87	-1.60	13.20
38	-0.41	0.38	-0.78	-0.82	0.77	-0.78	2.83	0.00	6.01	0.93	10.01
39	-0.50	-0.12	-0.69	-0.45	0.09	-0.16	1.37	1.46	3.52	3.30	6.22

40	-0.66	-0.64	-0.57	-0.03	-0.68	0.58	-0.02	3.01	1.16	5.70	2.60
41	-0.79	-1.09	-0.45	0.42	-1.38	1.33	-1.38	4.66	-1.24	8.25	-1.10
42	-0.98	-1.60	-0.36	0.86	-2.04	2.07	-2.84	5.78	-3.67	10.13	-4.85
43	-0.10	1.25	-1.10	-1.89	2.29	-2.50	5.41	-3.51	10.27	-4.26	16.69
44	-0.34	0.75	-1.06	-1.39	1.43	-1.73	4.01	-1.83	8.03	-1.74	13.29
45	-0.56	0.20	-0.83	-0.96	0.62	-0.93	2.57	-0.28	5.68	0.67	9.52
46	-0.64	-0.28	-0.77	-0.54	-0.12	-0.27	1.21	1.31	3.31	3.12	5.97
47	-0.68	-0.82	-0.67	-0.03	-0.84	0.45	-0.32	2.90	0.92	5.59	2.38
48	-0.86	-1.21	-0.57	0.35	-1.49	1.26	-1.53	4.55	-1.38	8.10	-1.27
49	-1.03	-1.75	-0.36	0.85	-2.24	1.98	-3.00	5.99	-3.75	10.53	-4.90
50	-	-	-1.32	-2.00	2.00	-2.66	5.10	-3.79	9.67	-4.63	15.97
51	-0.42	0.40	-1.13	-1.54	1.16	-1.93	3.48	-1.94	7.17	-1.91	11.95
52	-0.65	-0.49	-0.90	-0.82	-0.17	-0.51	0.83	0.96	2.80	2.76	5.15
53	-1.01	-1.46	-0.73	0.06	-1.63	0.93	-1.78	3.88	-1.80	7.28	-1.52
54	-1.32	-2.07	-0.78	0.55	-2.95	1.51	-3.68	5.12	-4.41	9.10	-5.44
55	-0.42	-0.43	-0.38	-0.36	-0.70	-0.41	-0.82	-0.48	-0.75	-0.43	-0.76
56	-0.38	-0.45	-0.50	-0.53	-0.73	-0.62	-0.82	-0.66	-0.85	-0.90	-0.77

Appendix A.3: Wall CW2

Global response

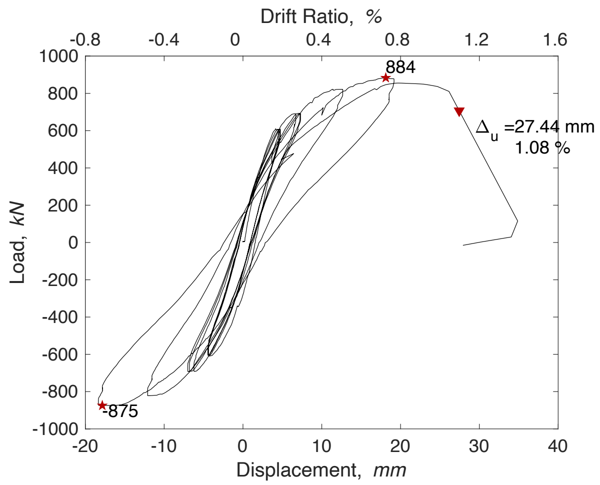

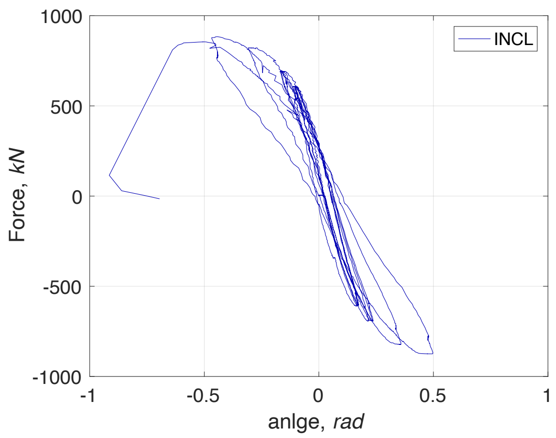

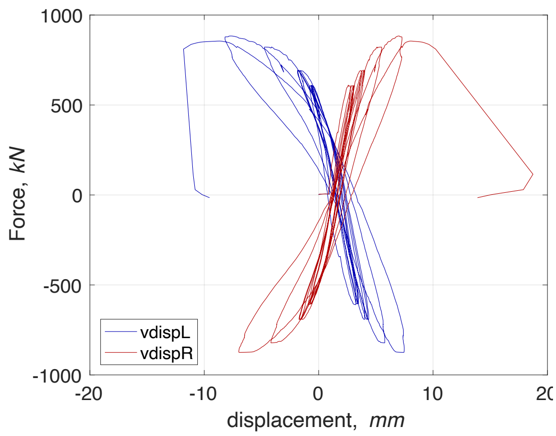

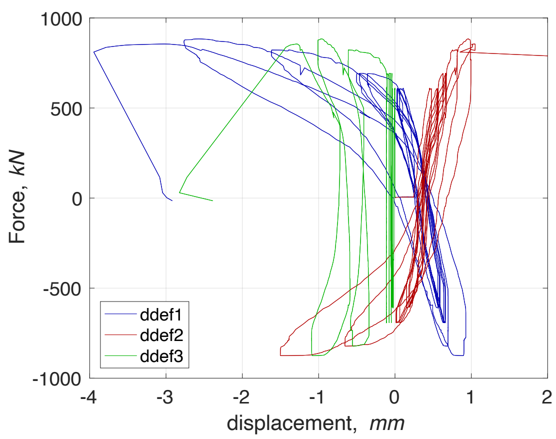

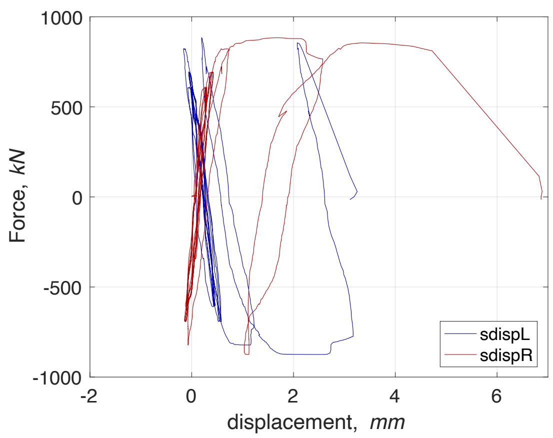

Table A-5. Wall CW2 data summary

Load Stage	LC kN	Δ^* mm	INCL rad	vdisp _L mm	vdisp _R mm	ddef1 mm	ddef2 mm	ddef3 mm	sdisp _R mm	sdisp _L mm
LS1'	349	2.01	-0.036	0.33	1.69	0.21	0.36	0.00	0.13	0.02
LS1	610	4.15	-0.098	-0.65	2.59	0.11	0.45	0.00	0.26	-0.05
LS2'	-344	-0.63	0.065	1.82	0.70	0.38	0.31	-0.02	0.07	0.23
LS2	-610	-4.35	0.168	3.24	-0.88	0.56	0.15	-0.03	-0.12	0.43
LS3	607	4.39	-0.094	-0.49	2.88	0.07	0.55	-0.03	0.27	0.01
LS4	-605	-4.22	0.168	3.35	-0.68	0.57	0.18	-0.03	-0.10	0.44
LS5	609	4.73	-0.102	-0.60	3.11	0.03	0.56	-0.04	0.29	0.00
LS6	-605	-4.35	0.170	3.44	-0.66	0.59	0.19	-0.04	-0.09	0.45
LS7	691	6.62	-0.151	-1.57	3.70	-0.34	0.63	-0.04	0.38	-0.06
LS8	-691	-6.19	0.217	4.02	-1.46	0.64	0.06	-0.05	-0.13	0.54
LS9	693	7.21	-0.166	-1.84	3.96	-0.46	0.66	-0.07	0.42	-0.06
LS10	-691	-6.46	0.223	4.16	-1.53	0.64	0.04	-0.08	-0.12	0.56
LS11	690	7.27	-0.166	-1.84	4.01	-0.49	0.67	-0.10	0.42	-0.05
LS12	-693	-6.87	0.233	4.33	-1.67	0.65	0.02	-0.11	-0.13	0.57
LS13	822	11.43	-0.275	-4.14	5.11	-1.39	0.76	-0.51	0.59	-0.13
LS14	-822	-12.09	0.359	5.77	-4.16	0.69	-0.65	-0.55	-0.07	1.15
LS15	884	18.12	-0.443	-7.67	7.00	-2.57	0.96	-0.96	1.67	0.19
LS16	-875	-17.85	0.487	7.33	-6.78	0.88	-1.44	-1.06	1.11	2.46
LS17	855	19.66	-0.508	-8.66	8.03	-3.02	1.05	-1.29	3.34	2.08

$^*\Delta$ =0.5*(hdisp_1 + hdisp_2)

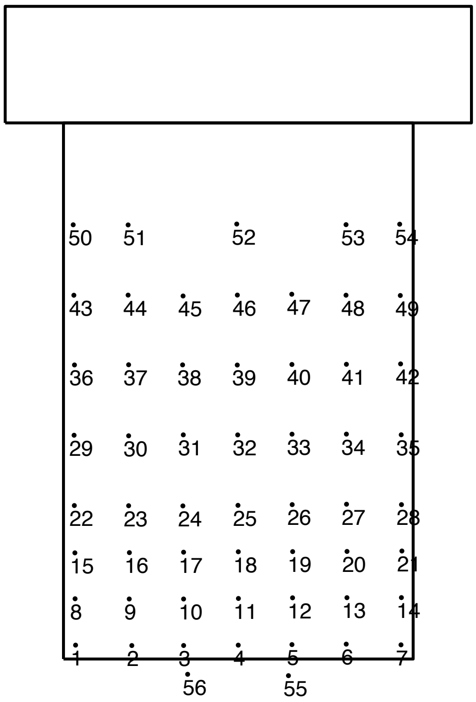

LED grid numbering

Table A-6. Relative displacements of LED grid of wall CW2

Relative horizontal displacements, mm

LED no.	LS1'	LS1	LS2'	LS2	LS7	LS8	LS13	LS14	LS17	LS18	LS19
1	0.16	0.30	-0.32	-0.74	0.22	-0.87	0.40	-1.10	0.61	-1.22	0.52
2	0.26	0.56	-0.12	-0.36	0.45	-0.42	0.71	-0.57	0.90	-0.84	0.76
3	0.17	0.33	-0.26	-0.52	0.33	-0.68	0.51	-0.96	0.68	-1.13	0.68
4	0.45	0.66	-0.01	-0.35	0.60	-0.50	0.73	-0.87	0.90	-1.01	0.98
5	0.23	0.35	-0.12	-0.50	0.37	-0.69	0.62	-0.88	0.91	-1.06	0.83
6	0.43	0.52	-0.07	-0.56	0.46	-0.58	0.80	-0.79	0.86	-1.19	0.98
7	0.32	0.62	-0.07	-0.51	0.69	-0.69	0.98	-1.06	1.37	-0.71	1.98
8	0.26	0.54	-0.43	-1.11	0.58	-1.35	0.90	-1.99	1.29	-2.87	0.91
9	0.23	0.62	-0.27	-0.97	0.51	-1.09	0.95	-1.82	1.38	-2.38	1.42
10	0.24	0.57	-0.36	-0.90	0.61	-1.17	0.90	-1.81	1.46	-2.36	1.45
11	0.28	0.59	-0.33	-0.93	0.76	-1.16	1.32	-1.56	1.89	-1.92	2.07
12	0.21	0.54	-0.32	-0.92	0.71	-1.10	1.25	-1.53	2.01	-1.70	2.22
13	0.26	0.53	-0.34	-0.97	0.63	-1.09	1.30	-1.52	2.06	-1.65	2.07
14	0.28	0.67	-0.34	-0.92	0.83	-1.04	1.47	-1.40	2.42	-1.36	3.07
15	0.35	0.82	-0.47	-1.32	1.02	-1.72	1.60	-2.81	2.47	-3.89	2.68
16	0.38	0.83	-0.44	-1.26	1.02	-1.60	1.57	-2.74	2.50	-3.77	2.72

17	0.39	0.83	-0.45	-1.29	1.06	-1.62	1.59	-2.64	2.46	-3.71	2.70
18	0.32	0.83	-0.46	-1.30	1.06	-1.65	2.08	-2.45	3.27	-3.43	3.46
19	0.43	0.84	-0.45	-1.22	1.19	-1.53	2.11	-2.25	3.37	-2.77	3.86
20	0.35	0.79	-0.44	-1.26	1.18	-1.54	2.12	-2.21	3.52	-2.82	3.92
21	0.29	0.82	-0.45	-1.27	1.11	-1.59	2.02	-2.25	3.39	-2.80	3.98
22	0.41	1.12	-0.69	-1.83	1.56	-2.34	2.40	-3.85	3.78	-5.26	4.18
23	0.54	1.11	-0.66	-1.93	1.69	-2.22	2.73	-3.64	3.78	-5.10	4.21
24	0.40	1.13	-0.55	-1.68	1.61	-2.16	2.81	-3.49	4.41	-4.91	4.77
25	0.43	1.14	-0.57	-1.75	1.61	-2.20	2.99	-3.48	4.78	-4.82	5.38
26	0.45	1.20	-0.59	-1.77	1.51	-2.16	2.93	-3.48	4.80	-4.76	5.41
27	0.50	1.22	-0.57	-1.74	1.67	-2.23	3.09	-3.28	4.96	-4.26	5.71
28	0.47	1.19	-0.57	-1.76	1.67	-2.23	3.01	-3.30	4.96	-4.27	5.70
29	0.66	1.62	-0.78	-2.41	2.36	-2.99	4.00	-5.10	6.40	-7.19	7.15
30	0.61	1.58	-0.89	-2.58	2.35	-3.15	4.15	-5.33	6.64	-7.30	7.46
31	0.67	1.64	-0.82	-2.38	2.41	-3.12	4.32	-5.08	6.97	-7.12	7.94
32	0.70	1.73	-0.77	-2.44	2.44	-3.12	4.37	-5.10	7.17	-7.14	8.08
33	0.65	1.63	-0.80	-2.44	2.32	-3.13	4.37	-5.09	7.01	-7.22	7.92
34	0.68	1.63	-0.76	-2.44	2.41	-3.12	4.34	-4.89	7.10	-6.68	8.03
35	0.56	1.56	-0.84	-2.49	2.30	-3.13	4.20	-5.00	6.88	-6.74	7.86
36	0.87	2.19	-1.08	-3.23	3.30	-4.20	5.88	-6.87	9.48	-9.59	10.59
37	0.84	2.16	-1.05	-3.16	3.27	-4.03	5.82	-6.78	9.33	-9.49	10.60
38	0.77	2.14	-1.08	-3.26	3.22	-4.14	5.75	-6.92	9.37	-9.58	10.73
39	0.89	2.14	-1.04	-3.15	3.33	-4.13	5.91	-6.77	9.51	-9.47	10.69
40	0.90	2.15	-1.00	-3.15	3.24	-4.07	5.79	-6.88	9.30	-9.58	10.63
41	0.87	2.18	-0.90	-3.12	3.12	-3.92	5.78	-6.69	9.30	-9.46	10.54
42	0.84	2.15	-1.06	-3.20	3.20	-4.16	5.79	-6.83	9.39	-9.45	10.64
43	1.00	2.70	-1.43	-4.03	4.08	-5.14	7.37	-8.70	11.59	-11.99	13.17
44	1.09	2.71	-1.23	-3.93	4.11	-4.99	7.27	-8.43	11.50	-11.70	13.05
45	1.00	2.67	-1.38	-3.95	4.09	-5.18	7.39	-8.60	11.79	-12.04	13.41
46	1.08	2.76	-1.30	-3.98	4.13	-5.19	7.40	-8.66	11.84	-12.03	13.42
47	0.98	2.72	-1.36	-4.01	4.08	-5.14	7.28	-8.69	11.66	-12.01	13.18
48	1.01	2.75	-1.33	-3.95	4.01	-5.08	7.36	-8.44	11.77	-11.80	13.28
49	1.09	2.66	-1.42	-3.96	4.20	-5.09	7.28	-8.63	11.69	-12.22	13.28
50	1.13	3.30	-1.59	-4.69	4.97	-5.99	8.65	-10.18	13.92	-14.22	15.78
51	1.33	3.32	-1.58	-4.86	5.04	-6.26	8.89	-10.53	14.03	-14.66	15.94
52	1.29	3.35	-1.59	-4.78	5.06	-6.17	9.01	-10.36	14.38	-14.48	16.38
53	1.23	3.24	-1.58	-4.78	4.97	-6.15	8.86	-10.44	14.13	-14.47	16.00
54	1.19	3.24	-1.63	-4.77	4.89	-6.19	8.72	-10.38	13.87	-14.51	15.74
55	0.29	0.32	-0.04	-0.29	0.29	-0.25	0.40	-0.31	0.50	-0.29	0.50
56	0.19	0.27	-0.08	-0.34	0.15	-0.37	0.21	-0.40	0.31	-0.42	0.28

Relative vertical displacements, mm

LED no.	LS1'	LS1	LS2'	LS2	LS7	LS8	LS13	LS14	LS17	LS18	LS19
1	-0.46	0.01	-1.13	-1.81	-0.24	-2.19	0.22	-2.65	1.48	-3.30	1.49
2	-0.51	-0.10	-1.12	-1.65	-0.31	-1.94	0.00	-2.43	0.79	-2.80	0.96
3	-0.64	-0.49	-0.97	-1.21	-0.70	-1.43	-0.50	-1.32	0.26	-1.28	0.40
4	-0.85	-0.90	-1.03	-1.10	-0.99	-1.19	-0.74	-0.74	-0.26	-0.58	-0.23
5	-0.75	-0.92	-0.85	-0.61	-1.21	-0.61	-1.12	-0.11	-0.78	0.26	-0.90
6	-1.01	-1.33	-0.69	-0.12	-1.80	0.03	-2.05	1.09	-1.78	1.89	-2.07
7	-0.87	-1.30	-0.57	0.12	-1.81	0.28	-2.33	1.13	-3.00	1.92	-3.71
8	-0.45	0.06	-1.25	-2.06	0.06	-2.48	0.69	-3.13	2.44	-3.91	2.93
9	-0.58	-0.18	-1.12	-1.66	-0.38	-1.97	0.16	-2.23	1.51	-2.54	1.90
10	-0.67	-0.49	-1.04	-1.32	-0.68	-1.52	-0.36	-1.39	0.55	-1.31	0.74
11	-0.73	-0.75	-0.95	-1.00	-0.91	-1.07	-0.44	-0.61	0.30	-0.33	0.33
12	-0.82	-0.98	-0.87	-0.61	-1.28	-0.60	-1.18	-0.12	-0.80	0.25	-0.91
13	-0.89	-1.19	-0.75	-0.25	-1.64	-0.20	-1.90	0.42	-2.07	1.05	-2.34
14	-0.99	-1.47	-0.60	0.14	-2.08	0.29	-2.71	1.15	-3.43	2.23	-4.15
15	-0.46	0.13	-1.38	-2.30	0.40	-2.78	1.25	-3.59	3.42	-4.52	4.10
16	-0.58	-0.21	-1.23	-1.81	-0.11	-2.14	0.53	-2.44	2.20	-2.88	2.65
17	-0.68	-0.50	-1.13	-1.44	-0.55	-1.65	-0.11	-1.50	1.02	-1.44	1.27
18	-0.78	-0.78	-1.02	-1.04	-0.96	-1.12	-0.40	-0.50	0.52	0.01	0.53
19	-0.89	-1.04	-0.90	-0.64	-1.39	-0.57	-1.27	0.09	-0.89	0.67	-0.99
20	-0.98	-1.32	-0.78	-0.21	-1.83	-0.05	-2.14	0.86	-2.36	1.81	-2.77
21	-1.09	-1.63	-0.64	0.28	-2.33	0.58	-3.05	1.81	-3.89	3.17	-4.58
22	-0.47	0.18	-1.47	-2.45	0.60	-2.97	1.72	-3.85	4.23	-4.81	5.00
23	-0.59	-0.16	-1.31	-1.99	0.07	-2.32	0.95	-2.71	2.98	-3.14	3.53
24	-0.73	-0.53	-1.23	-1.56	-0.47	-1.79	0.43	-1.68	1.92	-1.67	2.20
25	-0.86	-0.86	-1.10	-1.13	-1.02	-1.21	-0.45	-0.57	0.64	-0.05	0.74
26	-0.95	-1.15	-0.96	-0.69	-1.51	-0.60	-1.40	0.45	-1.00	1.30	-1.12
27	-1.09	-1.50	-0.82	-0.19	-2.07	0.06	-2.40	1.26	-2.63	2.37	-3.07
28	-1.20	-1.81	-0.67	0.35	-2.57	0.75	-3.35	2.25	-4.24	3.80	-4.95
29	-0.52	0.17	-1.66	-2.74	0.72	-3.31	2.31	-4.26	5.12	-5.26	5.92
30	-0.69	-0.23	-1.51	-2.21	0.06	-2.61	1.33	-3.03	3.57	-3.55	4.13
31	-0.82	-0.60	-1.36	-1.73	-0.55	-1.98	0.52	-1.88	2.25	-1.89	2.58
32	-0.96	-0.96	-1.25	-1.27	-1.13	-1.36	-0.55	-0.76	0.50	-0.24	0.59
33	-1.08	-1.27	-1.08	-0.78	-1.67	-0.68	-1.58	0.44	-1.19	1.45	-1.37
34	-1.21	-1.62	-0.92	-0.25	-2.22	-0.05	-2.58	1.42	-2.88	2.67	-3.36
35	-1.37	-2.04	-0.76	0.31	-2.87	0.75	-3.72	2.70	-4.65	4.51	-5.37
36	-0.61	0.13	-1.87	-3.02	0.65	-3.60	2.75	-4.63	5.82	-5.70	6.61
37	-0.78	-0.28	-1.71	-2.46	0.01	-2.88	1.57	-3.37	3.93	-3.91	4.47
38	-0.93	-0.68	-1.52	-1.91	-0.65	-2.18	0.42	-2.08	2.18	-2.09	2.44
39	-1.08	-1.05	-1.36	-1.42	-1.22	-1.52	-0.67	-0.91	0.35	-0.46	0.40

40	-1.22	-1.44	-1.20	-0.87	-1.87	-0.84	-1.78	0.33	-1.40	1.33	-1.63
41	-1.41	-1.86	-1.04	-0.36	-2.53	-0.11	-2.86	1.59	-3.13	3.12	-3.62
42	-1.54	-2.27	-0.86	0.25	-3.16	0.65	-4.05	2.92	-5.03	4.97	-5.77
43	-0.68	0.03	-1.96	-3.17	0.50	-3.80	2.54	-4.80	5.59	-5.89	6.36
44	-0.90	-0.43	-1.91	-2.64	-0.13	-3.17	1.40	-3.68	3.87	-4.23	4.34
45	-1.08	-0.82	-1.73	-2.12	-0.82	-2.37	0.17	-2.36	1.96	-2.41	2.25
46	-1.24	-1.24	-1.56	-1.61	-1.48	-1.74	-0.91	-1.12	0.19	-0.63	0.23
47	-1.41	-1.65	-1.39	-0.99	-2.09	-0.96	-2.06	0.20	-1.67	1.22	-1.92
48	-1.49	-1.99	-1.21	-0.42	-2.66	-0.23	-3.10	1.44	-3.41	2.89	-3.91
49	-1.64	-2.37	-0.96	0.20	-3.26	0.52	-4.19	2.72	-5.19	4.64	-5.90
50	-0.90	-0.08	-2.41	-3.61	0.31	-4.37	2.72	-5.45	5.76	-6.60	6.62
51	-1.09	-0.54	-2.09	-2.89	-0.30	-3.37	1.27	-3.95	3.74	-4.55	4.27
52	-1.46	-1.51	-1.78	-1.79	-1.75	-1.95	-1.23	-1.29	-0.24	-0.88	-0.21
53	-1.78	-2.29	-1.38	-0.66	-2.99	-0.45	-3.40	1.20	-3.71	2.69	-4.22
54	-1.97	-2.69	-1.17	-0.03	-3.66	0.34	-4.61	2.60	-5.67	4.58	-6.39
55	-0.19	-0.19	-0.13	-0.15	-0.22	-0.14	-0.22	-0.03	-0.11	-0.04	-0.07
56	-0.22	-0.18	-0.31	-0.50	-0.32	-0.52	-0.29	-0.43	-0.09	-0.48	-0.03

Appendix B: SDOF approach validation

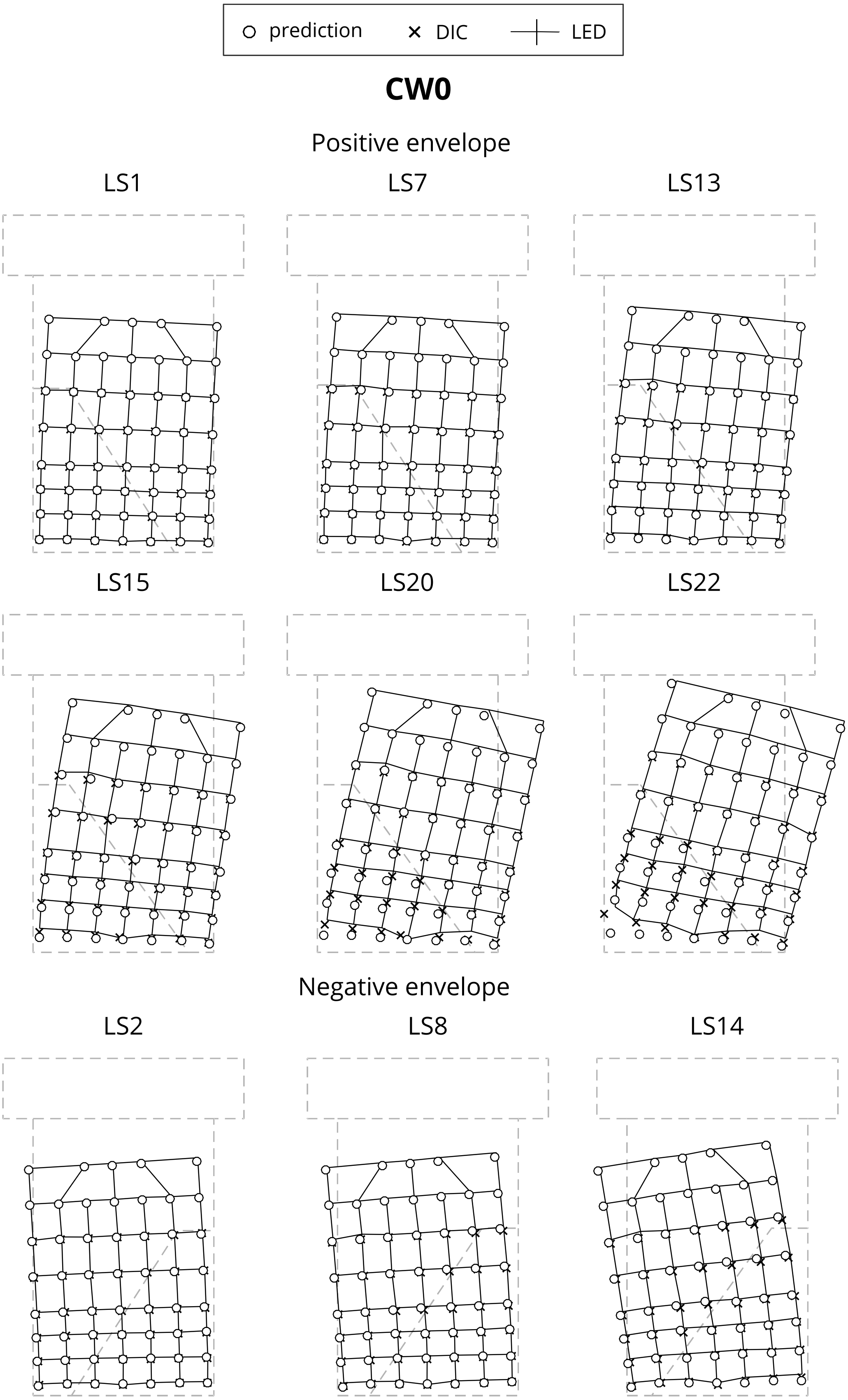

Figure B-1. Specimen CW0: predicted versus measured displacement patterns along the envelope of response magnified x15

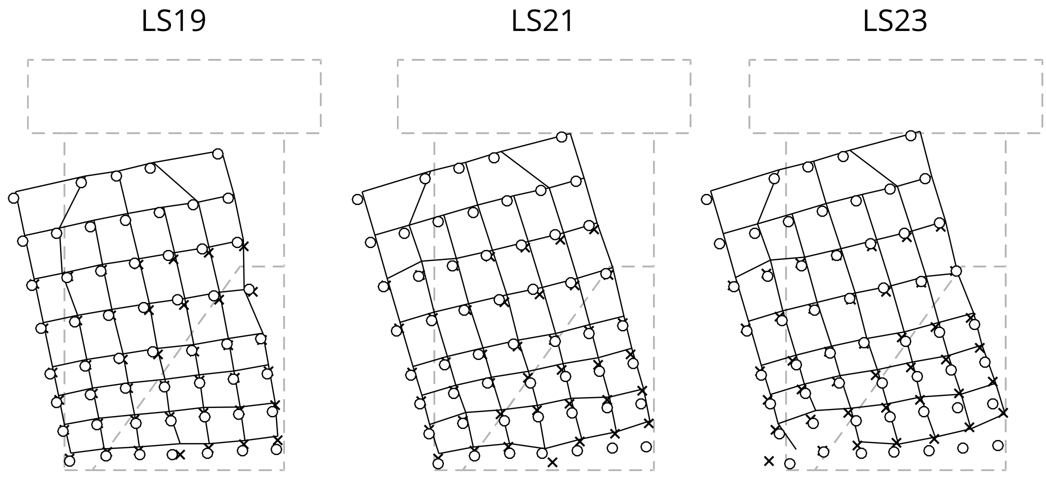

Figure B-1. Specimen CW0: predicted versus measured displacement patterns along the envelope of response magnified x15 (continued)

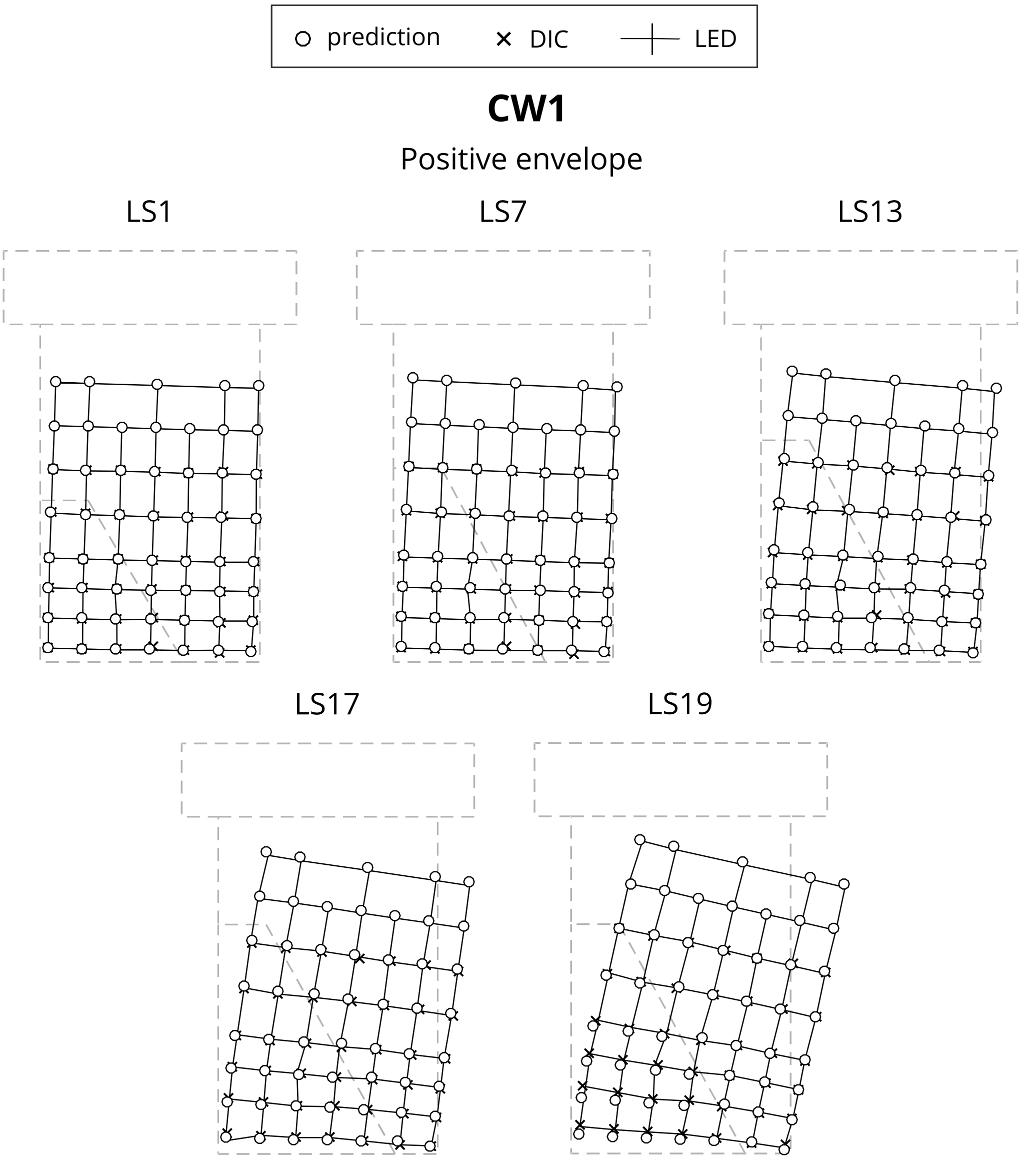

Figure B-2. Specimen CW1: predicted versus measured displacement patterns along the envelope of response magnified x15

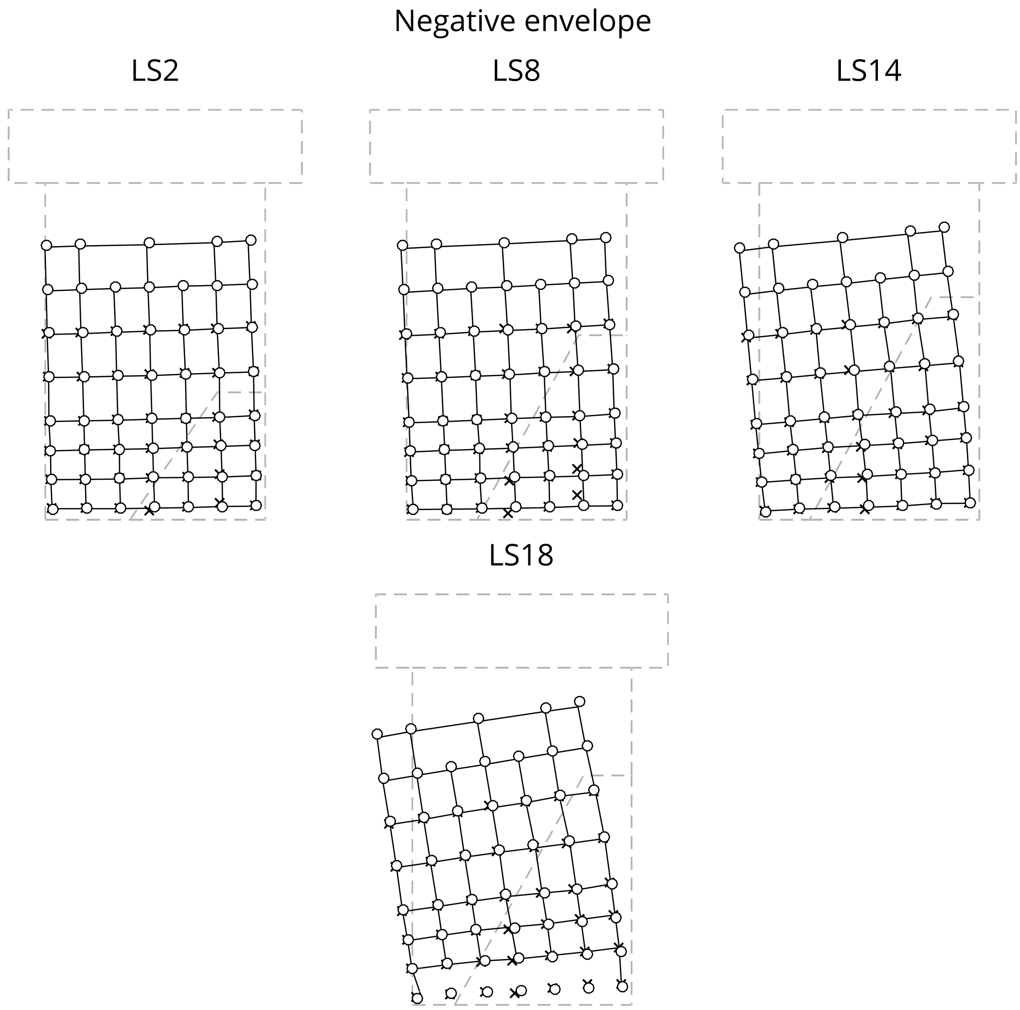

Figure B-2. Specimen CW1: predicted versus measured displacement patterns along the envelope of response magnified x15 (continued)

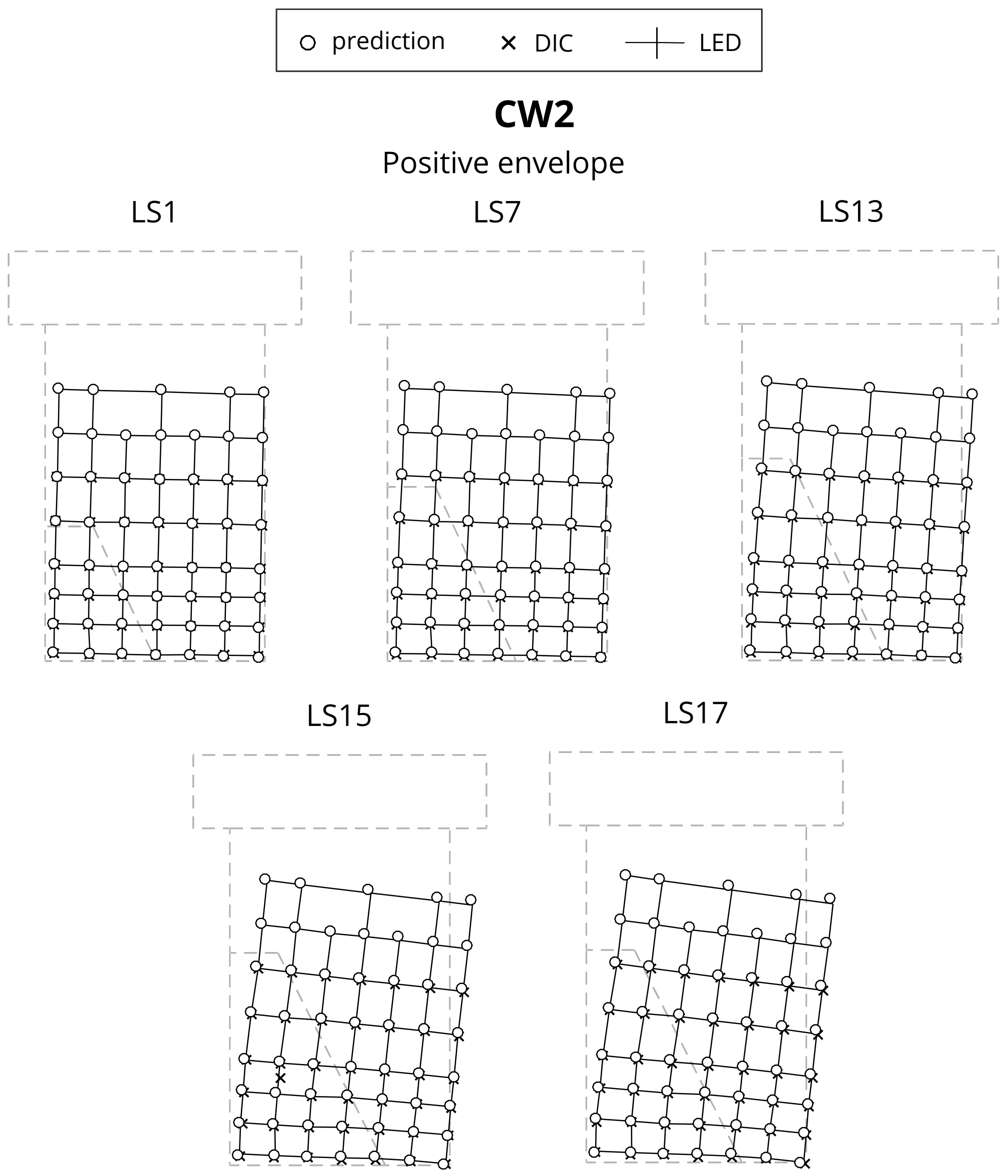

Figure B-3. Specimen CW2: predicted versus measured displacement patterns along the envelope of response (magnification x15)

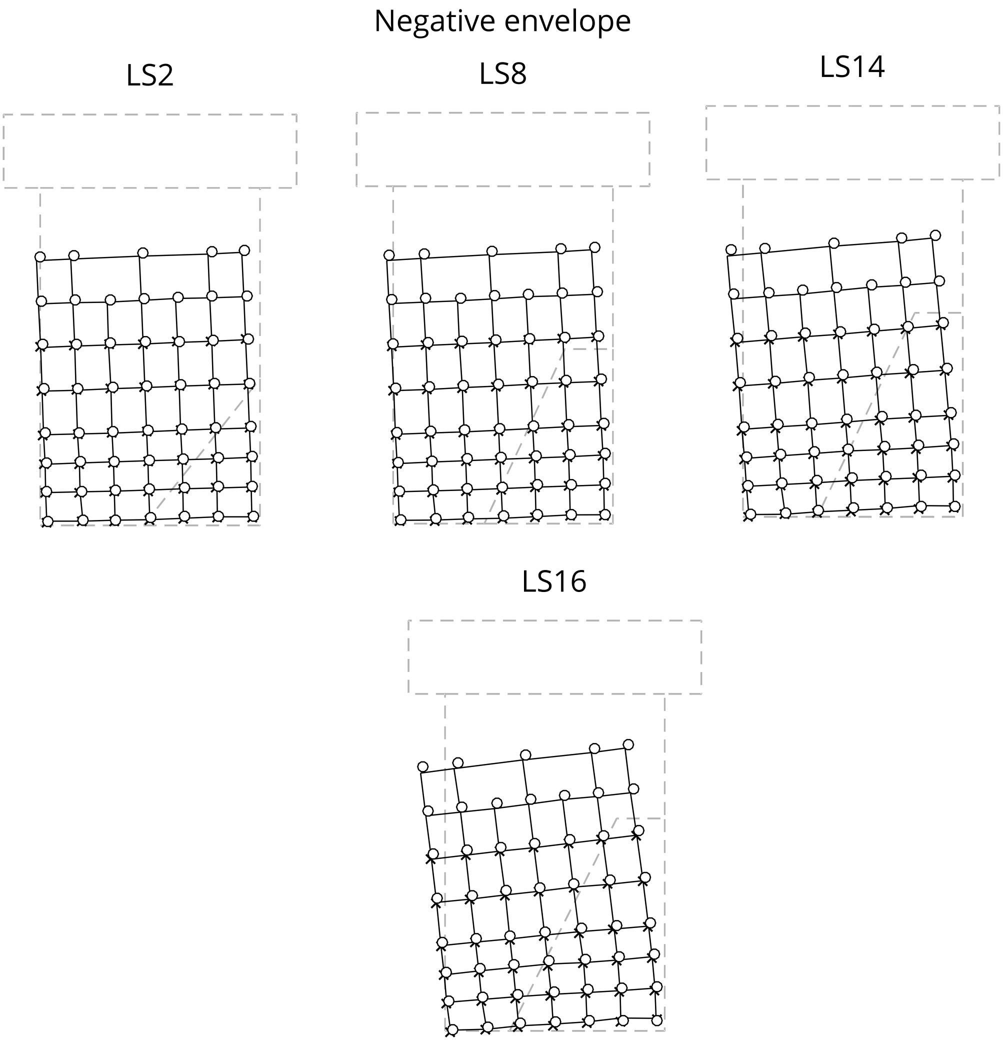

Figure B-3. Specimen CW2: predicted versus measured displacement patterns along the envelope of response (magnification x15, continued)